PEDRO PAZZOTO CACCIARI

A coupled TRS-DFN-DEM approach to assess the role of rock foliation on the stability of shallow tunnels in discontinuous rock masses

São Paulo
2019

PEDRO PAZZOTO CACCIARI

A coupled TRS-DFN-DEM approach to assess the role of rock foliation on the stability of shallow tunnels in discontinuous rock masses

Thesis presented to the Engineering School of University of São Paulo in conformity with the requirements for the degree of Doctor of Science.

Concentration area: Geotechnical Engineering

Advisor: Prof. Dr. Marcos Massao Futai

São Paulo

2019

Catalogação-na-publicação

Cacciari, Pedro
A coupled TRS-DFN-DEM approach to assess the role of rock foliation on the stability of shallow tunnels in discontinuous rock masses / P. Cacciari -- São Paulo, 2019.
202 p.

Tese (Doutorado) - Escola Politécnica da Universidade de São Paulo. Departamento de Engenharia de Estruturas e Geotécnica.

1.Geotecnia 2.Mecânica das Rochas I.Universidade de São Paulo. Escola Politécnica. Departamento de Engenharia de Estruturas e Geotécnica II.t.

Acknowledgments

The research work presented in this thesis has been generously supported by the company VALE SA (TUNELCON project); the National Council for Scientific and Technological Development (CNPq) (scholarships); and the Department of Economic Development, Science, Technology and Innovation of São Paulo (SDECTI) (DST unit and TLS equipment).

I would like to wholeheartedly thank my supervisor Dr. Marcos Massao Futai for giving me the opportunity and providing the means to pursue one of my life goals. Massao, I am deeply grateful for having you as my mentor and friend. It has been a great honor and privilege to be your student. I also would like to thank Silvia Suzuki for all her dedication and care with our research group.

I am grateful for being part of the GeoInfraUSP research group and the graduate program in Civil Engineering of the Engineering School of the University of São Paulo, where I was able to work with amazing people, including grad students and technicians, and learn from distinguishable professors.

On a personal level, I would like to thank my beloved wife Milene for her love and patience and for encouraging me to pursue the academic career. My parents Nadeia and Paulo and my sister Licia for the unconditional love and support given during this period. Finally, my newborn son Bruno, just for coming and bringing so much happiness to my life!

Abstract

For engineering purposes, hard rock masses at shallow depths are generally considered sets of discrete blocks defined by intersecting discontinuities such as bedding planes, foliation, banding contacts, fractures, shear zones, faults, etc. Under low confinement conditions, gravity-driven sliding on the discontinuities and rotation of the individual rock blocks are the major cause of stability problems in tunnels, while stress-induced failure of intact rock material is unusual. Therefore, the geometrical (shape, spatial orientation, size, and intensity) and mechanical (strength and deformability) characterization of geological discontinuities are essential in such cases. Among the numerical methods, the discrete element method (DEM) is the most suitable for representing discontinuous rock masses and simulating the aforementioned instability mechanisms.

Recently, terrestrial remote sensing (TRS) techniques have been used to create digital 3D rock mass models and perform discontinuity mapping, increasing the amount of discontinuity data (position, orientations, trace lengths, etc.) available in geological surveys. The results obtained from TRS mapping are suitable for generating stochastic discrete fracture network (DFN) models, which better represent the natural variability of the discontinuity geometrical parameters using their probability distributions. Moreover, the mechanical behavior of each DFN (each discontinuity set modeled) must be characterized considering the particularities of each geological structure type (e.g., fractures, foliations, faults, etc.).

This doctoral thesis presents a coupled TRS-DFN-DEM approach for modeling tunnels in discontinuous metamorphic rock masses. First, an extensive laboratory program, including direct shear tests and pull-off tests, showed major influence of the mica content on the mechanical behavior of isolated foliation planes. A comparison between pull-off tests, direct tension tests, and the Brazilian disc tests, indicated the first as a new alternative with practical advantages for assessing the tensile strength of rocks and geological structures. The laboratory results allowed the introduction of a new parameter, defined as the percentage of foliation surface area covered by mica (M_a), included as an independent variable of a 3D strength envelope for foliation planes.

Thereafter, a practical methodology was developed to create continuous DFNs along tunnels, based on detailed TRS geological mapping and automatic discontinuity analyses by window sapling methods. The continuous DFNs highlight the special variability of discontinuity

volumetric intensities along the tunnel axis, which increases the similarity between virtual (DFN-bases) and real (TRS-based) fracture trace maps. Moreover, the automation of complex discontinuity analyses and DFN generations reduces the time required for creating the DEM models from geological mapping of rock faces.

Finally, a case study showed that the mica content on foliation planes explains the actual stability of an old shallow tunnel constructed in a discontinuous gneissic rock mass. Thus, underestimating their strength by attributing null cohesions and tensile strength causes unrealistic instability conditions to the tunnel. Numerical analysis considering different weathering scenarios showed that major failures could occur in the tunnel depending on the weathering advance over time.

Keywords: Foliation, Shear Strength, Tensile Strength, Mica Content, Terrestrial Laser Scanner; Discrete Fracture Network; Discrete Element Method.

Resumo

Para propósitos de engenharia, maciços rochosos em profundidades rasas são, geralmente, considerados conjuntos de blocos definidos por descontinuidades como acamamento, foliação, bandamento, fraturas, zonas de cisalhamento, falhas e etc. Em condições de baixo confinamento, escorregamentos e rotações de blocos individuais (por gravidade), são a principal cause de problemas de estabilidade em túneis, enquanto rupturas induzidas por tensões não são usuais. Portanto, as características geométricas (forma, orientação espacial, tamanho e intensidade) e mecânicas (resistência e deformabilidade) das descontinuidades são essenciais nestes casos. Dentre os métodos numéricos existentes, o método dos elementos discretos (MED) é o mais adequado para representar maciços rochosos descontínuos e simular os problemas de estabilidade anteriormente mencionados.

Recentemente, sensoriamento remoto terrestre (SRT) tem sido utilizado para criar modelos digitais 3D de maciços rochosos para fins de mapeamento de descontinuidades, aumentando a quantidade de dados (posição, orientação, comprimento dos traços, etc.) disponíveis em investigações geológicas. Os resultados obtidos a partir de mapeamento via SRT são adequados para gerar modelos de redes discretas de fraturas (RDF), que representam, adequadamente, a variabilidade natural dos parâmetros geométricos das descontinuidades a partir das funções de densidade de probabilidade. Além disso, o comportamento mecânico de cada RDF (cada conjunto de descontinuidades) precisa ser caracterizado considerando as particularidades de cada tipo de estrutura geológica (e.g. fraturas, foliação, falhas e etc.)

Esta tese de doutorado apresenta uma técnica baseada no acoplamento entre SRT-RDF-MED para modelar túneis construídos em maciços rochoso metamórficos descontínuos. Primeiramente, uma campanha laboratorial extensiva, incluindo testes de cisalhamento direto e de arrancamento, mostrou forte influência da quantidade de mica no comportamento mecânico de planos de foliação isolados. Uma comparação entre testes de arrancamento, tração direta e compressão diametral mostrou que o primeiro se trata de uma nova alternativa com vantagens práticas para investigar a resistência à tração de rochas e estruturas geológicas. Os resultados de laboratório possibilitaram a introdução de um novo parâmetro, definido como a porcentagem da área coberta por mica nos planos de foliação (M_a), incluído como variável independente em uma envoltória de resistência 3D para planos de foliação.

Uma metodologia prática foi desenvolvida para criar RDFs continuas ao longo de túneis, baseando-se mapeamento detalhado via SRT e análises de descontinuidades automáticas, pelo método de janelas de amostragem. As RDFs contínuas evidenciam a variabilidade de intensidade volumétrica das descontinuidades ao longo do túnel, aumentando a similaridade entre mapas de traços de fraturas virtuais (baseados em RDFs) e reais (baseados em SRT). Além disso, a automatização de análises de descontinuidades complexas e da geração de RDFs reduz o tempo necessário para criação de modelos pelo MED a partir do mapeamento geológico de afloramentos rochosos.

Por fim, um estudo de caso mostrou que a quantidade de mica nos planos de foliação explica o atual estado de estabilidade de um túnel antigo, construído em maciço rochoso gnáissico descontínuo. Portanto, subestimar a resistência desta estrutura geológica, anulando sua coesão e sua resistência à tração, causa condições de estabilidade irreais para o túnel. Análises numéricas com diferentes cenários de alteração por intemperismo mostraram que problemas de estabilidade poderiam ocorrer neste túnel, dependendo do avanço da alteração causada por intemperismo ao longo do tempo.

Palavras chave: Foliação, Resistência ao Cisalhamento, Resistência à Tração, Teor de Mica, Escâner a Laser Terrestre, Rede Discreta de Fraturas; Método dos Elementos Discretos.

List of Symbols

P_{32}	Volumetric intensity
P_{32}^{i}	Volumetric intensity of the ith tunnel position
P_{32}^{t}	Volumetric intensity of a finite section of the tunnel
$Er(i)$	Volumetric intensity error
P_{21}	Trace intensity
C_{21}	Constant of proportionality between P_{32} and P_{21}
P_{10}	Linear intensity
k	Fisher dispersion factor
T_{cc}	Trace with both ends contained
T_{tc}	Trace with one end contained and the other end censored
T_{tt}	Trace with both ends censored
l_m	Measured mean trace length
l_{sd}	Standard deviation of measured trace lengths
μ	Unbiased mean trace length
σ	Standard deviation of unbiased trace lengths
μ_D	Mean discontinuity diameter
σ_D	Standard deviation of discontinuity diameters
$f(l)$	Probability density function of measured trace lengths
$g(l)$	Probability density function of unbiased trace lengths
$g(D)$	Probability density function of discontinuity diameters
$E(D^n)$	nth moments of $g(D)$
$E(l^n)$	nth moments of $g(l)$
N	Number of discontinuities intersecting a sampling window
N_{min}	Minimum number of discontinuities intersecting a sampling window
N_l	Number of foliation planes cutting the scanline
L_T	Total scanline length
S_i	Area of each disk-shaped discontinuity in the DFNs
V	Volume of the DFN domain
$\bar{\sigma}_{BDT}$	Average tensile strength obtained by BDTs
$\bar{\sigma}_{DTT}$	Average tensile strength obtained by DTTs
$\bar{\sigma}_{POT}$	Average tensile strength obtained by POTs

σ_{BDT}	Tensile strength obtained by BDT
σ_{DTT}	Tensile strength obtained by DTTs
σ_{POT}	Tensile strength obtained by POTs
σ_c	Uniaxial compressive strength
d_{fp}	Failure plane depth
d_{pc}	Partial core depth
d_s	Distance between core and failure plane depths
$\Delta \mathrm{F}_n$	Change in normal force
$\Delta\delta_n$	Change in normal displacement
$FM_a^{\sigma_t,c,\varphi}$	Mica degradation factors for tensile strength, cohesion and friction angle
K_{ne}	Equivalent normal stiffness of the rock mass
c_{max}	Maximum cohesion of the 3D strength envelope for foliation planes
c_{min}	Minimum cohesion of the 3D strength envelope for foliation planes
$n_{t,c,\varphi}$	Third parameter of the 3D strength envelope for foliation planes
$\alpha_{t,c,\varphi}$	Second parameter of the 3D strength envelope for foliation planes
$\beta_{t,c,\varphi}$	First parameter of the 3D strength envelope for foliation planes
δ_n	Normal displacement
δ_s	Shear displacement
σ_n	Normal stress
σ_s	Shear stress
σ_{sp}	Peak shear strength of foliation planes (laboratory tests)
σ_{spp}	Postpeak shear strength of foliation planes (laboratory tests)
σ_t	Tensile strength
σ_{tmax}	Maximum tension cut-off of the 3D strength envelope for foliation planes
σ_{tmin}	Minimum tension cut-off of the 3D strength envelope for foliation planes
φ_{max}	Maximum friction angle of the 3D strength envelope for foliation planes
φ_{min}	Minimum friction angle of the 3D strength envelope for foliation planes
φ_r	Residual friction angle
M_a	Percentage of foliation surface area covered by mica
c	Cohesion
φ	Peak friction angle
E	Young modulus

ν	Poisson ratio
η	Porosity
R^2	Coefficient of determination
K_s^p	Peak shear stiffness of foliation planes (laboratory tests)
K_s	Shear stuffiness of foliation fractures (numerical analysis)
K_n	Normal stuffiness of foliation fractures (numerical analysis)
K_s^{pp}	Postpeak shear stiffness of foliation planes (laboratory tests)
ψ_p	Peak dilation angle of foliation planes (laboratory tests)
ψ_{pp}	Postpeak dilation angle of foliation planes (laboratory tests)
J_a	Joint alteration number
I_{d2}	Alterability index

List of Abbreviations

AD	Average displacements of the tunnel face
ANOVA	Analysis of variance
ASTM	American society for testing and materials
BDT	Brazilian disc test
C-DFN	Continuous discrete fracture networks
CNL	Constant normal load
CNS	Constant normal stiffness
D	Displacement magnitude thresholds
DEM	Discrete element method
DFN	Discrete fracture network
DST	Direct shear test
DTT	Direct tension test
EW	East-wall region of the tunnel
F1, F2, F3	Fracture sets 1, 2 and 3
FBV	Total failed brock volume
GSI	Geological strength index
HI	High influence of the foliation
ISRM	International society for rock mechanics
JCS	Joint compressive strength
JRC	Joint roughness coefficient
LI	Low influence of the foliation
MS1	Section 1 of the Monte Seco tunnel
MS2	Section 2 of the Monte Seco tunnel
MST	Monte Seco tunnel
NI	No influence of the foliation
OFP	Open foliation plane
PDF	Probability density function
POT	Pull-off test
PTC	Program termination criteria
Q	Q-rock mass classification system
R	Roof region of the tunnel
RMR_{14}	Rock mass rating (version 2014)

RVE	Representative volume element
SC	Percentage of slipping contacts near the tunnel face
Sn	Foliation planes
SPOT	Surface pull-off test
TI	Total influence of the foliation
TLS	Terrestrial laser scanning
TRS	Terrestrial remote sensing
UCT	Uniaxial compressive test
VMR	Vitória-Minas Railway
WC	Percentage of weathered contacts
WFP	Weathered foliation planes
WW	West-wall region of the tunnel

Table of Contents

Chapter 1

Introduction

Discontinuity is the general termination used to any planar geological structure within rock masses. For engineering purposes, discontinuities must be described geometrically (shape, spatial attitude, size, and intensity) and mechanically (strength and deformability), however, suitable field inspections and laboratory tests are hardly performed to obtain these parameters individually, considering the specific characteristics of each discontinuity type.

The first description that should be assigned to discontinuities during field mapping is the geological type. There are several types of planar geological structures with different characteristics, but they can be grouped into two sets: discontinuities formed by the mineral distribution on rocks, such as foliation, bedding planes, schistosity and veins; and discontinuities formed by mechanical processes (tectonism or tension reliefs), causing the loss of cohesion of finite planes, such as fractures, joints, and faults.

The mechanical behavior and geometrical properties of discontinuities are associated with the geological type. Discontinuities formed by mineral distributions can present expressive cohesion and tensile strength due to mineral binding along their planes. The mechanical behavior of fractures and joints, however, is well represented by friction-dependent models, such as Barton and Choubey (1977). Despite this difference, friction-based models are commonly used to all types of discontinuities due to the lack of laboratory tests and appropriate constitutive models. Therefore, the strength of rock foliation, bedding, etc., is often underestimated, as well as the general rock mass strength.

In most cases, the geometrical characterization of discontinuities consists in using deterministic values of discontinuity set orientation (dip and dip direction), size (or persistence) and linear frequency (or spacing), obtained by simplified field methods (hand-made scanlines and compass measurements). Thus, the true variability of geometrical parameters is not captured and assigned to the rock mass model. In most cases, this simplification is necessary because the amount of data available is not sufficient for determining the probability distributions of the geometrical parameter and creating stochastic Discrete Fracture Networks (DFN). Moreover, adopting finite sizes for the rock foliation and bedding planes, estimated by rock outcrop measurements, is at least questionable, considering the genesis of such structures (Cacciari and Futai 2016b). Therefore, the discontinuity type should also influence on the geometrical assumptions taken to perform discontinuity analyses, such as considering discontinuities as disk-shaped planes with finite sizes (common in DFN approaches).

Recently, terrestrial remote sensing (TRS) techniques has been used to create virtual 3D rock mass models and perform discontinuity mapping (Kemeny et al. 2006; Slob et al. 2007; Sturzenegger and Stead 2009; Lato et al. 2010, among others), increasing the amount of discontinuity data (position, orientations, trace lengths) available in geological surveys. Using these techniques, the discontinuity analyses can be improved by sophisticated window-sampling methods, and the DFN approach can be applied. The TRS-DFN combination is becoming the most suitable approach for creating discontinuous rock mass models used for slope stability analysis (Havaej et al. 2016). For tunnels, however, TRS-DFN approaches has not been used yet, especially with the implementation of automatic discontinuity analyses and taking the rock face orientation variability (walls and roof) into account.

The DFN approach is already implemented in commercial computer programs as a tool for creating discontinuities within the rock mass models. Recently, it has been implemented in the 3DEC software (Itasca 2014), which is a computer code based on the tridimensional distinct element method (DEM). Therefore, coupled TRS-DFN-DEM analysis is a modern approach, powerful for modeling discontinuous rock masses, but still not disseminated to the rock mechanics and tunneling community. The main reasons are the lack of practical and reliable methodologies integrating these techniques as well as the lack of examples showing the benefits of using it in real cases.

In this thesis, a coupled TRS-DFN-DEM methodology was developed for modeling tunnels in discontinuous rock masses. First, laboratory tests were performed to assess the shear and tensile strength of rock foliation, using direct shear tests, direct tension tests and pull-off tests (method proposed herein as a practical alternative for the direct tension test). Later, a practical method, coupling TLS, and DFN, was developed to create continuous fracture distributions along tunnels, based on terrestrial laser scanning geological mapping and automatic discontinuity analyses. Finally, the distinct element method was used to assess the role of a gneissic foliation on the stability of the Monte Seco tunnel (Vitória-Minas Railway), located in Espirito Santo (southeastern Brazil).

1.1 General objective

To develop a coupled TRS-DFN-DEM methodology for tunnel modeling and use it to assess the role of rock foliation on the stability of a shallow tunnel constructed in discontinuous rock mass.

Specific objectives:

The specific objectives were to:

1 - propose the use of pull-off test (POT) to assess the tensile strength of rock foliation;

2 - use direct shear tests (under constant normal stiffness condition) and POT to assess the shear and tensile strength of rock foliation planes with different mica content;

3 - propose an automatic methodology for modeling tunnels in fractured rock masses using TRS data to create continuous DFNs based on the volumetric intensity parameter; and

4 - integrate the results of specific objectives 1, 2 and 3 to perform stability analyses of the Monte Seco tunnel, considering particular characteristics of fresh and weathered foliation planes.

The objectives 1 to 4 are presented as scientific articles organized in individual chapters. Before introducing the results, a brief background is presented for a better understanding of the thesis, describing the previous works related to the influence of the mica content on the mechanical behavior of foliated rocks, and important aspects for creating DFNs and DEM models from natural rock exposures.

1.2 Influence of the mica content on the mechanical behavior of foliated rocks

It is an accepted knowledge that the metamorphic foliation creates anisotropic strength and deformability behaviors to rocks. Several studies have demonstrated this effect using laboratory tests and numerical analysis (Donath 1961, 1972; Attewell and Sandfordt 1974; Ramamurthy et al. 1993; Behrestaghi et al. 1996; Nasseri et al. 2003; Saroglou and Tsiambaos 2008; McLamore and Gray 2011; Cho et al. 2012; Park and Min 2015; Chen et al. 2016). Anisotropic rocks can have a visually homogenous composition (such as shales and slates). In these cases,

ubiquitous-joint (Sainsbury and Sainsbury 2017) and transversal isotropic (Amadei 1996) models can represent the mechanical behavior of the weak anisotropic direction (foliation direction). On the other hand, gneissic rocks for example, are strongly heterogeneous; thus, the foliation strength and deformability depend on its mineralogical composition and fabric.

Gneisses, for example, are metamorphic rocks composed by mafic and felsic bandings, with foliation defined by mineral alignment along planes. The foliation fabric (i.e., its spatial and morphological configuration), varies from almost flat planes to wavy and folded structures. The mica content on foliation also varies from planes fully covered by mica to planes with spars mica grains between prismatic grains.

Some studies have investigated the influence of the foliation fabric and mica content on the mechanical behavior of heterogeneous and anisotropic metamorphic rocks. Among them, McCabe and Koerner (1975) described qualitative aspects of the mica content on failure surfaces of mica-schist foliation planes after compression tests. Shea and Kronenberg (1993) quantified the mica content of cylindrical core specimens subjected to triaxial compression tests. In this case, the authors used modal quantifications to represent the entire specimens instead of isolated foliation planes after failure. Nevertheless, they observed clear decreasing strength and increasing ductility with increasing mica content in schists and gneisses. Later, Rawling et al. (2002) and Laws et al. (2003) investigated the mechanical behavior of foliated rock, with specific emphasis on influence of the mica content, but also associated with cylindrical core specimens rather than isolated foliation planes.

Considering the aforementioned studies, there is a lack of knowledge on the effects of mica content on the mechanical behavior of isolated foliation planes, including their shear and tensile strengths. This doctoral thesis investigates these behaviors by subjecting isolate foliation planes of a biotite-rich gneiss to shear and tension tests.

The shear strength of rock-isolated discontinuities is most often determined by direct shear tests (DST), in which the discontinuity plane is isolated inside a thin shear zone. The DST is traditionally used for “open” discontinuities, without inherent shear strength (cohesion). Some studies have performed DSTs of isotropic rocks (Petit 1988) and artificial rock materials (Cho et al. 2008) showing the development of “s-shaped” failure surfaces and *en-echelon* structures due to mixed shear and tensile fractures. Petit (1988) showed the similarity of such laboratory results with real fault plane structures (brittle regime) corresponding to small displacements.

Later, these finding were supported by numerical analyses (Cho et al. 2008; Bewick et al. 2014c, a, b). In this thesis, foliation planes were isolated in DSTs with the principal aim of assessing the effects of mica content on the shear strength of such geological structure. The influences of mineralogical features (especially the mica content) on the failure patterns of DSTs are also discussed.

At present, the tests most frequently used to assess tensile strength of rocks are the indirect Brazilian disc test (BDT) and the direct tension tests (DTT). Perras and Diederiches (2014) reviewed important aspects of these tests and presented correlations between them using a wide literature database. The correlations indicated that the tensile strength obtained by the BDT was approximately 5-30% higher than the tensile strength obtained by the DTT, depending on the rock type and specimen geometry. Aside from this difference, the BDT is generally preferable for laboratory investigations because the test procedure and specimen preparation are simpler, faster and less susceptible to bias. For these reasons, the BDT has been used in many rock mechanics studies, resulting in extensive literature on experimental data, numerical modeling and analytical solutions.

The pull-off test (POT) is a practical method for testing material strength; it is widely used for in situ tests of concrete and bound interfaces between different materials (Bungey and Madandoust 1992), but not in rock. The POT was selected for this study due to its practical advantages over the direct tension test (DTT), especially in terms of the specimen preparation process. In both POTs and DTTs, failure can occur at the weakest foliation plane along the cylindrical core specimen. Therefore, tests with predefined failure planes, such as the BDT, would not be suitable in this case. The POT was compared with DTT and BDT before applying it to obtain the tensile strength of foliation planes with different mica content.

1.3 Creating Discrete Fracture Networks and Discrete Element Models from rock exposures

Discrete fracture networks (DFN) are stochastic system of discontinuities distributed in space (Dershowitz and Einstein 1988). The basic geometrical parameters defining DFNs are the discontinuity intensity; discontinuity size, discontinuity positions, and discontinuity orientation. Probability density functions characterize discontinuity sizes, orientations and

positions; while the discontinuity intensity is usually a deterministic value, which represents the amount of discontinuity on a given domain.

Dershowitz and Herda (1992) presented an unified system for discontinuity intensity definition, which was later modified by the authors and used in the Fracman code (Golder Associates) (Table 1.1). This system uses two consecutive subscripts to represent the dimension of the sampling domain and the discontinuity feature, respectively.

Table 1.1: The "P-system" proposed by Dershowitz and Herda (1992) to define discontinuity intensity.

Dimension of discontinuity feature → Dimension of Measurement domain ↓	*0: Number of discontinuities*	*1: length of discontinuities*	*2: Area of discontinuity planes*	*3: Volume of discontinuities* (*aperture*)
1: Line Measure (Borehole or Scanline)	$\boldsymbol{P_{10}}$: Number of discontinuity per unit of scanline or borehole	$\boldsymbol{P_{11}}$: total length of aperture per unit of scanline or borehole		
2: Area Measure (sampling plane)	$\boldsymbol{P_{20}}$: Number of discontinuity per unit of sampling plane	$\boldsymbol{P_{21}}$: Length of discontinuity traces per unit area of sampling plane	$\boldsymbol{P_{22}}$: total area of aperture per unit area of sampling plane	
3: Volume (Rock Mass)	$\boldsymbol{P_{30}}$: Number of discontinuity per unit volume of rock mass		$\boldsymbol{P_{32}}$ Area of discontinuities per unit volume of rock mass	$\boldsymbol{P_{33}}$: Volume of aperture per unit volume of rock mass

The parameters with equal dimensions for the discontinuity feature and the sampling domain (P_{11}, P_{22} and P_{33}) consist in rock mass porosity measurements. P_{10} is commonly known as discontinuity frequency, which is the inverse of spacing. Geological mapping of rock outcrops and drill core surveys usually result in P_{10} and P_{21} measurements. These parameter can be used to estimate P_{32} by analytical methods (Zhang and Einstein 2000) or DFN simulations (Dershowitz and Herda 1992).

The definition of probability density functions (PDF) for discontinuity orientation, position and size depends on the geological mapping data. The PDFs for discontinuity orientation and position are defined using the original discontinuity mapping data. Usually, the isotropic Fisher distribution is representative for fractures and joints, consisting in the mean orientation (dip and dip direction) and the Fisher dispersion parameter (K). Discontinuity positions in space do not fall known continuous probability functions. Moreover, discontinuity mapping in limited rock mass exposures do not provide sufficient extent to define such PDFs in x, y and z directions. Therefore, the discontinuity positions usually follow the homogeneous Poisson distribution inside the DFN domains.

The PDF of discontinuity size is extremely important to the DFNs composed by non-persistent discontinuities, because it controls the final number of discontinuities inside the DFN domain. If P_{32} is used, for example, discontinuities will be created inside the DFN domain until the total discontinuity area per unit of rock mass (DFN domain volume) is reached. The final number of discontinuities inside the DFN domain can be either high if discontinuities are small, or low if discontinuities are large. Moreover, the size of discontinuities controls the number of remaining rock bridges, which have major importance to the mechanical behavior of the synthetic (numerical) rock mass created by the DFN-DEM coupling.

A suitable definition of a PDF for discontinuity size has to consider the following bias associated to non-persistent discontinuity traces apparent in limited rock exposures (Zhang and Einstein 1998; Mauldon 1998; Mauldon et al. 2001):

- The discontinuity shapes are unknown. Usually, the disc-shape is adopted because it simplifies the discontinuity analysis used for defining the size PDF.

- Discontinuity censoring. Part of the discontinuity traces are censored on the boundaries of the rock outcrops (i.e., their actual length is greater than their apparent length).

- The trace sizes do not represent directly the discontinuity size. Disc-shaped discontinuities of equal diameters and orientations can result in different trace lengths depending on their center positions (see example in Fig. 1.1). Likewise, disc-shaped discontinuities of equal center positions and diameters can result in different trace lengths depending on their orientations.

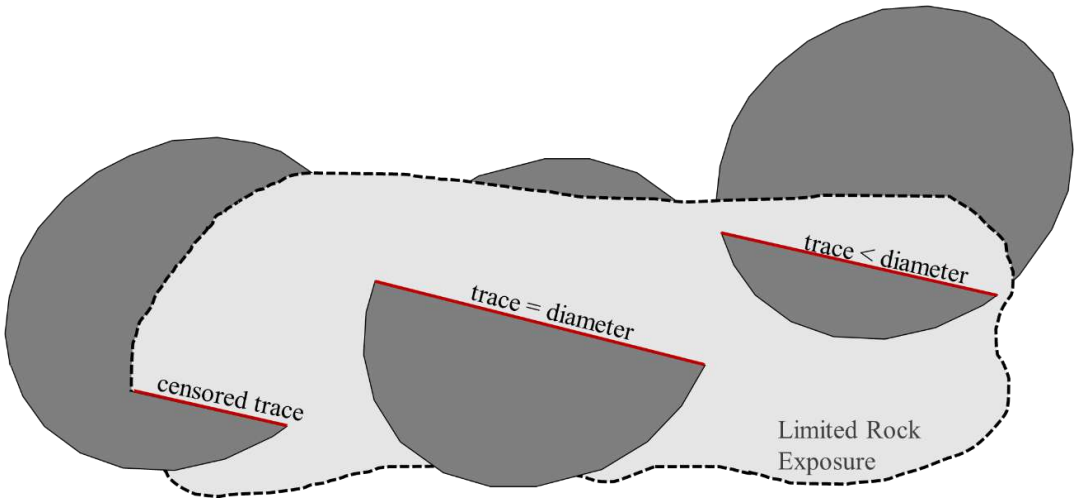

Fig. 1.1 Representation of bias associated to discontinuity sizes on rock limited rock exposures.

Advanced discontinuity analysis methods can overcome the aforementioned bias. Zhang and Einstein (Zhang and Einstein 2000) proposed a sequence of steps for defining the unbiased PDF of discontinuity size after all traces are identified and mapped on the rock exposure:

I - Obtain distribution form (normal, exponential, log-normal, gamma, etc.) of trace lengths directly measured on the rock exposures (biased).

II - Use sampling windows to obtain the unbiased mean trace length (μ) and standard deviation (σ), which corrects the censoring bias. The PDF of unbiased trace lengths [$g(l)$] is defined by assuming the same distribution form in I, with μ_l and σ_l.

III - Use an analytical solutions based on the moments of $g(l)$ and the PDF of discontinuity diameters [$g(D)$], based on the stereological relationship between trace length distributions and discontinuity diameter distributions developed by Warburton (1980):

$$(\mu^2 + \sigma^2) = \frac{2E(D^3)}{3\mu_D} \tag{1.1}$$

$$\mu = \frac{\pi[(\mu_D)^2 + (\sigma_D)^2]}{4\mu_D} \tag{1.2}$$

$$\frac{E(D^4)}{E(D^2)} = \frac{E(l^4)}{E(l^2)} \tag{1.3}$$

Where μ_D and σ_D are the mean and standard deviation of $g(D)$; $E(D^n)$ and $E(l^n)$ are the n^{th} moments of $g(D)$ and $g(l)$, respectively.

In II, different window sampling methods can be applied to obtain μ_l. Cacciari and Futai (Cacciari and Futai 2016b) compared different methods (Table 1.2) and concluded that the method proposed by Kulatilake and Wu (1984), modified by Wu et al. (2011) is has advantages over other methods.

Table 1.2 Characteristics of the mean trace length sampling methods (Cacciari and Futai 2016b).

Method	Window type	Orientation distribution-free method	Applied to non-parallel traces	Consider relative frequencies of traces depending on the rock face orientation
Kulatilake and Wu (1984)	Rectangular	No (depends on the definition a PDF for discontinuity orientation)	Yes	Yes
Mauldon (1998)	Any convex	Yes	No	Yes (but traces are considered parallel)
Mauldon (1998); Zhang and Einstein (1998)	Circular	Yes	Yes	No
Wu et al. (2011)	Rectangular	Yes	Yes	Yes

In III, the application of Eqs. 1.1, 1.2 and 1.3 is an interactive procedure, consisting in:

1) Guessing the $g(D)$ distribution form (log-normal, gamma, exponential, etc.) and obtaining $E(D^3)$ as a function of μ_D and σ_D.

2) Replacing the $E(D^3)$ expression in Eq. 1.1 and solving Eqs, 1.1 and 1.2 to find μ_D and σ_D values (considering that μ and σ are already obtained in II).

3) Obtaining the expressions and calculating the 4^{th} and 2^{th} moments of $g(D)$ in Eq. 1.3 (with the guessed distribution form in 1) and calculating de 1^{th} and 3^{th} moments of $g(l)$.

4) Comparing the left and right sides of Eq. 1.3. The closer the values, the better the distribution form adopted. Generally, the same distributions ordinarily used for trace length are likely to give the best-fit for discontinuity diameters. However, with this method the g(D) and $g(l)$ forms are not necessarily the same.

After obtaining $g(D)$, the DFNs can be generated. There are commercial programs with DFN generators implemented, such as Fracman (Golder Associates) and 3DEC (Itasca 2014). In 3DEC, the DFN are used to build the DEM block models useful for multiple applications, such as tunnel and slope stability analyses (Cacciari et al. 2015; Cacciari and Futai 2016a; Havaej et al. 2016). Fig. 1.2 show an example of 3DEC block model created after cutting 3 discontinuity sets, starting with the persistent discontinuity set (Fig. 1.2a) (e.g., rock foliation planes), followed by the DFNs of each non-persistent fracture set (Figs. 1.2b and c).

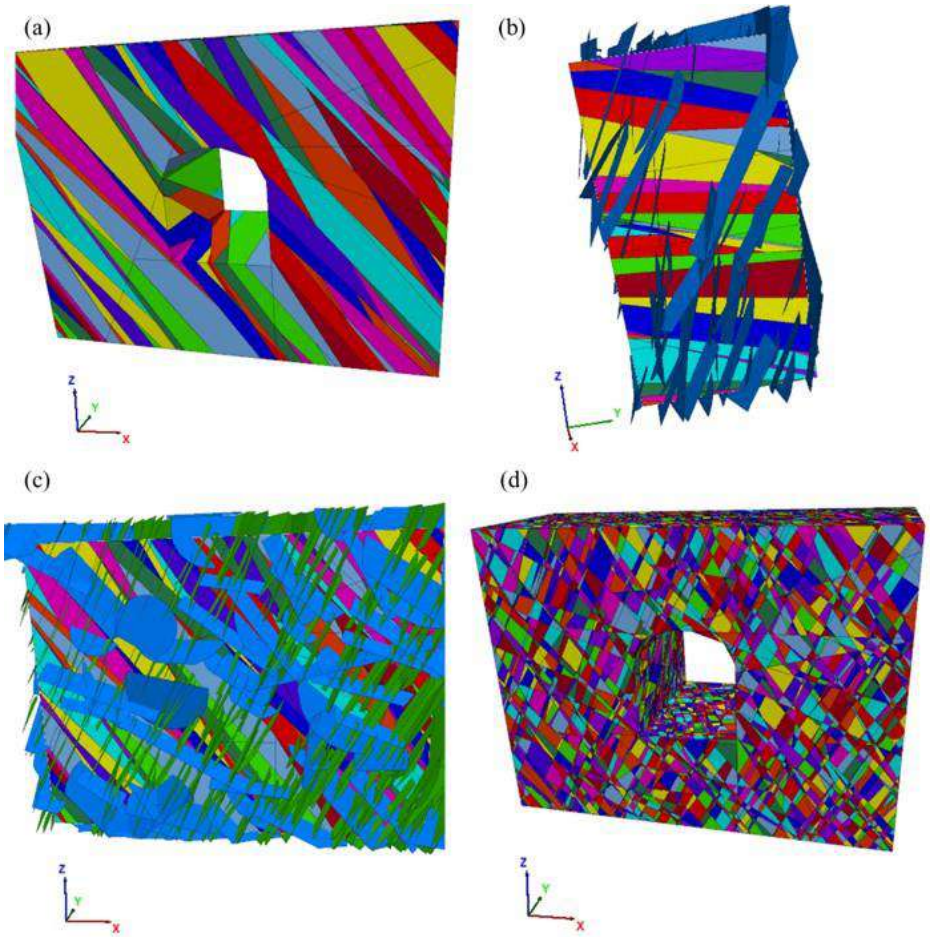

Fig. 1.2. Discontinuity cutting sequence to generate the 3DEC block model of a tunnel (Cacciari et al. 2015).

Chapter 2

Assessing the tensile strength of rocks and geological discontinuities via pull-off tests

This chapter presents an article published on the **International journal of Rock Mechanics and Mining Sciences. DOI: 10.1016/j.ijrmms.2018.03.011**
Authors: Pedro P. Cacciari & Marcos Massao Futai.

Abstract

The pull-off test (POT) is a practical method for testing material strength; it is widely used for in situ tests of concrete and bound interfaces between different materials. The POT is closely related to the direct tension test (DTT) once the partial core is submitted to only a vertical tension force until failure. At present, the tests most frequently used to assess tensile strength of rocks are the indirect Brazilian disc test (BDT) and the DTT. Considering the practical advantages of the POT for concrete materials and interface tensile strength assessment, this paper introduces this method for rock engineering applications, particularly in situ. A laboratory campaign was conducted to show the use of the POT to be a practical alternative for tensile strength assessment of rocks and geological discontinuities. Four visually homogeneous and isotropic rock types were tested by the POT, BDT, and DTT for comparison and test validation. Moreover, the POT was used to assess the tensile strength of foliation and banding planes of a gneiss. Recommendations are given for the application of the POT in the laboratory and in situ (with a practical example) using rock blocks or outcrops.

Keywords: Pull-off test; Tensile strength; Direct tension test; Brazilian disc test.

2.1 Introduction

The pull-off test (POT) is a practical method for testing material strength; it is widely used for in situ tests of concrete and bound interfaces between different materials, but not in rock. For these purposes, the POT is classified as a partially destructive technique that is used to assess the surface zone strength of structures (Bungey and Madandoust 1992). The test consists of pulling off a metal disc attached directly to the surface of a partially drilled core (Fig. 2.1a). Epoxy resins are used to attach the metal disc to the surface to ensure that the material fails. Although the POT is an established method for the in situ testing of concrete materials, there are no scientific reports discussing its particularities and practical advantages for rock engineering. This paper presents the equipment, methodology, results and correlations to determine the in situ tensile strength of rock using the POT.

The POT is closely related to the direct tension test (DTT) once the partial core in Fig. 2.1a is submitted to only a vertical tension force until failure. However, as verified by Bungey and Madandoust (Bungey and Madandoust 1992), the boundary conditions of the POT create heterogeneous stress distributions, concentrating the higher tension stresses at the core base peripheries. Thus, in the POT, failure is likely to occur at the core base unless there is a weaker zone/plane along the partial core.

Considering that the POT is applied orthogonally to the concrete structure surfaces, it becomes attractive for assessing the bond strength of interfaces between overlapping materials, such as concrete repairs, porcelain tiles, and mortar layers. Austin et al. (1995) evaluated the POT for the bound strength assessment of overlay interfaces considering different geometries (interface depth), material mismatching, and surface conditions. This subject has garnered the interest of many concrete and building material researchers (Bonaldo et al. 2005; Momayez et al. 2005; Szemerey-Kiss and Török 2017). As described by ASTM (2013), the POT (applied to concrete with repairs) can provide three valid failure modes: substrate material failure, bond failure (concrete/overlay interface) and overlay material failure. Bond failure at the epoxy and overlay interface is not suitable for characterizing the material strength.

Similar failure modes are expected in other materials, such as rocks; thus, the POT can be useful for assessing the tensile strength. However, to our knowledge, no previous studies have used the POT for rocks or compared it with other tensile strength testing methods often used in rock mechanics. Similar to concrete, the failure of homogeneous and isotropic rocks is likely to occur

at the base of the core (mode 1L in Fig. 2.1b) due to the stress concentrations associated with the test boundary. Failure can also occur along the core, although this situation is less likely (mode 1U in Fig. 2.1a). In heterogeneous and anisotropic rocks, failure is likely to occur through the weaker region or geological discontinuity along the core (2L in Fig. 2.1c). In the case of a rock core crossing two or more overlayered rock types (or petrological unities), such as in heterogeneous gneiss with mafic and felsic beddings, failure mode 3L (Fig. 2.1d) is likely to occur through contact. Other failure modes are less likely (dashed white lines in Fig. 2.1b, c and d) but not impossible; for example, such modes may occur in the case of cores crossing high-tensile-strength geological discontinuities (Shang et al. 2016) or cores with micro-fissures along the intact rock materials.

At present, the tests most frequently used to assess tensile strength of rocks are the indirect Brazilian disc test (BDT) and the DTT. Perras and Diederiches (Perras and Diederichs 2014) reviewed important aspects of these tests and presented correlations between them using a wide literature database. The correlations indicated that the tensile strength obtained by the BDT (σ_{BDT}) was approximately 5-30% higher than the tensile strength obtained by the DTT (σ_{DTT}) depending on the rock type and specimen geometry. Aside from this difference, the BDT is generally preferable for laboratory investigations because the test procedure and specimen preparation are simpler, faster and less susceptible to bias. For these reasons, the BDT has been used in many rock mechanics studies, resulting in extensive literature on experimental data, numerical modelling and analytical solutions (Li and Wong 2013).

Considering the practical advantages of the POT for concrete materials and interface tensile strength assessment, this technical note introduces this method for rock engineering applications, particularly in situ. A laboratory campaign was conducted to show the use of the POT to be a practical alternative for tensile strength assessment of rocks and geological discontinuities. Four visually homogeneous and isotropic rock types were tested by the POT, BDT, and DTT for comparison and test validation and used to evaluate the influence of the core depth on σ_{POT}. Moreover, POTs were performed on anisotropic and heterogeneous gneiss to evaluate the σ_{POT} of geological discontinuities and characterize the different failure modes associated with the rock fabric. The practical advantages of the POT over other standard tensile strength tests for rock materials are discussed, and recommendations are given for the application of the POT in the laboratory and in situ (with a practical example) using rock blocks or outcrops.

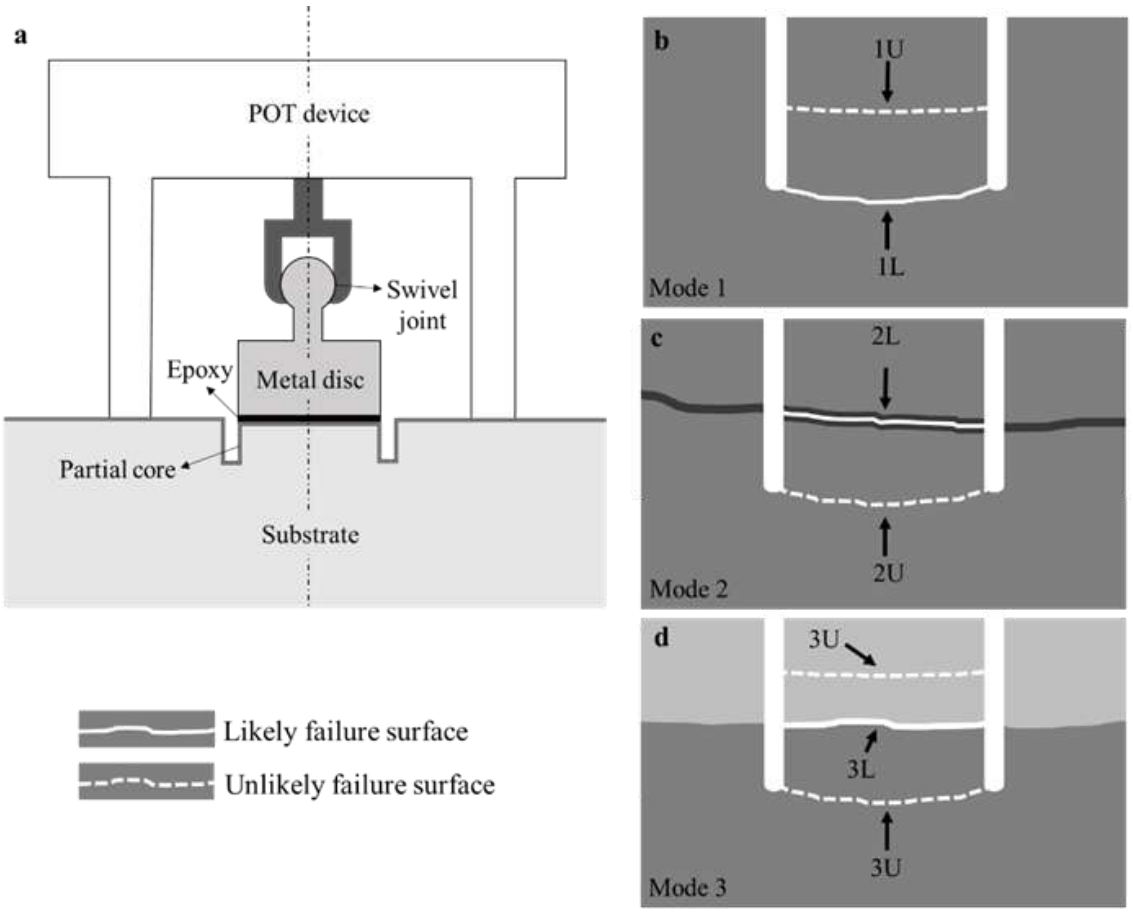

Fig. 2.1. POT failure modes in rocks and geological discontinuities indicating the likely (L) and unlikely (U) failure surfaces. a. Pull-of test setup. b. Mode 1; c. mode 2 and d. mode 3.

2.2 Materials and Methods

Five rock types were used in this work: marble (basic mineralogical composition: calcite and dolomite); red granite (basic mineralogical composition: feldspar, quartz, and biotite); white granite (basic mineralogical composition: feldspar, quartz, grenade, and biotite); andesite (basic mineralogical composition: plagioclase, pyroxene, chlorite and quartz) and para-gneiss (basic mineralogical composition: quartz, feldspar, biotite and cordierite). The marble, granites, and andesite are visually homogeneous with expected isotropic behaviour; thus, they were used to compare the POT, BDT, and DTT and evaluate the variation in σ_{POT} with the partial core depth. All specimens used in each test (POT, BDT and, DTT) were removed from the same rock block to avoid major differences between specimen groups. The gneiss was used to assess the tensile strength of geological discontinuities and lithological unity (mafic and felsic bedding) contacts.

Additionally, a biotite ortho-gneiss (quartz, feldspars, and biotite) block was used to exemplify the POT applied in situ.

2.2.1 Pull-off test

The POT was performed with an automated pull-off tester (Fig. 2.2a) commercially known as DY-216^{TM}, manufactured by Proceq SA (Schwerzenbach, Zürich Switzerland). The DY-216^{TM} is a portable, lightweight and practical operation instrument, with a tensile load ranging from 1.6 to 16 kN (0.81 to 8.1 MPa for 50 mm-diameter cores). The main advantage of this equipment is the built-in feedback controlled motor, which provides a fully automated test with a constant load rate, avoiding the operator influence of manual devices. The load range of the DY-216^{TM} was not suitable for the andesite because of the high tensile strength of this rock type (>10 MPa). In this case, a metal bar was adapted to a DL-10000^{TM} universal machine (maximum load of 100 kN), manufactured by Emic SA (São José dos Pinhais, Paraná Brazil), to hold the specimen during the test (Fig. 2.2b). Torsion and bending effects were minimized on the POT using swivel joints connecting the load equipment to the metal discs (Figs. 2.2a and b).

For POT, the rock blocks were drilled using the DD-160 drilling machine manufactured by Hilti SA, with a 50 mm-diameter (internal) diamond core bit, resulting in 49.4-49.6 mm core diameters. The rock block surfaces were kept horizontal and perpendicular to the drilling machine to avoid inclined cores. Stainless steel discs with diameters of 50 mm and thicknesses of 25 mm were fixed to the core surfaces using an epoxy adhesive commercially known as Araldite AV138^{TM} (with the HV998^{TM} hardener resin), manufactured by Huntsman SA (The Woodlands, Texas USA). All tests were conducted with a constant load rate of 0.04 MPa/s until failure (ASTM 2013).

POTs or DTTs with epoxy/rock interface failure are invalid; thus, they must be discarded and repeated. Surface POTs (SPOTs), in which a metal disc is directly attached to the surface (without drilling), were also performed on the marble, granites, and andesite. The results indicated that the SPOT failure is likely to occur on the epoxy-rock interface (invalid) after approximately 7.0 MPa using the Araldite AV138^{TM}. For most concrete materials, this value does not exceed the σ_{POT}; however, it does for several rock types (such as the red granite and andesite), causing invalid failure. The numerical analyses of the POT on partial cores presented by Bungey and Madandoust (Bungey and Madandoust 1992) showed that high tensile stresses

are concentrated not only on the core base periphery but also on the core surface centre because of the load geometry. Moreover, the specimen preparation procedure (in both the DTTs and POTs) typically involves cutting and polishing processes that can damage the surface used for the epoxy attachment. Therefore, invalid failure often occurs in the POTs, particularly for the high-strength materials. After several invalid failures with different surface conditions (polished, saw and rough), we decided to add a lateral reinforcement (approximately 2 mm thick) to all POT and DTT specimens (Figs. 2.2a and d). This problem was solved with this adjustment, and valid partial core POTs and DTTs were conducted with a tensile stress of 15.0 MPa. However, only the marble and white granite were used for the SPOT, as the lateral reinforcement cannot be used in this case.

The DY-216^{TM} equipment does not measure the vertical displacement during the test; therefore, only the tensile stress at failure (σ_{POT}) was recorded as the ultimate tensile force divided by the core top surface area. Both the core and failure depths were measured using a calliper. Four measurements were taken for each test in opposite and perpendicular positions, at the base of the core (core depth) and at the edge of the failure plane (failure depth). The distance between the core and failure depth (d_s) was calculated and used to evaluate the influence of the POT boundary condition on the σ_{POT} measured.

2.2.2 Direct tension test

The same universal machine described above was used for the DTT. In this case, two swivel joints were used at the specimen ends (Fig. 2.2c) to minimize torsion and bending effects. The preferable geometry for the DTT is the dogbone because it induces failures at the central region of the specimen (Perras and Diederichs 2014). However, it makes the specimen preparation process difficult; thus, it is rarely employed (Hashiba et al. 2017). As in several previous works (Coviello et al. 2005; Erarslan and Williams 2012; Liu et al. 2014; Shang et al. 2016; Hashiba et al. 2017), cylindrical specimens were used for the DDT. Care was taken in the specimen preparation to ensure parallel end-surfaces (with diameters of 49.4 to 49.6 mm), and the same discs used in the POT were attached to them (with the same epoxy resin). In both the POTs and DDTs, the specimen and metal disc diameters were nearly identical to minimize load eccentricity problems. Fig. 2.2d shows an example of a cylindrical specimen prepared for DTT before and after adding the epoxy lateral reinforcement. The DTT specimen lengths were

between 100 and 115 mm, depending on the rock block dimensions. The same load rate of the POT was used in all DTTs.

2.2.3 Brazilian disc test

The BDTs were performed using specimens with the same diameters of the POTs and DTTs, with thicknesses of 26-29 mm. Two steel loading jaws, designed as recommended by ISRM (1978), were adjusted to the DL-10000^{TM} universal machine (Fig. 2.2e), and the same load rate of the DTTs and POTs was used. Spherical seats were used to provide flexible linkage between the external load system and jaws.

Fig. 2.2. a. POT with the DY-216 device; b. POT with the Emic DL-10000^{TM}; c. DTT in progress; d. DTT specimen preparation and e. BDT according to ISRM (ISRM 1978).

2.3 Results and discussion

The main issue of the POT is the boundary condition of partially drilled cores that generate high and heterogeneous stress concentration along the core base. As a result, the σ_{POT} can vary with the core depth. For concrete, Bungey and Madandoust (Bungey and Madandoust 1992) found that σ_{POT} decreases with the core depth, with a minimum value approximately 30% lower than that of the SPOT; however, in their case, σ_{POT} tended to remain constant after a depth of 15 mm, irrespective of the concrete type. Moreover, the disc material (aluminium or steel) did not affect the maximum theoretical stress (at the core base periphery) for discs having a thickness of 20 mm (or higher) and diameter of 50 mm. Considering that rocks can present different behaviours, it is important to perform the POT at different depths and with different rock types to verify the influence of the boundary conditions on the σ_{POT}.

2.3.1 Variation of the POT with the core depth

The marble was the first rock tested to evaluate this effect at seven different core depths (SPOT, 10, 25, 40, 55, 70 and 85 mm). After analysing the results, the andesite was tested at five different core depths (10, 25, 40, 55 and 70 mm), the white granite at three core depths (SPOT, 10 and 40 mm), and the red granite at two core depths (10 and 40 mm). Four tests were performed for each core depth and rock type to avoid misinterpretations due to the natural material strength variability. The same core depths were not used for all rock types because of the small dimensions of some of the available blocks. However, a wide range of core depths could be evaluated for the rock types with the highest (andesite) and lowest (marble) tensile strengths. Fig. 2.3a shows the variation of σ_{POT} with the core depth and the failure modes associated with each test.

Fig. 2.3 clearly shows that the core depth does not substantially affect the σ_{POT} after 10 mm cores for all rock types used in this work. One-way analysis of variance (ANOVA) were performed to verify statistical differences in mean values of σ_{POT} among the partial core depth groups. As expected, only the SPOT from the white granite indicated significant difference (SPOT vs. 10 mm P=0.007; SPOT vs. 40 mm P=0.011). Statistically significant differences among partial core depths were not observed for the other rock types (marble P=0.477; red granite P=0.446 and andesite P=0.183).

The boundary conditions of the POT induced failure mode 1L (Fig. 2.1b) on all andesite and granite specimens, except for one red granite test (black triangle in Fig. 2.3a). However, the POT in marble specimens did not show the same effect, as mode 1U occurred in the major part of the tests. Fig. 2.3b shows that the σ_{POT} of marble did not vary with d_s, indicating that the failure depth is controlled by the natural material variability and not by the POT boundary effects. This failure can be related, for example, to the possible existence of micro-fissures along the core length associated with the perfect cleavage of dolomite and calcite.

The σ_{POT} obtained by the SPOT on marble did not differ from the partial cores, indicating that the POT boundary condition is clearly inexpressive for this rock type. However, this difference was clear on the white granite specimens, where the 10 and 40 mm POT presented mean σ_{POT} values approximately 25% lower than those for the SPOT. This result corresponds well with the findings of Bungey and Madandoust (Bungey and Madandoust 1992) (maximum 30% difference after a 15 mm core depth in their case); however, the finding could be verified for only this rock type. Considering these results, POT tests can be performed in partially drilled cores after a 10 mm depth for homogenous and isotropic rocks without significant changes to the σ_{POT}. However, when the epoxy lateral reinforcement is used, the distance between the epoxy resin and the base of the core becomes too low, hindering the distinction between the 1L and 1U failure modes.

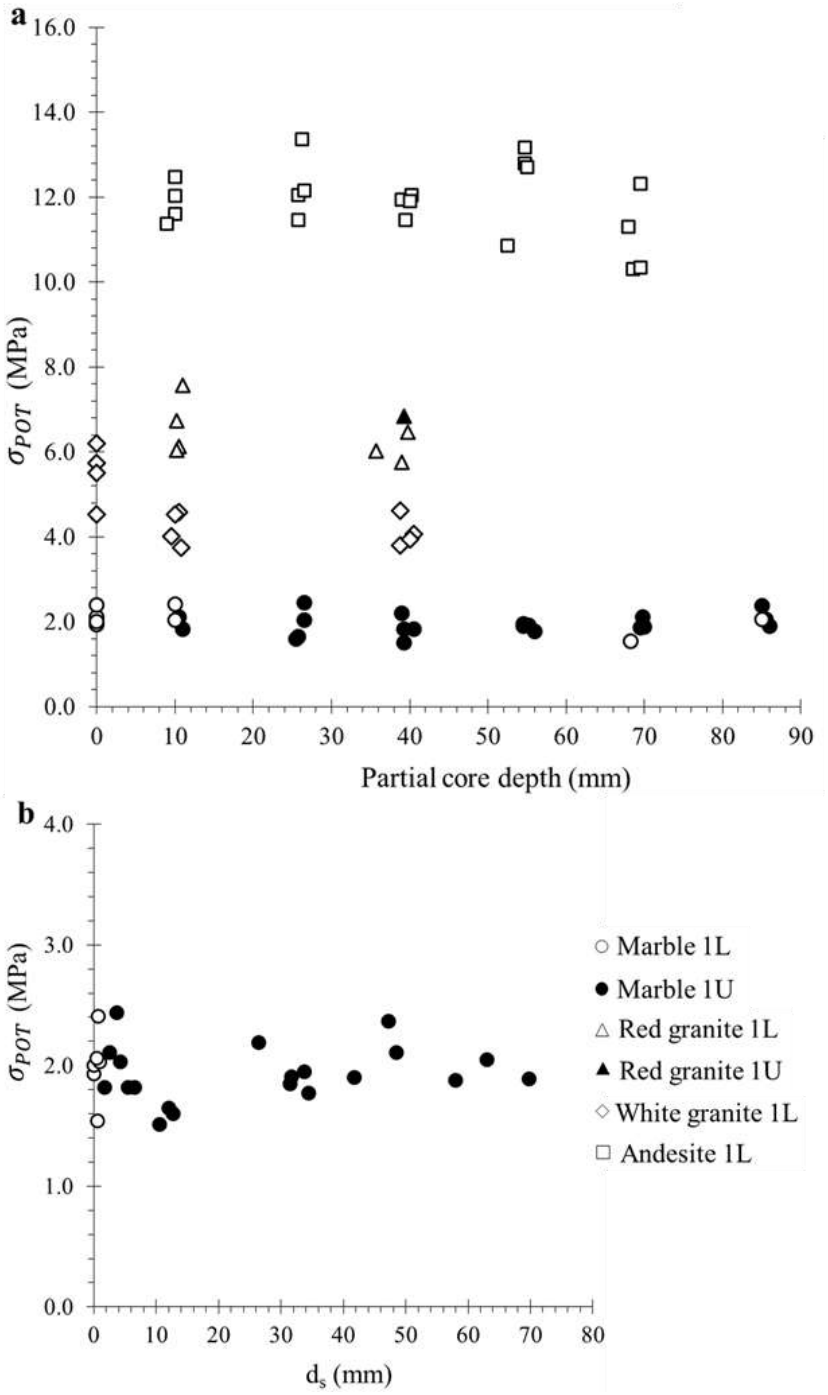

Fig. 2.3. a. σ_{POT} variation with the partial core depth; b. σ_{POT} variation with d_s for the marble.

2.3.2 Comparison between tests

Five DTT and BDT were performed with each rock type to compare the results obtained by the POT. Table 2.1 summarizes the tensile strength results of these tests and important specimen characteristics. Table 2.1 and Fig. 2.4 show the correlation of mean tensile strengths obtained

by the DDT ($\bar{\sigma}_{DTT}$), POT ($\bar{\sigma}_{POT}$) and BDT ($\bar{\sigma}_{BDT}$). $\bar{\sigma}_{POT}$ was calculated using all partial core specimens (core depth ≥ 10 mm), as they did not significantly change for any rock type (Fig. 2.3). Fig. 2.5 shows examples of DTT, BDT and POT specimens after failure.

Fig. 2.4 illustrates that the mean tensile strengths from all tests are linearly correlated for the range of strengths and rock types used. $\bar{\sigma}_{POT}$ was approximately 12% lower than $\bar{\sigma}_{DTT}$, indicating that the POT boundary conditions indeed influence the results, as expected by the majority of 1L modes in Fig. 2.3a. Interestingly, the $\bar{\sigma}_{POT}$ and $\bar{\sigma}_{DTT}$ of the marble were highly similar; thus, the POT boundary conditions did not influence the failure mode (Fig. 2.3) or the $\bar{\sigma}_{POT}$ for this rock type. The differences between the DTT and POT were clearly less pronounced for the granites than for andesite. Both granites are coarse-grained phaneritic rocks (as is the marble used), whereas the andesite is a fine-grained aphanitic rock; thus, the difference between $\bar{\sigma}_{POT}/\bar{\sigma}_{DTT}$ observed for these rocks can be related to these mineralogical characteristics. The POT failure surfaces of both granites and marble specimens are irregular along mineralogical connections and cleavages, whereas the POT failure surfaces of andesite are ostensibly concave-shaped (Fig. 2.5c), indicating that the mineralogical properties do not play a significant role in the crack initiation and propagation in this case. Numerical analyses using fracture mechanics models are in progress to investigate these aspects affecting the POT results; however, these analyses are beyond the scope of this technical note.

The results in Fig. 2.4 suggest that σ_{DTT} and σ_{BDT} could be predicted by the POT for isotropic and homogeneous rocks, and the σ_{DTT} and σ_{POT} values are similar for coarse-grained rocks. This study is limited to four rock types, and reliable correlation factors may require an extensive laboratory database. However, care was taken to use four (visually homogeneous and isotropic) rock types covering a wide range of tensile strength values (2 to 15 MPa). Thus, the correlations presented are promising but not definitive, and the correlation coefficients will likely decrease with an increasing number of rock types tested.

Fig. 2.4a shows that $\bar{\sigma}_{BDT}$ was approximately 20% higher than $\bar{\sigma}_{DTT}$, and Fig. 2.4b shows that $\bar{\sigma}_{BDT}$ was approximately 37% higher than $\bar{\sigma}_{POT}$. The differences between the tensile strengths obtained by the direct (DTT) and indirect (BDT) tests have been under debate for decades. The results found herein are consistent with several reported experimental works recently compiled by Perras and Diederiches (Perras and Diederichs 2014). Moreover, these differences in magnitude between σ_{BDT} and σ_{DTT} are within the range found by Shang et al. (Shang et al. 2016) ($\bar{\sigma}_{BDT}/\bar{\sigma}_{DTT} \approx 1.2$ for a sandstone), Erarslan and Williams (Erarslan and Williams 2012)

($\bar{\sigma}_{BDT}/\bar{\sigma}_{DTT} \approx 1.6$ for a granite) and Hashiba et al. (Hashiba et al. 2017) ($\bar{\sigma}_{BDT}/\bar{\sigma}_{DTT} \approx 1.3$ for a tuff), who used similar test configurations (cylindrical specimens with epoxy attachments for DTTs and the ISRM (ISRM 1978) loading jaws for BDTs) and visually homogeneous and isotropic rocks. Perras and Diederiches (Perras and Diederichs 2014) described several possible reasons for this experimental result, including suppressed crack growth in the BDT and possible differences in mineralogy and specimen variability, particularly in heterogeneous and anisotropic rocks. However, the theoretical reasons for such results remain unclear, as numerical analyses do not reproduce the same experimental trends, resulting in similar σ_{BDT} and σ_{DTT} values (Tang et al. 2017).

The results in Fig. 2.4 confirmed that the heterogeneous stress distribution caused by the POT boundary condition underestimates the tensile rock strength. Aside from this fact, the difference between the tensile strengths obtained from the DTT and POT found here were significant only when associated with failures at the base of the partial core and did not exceed the differences commonly observed between tensile tests applied for rocks. Thus, the POT can be considered a practical alternative to estimate the tensile strength of rocks using a direct tension test. Further research using different rock types will improve the correlation between the POT and DTT, enabling the direct tensile strength of rocks to be predicted more accurately by POT.

Table 2.1 Summary of DTT, POT and BDT results.

Rock type	POT $\bar{\sigma}_{POT}$/s.d. (MPa)	DTT Specimen name	H (mm)	D (mm)	γ (kN/m^3)	σ_{DTT} (MPa)	$\bar{\sigma}_{DTT}$/s.d. (MPa)	BDT Specimen name	H (mm)	D (mm)	σ_{BDT} (MPa)	$\bar{\sigma}_{BDT}$/s.d. (MPa)
Marble	1.95/ 0.25	DT-M1	117.1	49.3	28.4	2.43	1.70/ 0.44	BT-M1	26.8	49.3	2.68	2.70/ 0.09
		DT-M2	117.2	49.2	28.4	1.40		BT-M2	25.8	49.3	2.65	
		DT-M3	100.1	49.2	28.5	1.78		BT-M3	27.4	49.2	2.73	
		DT-M4	119.2	49.3	28.4	1.52		BT-M4	25.0	49.5	2.82	
		DT-M5	117.2	49.3	28.4	1.37		BT-M5	27.6	49.2	2.59	
White granite	4.16/ 0.36	DT-WG1	111.0	49.4	26.1	3.66	4.92/ 0.82	BT-WG1	29.0	49.4	5.74	6.51/ 1.25
		DT-WG2	95.8	49.3	26.1	5.42		BT-WG2	26.5	49.3	5.17	
		DT-WG3	111.3	49.5	26.1	5.53		BT-WG3	26.0	49.5	8.45	
		DT-WG4	95.8	49.3	26.1	4.52		BT-WG4	25.0	49.5	6.35	
		DT-WG5	111.0	49.4	26.1	5.49		BT-WG5	26.0	49.5	6.85	
Red granite	6.40/ 0.67	DT-RG1	111.5	49.5	26.3	6.81	6.66/ 0.19	BT-RG1	27.0	49.5	7.47	7.76/ 1.07
		DT-RG2	111.7	49.4	26.2	6.99		BT-RG2	28.3	49.5	6.72	
		DT-RG3	111.6	49.4	26.3	6.47		BT-RG3	27.8	49.5	6.91	
		DT-RG4	112.8	49.5	26.3	6.89		BT-RG4	26.7	49.6	8.41	
		DT-RG5	113.4	49.5	26.2	6.80		BT-RG5	26.1	49.5	9.27	
Andesite	12.00/ 1.02	DT-A1	106.2	49.3	25.6	13.82	13.91/ 0.80	BT-A1	26.0	49.5	17.28	16.77/ 1.40
		DT-A2	106.0	49.3	25.6	14.20		BT-A2	25.1	49.2	16.60	
		DT-A3	106.0	49.3	25.5	13.05		BT-A3	25.0	49.2	18.80	
		DT-A4	106.1	49.3	25.6	13.32		BT-A4	29.5	49.5	16.13	
		DT-A5	106.0	49.3	25.6	15.11		BT-A5	28.6	49.5	15.03	

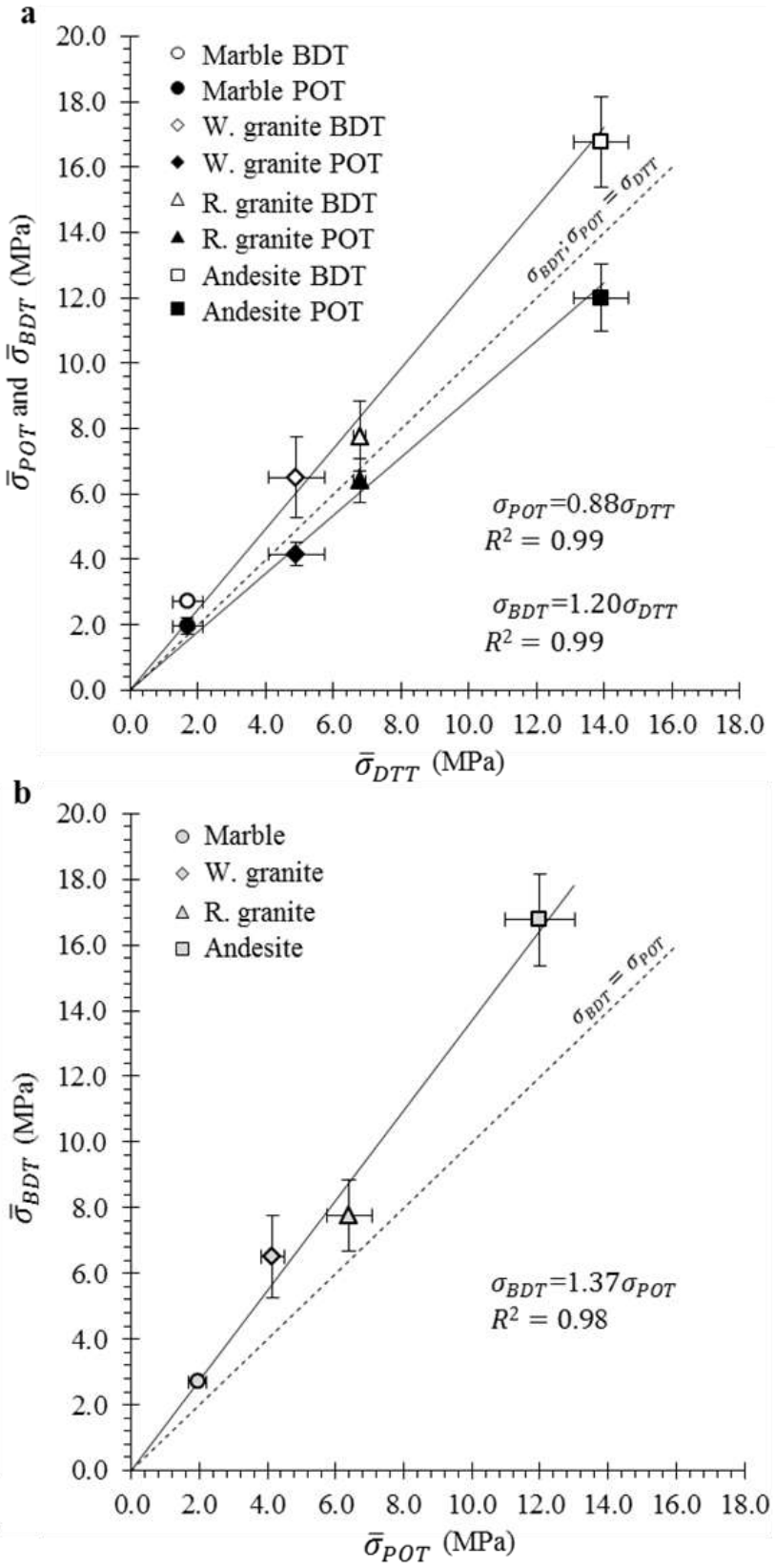

Fig. 2.4. Comparison between tests. a. DTT x POT and DTT x BDT; b. POT x BDT.

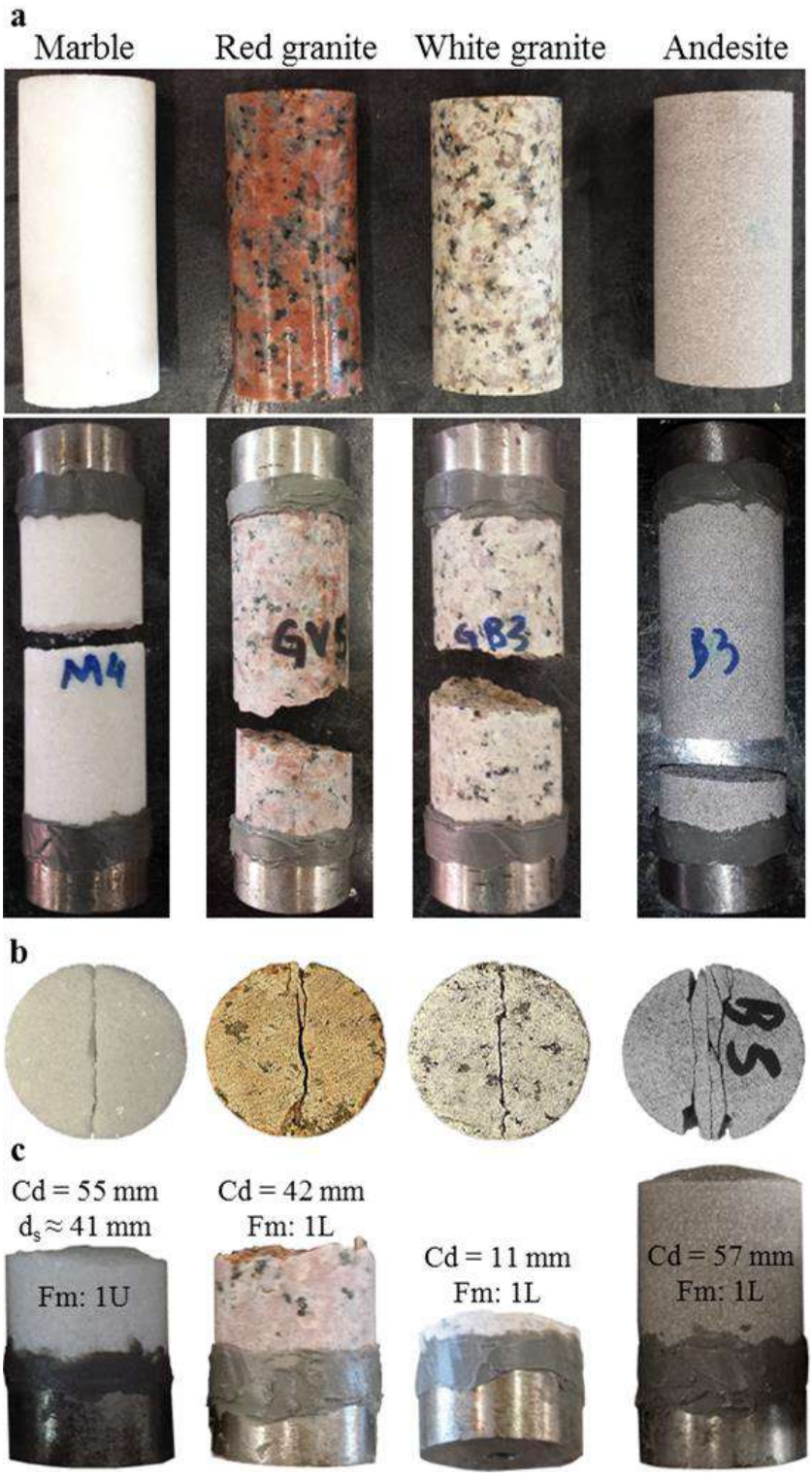

Fig. 2.5. Examples of a. DTT, b. BDT and c. POT specimens of each rock type (Cd and Fm are the core depths and failure modes of the POT in these examples).

2.3.3 Tensile strength of geological discontinuities

The para-gneiss was used to exemplify the different failure modes associated with discontinuities and contacts crossing anisotropic and heterogeneous rocks (Figs. 2.1c and d). A 100 mm-diameter diamond core bit was used to extract three larger samples from a gneiss block perpendicular to the foliation or bedding planes. Next, the 50 mm core bit (the same as that used to prepare all POTs) was used to drill internal partial cores subjected to the POTs. After each POT was performed, the 100 mm specimens were cut at the base of the core, and another POT was prepared in the same direction. Therefore, the σ_{POT} of the rock foliation and bedding planes along these specimens could be assessed, enabling the verification of the different failure modes influenced by these structures.

Fig. 2.6 shows the specimens tested, indicating the internal partial core depth (black line), failure depth (red dashed line), failure mode and σ_{POT} of each POT conducted along the specimens. In specimen I (Fig. 2.6a), a 100 mm core with a thick coarse-grained felsic bedding (composed mainly of quartz and feldspar) between two mafic fine-grained beddings with expressive biotite content along the foliation planes could be extracted. The first POT (IA) failed through the upper bedding contact (failure mode 3L shown in Fig. 2.1d), and a tensile strength of 0.91 MPa was recorded. The second POT (IB) failed through a weaker foliation plane (failure mode 2L shown in Fig. 2.1c) below the lower bedding contact (see detail shown in Fig. 2.1a), and the recorded tensile strength was considerably higher (2.96 MPa). This result is clearly related to the different mineralogical compositions of each bedding contact, as the upper presents a thick biotite layer that can be observed in both the 100 mm and 50 mm cores in Fig. 2.6a.

Figs. 2.6b and c show the other POT conducted perpendicular to the foliation/bedding planes, indicating that in this condition, failure modes 2L and 3L occur through the geological structures with the lowest tensile strengths. Failure at the base of the partial cores (2U or 3U in Figs. 2.1c and d) did not occur in these tests because the weakest foliation or bedding planes were not coincidentally positioned in this portion. Test IIIB in Fig. 2.6c was drilled propositionally with the partial core base, just below the lower contact of a thin felsic bedding, aiming to induce failure through this plane (considering the stress concentration at the base of the partial core induced by POT boundary conditions). Nevertheless, failure occurred through the upper bedding contact.

Austin et al. (Austin et al. 1995) showed that the bond strength (concrete/repair interface strength) obtained by the POT could be underestimated depending on the distance between the interface and the base of the partial core (d_s). The tests performed by these authors showed that the stress at failure (through the interface) for d_s=2 mm was approximately 15% lower than that for d_s = 15 mm. Moreover, finite element analyses showed that the stress variation at the interface is moderate for d_s=10 mm and nearly inexpressive for d_s=15 mm. Analogously, in the POT (see Fig. 2.5), d_s can be used to verify whether the tensile strength of the geological discontinuities is underestimated. Failure depth d_s was higher than 11 mm for all cases shown in Fig. 2.6, indicating that the POT boundary conditions did not considerably affect the tensile strengths obtained.

In some cases, the weaker foliation planes can be visually predicted by the apparent mica content exposed (such as in test IA). However, this is not always clear, as some incipient foliations can present unexpected low tensile strengths without a visual difference in mineralogical composition among other planes. Specimen II in Fig. 2.6b did not present any foliation plane or bedding contact with visually discrepant mica content in the outer perimeter of the 100 mm cylinder, but the tensile strength of specimen IIC was highly similar to that of IA. Gneisses are heterogeneous and anisotropic rocks; thus, the geological structures (foliation and bedding) should present discrepant tensile strengths along the specimens. Anisotropic rocks with more homogenous composition (such as fine-grained shales and slates) may not present the same discrepancy; thus, it is possible that the failure mode 1L occurs more frequently in these cases.

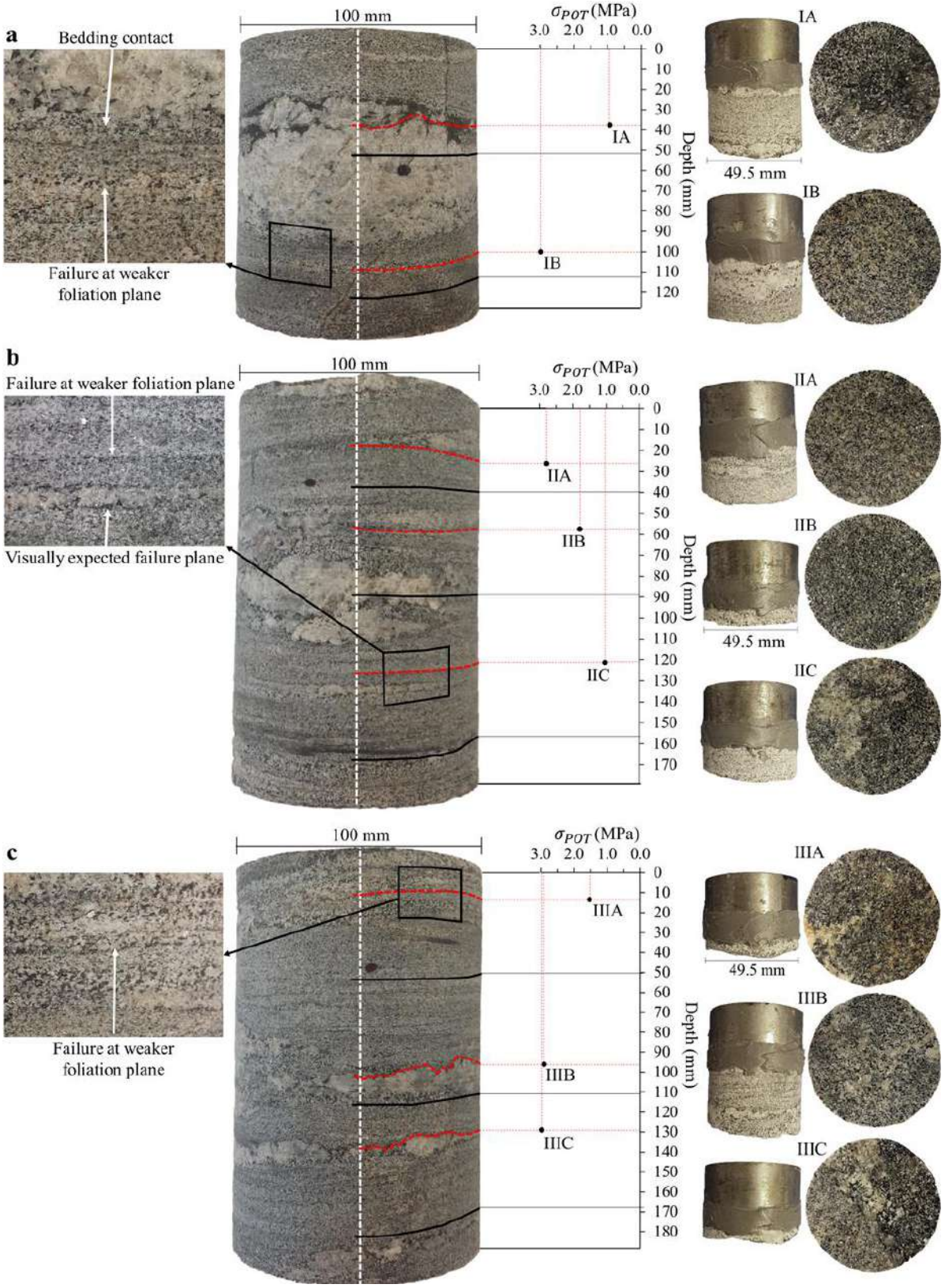

Fig. 2.6. POT perpendicularly to gneissic foliation and bedding planes using. a. Specimen I; b. Specimen II and c. specimen III. The black and red dashed lines mark the POT partial core and failure depths, respectively.

2.3.4 Practical advantage of POT

The POT is important to the construction and building materials industry because it is a practical method that can be used in situ to estimate the tensile strength of materials and repair interfaces. As shown by the previous sections, the POT can also be used to estimate the tensile strength of rocks and geological discontinuities.

Fig. 2.7 shows a systematic example of a POT simulating in situ conditions using a foliated biotite ortho-gneiss block. The flatter surfaces of rock blocks and outcrops (discontinuity planes, for example) can be selected to facilitate the POT (such as the face subparallel to the gneissic foliation in Fig. 2.7a). A small section of the surface (such as the corner highlighted in Fig. 2.7a) must be ground to drill the partial core, apply the adhesive resin, and attach the metal disc to the top of the core. The grinded surface must be sufficiently large to ensure that the POT device is parallel to the partial core top (Fig. 2.7b). The POT device must be chosen considering the expected σ_{POT}. Devices with lower load ranges are more accurate for measuring lower tensile stresses. For the example in Fig. 2.7, the DNTT-5^{TM} device, manufactured by Dinateste SA (São Paulo, São Paulo Brazil), was used before the DY-216^{TM} because it is accurate for measuring tensile stresses from 0.25 MPa using 50 mm metal discs (0.5 to 5.0 kN load range). The specimen failed after 3.15 kN; thus, the DY-216^{TM} could also be used in this case. Fig. 2.7c shows the specimen after failure.

Partial cores from 10 to 60 mm can be drilled manually using small machines, such as grinders (Fig. 2.7a) or drillers, with a constant water flow. However, deeper cores may require larger and more powerful tools, which are typically available in construction environments. It may be difficult to attach metal discs to non-horizontal surfaces due to the epoxy adhesive complete cure time. However, rock blocks removed from the excavations are often available and can be used instead of non-horizontal outcrop surfaces. The cure time depends on the adhesive type. The Araldite AV138^{TM} complete cure takes 24 h, but this time can be reduced in the laboratory using an oven (complete cure in 1 h at 100 °C). In situ, it is difficult to accelerate the cure time by heating the epoxy; however, other adhesives with shorter cure times can be used instead. The methacrylate-based adhesive, commercially known as Plexus MA300^{TM} and manufactured by ITW SA (Glenview, Illinois USA), has a complete cure time of less than 60 min at 25 °C; however, after 4 min, the adhesive is sufficiently rigid to keep the metal disc still at any inclination. Tests performed using this product indicated that invalid failures (adhesive/rock interface) occur after tensile stresses of approximately 6.5 MPa. Thus, this product is suitable

for geological discontinuities and weaker rocks (used in the example presented in Fig. 2.7) but would not be useful for the andesite and red granite tested herein.

The overall results revealed the POT to be an effective method for assessing the tensile strength of rocks and geological discontinuities using rock blocks and outcrops. The POT may not be preferred in the laboratory because the BDT is also a practical method and does not require adhesives to be attached to specimens via metal discs. However, the tensile strength is often overestimated by BDTs compared to that estimated by DTTs. Moreover, the BDT is not an appropriate method for assessing the tensile strength of geological discontinuities of heterogeneous and anisotropic rocks (see Figs. 2.6 and 2.7) because it would be necessary to determine the weaker foliation/bedding plane and prepare the specimens positioning in the middle of the rock disc. Considering the results presented in Fig. 2.6, the POT can be used in the laboratory to profile the tensile strength of geological structures along rock cores, providing results that better indicate the natural variability associated with the fabric of heterogeneous and anisotropic rocks.

Fig. 2.7. a. Biotite gneiss block, grind and drill tools and the selected section used to exemplify the in situ POT; b. POT performed with the DNTT-5^{TM} equipment; c. specimen after failure.

2.4 Conclusions

The following summary and conclusions can be provided for the study conducted:

1. The POT is a practical method for estimating the direct tensile strength of rocks and geological discontinuities and can be employed in situ. For visually homogeneous and isotropic rocks, the test can be performed in partial cores with depths of 10 mm without significant

changes in σ_{POT}. However, deeper cores are preferable (20 mm, for example) to facilitate the differentiation between the 1L and 1U failure modes (Fig. 2.1b).

2. The POT failure modes must be described because they are important for verifying the influence of the partial core boundary conditions that underestimate the tensile strength. For the visually isotropic and homogeneous rocks used, failing majorly at the base of partial cores (modes 1L Fig. 2.1b), the σ_{POT} is underestimated by approximately 12%. For POTs failing with random d_s (such as the marble used herein), the σ_{POT} is not underestimated compared to σ_{DTT}. Finally, for POTs failing through geological discontinuities close to the partial core base (for example, $d_s \leq 10$ mm), σ_{POT} may be underestimated by approximately 15% or less, depending on d_s (based on the interface strength research presented by Austin et al. (Austin et al. 1995). However, if failure occurs through discontinuities far from the partial core base (for example, $d_s \geq 15$ mm), σ_{POT} is likely not underestimated compared to that estimated by the DTT.

3. The results indicate that the POT is suitable for assessing the tensile strength of geological discontinuities along anisotropic and heterogeneous rocks because it captures the natural strength variability of the rock fabric. In situ, the POT can be applied perpendicular to large bedding and foliation planes exposed on rock outcrops and blocks.

4. Further experiments are required to extend the number of rock types tested by the POT, DTT, and BDT, improving the correlations between tests. Moreover, numerical analyses using fracture mechanics principles are required to better explain and quantify the difference between σ_{POT}, σ_{DTT} and σ_{BDT} for rocks and geological discontinuities associated with the failure modes observed in laboratory tests.

Chapter 3

Effects of Mica Content on Rock Foliation Strength

This chapter presents an article submitted to an international journal.
Authors: Pedro P. Cacciari & Marcos Massao Futai

Abstract

Foliation is a planar geological structure characterized by the alignment of minerals, including mica grains. Foliated metamorphic rocks exhibit anisotropic mechanical behaviors, wherein the weakest properties are usually oriented parallel to the foliation planes. Rock mechanics research on this subject has been focused on characterizing the full anisotropic behaviors of rocks with stresses applied parallel, oblique and perpendicular to the anisotropy direction (foliation planes). However, less effort has been given to characterizing the mechanical behaviors of isolated foliation planes and describing the influences of mineralogical properties on the weaknesses associated with such geological structures. This paper presents a laboratory testing program, including direct shear tests and pull-off tests, to characterize the influences of mica content on the shear and tensile strengths of foliation planes of the biotite gneiss (which is basically composed of biotite, quartz and feldspar). Direct shear tests were performed under constant normal load and constant normal stiffness boundary conditions, wherein the foliation planes were isolated in 1 cm-thick shear zones. The mica content was estimated by a practical digital image analysis approach that was capable of quantifying the percentage of biotite area on the foliation surfaces that failed in shear and tension. The results showed that the mica (e.g., biotite) content had substantial effects on the mechanical behaviors of isolated foliation planes, especially on the peak shear and tensile strengths. A practical 3D strength envelope was proposed that included the mica content as an independent variable, which can be quantified from foliation surfaces on rock blocks and outcrops. The results provided new insights into the influences of mica-rich foliation planes on the mechanical behaviors of metamorphic rocks, which is directly applicable to rock engineering problems.

Keywords: Foliation; Mica Content; Shear Strength; Tensile Strength; Direct Shear Tests; Pull-off Tests.

3.1 Introduction

Foliation is a planar geological structure of metamorphic rocks formed by mineral recrystallization and alignment during metamorphism (high pressure and temperature conditions). During this process, minerals are aligned in planes, which creates discontinuities with different mineralogical compositions.

In the current state of rock mechanics, it is a common assertion that foliated metamorphic rocks are likely to exhibit anisotropic strength and deformability. Generally, uniaxial and triaxial (axisymmetric) tests are applied to cylindrical core specimens extracted with different orientations (angles between the diamond core bit axis and the foliation normal vector). However, few studies have associated the testing results with the mica content and distribution in the specimens. McCabe and Koerner (1975) performed compression and tension tests on mica schist samples and examined the fracture surfaces after failure, wherein they described the qualitative aspects of the mica content. Shea and Kronenberg (1993) observed decreasing strength and increasing ductility with the mica content increase in schists and gneisses. In their study, the volume fraction of mica was quantified and varied from 15-75%. Behrestaghi et al. (1996) tested four metamorphic rock types with different mineralogical properties and showed that rocks with greater mica contents have lower tensile and compressive strengths. Rawling et al. (2002) investigated the dilatancy, strength anisotropy, crack geometry and coalescence associated with biotite foliation in a gneiss. Laws et al. (2003) also observed a decrease in strength and a transition from brittle to ductile behaviors with increasing mica content.

Considering the aforementioned studies, the fact that higher mica contents result in lower strengths for foliated rocks is accepted by the rock mechanics community. The main advantage of using compression tests for cylindrical specimens is that the strength can be fully characterized against the anisotropy orientation. Thus, different failure envelopes can be assigned to the intact anisotropic rock depending on the directions of the principal stresses and the foliation orientation. Such results can be used to calibrate ubiquitous joint and transversally isotropic models implemented in computer programs, e.g., Sainsbury and Sainsbury (2017). On the other hand, this approach overlooks the following important aspects related to the foliation planes and their occurrence in engineering structures:

1 - When performing uniaxial or axisymmetric compressive tests, failure hardily occurs through a single and isolated foliation plane; some parallel and perpendicular cracks are often observed

(Basu et al. 2013). Therefore, the strength and deformability cannot be totally associated with the mechanical parameters of a single foliation plane.

2 - The postpeak behavior of an isolated foliation plane cannot be investigated using uniaxial or axisymmetric compressive tests because the dilation effects cannot be attributed to a single foliation.

3 - These tests are not suitable to simulate the constant normal stiffness (CNS) boundary condition, which should be considered in several rock engineering cases, such as tunnels.

Aspect number 1 becomes more critical for anisotropic and strongly heterogeneous rocks (such as gneisses) because the strength of the rock foliation and banding varies substantially along the cylindrical core specimens depending on their mica content and the overall mineralogical compositions. Using direct shear tests (DSTs), one can isolate the aimed foliation plane inside a shear zone and attribute the mechanical parameters to the geological structure. Mello et al. (2004) reported extremely low strengths (cohesion intercept of 0.055 MPa and a friction angle of 22.5°) associated with weathered layers of biotite schists using DSTs. With synthetic rock specimens, Niemeijer and Spier (2005) performed ring shear tests on different halite-muscovite mixtures to verify the influence of the phyllosilicate content on the shear strengths of fault gouges.

DSTs are traditionally conducted under constant normal load (CNL) boundary conditions, which are widely used in rock mechanics. Under CNL conditions, the normal force applied on the discontinuity plane is constant during testing. Thus, the slipping block is free to dilate once the shear force is applied. This condition represents a typical rock slope problem, in which the normal load depends only on the weight of the slipping block. However, CNL conditions are unrealistic for several rock engineering problems (Thirukumaran and Indraratna 2016) where the rock block is confined by the surrounding rock mass, such as in tunnels and in slopes reinforced by cable bolts. Therefore, several authors (Leichnitz 1985; Saeb and Amadei 1992; Indraratna and Haque 1997; Seidel and Haberfield 2002; Jiang et al. 2004; Park et al. 2013) have performed DSTs under CNS boundary conditions, in which a normal stiffness (K_{ne}) is used to represent the deformability of the external system (rock mass). The CNS conditions in DSTs are idealized as a simple spring system, as shown hereafter:

$$\Delta F_n = K_{ne} \Delta \delta_n \tag{3.1}$$

where ΔF_n and $\Delta \delta_n$ are the changes in normal load and normal displacement, respectively, which are monitored during testing.

The tensile strengths of metamorphic rocks are also strongly influenced by foliation. Similar to shear strengths, the influences of foliation on the tensile strengths of rocks are usually assessed by indirect and direct tensile strength tests with specimens drilled with different foliation orientations. More recently, Shang et al. (Shang et al. 2016) performed several direct tension tests with the tension load exclusively applied perpendicular to the bedding planes, joints and veins of sandstone specimens and discussed some effects of the mineralogical composition and weathering on the tensile strength results. However, the direct influences of the mica content on the tensile strengths of isolated foliation planes have not been investigated to date.

As mentioned above, no studies have been reported that quantitatively show the influence of the mica content on the mechanical behaviors of isolated foliation planes from natural rock specimens. This work presents a laboratory testing program, including DSTs (under CNL and CNS conditions) and pull-off tests (POTs), to assess the mechanical behaviors of isolated foliation planes with different mica contents. Biotite gneiss, which is basically composed of biotite, quartz and feldspar, was selected due to the facility of identifying biotite grains (dark mineral) among quartz and feldspar grains (light-gray minerals). The percentages of biotite area (M_a) covering the failed surfaces of the DST and POT specimens were estimated by digital image analysis and associated with the DST and POT. The association between the POT and DST results shows substantial influences of the mica content on the shear and tensile strengths of foliation planes. Moreover, M_a was included as an independent variable on a 3D strength envelope for foliation planes with variable mica contents. Thus, M_a is introduced as a practical rock engineering parameter that could be quantified in the field for predicting the shear and tensile strengths of foliation planes.

This laboratory study was developed by the Geotechnical Engineering Research Group (GeoInfraUSP) of the University of São Paulo, which was motivated by recent studies of old tunnels from Brazilian railways that were constructed in foliated gneissic rock masses (Cacciari and Futai 2016b, 2017). The influences of mica content on the mechanical behaviors of foliation planes have major importance for understanding the stability state of these tunnels and other engineering structures constructed in mica-rich gneissic rock masses.

3.2 Materials and methods

The shear and tensile strengths of gneissic foliation planes were assessed on a laboratory scale by DSTs under CNL and CNS conditions and by POTs. A biotite gneiss from Minas Gerais state (Brazil) was selected for this study. Biotite gneiss is the main lithological unit of the Mantiqueira complex, which composes the crystalline basement of the Araçuaí orogenic belt. The Mantiqueira complex covers a wide area of southeastern Brazil. Several tunnels and slopes from railways and roads have been constructed on biotite gneiss (or similar rock types). The rock blocks used in this study were taken from the Ana Matos tunnel, which belongs to the Vitória-Minas railway. This tunnel was built in the 1950s and is 400 m long and mostly unsupported (only a few small sections are supported with structural concrete liners).

The main composition of the biotite gneiss is quartz, feldspar and biotite, which were identified in thin sections. Other minerals, such as hornblende and pyroxene, are also present in the biotite gneiss in insubstantial amounts (<2%). The rock foliation and banding of the biotite gneiss is well defined by aligned biotite layers interleaved with quartz and feldspar layers. Fig. 3.1a shows an example of a biotite gneiss block, and Fig. 3.1b shows a saw-cut surface of this block highlighting the foliation planes filled with biotite grains (dark grains).

Fig. 3.1b shows that the biotite content and distribution are variable on the foliation planes of the biotite gneiss. Fig. 3.2a shows a specimen taken from a felsic banding. The red-painted rectangles delineate two thin sections taken from this specimen. Quartz and feldspar are predominant on felsic bandings, while biotite occurs in thin layers of agglomerated grains (such as the planes highlighted by the thin section micrographs I and III in Fig. 3.2) and thick layers of feldspar grains (such as the plane highlighted by the thin section micrograph II in Fig. 3.2). Thin layers of agglomerated biotite grains are often discontinuous, containing several quartz and feldspar bridges (e.g., micrograph I in Fig. 3.2). In some cases, these planes are visually continuous (e.g., micrograph III in Fig. 3.2). Between biotite layers, the rock is predominantly composed of quartz and feldspar, and the biotite content is minimal (e.g., micrograph IV in Fig. 3.2)

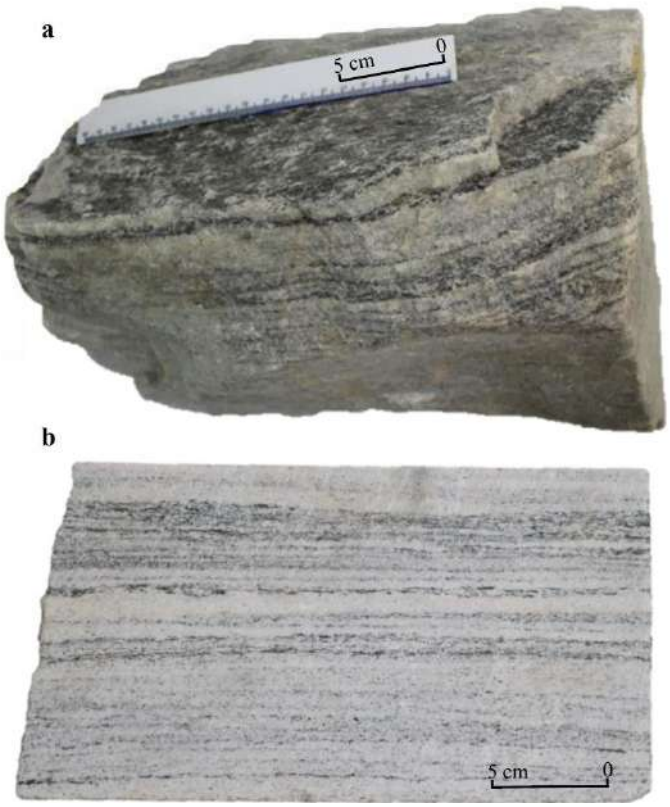

Fig. 3.1. Example of (a) a biotite gneiss block used to prepare specimens, and (b) a saw-cut surface of the same block.

Fig. 3.2b shows a specimen taken from a mafic banding of the biotite gneiss. On mafic bandings, biotite is predominant, while quartz and feldspar occur as nonpersistent bodies and inclusions within the thick biotite layer (details in micrographs V and VI). In some cases, the biotite layer is thicker than the shear zone isolated on the DST specimens, which will be discussed further.

Biotite is the only dark mineral with a substantial content in the biotite gneiss, making it easy to identify and quantify on macroscopic specimens. In this case, it was possible to use image analyses to quantify the percentage of biotite covering the failed surfaces of DST and POT. Therefore, this is a suitable rock type to investigate the effect of mica content on the tensile and shear strength of rock foliation planes.

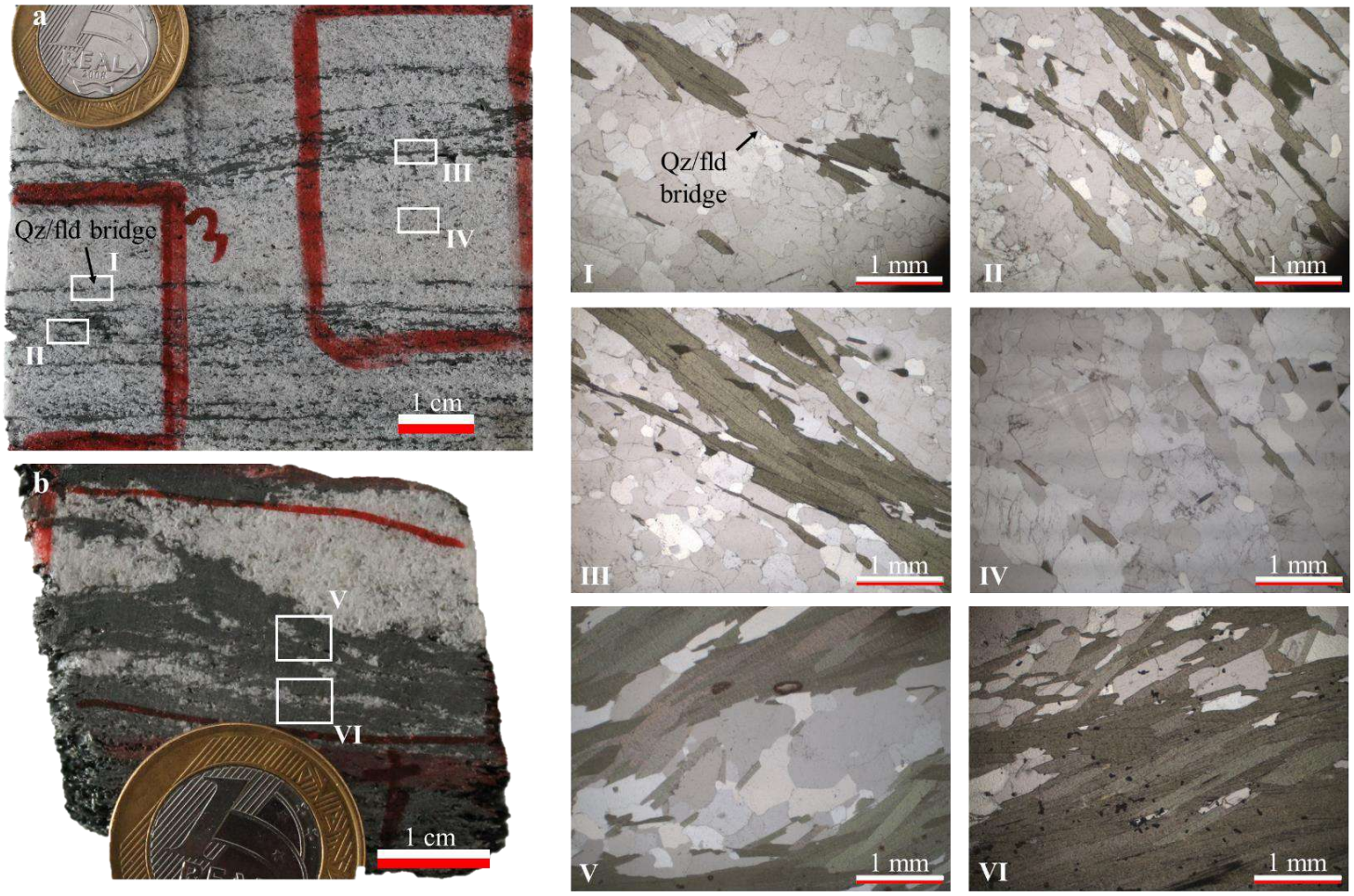

Fig. 3.2. Biotite content and distribution on (a) felsic and (b) mafic bandings. In micrographs I, II, III and IV, the biotite grains are the light brown to dark brown/green grains, and the quartz/feldspar grains are the white to light-gray grains.

3.2.1 Pull-off tests

POTs were recently introduced to rock mechanics applications (Cacciari and Futai 2018a). POTs consist of pulling a metal disc attached to a partial core drilled against a flat rock surface (Fig. 3.3a). In this case, all tests were performed perpendicular to the foliation planes, and only the peak tension stress was recorded and interpreted as the tensile strength of the failed foliation plane. The POT was selected for this study due to its practical advantages over the direct tension test (DTT), especially in terms of the specimen preparation process. In both POTs and DTTs, failure can occur at the weakest foliation plane along the cylindrical core specimen. Therefore, tests with predefined failure planes, such as the Brazilian disc test, would not be suitable in this case.

A total of 20 POTs were performed on 5 different rock blocks, which were visually inspected and selected to cover a wide range of mica content. In addition to the peak tension stress (tensile strength from the POT), the partial core depth (d_{pc}) and the failure plane depth (d_{fp}) were also recorded. Note that d_{pc} was defined during the test preparation and controlled by marking the core drill bit, which varied from 25 to 60 mm. d_{pc} and d_{fp} are important to understand the influence of the boundary conditions of the POT on the tensile strength results (Cacciari and Futai 2018b).

3.2.2 Direct shear tests

The DSTs were performed on a servo-controlled direct shear machine. Servo-controlled testing machines operate in fast response closed-loop systems enabling precise, automatic and continuous control of any independent variable (such as load or displacement) measured during tests (Hudson et al. 1972). The direct shear structure supports up to 300 kN in both vertical (normal) and horizontal (shear) directions, and the loads and displacements are measured in each actuator by independent load-cells and linear variable differential transformers (LVDTs) (Fig. 3.3c). During the DSTs, the lower shear box moves horizontally (i.e., the *y*-direction), and all other degrees-of-freedom are restricted. The double-swivel arm system connected to both sides of the upper shear box and enables all possible degrees-of-freedom (rotations and translations) except *y*-translation.

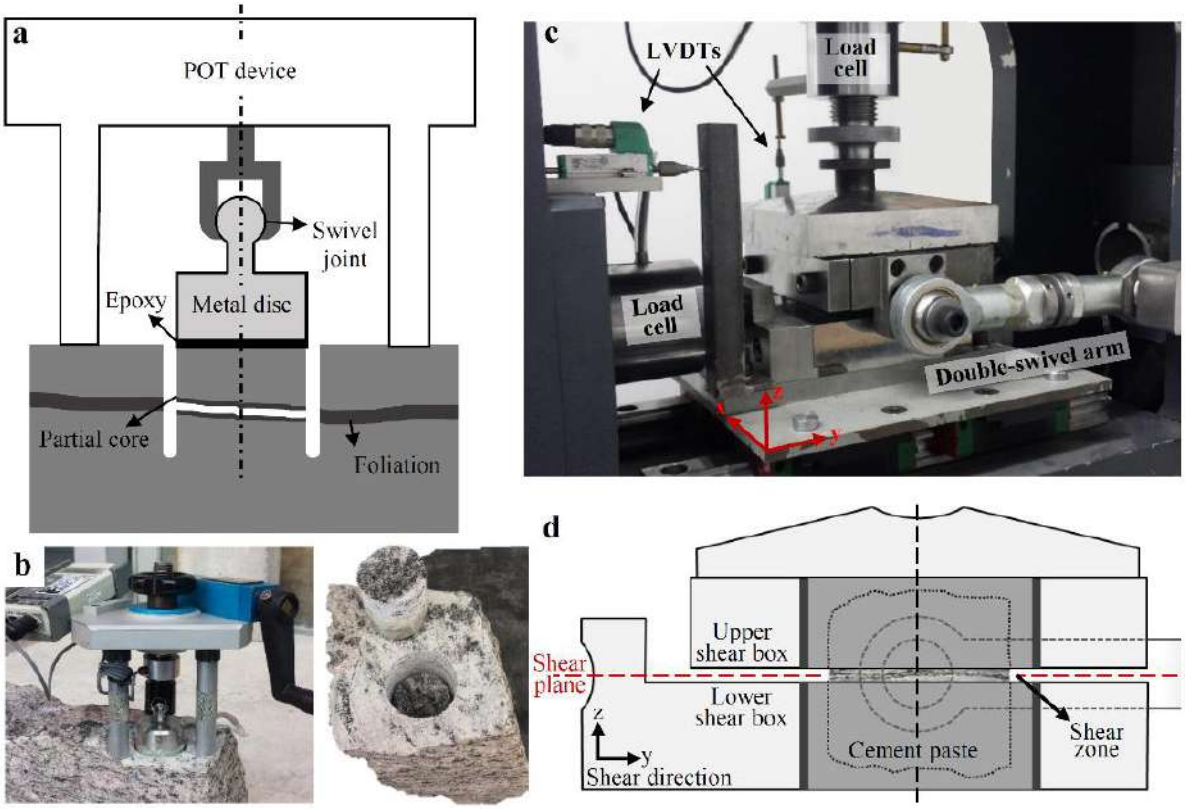

Fig. 3.3. (a) POT sketch and (b) test example (Cacciari and Futai 2018a). (c) DST system. (d) Mounted shear box sketch.

All DST specimens were rectangular and cut with a diamond saw. First, the target foliation plane was selected and marked approximately in the middle of a 1 cm-thick shear zone (Fig. 3.4a). The shear zone was kept horizontally oriented and placed on the top of the lower metal box, and a stiff cement paste (water/cement ratio of 0.27) was used to fill the empty space. The width and length of the shear zones ranged from 50-75 mm and 80-90 mm, respectively, and the specimen's longer side (length) was always positioned parallel to the shear direction. In this step, care was taken to hold the shear zone in the middle of the metal box to guarantee that the normal load was applied on the center of the specimen during the DSTs. After a few hours, the shear zone was isolated with Styrofoam of 1 cm thickness and adhesive tape, and the upper metal box was positioned and filled with cement paste. Two L-shaped steel bars were placed at opposing corners of the metal boxes before filling the upper box to guarantee their vertical alignment. The specimens were kept in a wet chamber for 5-7 days before testing. Fig. 3.4b shows that the 1 cm-thick shear zone is isolated inside the specimen and that the selected foliation plane is approximately aligned with the shear plane of the DST shear box.

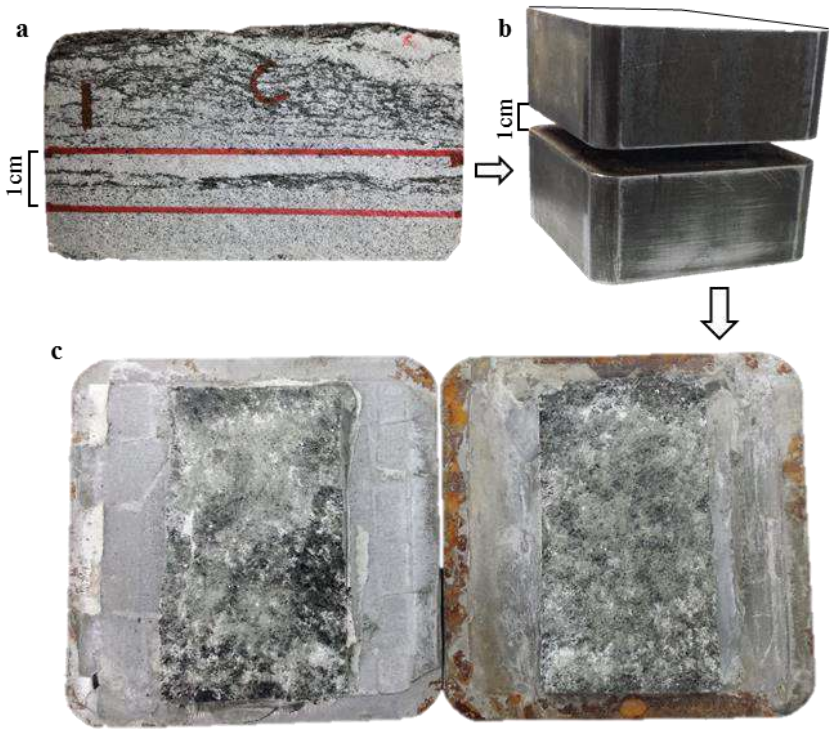

Fig. 3.4. (a) Selected foliation plane; (b) isolated shear zone inside the shear box; and (**c**) failed foliation plane after the DST.

The DSTs were performed in two stages to preserve the integrity of the surface minerals for image analyses. In the first stage (peak DST), the normal stress was applied until the desired initial normal stress value (σ_n), which was followed by a constant shear rate of 0.05 mm/minute. In the case of transitional (brittle-ductile) failures, the end of the peak DST stage occurred after completing the strain-softening curve (Fig. 3.5a). In the case of brittle-like failures, wherein the shear stress abruptly decreases due to energy releases, the end of the peak DST stage occurred after completing the reloading step (repositioning the specimen to the maximum recorded displacement or higher) (Fig. 3.5b).

After the peak DSTs, the specimens were removed from the DST box, and photographs were taken for the image analyses used to quantify the mica content. In the second stage (postpeak DST), the specimens were carefully remounted inside the DST box, and the same σ_n was applied, which was followed by a constant shear rate of 0.1 mm/minute until the shear displacement reached at least 10% of the specimen length (i.e., between 8.0 and 9.0 mm).

The analyzed DST parameters were the shear strength, shear stiffness and dilation angle in both the peak and postpeak stages. The specimens were not subjected to normal stresses higher than the initial normal stress used in the DSTs to avoid major damage to the foliation surface (especially in the case of high mica contents). Thus, the vertical load stage did not reach the full nonlinear behavior of joint closure; consequently, the normal stiffness is not analyzed herein.

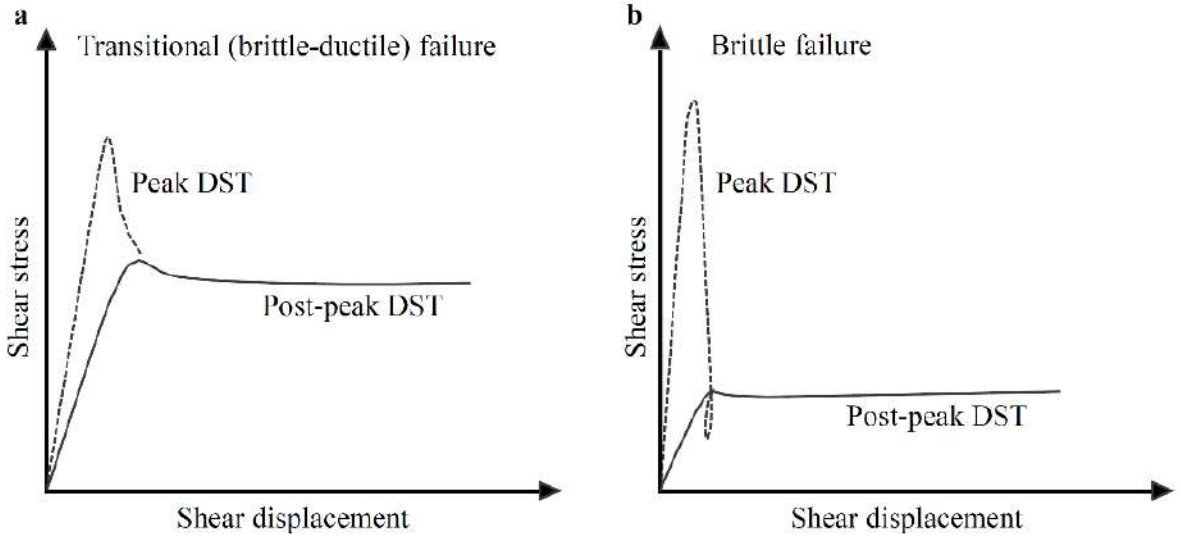

Fig. 3.5. Hypothetical examples of (a) transitional (brittle-ductile) and (b) brittle failures during two-stage DSTs.

A total of 38 DSTs were performed, including 28 under CNL conditions (named CNL01 through CNL28) and 10 under CNS conditions (named CNS01 through CNS28), on samples that were visually inspected and selected to cover a wide range of mica contents. The applied values of σ_n were 0.5, 1.5, 2.5, 3.5, 5.0 and 8.0 MPa. For the DSTs under CNS conditions, a single normal stiffness (K_{ne}) value of 7.5 MPa/mm was used. The estimate of K_{ne} based on the model proposed by Johnston (1987), which is usually used for rock mechanics problems and accounts for the deformability modulus and the Poisson's ratio of the rock mass surrounding the shearing discontinuity. Moreover, after performing DSTs under CNL conditions, the amount of dilation indicated that K_{ne}=7.5 MPa was a suitable value for observing significant normal stress changes without excessively extrapolating the initial normal stress range used (0.5 to 8.0 MPa). Applying the laboratory results to stability analyses of the Ana Matos tunnel

is not within the scope of this work. However, K_{ne}=7.5 MPa/mm simulates the sections of the Ana Matos tunnel with the worst rock mass quality, which makes the results useful for future applications.

3.2.3 Mica content estimation

The biotite content was obtained by quantifying the percentage of biotite area (M_a) on the failed planes of the POT and DST specimens by an interactive process using ImageJ (Rasband 2004). This software has a feature to adjust the maximum and minimum threshold values for different colors. The grayscale varies from 0 (black) to 255 (white). Quartz and feldspar grains, which vary from 220 to 155, are much whiter than biotite, which varies from 10 to 80. All photographs were taken with the same camera resolution (12 MP) and illumination.

The procedure was interactive, consisting of uploading the photograph to ImageJ (Fig. 3.6a) and changing it to grayscale (Fig. 3.6b). Then, only the maximum threshold was reduced until all the white to light-gray minerals (quartz and feldspar) were marked in green (Fig. 3.6c). In this step, zoom was used in specific regions of the image to verify that the threshold used was suitable by selecting only the desired grains. The final biotite-covered area is the remaining area after removing the green selection (Fig. 3.6d). Figs. 3.6e and f show the magnified images with the appropriate selection of quartz and feldspar grains. It is interesting to note that the original and grayscale images are almost identical because the original mineral colors are similar to the opposing grayscale values.

ImageJ is commonly used for mineralogical analyses, such as quantifying mineral contents, shapes and sizes (Cox and Budhu 2008; Ghazvinian et al. 2015; Spagnoli et al. 2016). The biotite gneiss facilitates this process because biotite is the only dark-color mica mineral with a relevant content in this rock, which facilitates its identification. The two-stage DST described before caused minor frictional damage to the surfaces, thereby avoiding crushing and spreading of biotite minerals.

For the POTs and DSTs, both sides of the failed planes were analyzed, and the highest M_a value was considered the most representative. Therefore, the M_a measured herein is not the "true" biotite area on the foliation planes. Attempts of overlapping both failure plane sides to calculate the "true" M_a produced unsatisfactory results because of the bias caused by the hand-made

alignment process. Another important aspect is the practical application of the M_a parameter. In field cases, usually only one side of the foliation planes is available—on rock exposures of failed blocks—for taking photographs and quantifying M_a.

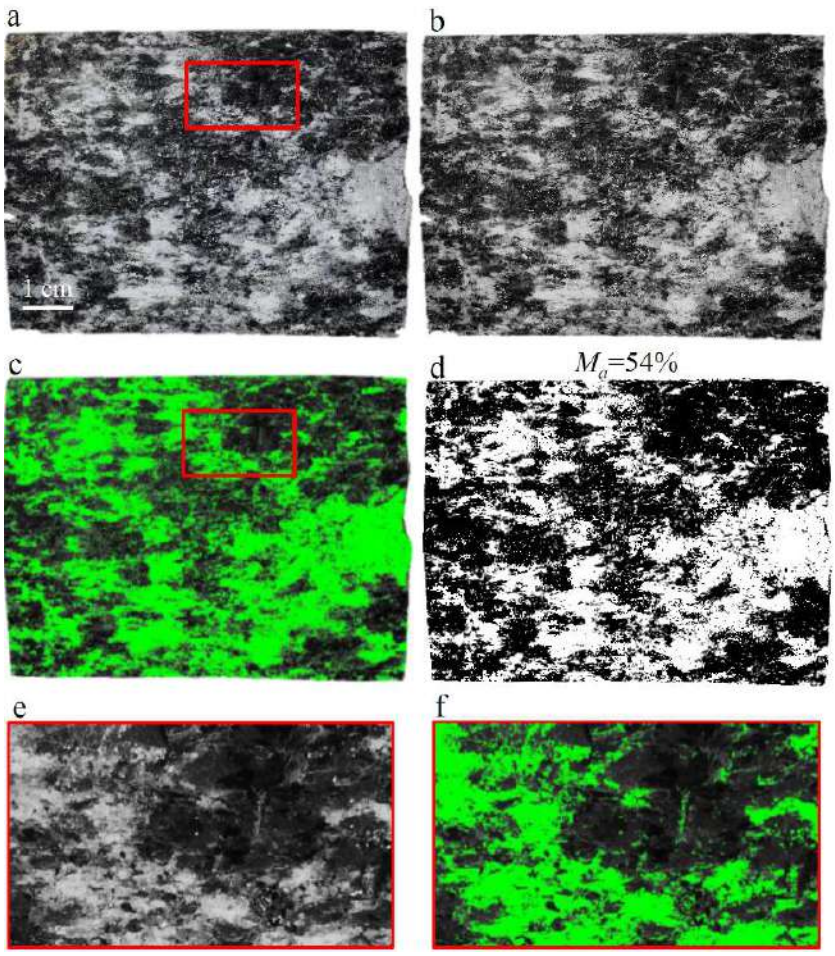

Fig. 3.6 Method used for estimating M_a. (a) Original surface photograph; (b) grayscale photograph; (c) marked grayscale interval for minerals other than biotite; (d) mask of the final biotite-covered area; and (e) and (f) details in (a) and (c).

3.3 Results and discussion

The principal aim of the laboratory tests was to assess the influences of the mica content on the shear and tensile strengths of foliation planes. The image analyses described in Section 3.2.3 were performed in all POTs and DSTs. Fig. 3.7 shows different examples of M_a quantifications on foliation planes with low, intermediate and high biotite contents, wherein both the original

photographs and the masks of the final biotite-covered area are shown. The influence of M_a on the POT and DST results is discussed in the following sections.

Foliation planes with high M_a values represent the weakest planes in anisotropic and heterogeneous rocks, such as gneisses. Usually, it is possible to predict extreme M_a values (e.g., >80% or <10%) by the visual aspect of the mica layer on the lateral sides of the DST specimens (thickness and continuity indicated in Fig. 3.2). On the other hand, intermediate M_a values are hard to predict before analyzing the failed foliation surfaces.

It is important to mention that specimens with M_a >90% are likely to break during the preparation process due to the vibration of the cutting machine, especially specimens having thick layers of agglomerated biotite grains. Approximately 50% of the POT and DST specimens broke during the preparation process and could not be tested.

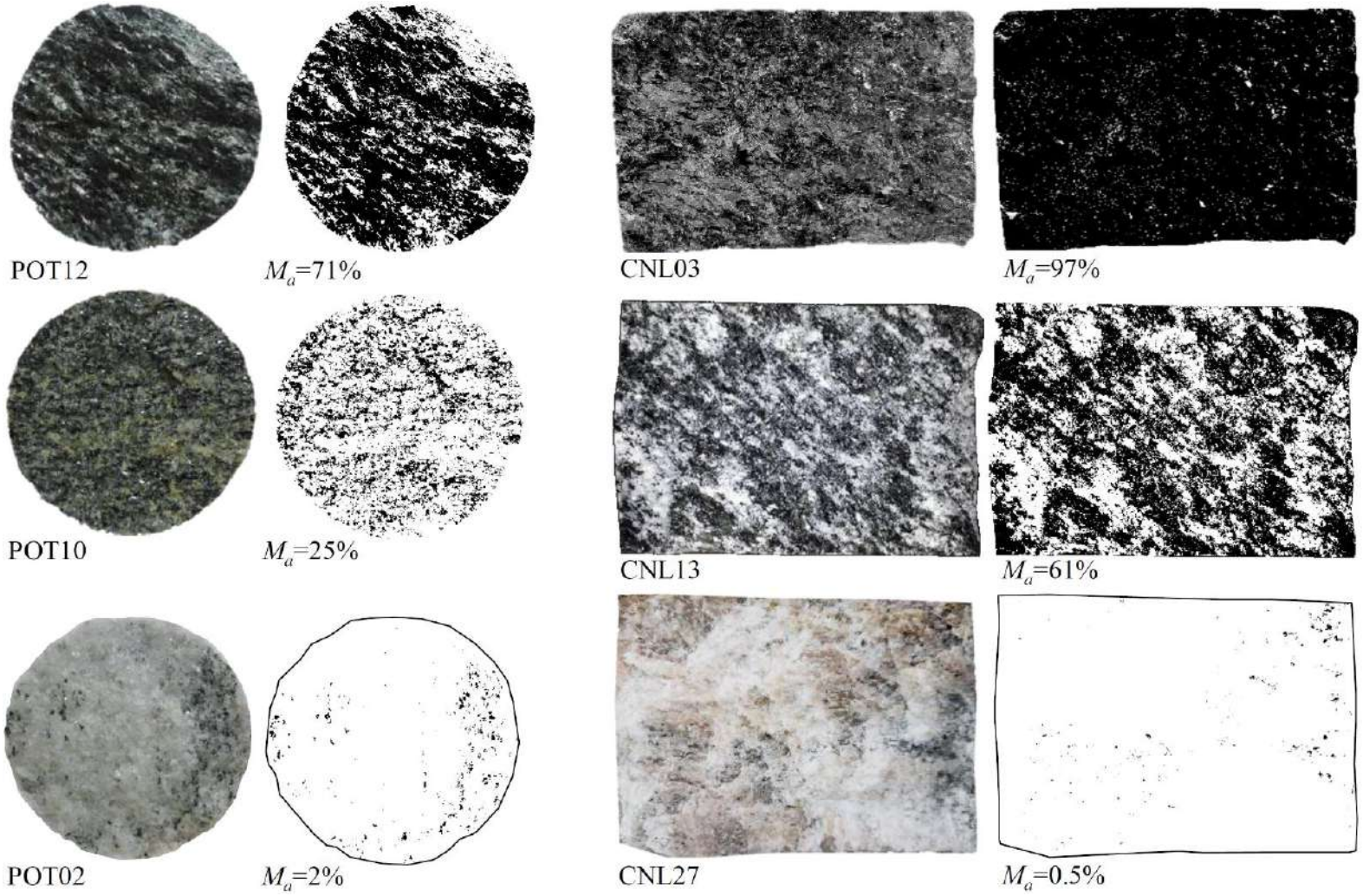

Fig. 3.7 M_a examples of the foliation surfaces of the POT and DST specimens.

3.3.1 POT tensile strength vs M_a

Fig. 3.8 shows the variation in the POT tensile strength (σ_t) with respect to M_a. As M_a varies from 0 to 100%, there are two strength thresholds indicated in Fig. 3.8. The lowest recorded value was 0.055 MPa for a M_a of 98%, and the highest recorded value was 5.55 MPa for a M_a of 1.9%. It is interesting to note that the tensile strength exhibits a steep decrease when M_a increases from 20% to 60%, which indicates that the tensile strength is sensitive to small M_a variations in this interval. When M_a is 70% or higher, the tensile strengths recorded were always less than 0.5 MPa.

It is important to note that failures at the core base peripheries occurred only in specimens on the upper strength threshold (M_a <2%). For all other cases, the distance between d_{pc} and d_{fp} was always greater than 11 mm; thus, the POT tensile strengths can be assumed to be equal to the direct tensile strengths of these foliation planes (Austin et al. 1995; Cacciari and Futai 2018a, b). For the cases where d_{pc} = d_{fp}, the POT tensile strength is likely underestimated by approximately 10 to 12% compared to the direct tensile strength.

The two strength thresholds and the stress decrease in the POT results indicate that the tensile strength varies nonlinearly with respect to M_a, and the correlation between these parameters should present two inflections: one inflection after the upper M_a threshold, and the other inflection before the lower M_a threshold. Based on this observation, the following function (Eq. 3.2) was tested and showed a good fit to the data:

$$\sigma_t = \beta_t/(1 + (\alpha_t M_a)^{n_t}) \tag{3.2}$$

The parameter β_t (in MPa) represents the mean tensile strength for negligible mica contents (i.e., the maximum tensile strength), while α_t and n_t are unitless adjustment parameters. The black dashed line in Fig. 3.8 indicates the assumed correlation between the direct tensile strength and M_a for biotite gneiss, which uses the parameters obtained by the nonlinear regression process. It is worth mentioning that, the rock foliation is perpendicular to the tension load even when M_a<2%.

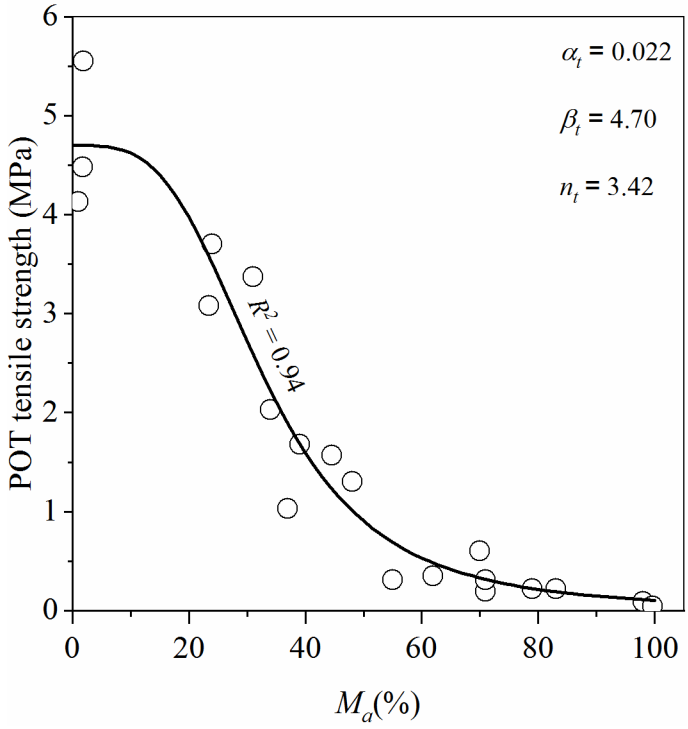

Fig. 3.8. Variations in the POT tensile strength with respect to M_a.

3.3.2 DSTs under CNL conditions

Fig. 3.9 shows the DSTs of specimens with M_a >87% under CNL conditions. Both the shear stress (σ_s) and normal displacement (δ_n) are presented with respect to the shear displacement (δ_s). In this figure, the peak and postpeak DSTs predominately indicate failures with progressive strain-softening behaviors. It is possible to see that the maximum shear stresses in the postpeak stage tend to reach the same final shear stresses measured in the peak stage.

In the peak stage, the shear zone is an intact rock specimen with an isolated foliation plane. This type of intrablock structure (Day et al. 2017) does not behave as an open joint, which has a deformability that is considerably lower than that of the coupled system (rock, cement paste and metal box). However, the major part of the displacements measured during shear can be attributed to the deformability of the shear zone because it is the only unconfined part in the system (Figs. 3.3 and 3.4). Therefore, the dilation and stiffness measured during the peak DSTs cannot be entirely associated with the shear zone; nevertheless, these measurements are useful parameters for analyzing the differences in specimens, as the cement paste composition and metal box are the same for all DSTs.

Nevertheless, the shear stiffness in the peak stage is consistently higher than that in the postpeak stage, which indicates that open joints have higher deformability than intrablock structures (e.g., shear zones with isolated foliation planes). Moreover, the reduction in the shear stiffness before failure (peak stage) occurs alongside an increase in the dilation rate due to cracks being created between grains. The details of specimens CNL03 and CNL04 (Fig. 3.9) indicate the beginning and end of this process. With the exception of CNL04 (σ_n=3.5 MPa), all tests showed dilative behaviors during the crack initiation process. Although CNL04 did not dilate, the contraction rate almost ceased before failure and started again after the peak contour was completed. The contractile behaviors in both the peak and postpeak stages are related to biotite content and thickness in the isolated shear zone (this subject is discussed further).

Fig. 3.10 shows the DSTs under CNL conditions from specimens with intermediate M_a values. The brittle or quasi-brittle behaviors were predominant among these specimens. Only CNL08, CNL11, CNL20 and CNL22 exhibited transitional (brittle-ductile) behaviors without shear stress drops after failure as a result of their high M_a values: 71, 77, 78 and 79%, respectively. For most specimens, dilation occurred during both the peak and postpeak DST stages. In the case of specimens CNL13, CNL15 and CNL21, late contraction occurred during the postpeak DSTs after 4 mm of shear displacement. This behavior is due to upper shear box rotations caused by the created surface morphology and late failures of the shear zone fragments (previously fissured during the peak DST stage).

Fig. 3.11 shows the DSTs from the specimens with M_a <5%, which exhibit brittle-like failures with abrupt shear stress drops. In this case, only the peak stage is used because the shape of the failure surface is not suitable for obtaining a valid postpeak strength. Characteristics of the failure surface morphologies and their influences on the DST results are discussed further in detail.

These results in Fig. 3.11 represent the highest shear strengths obtained for each normal stress level. No contraction was observed in these cases, which is likely because the quartz and feldspar are much less deformable than biotite. The dilation rate also increased significantly as a result of the crack initiation process. However, the abrupt shear stress drop at failure disturbs the normal vs. shear displacement curve, which hinders the visualization of the progressive reduction in the dilation rate. In this case, the normal displacement (δ_n) vs. shear displacement (δ_s) curve is shown until the shear stress drop occurs.

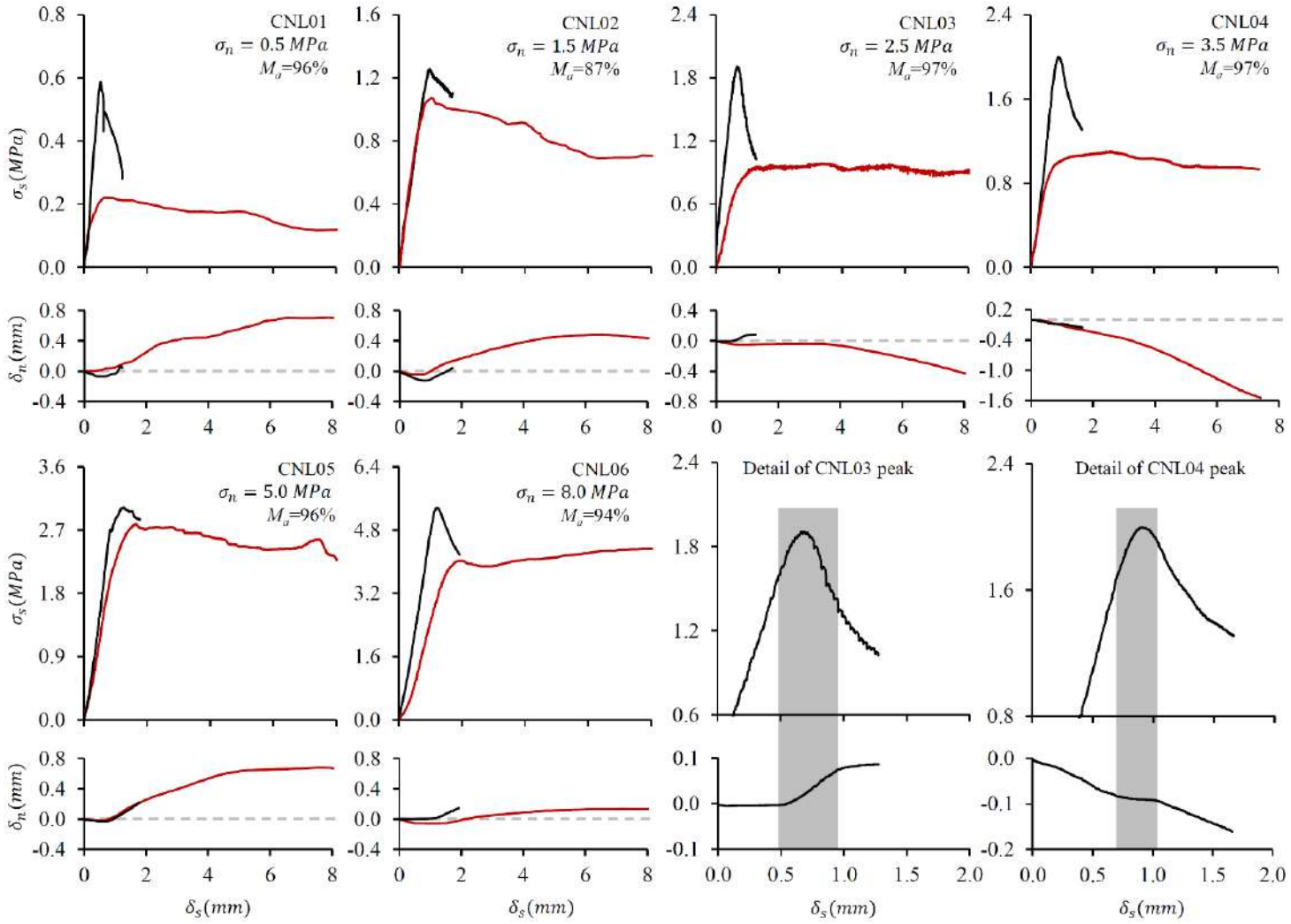

Fig. 3.9. DSTs under CNL conditions from specimens having M_a >87% (black lines are the peak DSTs, and the red lines are the postpeak DSTs).

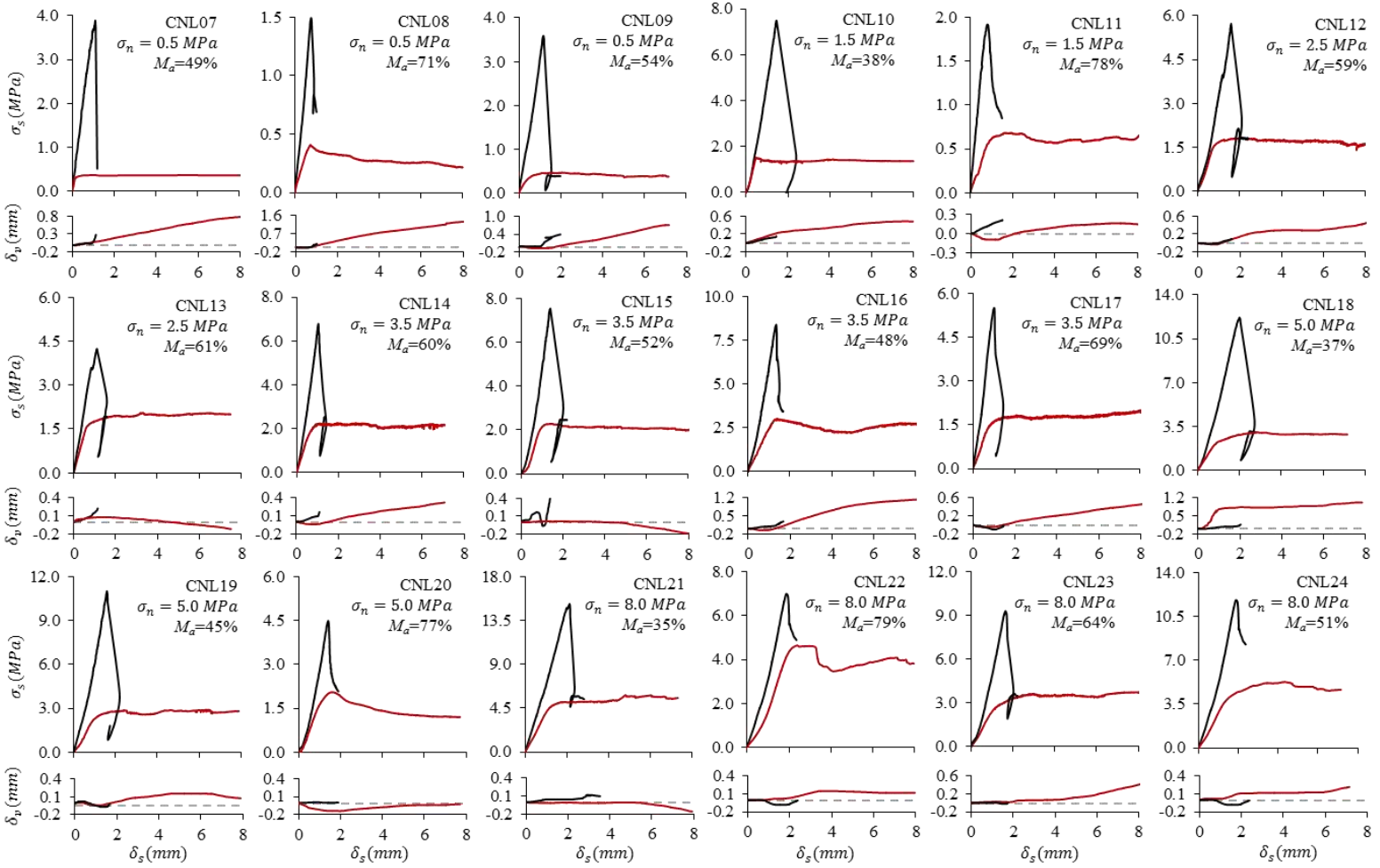

Fig. 3.10. DSTs under CNL conditions from specimens having intermediate M_a values (black lines are the peak DSTs, and the red lines are the postpeak DSTs).

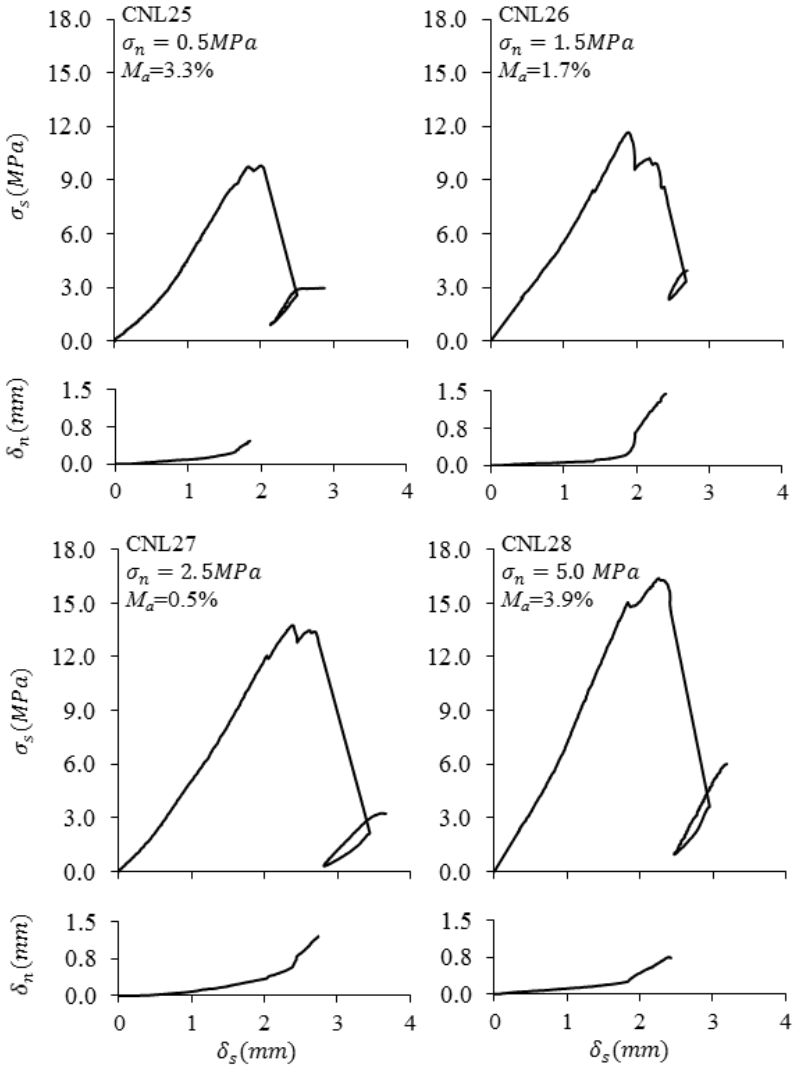

Fig. 3.11. DSTs under CNL conditions from specimens with M_a <5%

3.3.3 DSTs under CNS conditions

Fig. 3.12 shows the DSTs performed under CNS conditions with various M_a values. Specimens DST29 through DST35 have M_a>80% and were tested with the same initial normal stresses as the specimens in Fig. 3.9 (CNL conditions). Fig. 3.13a shows the responses of σ_s with respect to the normal stresses for specimens with similar M_a values (>80%) and different initial normal stresses. Fig. 3.13b plots σ_s against σ_n for specimens with the same initial normal stresses (e.g., 2.5 MPa) and different M_a values.

With the exception of CNS08 and CNS09, all specimens dilated during the peak and postpeak DSTs under CNS conditions (Fig. 3.12). Thus, the normal stress and, consequently, the shear stress increased during shear. It is interesting to note that the normal stress increase in the peak stage (due to dilation) was significant using K_{ne}=7.5 MPa/mm. For example, CNS02 showed a final normal stress that was over 30% higher than the initial assigned normal stress. Therefore, under CNS conditions, the fracturing process of foliation planes can be substantially impaired depending on the K_{ne} value. The K_{ne} value used herein is realistic for shallow tunnels constructed in moderately fractured hard rock masses. The contractive behaviors of specimens CNS08 and CNS09 are related to the thickness and morphological characteristics of the biotite layer. The characteristics of the biotite layer thickness and its influence on the DST results are discussed further in detail.

In the postpeak stage, the DST specimens are similar to open joints, in which the normal stress tends to increase parallel to the shear strength envelope. The surface morphologies created after the peak DSTs are different among the various specimens; thus, the postpeak dilation and, consequently, the normal stress increases are different for each specimen (Fig. 3.13). However, for specimens of similar M_a values (Fig. 3.13a), it is possible to note that the normal stresses increases are approximately equal, indicating that they could belong to the same postpeak strength envelope. For specimens with different M_a values (Fig. 3.13b), there is a modest difference in the normal stress increase rate, indicating that they belong to different postpeak strength envelopes.

Three shear stress values are highlighted with symbols in Fig. 3.13: the peak shear strength (peak stage), the postpeak shear strength and the ultimate shear strength (postpeak stage). The postpeak shear strength is the shear stress value reached before the stress path is drastically changed due to dilation.

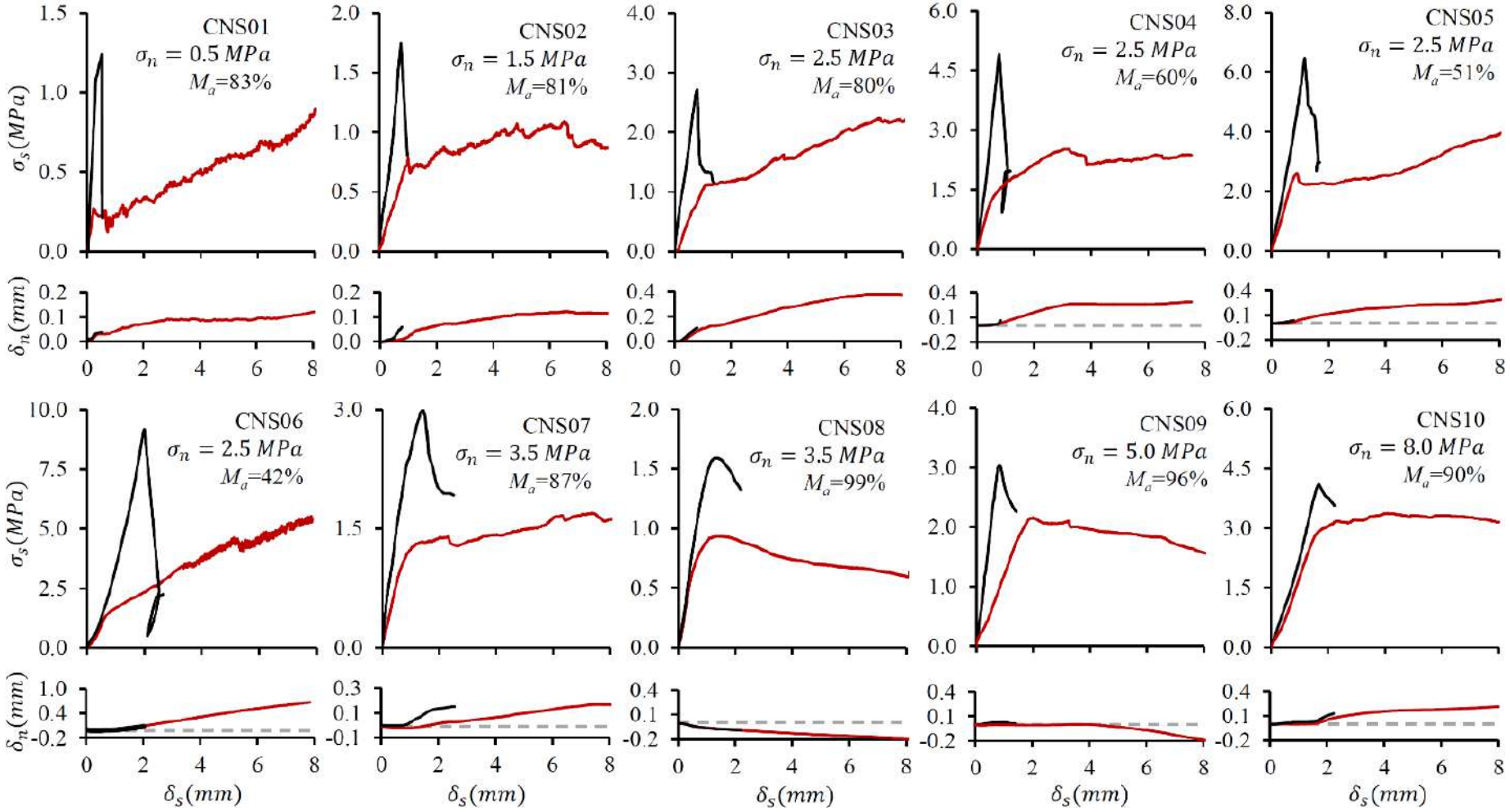

Fig. 3.12. DSTs under CNS conditions (black lines are the peak DSTs, and red lines are the postpeak DSTs).

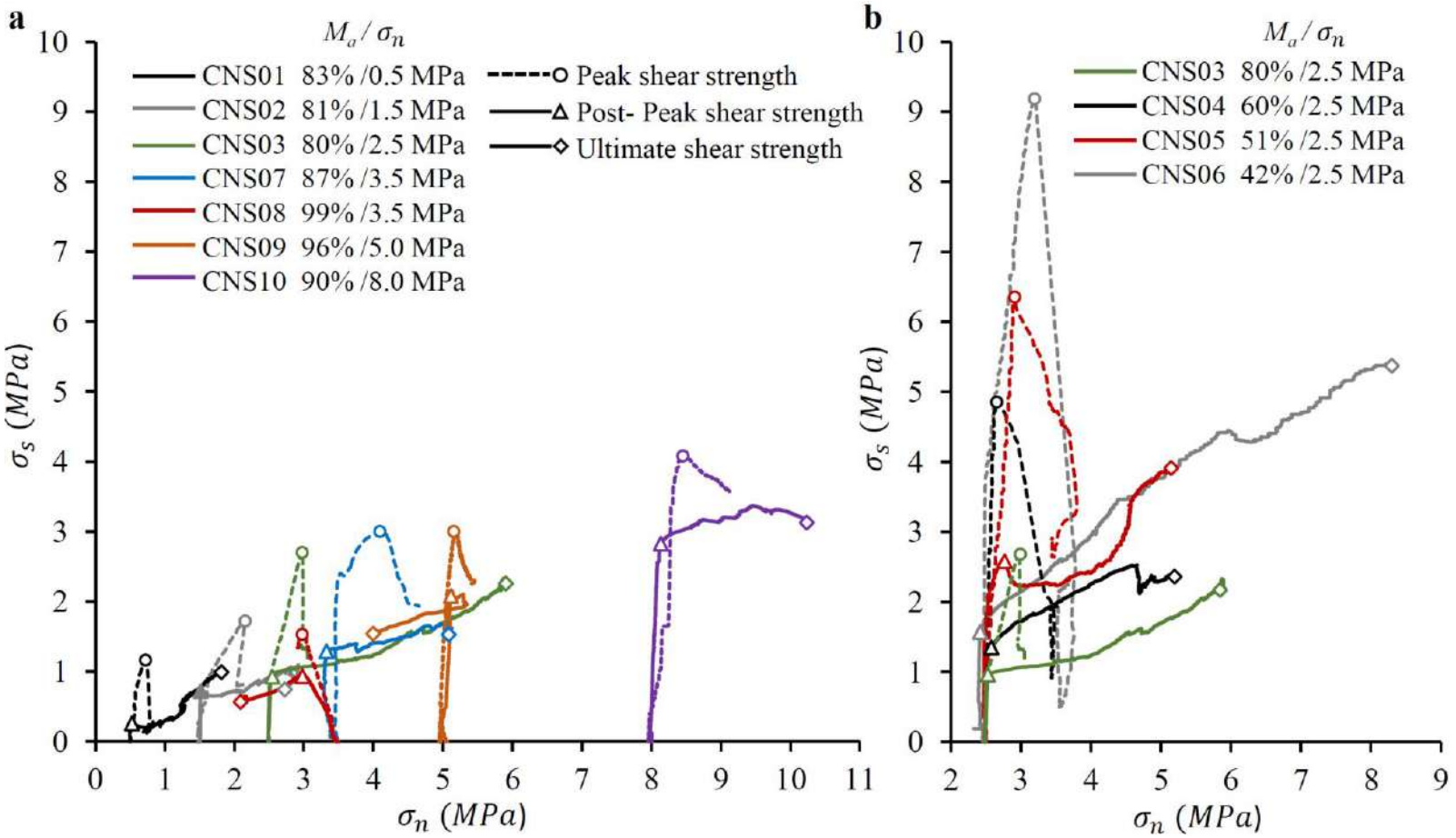

Fig. 3.13. Plots of σ_n vs σ_s from the DSTs under CNS conditions. (a) DSTs of specimens with high M_a values and increasing σ_n. (b) Specimens with decreasing M_a values and σ_n=2.5 MPa.

3.3.4 Influence of M_a on the DST results

In this section, the influences of M_a on the important mechanical parameters obtained from the peak and postpeak DSTs, including the shear strength, dilation and shear stiffness, are analyzed. The most important parameter taken from DSTs is the peak shear strength because it is used to estimate strength envelopes, which can be applied in practical cases. Moreover, the measured peak shear strength is not affected by the overlap of different materials (metal box, cement paste and anisotropic rock), as is the displacement and, consequently, the stiffness.

3.3.4.1 Influence of M_a on the shear strength

Fig. 3.14 shows the variations in the peak shear strength from the DSTs under CNL and CNS conditions with respect to the normal stress (at peak) and M_a (grayscale). These results indicate the major influence of the biotite content on the peak shear strengths of foliation planes. The black lines in Fig. 3.14 show an interpretation of the extreme peak shear strength envelopes for M_a=0% and 100%. The higher the normal stress is, the greater the influence of M_a on the shear strength, which indicates that for linear Mohr-Coulomb envelopes, both the cohesion and friction coefficient are inversely proportional to M_a.

Fig. 3.15 shows the variations in the postpeak shear strength from the DSTs under CNL and CNS conditions with respect to the normal stress (at peak) and M_a (grayscale). Fig. 3.15a shows that higher M_a values (whiter symbols) tend to concentrate at the lower bound of the shear strength range, whereas lower M_a values (darker symbols) tend to concentrate at the higher bound of the shear strength range. However, it is clear that the postpeak shear strength is less influenced by M_a than the peak shear strength (Fig. 3.14).

By making an association with the failure criteria introduced by Barton and Choubey (Barton and Choubey 1977), the M_a is probably changing the joint compressive strength (JCS) and the residual friction angle (φ_r), but it does not directly affect the joint roughness coefficient (JRC). In other words, after failure, one cannot analyze only the percentage of mica on the surface area because the created surface morphology is, at least, equally important to the shear strength determination. Moreover, JCS and φ_r also depend on the mineralogical composition of the rock and the thickness of the biotite layer.

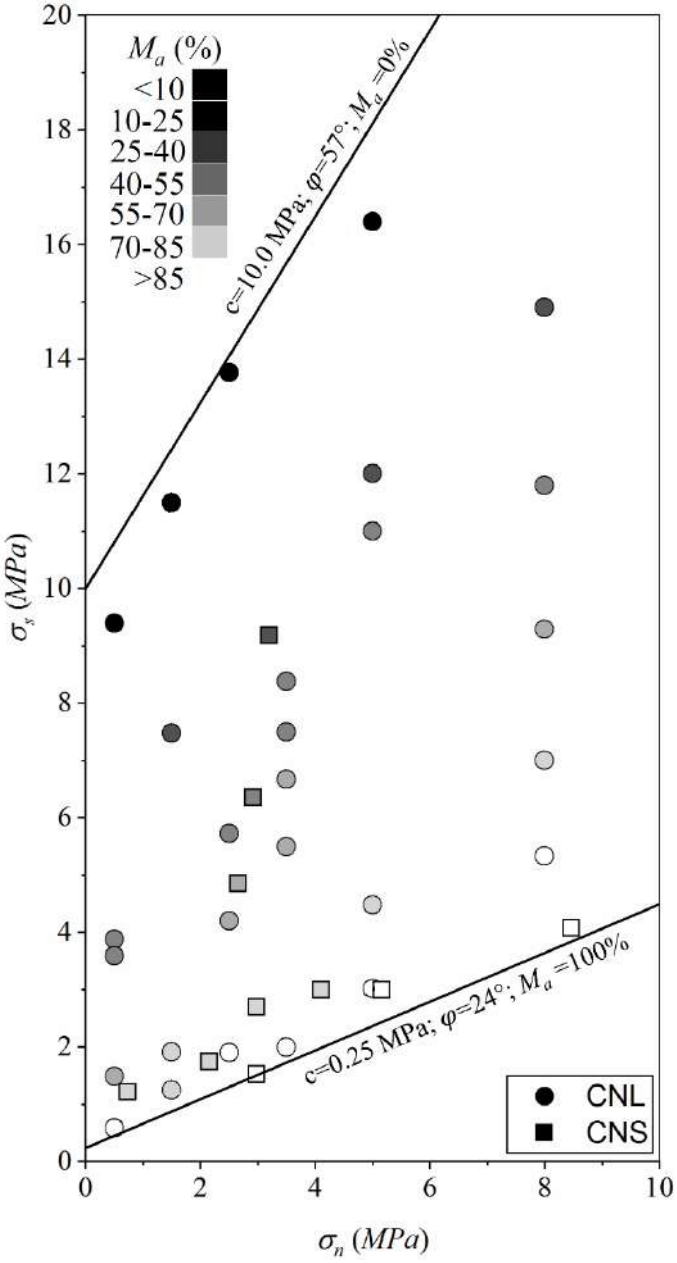

Fig. 3.14. Influence of M_a on the peak shear strength (for DSTs under CNL and CNS conditions).

Analyzing the effects of M_a on JCS and φ_r for creating different strength envelopes is not within the scope of this paper. Analyzing these effects would be difficult with natural rock foliation planes because it would require a certain number of failed foliation surfaces (after peak DST) with similar morphologies (similar JRCs) to isolate the M_a effect on their compressive strengths

and residual friction angles. However, rough estimates of the extreme JRC, JCS and φ_r values are presented in Fig. 3.15a. From all DST specimens, the JRC varied from 4 to 10 using the manual profilometer (Barton's comb) and the visual classification standard (Barton and Choubey 1977). The JCS and φ_r varied from 130 to 20 MPa and from 27° (basic friction angle) to 15°, respectively. Both JCS and φ_r were estimated using the rebound of the Schmidt hummer on two block surfaces: one surface had M_a>90% and a thick biotite layer (mafic bending surface), and the other was a saw-cut surface basically composed of quartz and feldspar (M_a<10%). It is possible to see that all DSTs are within the interval defined by these two envelopes (Fig. 3.15a).

Fig. 3.15b shows the variations in the individual friction coefficients from each postpeak DST with respect to M_a. In this case, the maximum shear stress is normalized by the applied normal stress, and any possible nonlinearity of the strength envelope or apparent cohesion is ignored. The moderate coefficient of determination in Fig. 3.15b (R^2=0.5) also indicates that M_a has a partial importance on the shear strengths of foliation planes after failure (i.e., after the peak DSTs). Fig. 3.15b shows that mica-rich foliation planes can have extremely low friction coefficients (as low as 0.3) after peak failure (by shear or tension).

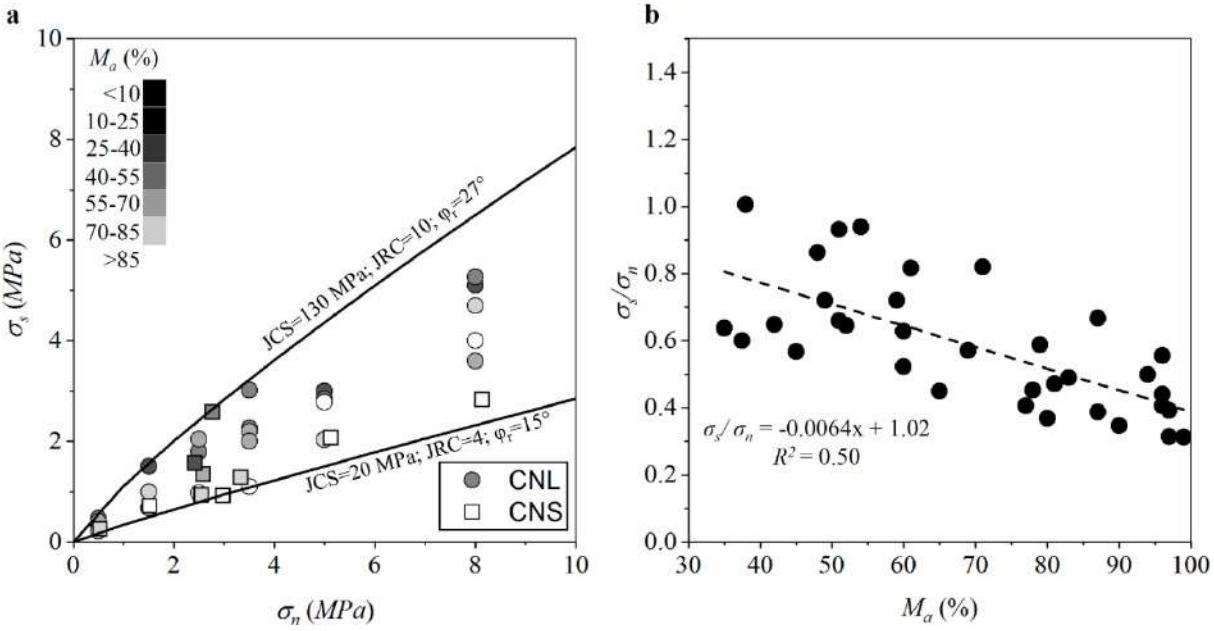

Fig. 3.15. (a) Postpeak shear strengths for different normal stresses. (b) Friction coefficients variations with respect to M_a.

3.3.4.2 Influences of M_a on the shear stiffness and dilation

Fig. 3.16a shows the peak shear stiffness decreases as the M_a increases. In this case, the initial normal stress effect could be observed from an approximated data segmentation in two sets: 0.5 to 2.5 MPa and 3.5 to 8.0 MPa). The linear regressions show relatively high coefficients of determination for each set; thus, shear zones with high biotite contents are significantly more deformable than those with low biotite contents. In contrast, the shear stiffness of the postpeak stage (Fig. 3.16b) did not vary significantly with respect to M_a. The shear stiffness range is significantly reduced from the peak stage (values from 1 to 10 MPa/mm) to the postpeak stage (values from 0.3 to 4.5 MPa/mm).

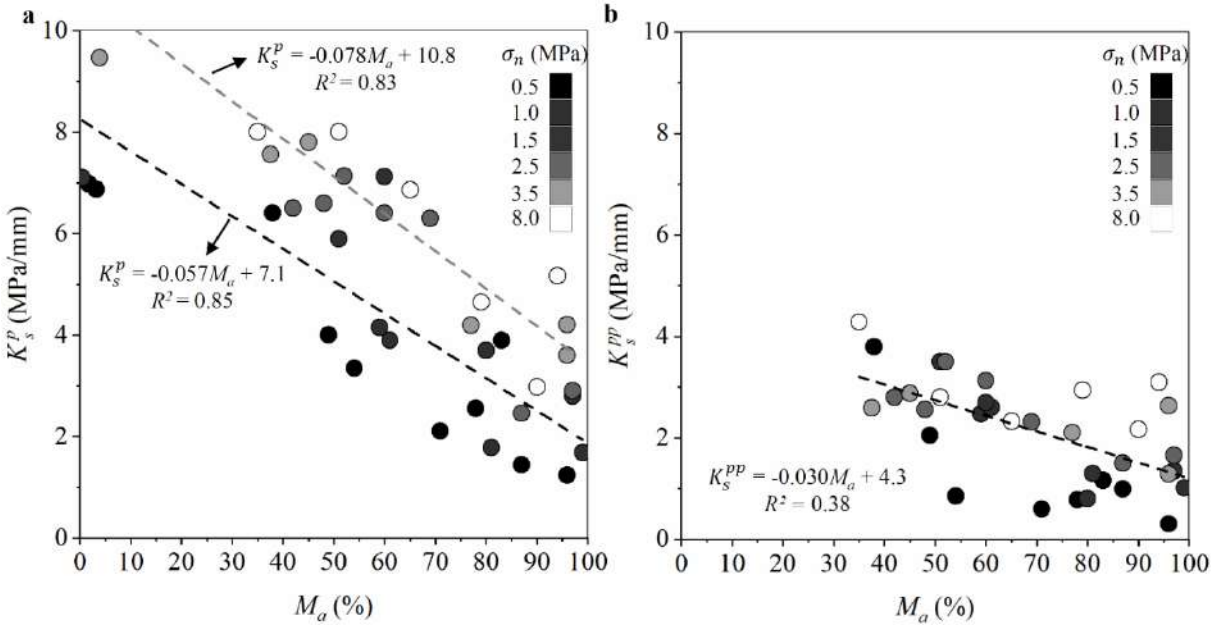

Fig. 3.16. Variations in shear stiffness with respect to M_a for (a) peak DSTs and (b) postpeak DSTs.

Fig. 3.17 shows the variations in the peak and postpeak dilation angles with respect to M_a. Fig. 3.17a shows that there is a clear decrease in the peak dilation angle with increasing M_a; however, the data are dispersed, especially for intermediate M_a values, and no normal stress effects were observed in this case. Nevertheless, there is a clear difference between dilation angles from the shear zones resulting in foliation planes almost covered by biotite (M_a >80%

and ψ_p<15°) and the shear zones resulting in foliation planes with almost no biotite (M_a <5% and ψ_p>45°). This result indicates that high biotite contents facilitate the fracturing process during peak DSTs. In the postpeak stage, no correlation was observed between the dilation angle and M_a, wherein the mean dilation angle was 9.6° and the corresponding standard deviation was 3°. Similar to the shear stiffness, the dilation angle is significantly reduced from the peak to the postpeak stage, which indicates the dilative behavior of the fracturing process. DST specimens with contractive behaviors were not included in these analyses.

The fact that both the shear stiffness and dilation were not significantly affected by M_a during the postpeak stage was expected after the results in Fig. 3.15, especially for the postpeak dilation angle, which is completely dependent on the surface morphology created after the peak stage.

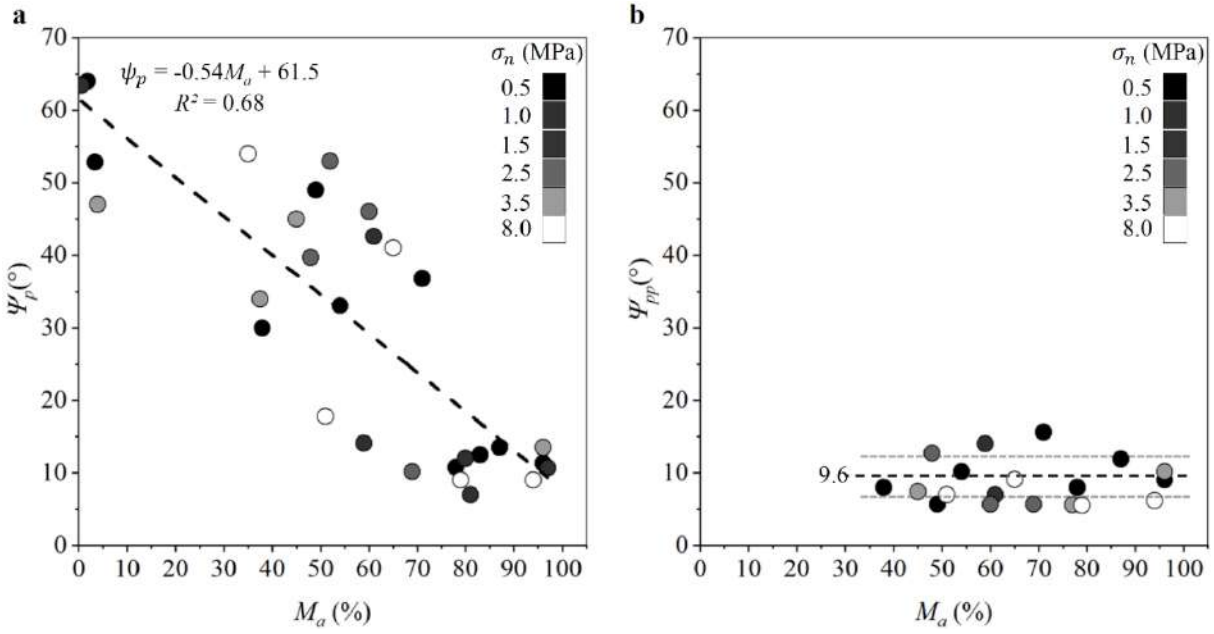

Fig. 3.17. Variations in the dilation angle with respect to M_a for (a) peak DSTs and (b) postpeak DSTs.

3.3.5 Influence of biotite thickness on the DST results

Specimens with high M_a values exhibited different DST results depending on the biotite thickness of the foliation plane on the isolated shear zone. From all the DST results with M_a >85%, CNL03, CNL04, CNS08 and CNS09 did not dilate during the peak or postpeak stages. Figs. 3.18a and 3.18b show the isolated shear zones of these specimens and the resulting failure

paths. In these specimens, the contraction in the peak stage is due to the high deformability of the thick biotite layer. The contraction in the postpeak stage increases as the shear zone crushing increases. After the postpeak stage, these shear zones were hardly crushed, as shown by the example of CNL04 in Fig. 3.18c.

Specimens with high M_a values (>85%) and thin biotite layers dilated in both peak and postpeak stages. Fig. 3.18d shows the fracture paths after the peak stages of specimens CNL02, CNL05 and CNS02, which indicated failures along the thin biotite layers inside the shear zones. In these cases, the surface damage is reduced because the thin biotite layer is rapidly crushed and the quartz/feldspar grains become in contact, which increases the compressive strength of the opposing foliation walls. Fig. 3.18e shows an example of the CNS02 surface after each DST stage.

It is interesting to note that the thickness of the biotite layer becomes very important under CNS conditions. Comparing the DSTs of specimens CNS02, CNS08 and CNS09, the dilation of CNS02 increased the normal stress at peak by approximately 30%, increased the peak shear strength, and maintained the residual stress increase during the postpeak stage (Fig. 3.13). In contrast, the contraction of specimens CNS08 and CNS09 caused normal stress relief and subsequent shear strength reduction, but this process occurred for different reasons in each specimen. CNS08 is a thick biotite layer (Fig. 3.18a), which contracted in both peak and postpeak stages due to its high deformability and weakness (same as specimens CNL03 and CNL04). CNS09 is a shear zone with a set of biotite layers interlocked with quartz and feldspar (Fig. 3.18b). In this case, the specimen exhibited a small dilation in the peak stage, which explains the small increase in the peak normal stress and shear strength (Fig. 3.13). At the beginning of the postpeak stage, the specimen dilated as an open foliation plane, thereby increasing the normal and shear stresses (Fig. 3.13). However, after 2.5 mm of shear displacement, the specimen started to fracture in multiple biotite layers, thereby crushing the shear zone structure, and leading to contraction and strength reduction. Fig. 3.18b compares specimen CNS09 before the DST and after each DST stage.

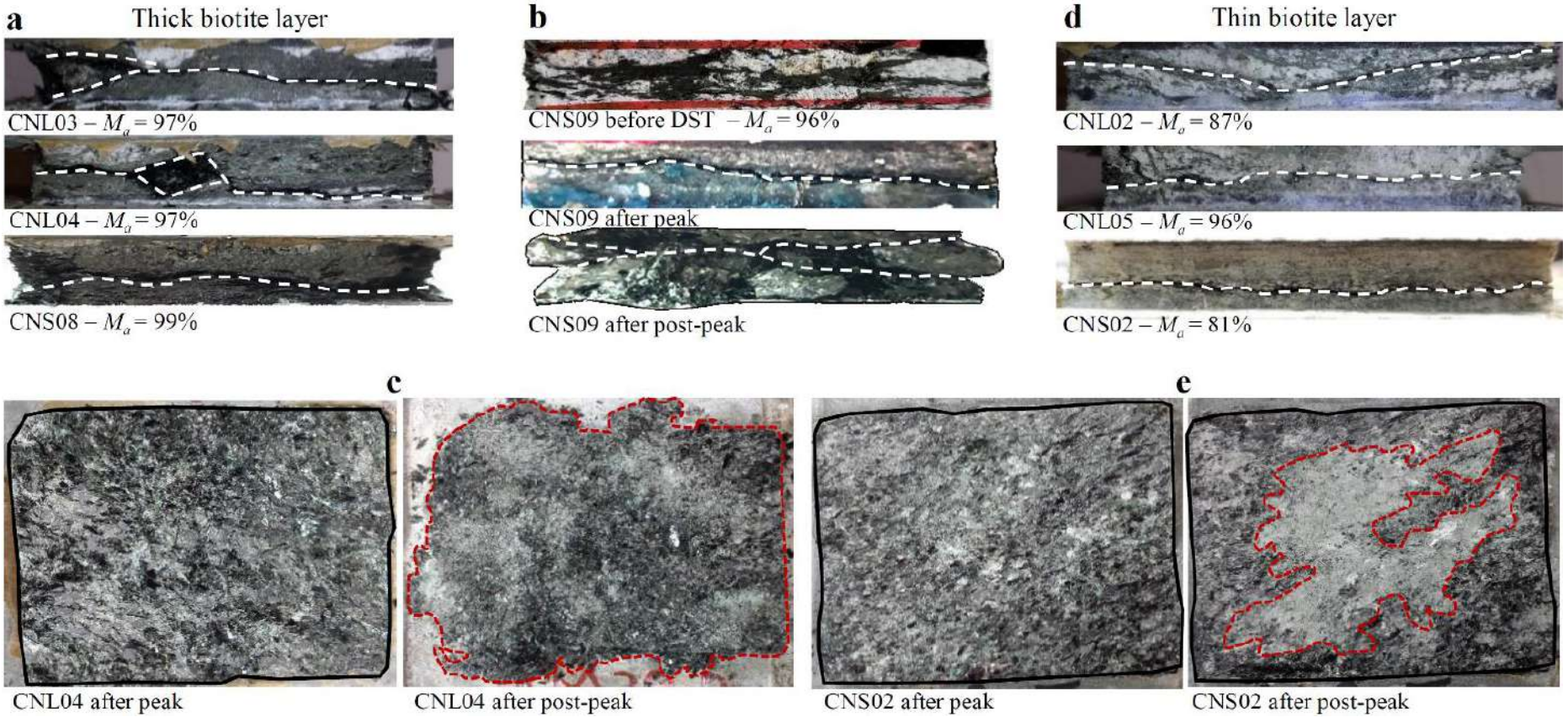

Fig. 3.18. Failure patterns associated with different biotite thicknesses. (a) Examples of thick biotite layers, (b) detail of specimen CNS09, (c) detail of specimen CNL04, (d) specimens with thin biotite layers, and (e) detail of specimen CNS02.

3.3.6 Influence of M_a on the failure patterns

DSTs of intact brittle rocks result in nonplanar failure surfaces due to the lateral unconfinement of the isolated shear zone. Petit (Petit 1988) performed DSTs on sandstones and demonstrated the formation of different failure patterns with the increase in the normal stress (under CNL conditions), including "S-shaped" failure surfaces for lower normal stress confinements, followed by en-echelon fractures as the normal stress increases. During DSTs, the stresses concentrate in the opposed top and bottom of the shear zone due to the applied and restricted displacements on the upper and lower shear boxes. Cho et al. (Cho et al. 2008) showed these mechanisms occurring in concrete specimens, and both Cho et al. (Cho et al. 2008) and Bewick et al. (Bewick et al. 2014c, a) explored these failure mechanisms using the discrete element method.

In this study, the foliation was always aligned parallel to the shear planes (Fig. 3.4) regardless of the biotite content. However, as M_a decreases, the influence of the foliation inside the shear zone on the final failure patterns decreases. From all the DST results, the failure surfaces can be classified into four types: total influence of the foliation (TI), high influence of the foliation (HI), low influence of the foliation (LI), and no influence of the foliation (NI). Examples of these failure modes are presented in Fig. 3.19, which shows the shear zone before the DST and before the peak stage and includes sketches of the fracture paths along the biotite grains (red shaded zone) and along the quartz and feldspar grains (red dashed lines).

TI failure occurs along the isolated foliation planes, such as the aforementioned examples in Fig. 3.18 and CNL01 and CNS03 in Fig. 3.19a. In this case, specimens usually show high M_a values and continuous biotite layers (Fig. 3.2). As the number of quartzo-feldspathic bridges increases and M_a decreases, HI and LI failure surfaces are generated. In specimen CNL14 (Fig. 3.19b), failure occurred almost entirely along the foliation plane, whereas in specimen CNL18 (Fig. 3.19c), the failure likely started at the opposed top and bottom of the shear zone and obliquely propagated until the foliation plane was reached. Thus, specimens such as CNL14 were classified as HI, and specimens such as CNL18 were classified as LI. Finally, specimens without significant biotite contents (extremely low M_a values) exhibited NI failure surfaces with the same patterns observed by Petit (Petit 1988), Cho et al. (Cho et al. 2008) and Bewick et al. (Bewick et al. 2014c, a) for brittle isotropic rock materials (Fig. 3.19d).

Table 3.1 shows a summary of the failure surface types, M_a ranges and foliation plane characteristics (Fig. 3.2) for each DST specimen (under CNL and CNS conditions). It is interesting to note that for specimens without clear biotite-defined foliation planes (NI), the anisotropy (orientation of the quartz-feldspar grains) does not affect the failure mode on direct shear. Moreover, a greater number of en-echelon fractures were observed as the normal stress increased, as shown by the different fracture patterns of specimens CNL28 (σ_n=5.0 MPa) and CNL25 (σ_n=0.5 MPa). As indicated in Fig. 3.19d, fractures crossed the defined boundary of the shear zone toward the cement-confined portions of the specimens. The postpeak stages of such specimens were not performed for this reason.

In the triaxial tests performed by Shea and Kronenberg (Shea and Kronenberg 1993), the transition from brittle to ductile behaviors was closely associated with the increase (in dimension and number) of quartzo-feldspathic bridges between biotite grains. In this work, the percentage of quartzo-feldspathic bridges is defined as a percentage, by 100-M_a, and failure brittleness can be associated with the difference between the peak and postpeak shear strengths (shear stress drop) after failure ($\sigma_{sp} - \sigma_{spp}$). Fig. 3.20 shows that $\sigma_{sp} - \sigma_{spp}$ decreases as M_a increases (i.e., the percentage of quartzo-feldspathic bridges decreases). Essentially, ductile failures without strain-softening behaviors were not observed in this work. However, TI specimens exhibited lower $\sigma_{sp} - \sigma_{spp}$ values, which characterizes a brittle-ductile transition. As M_a decreases and $\sigma_{sp} - \sigma_{spp}$ increases, the failure becomes brittle, resulting in HI, LI and, finally, NI surfaces. It is possible that foliation planes with high mica content (TI) isolated in DSTs would exhibit ductile failures for normal stresses significantly higher than 8.0 MPa.

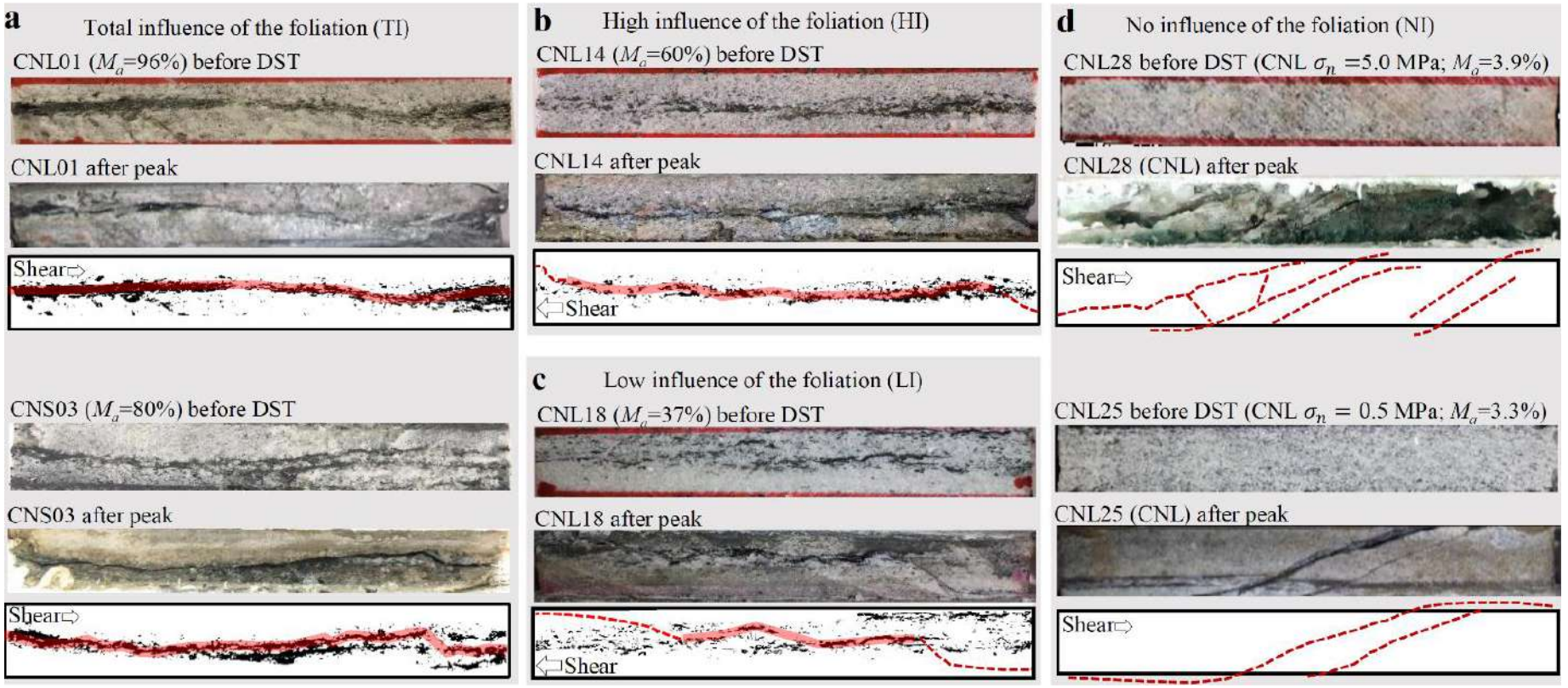

Fig. 3.19. Examples of failures observed in DSTs: (a) TI failures on specimens CNL01 and CNS03, (b) HI failure on specimen CNL14, (c) LW failure on specimen CNL18, and (d) NI failures on specimens CNL28 and CNL25.

Table 3.1. Summary of the mineralogical and mechanical characteristics of the foliation planes and their resulting failure surfaces.

Number of specimens	Biotite distribution	M_a range	Failure surface	Usual strength and deformability characteristics
3	Thick continuous biotite layer	>95%	TI	Transitional (brittle-ductile) behaviors; lowest shear and tensile strengths; contraction during shear; strength reduction under CNS conditions.
13	Thin continuous biotite layer	>75%	TI	Transitional (brittle-ductile) behaviors; Low shear and tensile strengths; dilation during shear; strength increase under CNS conditions.
14	Thin discontinuous biotite layer	45< M_a <75%	HI	Brittle failures; low-intermediate shear and tensile strengths; dilation during shear; strength increase under CNS conditions.
4	Thin discontinuous biotite layer	30< M_a <45%	LI	Brittle failures; Intermediate-high shear and tensile strengths; dilation during shear; strength increase under CNS conditions.
4	Nonvisible biotite layer	M_a <5%	NI	Brittle failures; Highest shear and tensile strengths; dilation during shear (peak stage); strength increase under CNS conditions (peak stage).

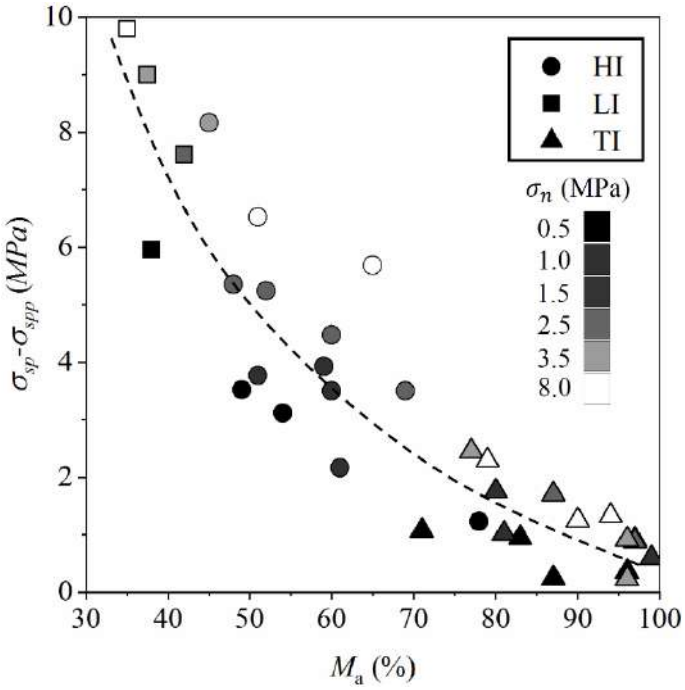

Fig. 3.20. Influence of M_a on the difference between peak and postpeak strengths.

3.4 Three-dimensional peak strength envelope for foliation planes with variable mica contents

This section presents a comprehensive analysis of the peak DST results to define a 3D strength envelope including the parameter M_a as an independent variable. The 3D peak strength envelope is based on the following two assumptions:

1 - The cohesion (c) and the friction angle (φ) vary with respect to M_a by the same mathematical function used for σ_t (Eq. 3.2 and Fig. 3.8):

$$c = \beta_c/(1 + (\alpha_c M_a)^{n_c}) \tag{3.3}$$

$$\varphi = \beta_\varphi/(1 + (\alpha_\varphi M_a)^{n_\varphi}) \tag{3.4}$$

In this case, β_c and β_φ represent the maximum c and φ, respectively, for M_a=0%.

2 - The shear strength varies linearly with the normal stress, following the Mohr-Coulomb equation:

$$\sigma_s = \sigma_n \tan\varphi + c \tag{3.5}$$

Figs. 3.21a and 3.21b show the experimental φ and c values from different mean M_a values, indicating a good fit of Eqs. 3.3 and 3.4 (which justifies assumption 1). Figs. 3.21c (same results presented in Fig. 3.8) and 3.21d show all the peak shear and tensile strength values obtained from the DSTs and POTs, respectively, in a single chart. The mean M_a values of the representative linear envelopes in Fig. 3.21d were used to determine φ and c and generate the correlations in Figs. 3.21a and 3.21b. The envelopes in Fig. 3.21d indicate that the variation in the peak shear strength is approximately linearly with the normal stress for different M_a values, which justifies assumption 2.

The reductions in the tensile strength, cohesion and friction angle with increases in M_a can be compared using the mica degradation factor (FM_a):

$$FM_a^c = \frac{c_{max} - c}{c_{max} - c_{min}} \tag{3.6}$$

$$FM_a^{\varphi} = \frac{\varphi_{max} - \varphi}{\varphi_{max} - \varphi_{min}} \tag{3.7}$$

$$FM_a^{\sigma_t} = \frac{\sigma_{t_{max}} - \sigma_t}{\sigma_{t_{max}} - \sigma_{t_{min}}} \tag{3.8}$$

Fig. 3.22 shows the variations in the mica degradation factors from Eqs. 3.6, 3.7 and 3.8 with respect to M_a, indicating good agreement between the FM_a values calculated by the mathematical fittings of Eqs. 3.2, 3.3 and 3.4 (lines) and the experimental data (symbols). As FM_a is a normalized parameter, it shows that the tensile strength is more sensitive to the mica content than the cohesion or friction angle.

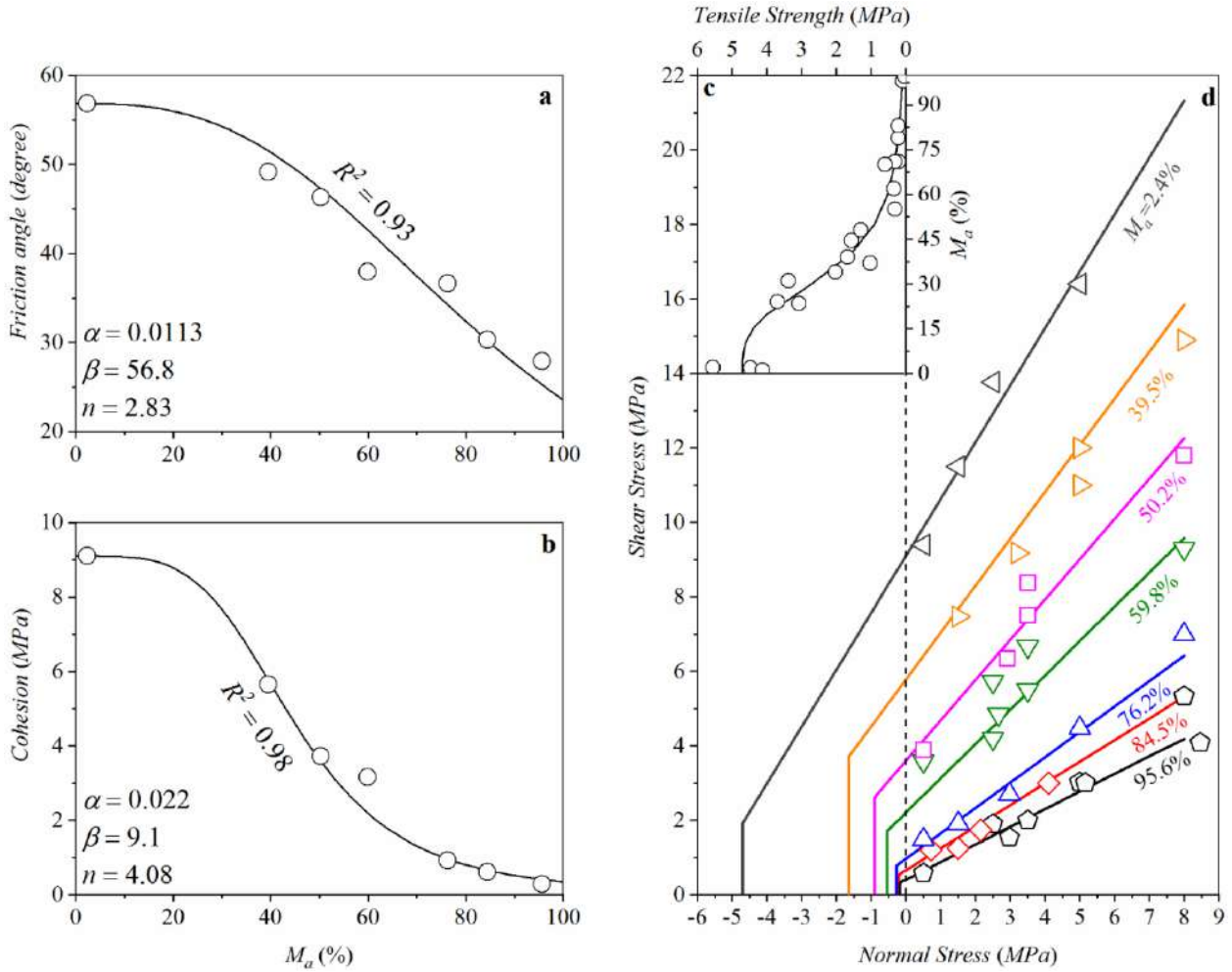

Fig. 3.21. Variations in (a) friction angle, (b) cohesion, and (c) POT tensile strength with respect to M_a. (d) Representative shear strength envelopes with respective tensile strength cut-offs.

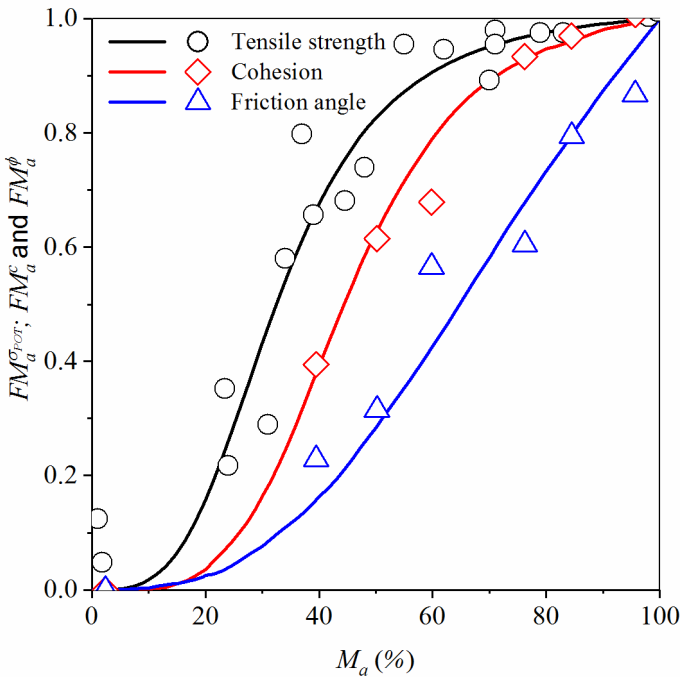

Fig. 3.22. Variations in the mica degradation factors (FM_a) with respect to M_a. The lines and symbols represent the mathematical model and the experimental data, respectively.

By substituting Eqs. 3.3 and 3.4 in Eq. 3.5, it is possible to generate the 3D shear strength envelope of biotite gneiss foliation planes, wherein M_a is included as an independent variable. The constant parameters of this envelope are $\alpha_{c,\varphi}$, $\beta_{c,\varphi}$ and $n_{c,\varphi}$, which are obtained individually for each case (Figs. 3.21a and 3.21b). Fig. 3.23a shows the 3D shear strength envelope with the experimental data, and Fig. 3.23b shows a comparison between the experimental and predicted shear strengths using this 3D envelope. The good agreement between the predicted and experimental shear strengths and the high coefficients of determination in Fig. 3.23b indicate that this 3D envelope is suitable for representing the shear strengths of foliation planes with different mica contents.

For higher normal stresses, it is possible that the shear stress varies nonlinearly with the normal stress, and a more complex model should be considered. However, this was not the case for normal stresses less than 8 MPa. The tensile strength curve obtained in Fig. 3.8 is used to assign the tension cut-offs, characterizing a full strength envelope (shear and tension) for foliation planes with variable M_a.

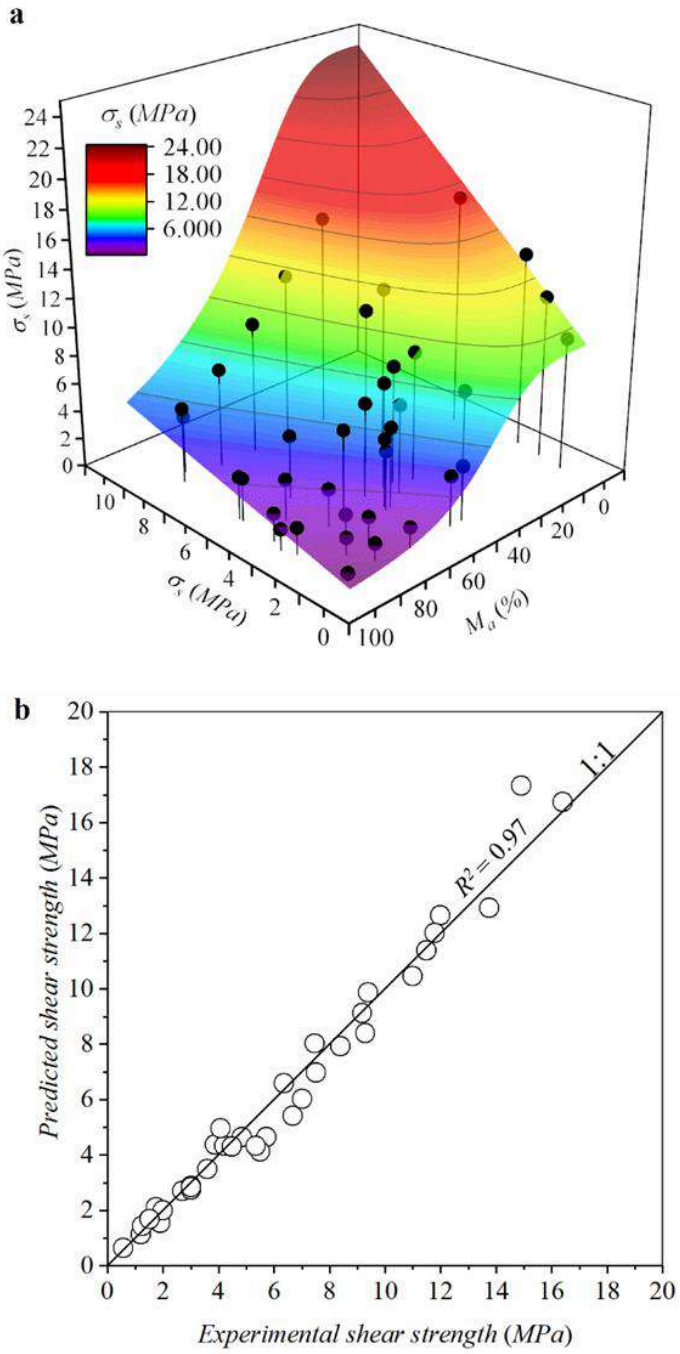

Fig. 3.23. (a) 3D shear strength envelope obtained by regression of Eqs. 3.3 and 3.4. (b) Comparison between experimental and predicted peak shear strengths.

The M_a parameters are obtained from a single surface of a failed foliation plane. In the field, M_a can be assessed on exposed foliation planes from rock blocks or outcrops. Fig. 3.24 shows an example of M_a calculated from the foliation surface of a biotite gneiss rock block. This value of M_a (64%) could be substituted in Eqs. 3.2, 3.3 and 3.4 to estimate the equivalent strength

envelope of such a foliation plane. It is important to mention that the previous analysis is based on laboratory-scale specimens and does not account for possible scale effects associated with larger foliation planes, such as waviness. This subject is under investigation by the GeoinfraUSP research group for future publications.

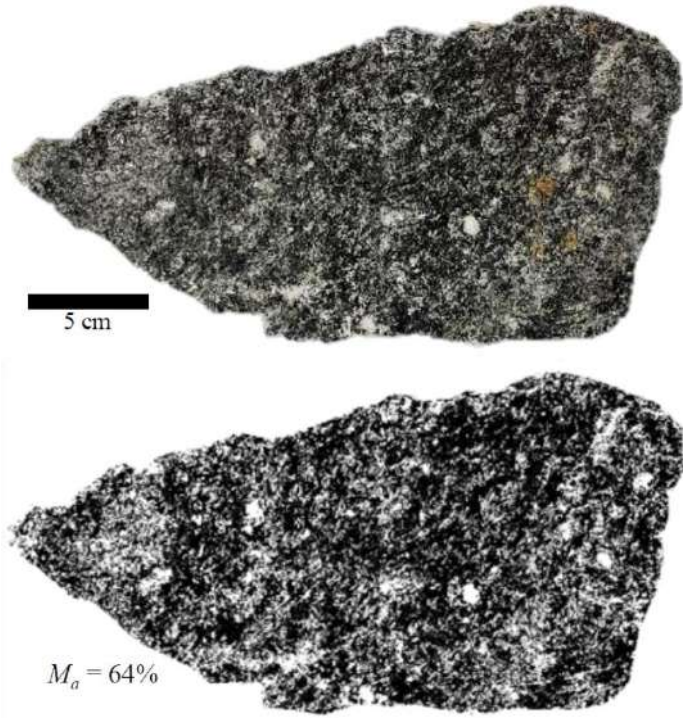

Fig. 3.24. (a) Example of M_a quantification on the exposed foliation surface of a rock block.

3.5 Conclusions

The following summary and conclusions can be provided for the study conducted:

1. This paper showed an extensive laboratory testing program that included DSTs and POTs of isolated foliation planes with variable mica content. The image analysis method used for quantifying M_a was simple and efficient because biotite was the only dark mineral with a substantial content in the biotite gneiss. The two-step DST was used to avoid major damage to the foliation surfaces before quantifying M_a.

3. The POTs showed that the tensile strength varies nonlinearly with respect to M_a, and the power function with 3 constant parameters (α_t, β_t and n_t) showed a good fit to the data. For the biotite gneiss, the tensile strength varied from 0.055 MPa (M_a of 98%) to 5.55 MPa (M_a of 1.9%).

4. DSTs were performed under CNL and CNS conditions. The peak shear strength was strongly influenced by M_a. In the postpeak stage, M_a had a partial effect on the shear strength because of the variable failure surface morphologies created after the peak stage. The same effects were observed on the postpeak shear stiffness and dilation angle. Thus, the M_a parameter alone is effective in predicting the peak shear strengths of foliation planes but not in predicting their postpeak behaviors. Future research is necessary to associate M_a with the morphological parameters of foliation surfaces.

5. Most foliation planes dilated during the peak stage due to the mineral fracturing process and during postpeak stages due to the surface morphology. Under CNS conditions, this dilation caused an increase in normal stress; hence, the shear strength increased in both DST stages. On the other hand, shear failures of the foliation planes with high M_a values and thick biotite layers occurred as a result of normal stress relief caused by excessive damage (contraction), which reduced the shear strength. It is important to mention that the shear zones in DSTs are laterally unconfined, which may not be the case in most real CNS conditions.

6. Finally, a nonlinear 3D peak strength envelope that included M_a as an independent variable was obtained using Eqs. 3.3 and 3.4 to express the cohesion and friction angle against M_a, wherein these functions were included on the Mohr-Coulomb failure criteria. Moreover, the tensile strength obtained by the same function (different constant parameters) was used as the tension cut-off for the strength envelope. The good fit obtained indicates that this 3D envelope is suitable for low confinement conditions (normal stress less than 10 MPa).

Chapter 4

Modeling a Shallow Rock Tunnel Using Terrestrial Laser Scanning and Discrete Fracture Networks

This chapter presents an original article published on ***Rock Mechanics and Rock Engineering*** **(DOI: 10.1007/s00603-017-1166-6).**
Authors: Pedro P. Cacciari & Marcos Massao Futai

Abstract

Discontinuity mapping and analysis are extremely important for modeling shallow tunnels constructed in fractured rock masses. However, the limited exposure and variability of rock face orientation in tunnels must be taken into account. In this paper, an automatic method is proposed to generate discrete fracture networks (DFNs) using terrestrial laser scanner (TLS) geological mapping and to continuously calculate the volumetric intensities (P_{32}) along a tunnel. The number of fractures intersecting rectangular sampling planes with different orientations, fitted in tunnel sections of finite lengths, is used as the program termination criteria (PTC) to create multiple DFNs and to calculate the mean P_{32}. All traces and orientations from three discontinuity sets of the Monte Seco tunnel (Vitória Minas Railway) were mapped and the present method applied to obtain the continuous variation in P_{32} along the tunnel. A practical approach to creating single and continuous DFNs (for each discontinuity set), considering the P_{32} variations, is also presented, and the results are validated by comparing the trace intensities (P_{21}) from the TLS mapping and DFNs generated. Three examples of 3DEC block models generated from different sections of the tunnel are shown, including the ground surface and the bedrock topographies. The results indicate that the proposed method is a practical and powerful tool for modeling fractured rock masses of uncovered tunnels. It is also promising for application during tunnel construction when TLS mapping is a daily task (for as-built tunnel controls) and the complete geological mapping (traces and orientations) is available.

Keywords: Discontinuity; Terrestrial Laser Scanner; Discrete Fracture Network; Tunnel

4.1 Introduction

Hard rock masses at shallow depths are generally considered sets of discrete blocks formed by intersecting discontinuities such as bedding planes, fractures, shear zones and faults. Under this condition, failure in tunnels is generally controlled by gravity-driven sliding on the discontinuities and rotation of the individual rock blocks, while stress-induced failure of intact rock material is unusual. Moreover, the stress state in shallow tunnels can be strongly influenced by the ground surface and bedrock topographies. Thus, to evaluate the stability of blocks around the excavation area, it is important to generate models that include these structures, which requires geological investigation (drilling boreholes and geophysics) at the tunnel site.

Considering the importance of reliable discontinuity mapping and analysis for near surface tunnel modeling, the geological and geotechnical surveys of rock discontinuities should be performed in detail, evaluating the geometrical (orientation, position, shape, size and intensity) and strength parameters of each discontinuity set along the tunnel. After discontinuity mapping and statistical analysis, models with fracture distributions are generated to represent the rock mass. Currently, the most commonly used approach to generate these models is the Discrete Fracture Network (DFN), available in commercial programs such as 3DEC (Itasca 2014). In DFN, some of the discontinuity geometrical parameters are described by probability density functions (PDF) obtained by discontinuity analysis of the geological mapping data. Using 3D images obtained by terrestrial remote sensing (TRS) techniques, it is much easier to obtain the large amount of data required to define these functions, and the assessment can be equally made in all regions of the rock outcrop (e.g., tunnel wall or roof).

Several authors (Crosta 1997; Kemeny et al. 2006; Strouth and Eberhardt 2006; Slob et al. 2007; Ferrero et al. 2008; Sturzenegger and Stead 2009; Lato et al. 2010; Mah et al. 2011) have used TRS to perform discontinuity mapping in point clouds or digital models of rock outcrops, overcoming the difficulties and limitations associated with hand-made geological mapping. Using TRS technology can increase the detail of discontinuity mapping (large volume and areal extent of orientation and trace length measurements), thereby facilitating the use of sophisticated discontinuity analyses. Sturzenegger et al. (2011) explored the potential of close-range TRS for estimating unbiased mean trace length (μ) and trace intensity by applying multiple discontinuity analyses (Zhang and Einstein 1998, 2000; Mauldon 1998) to rock slopes. The authors also used DFN models that emphasized the quantitative characterization of block sizes and shapes. Ferrero and Umili (2011) used a digital photograph of a rock slope to perform

trace mapping and applied circular sampling windows with different diameters and positions to compare the discontinuity sizes and intensities obtained using different methods (including the method proposed in Zhang and Einstein (2000)).

Discontinuity mapping and analyses obtained using TRS have frequently been used to create 3D block models of rock slopes (Firpo et al. 2011; Curtaz et al. 2014; Francioni et al. 2014; Havaej et al. 2016; Spreafico et al. 2016). Using DFNs (defined PDF of discontinuity orientation and size, and volumetric intensities), Havaej et al. (Havaej et al. 2016) also compared block models that were created stochastically with block models that were created deterministically, using mean discontinuity spacing and persistence (in %). The authors determined that the DFN approach better captures the variability among block failures observed in the field.

The number of published works that integrate TRS, DFN and 3D block model generation is more restricted with regard to applications to tunnels. Fekete and Diederichs (Fekete and Diederichs 2013) integrated terrestrial laser scanning (TLS) and discontinuum modeling to assess the stability of a tunnel using two different approaches: inserting discontinuities corresponding to the same TLS-measured positions and orientations and utilizing mean discontinuity spacing and persistence. Cacciari and Futai (Cacciari and Futai 2016b) compared the results obtained when different window-sampling methods were applied to TLS discontinuity mapping of a tunnel, considering variations in the rock face orientation. These authors also presented a block model example that was created using measured spacing, estimating the persistence by the relationship between the mean trace length and the excavation size (Kim et al. 2007). However, neither of these studies used DFNs that were stochastically defined via discontinuity mapping and analyses.

In engineering practice, TRS, sophisticated discontinuity analyses and DFN are rarely used to create 3D models for stability analyses of tunnels, mainly because TRS is rarely used for geological mapping during construction. Moreover, geological mapping is only the first step; several discontinuity analyses must be performed before creating relabeled DFNs and block models. The need for practical and fast discontinuity analysis methodology increases when large amounts of data are available; thus, automatic discontinuity analysis has been implemented in recent years. Zeeb et al. (2013) used an automatic method for the discontinuity analysis of 2D lineament maps obtained via satellite and aerial photographs. Umili et al. (2013) used an automatic method for discontinuity trace mapping and the analysis of natural rock

outcrops, assuming that discontinuity traces can be geometrically identified as edges of the surface. The authors also emphasized the validity of the automatic trace mapping method for natural outcrops; however, in artificial outcrops (such as tunnels or mining slopes), the presence of artificial edges significantly decreases the validity of the method. Nevertheless, we were unable to find any publications in which automatic discontinuity analyses associated with stochastic DFN modeling, particularly for tunnels, has been applied to TRS discontinuity data in which different rock face orientations are considered.

Along Brazilian railways, there are several old, shallow tunnels with exposed rock faces with lengths varying from hundreds of meters to a few kilometers that feature a similar geometry. In the past few years, sporadic failures of small blocks have occurred in some of these tunnels, indicating the need to reassess the stability conditions. Moreover, these railways have intense train traffic responsible for transporting a large portion of exported raw materials, such as iron ore and grains. Thus, halting the use of these tunnels for support application entails large financial and logistical losses, as, in most cases, there are no alternative routes for trains. Therefore, a partnership was established between the research group GeoinfraUSP (University of São Paulo) and the mining company Vale SA to develop a reliable methodology to assess the stability state of these tunnels, including the use of TLS and DFN for creating 3D block models.

The DFN models are created by stochastic processes in which discontinuities are generated inside a volumetric domain until an intensity-based program termination criteria (PTC) is reached. The PDF defined for each discontinuity size and orientation are obtained via statistical analyses of the field mapping data, in which discontinuities are generally assumed to be disks with center positions following the homogeneous Poisson distribution inside the DFN domain. Thus, when the PDF of a discontinuity diameter and orientation is well defined, samples of these parameters inside the DFN model are expected to be statistically similar to those measured in the field, regardless of their positional distribution in space. Similarly, DFN-model-generated trace maps of tunnels can generate areal intensity parameters that are similar to those measured via TRS mapping, but the distribution of traces along the tunnel axis may be significantly different, depending on the sampling area size and the heterogeneity of the discontinuity distribution in the rock mass.

Han et al (2016) used a 1.8 m x 80 m rectangular sampling window obtained from a tunnel to perform discontinuity mapping and generate 3D DFN models of a dam site. In this work, an

optimum DFN model was established by comparing the discontinuity orientation and trace results between field mapping and DFN simulations generated using a single volumetric intensity (P_{32}) value for each discontinuity set. Despite the low similarity between trace maps obtained via optimum DFN and field mapping, the authors found that this method satisfactorily represented the 3D dam site. However, once the tunnel is not only the sampling surface, but also the object modeled, this process can be inefficient and time consuming, depending on the size of the sampling surface and the heterogeneity of the distribution of traces along the tunnel. In cases such as the tunnels from the Vitória Minas Railway (VMR), containing hundreds of meters of uncovered rock face, it is worth using an automatic process to create DFN models that consider the discontinuity intensity variability continuously along the tunnel (using consecutive P_{32} values for each discontinuity set), thereby increasing the similarity between DFNs and field (or TRS) mapping.

Considering the lack of practical and reliable approaches integrating TRS and stochastically generated DFNs for tunnel modelling in fractured rock masses, the present work presents an automatic methodology for modeling rock tunnels using TLS discontinuity mapping and DFN-3DEC models that consists of three main steps:

I. Implementations of automatic discontinuity analyses suitable for tunnels using window-sampling methods (Zhang and Einstein 2000; Wu et al. 2011) and considering the influence of different rock face orientations.
II. Implementation of automatic P_{32} calculation along tunnels, using discontinuity analyses results (statistical descriptions of discontinuity geometrical parameters).
III. Implementation of an automatic computational approach to create single and continuous DFNs along tunnels using the consecutive results of steps **I** and **II**.

A TLS point cloud was used to perform discontinuity mapping of 324 m of the Monte Seco tunnel (which contains a fully exposed rock face) along the VMR in Brazil (Fig. 4.1). Measurements of orientations and trace lengths were performed manually on TLS 3D images. Important considerations about the TLS mapping of tunnels are presented before the automatic methodology is introduced. Steps **I**, **II** and **III** were applied to the Monte Seco tunnel, and P_{32} values were calculated along the tunnel to generate continuous DFNs. Comparisons between TLS and DFN trace intensities (P_{21}) were used to evaluate discontinuity distributions along the tunnel and to validate the proposed methodology.

Several geotechnical investigations were performed at the tunnel site, including three drilling boreholes and eight electrical imaging profiles used to interpret the bedrock position (Cacciari 2014). Fig. 4.1 shows the location of the tunnel, the topographic map of the scanned portion and the locations of the geoelectrical imaging profiles. The surface of the scanned portion of the Monte Seco tunnel is a valley with steep slopes, located between the BR-101 federal road (intense traffic) on the east side and a local road on the west side. Both the ground surface and the bedrock were included in the DFN-3DEC models to associate the important geometrical parameters for generating block models of shallow tunnels. Different examples are shown to indicate the variability of the models obtained when all these parameters are evaluated.

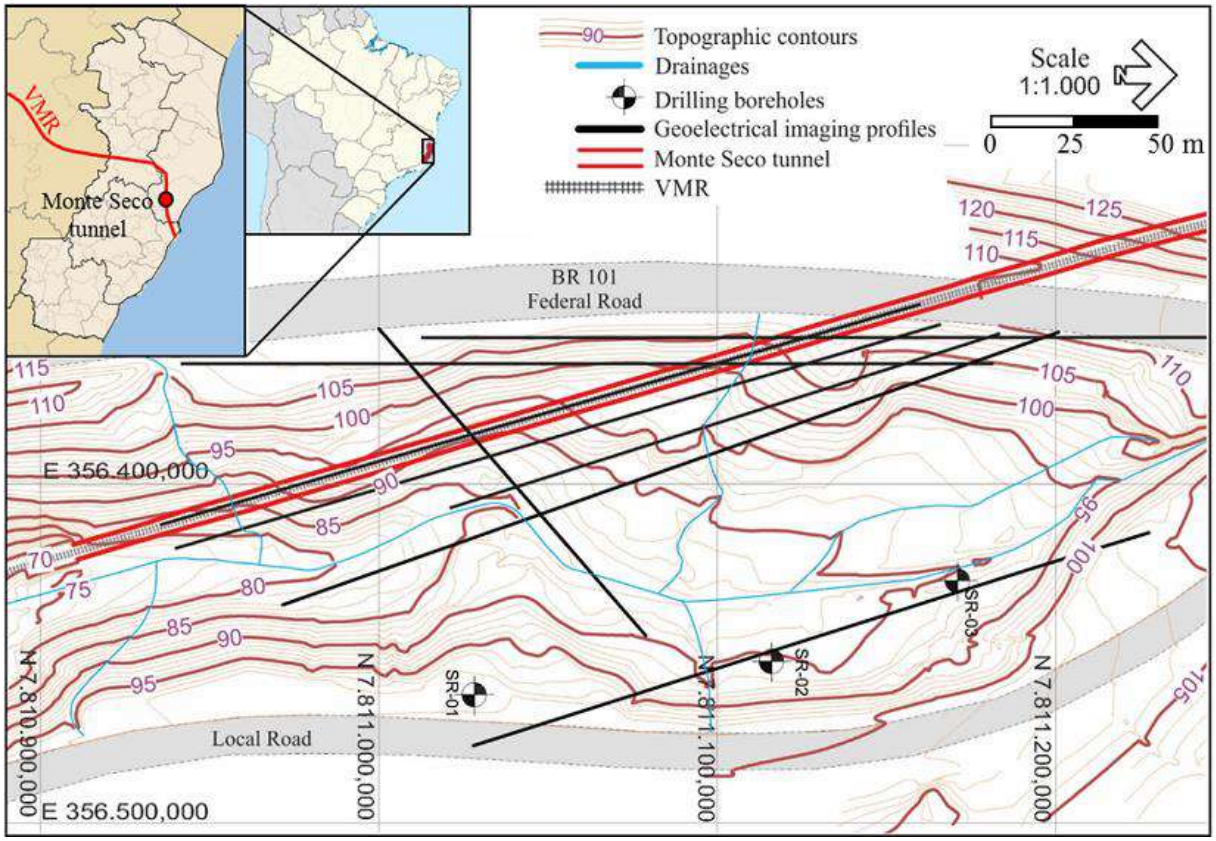

Fig. 4.1. Location of the first 340 m of the Monte Seco tunnel and geotechnical investigations performed at the tunnel site.

4.2 Discontinuity mapping using TLS in tunnels

The Faro Focus 3D laser scanner (Faro Technologies 2016) was used to scan 324 m of the Monte Seco tunnel beyond VMR. This scanner takes measurements at a speed of 976,000

points/second and was always positioned between rails, in the center of the tunnel and at orthogonal distances of approximately, 2.7 m from each wall. The spacing between scan stations was 10 m, with a 360° rotation time of 7.3 minutes. Occlusions caused by scanning irregular rock faces (Lato et al. 2010) were avoided by aligning consecutive scan stations (Cacciari and Futai 2016b).

The point registration accuracy of TLS decreases as the distance from the scanner increases; thus, for each scan station, points farther than 10 m from the scan position (along the tunnel axis) were deleted before aligning consecutive scans. A simple laboratory test was performed to evaluate the instrument noise in measurements of target surfaces positioned at different distances between the scan stations, using the same scanner and scan configurations (including a measurement speed of 976,000 points/second and a rotation time of 7.3 minutes) in the tunnel. Three perfectly flat vinyl surfaces (15 x 15 cm) were positioned between two scan stations at a constant orthogonal distance of 2.7 m from the scan alignment axis (equivalent to the orthogonal distance from the walls to the tunnel axis) and with a constant height of 1.5 m from the room floor. Because the problem is symmetric, only the first half of the space between scan stations was considered; thus, the distances (along the scan alignment axis) from the first scan station to the target surfaces were 0.0 m (surface 1), 2.5 m (surface 2) and 5.0 m (surface 3). After data acquisition and scan alignment, the maximum amplitude deviations of the final point cloud from a perfectly flat plane were 4.1 mm for surface 1, 1.3 mm for surface 2 and 0.9 mm for surface 3. The higher amplitude deviation (higher point cloud noise) of surface 1 was due to its 10-m distance from the second scan station. Mah et al. (2016) conducted a similar experiment in a tunnel (in situ) using rock-bolt face plates as the flat surface reference and obtained results similar to those presented herein.

Considering the aforementioned scanning configurations used in the Monte Seco tunnel, the density of the final point cloud varied with the distance between each two consecutive scan stations. The lower densities were approximately 6 points/cm^2, located at distances approximately 5 m from each scanner position, whereas highest densities were approximately 30 points/cm^2, located in front of each scanner position. The mean density of the tunnel section between each pair of consecutive scan stations was approximately 16 points/cm^2. Lato et al. (2009) used point clouds from aligned scan stations with a mean density of 4 points/cm^2 to perform discontinuity mapping, indicating that the densities obtained herein are suitable for the same application.

The discontinuity mapping using TLS consists in finding the geological structures in the point cloud (or digital model) and taking measurements. Orientations were obtained by fitting planes in coplanar regions of identified discontinuities and converting the normal vector of each plane to dip and dip direction. The positions (x,y,z) of discontinuity measurements were also taken. The trace lengths were measured by fitting polylines in each discontinuity trace identified. Trace mapping was carefully performed, and only the visible portions of traces were considered; thus, discontinuities visually different in TLS point clouds were not connected by the same trace, preserving the rock bridges between them and the true variability of the measured trace lengths along the tunnel. Polyworks software (InnovMetric Software 2014) was used for all discontinuity measurements described.

Discontinuity mapping was performed by geologists who had experience in TLS point cloud inspection and previous knowledge of the structural geology of the tunnel's site (e.g., lithology, types of discontinuities, mean orientations). Moreover, hand-made geological mapping was performed (Cacciari 2014; Cacciari and Futai 2016b) during field surveys for comparison with TLS mapping. The surfaces that are generated by blasting and cutting are often irregular and display random orientations; thus, discontinuity planes could be distinguished from these surfaces by identifying the systematic repetitions of their sub parallel traces in the TLS point cloud and comparing their structural attitudes with previous measurements in the field. The sub parallel discontinuities of a given set were better visualized by rotating the point cloud until the exposed planes (with the corresponding measured orientations) were perpendicular to the computer screen.

Discontinuities can only be mapped (orientation and trace length measurements) in the point cloud if their planes are sufficiently exposed. As discussed by Cacciari and Futai (Cacciari and Futai 2016b), a great part of discontinuity traces apparent in tunnels can be visualized and measured, but their exposed areas are too limited for an orientation measurement. Thus, it is not possible to associate one orientation measurement to each trace identified. Furthermore, the level of exposure of discontinuities depends on several aspects (Lato et al. 2010; Cacciari and Futai 2016b), including:

- The damage to the rock face caused by the type of excavation (blasting, cutting, etc.);
- The number and volume of failed blocks, which varies with the strength and geometry characteristics of each discontinuity set;

- The orientation bias (Terzaghi 1965), which describes the occurrence probability of a discontinuity set on a given rock face orientation.

Therefore, care must be taken to find representative sampling areas for discontinuity analyses of tunnels, where all three aspects strongly influence the discontinuity mapping results. Considering these aspects, orientation measurements were obtained only in well-exposed portions of the discontinuities that were apparent in the tunnel rock face. A minimum amount of exposed area was not established because of the excessive amount of time required for a preliminary check before taking measurements. However, most of the orientations were measured in exposed areas with more than 10-cm lengths in any direction. The ratio between the number of orientation and the trace-length measurements was approximately 0.4, indicating that poorly exposed planes were consistently avoided. Discontinuities for which there were no orientation measurements were assigned to a set by comparing their trace orientations with the nearest sub parallel discontinuities with both trace and orientation measurements.

In the present work, the tunnel was sub divided into three regions: the east wall (EW), the west wall (WW) and the roof (R). Each of these regions was separated from the others using independent point clouds (loaded in the same Polyworks project file), so the regions could be hidden or shown during discontinuity mapping and the limits between them (Fig. 4.2a) could always be identified. Trace lengths and orientations were measured in each of these regions so that their locations could be identified in the data exported from Polyworks.

Generally, discontinuities are considered to be disk-shaped planes in DFNs; thus, traces must be interpreted as chords of these disks during discontinuity mapping in TLS point clouds. Nevertheless, different rock face orientations in tunnels lead to different possible interpretations of the lengths of these chords. For example, Fig. 4.2a depicts the complete contour of the intersections between three mapped discontinuities and the tunnel rock face (3D discontinuity trace), and Fig. 4.2b shows a schematic of a cross-section of the tunnel through discontinuity number 3 in Fig. 4.2a. In Fig. 4.2b, the numbers 1, 2 and 3 are the mapped vertices of the 3D trace (vertices of the inserted polyline), positioned on the end-points and middle-points (limits between R, EW and WW regions). The distances between 1-2 and 2-3 are the censored chord lengths **a** and **b**, respectively. The distance between 1-3 is the chord length **c,** which is not censored in the rock face of the tunnel.

As presented in detail below, rectangular sampling windows were fitted in R, EW and WW regions to estimate the unbiased mean trace lengths (equivalent to unbiased mean chord lengths)

along the tunnel. For each one of these regions, the end-points and middle-points (Fig. 4.2b) mapped in TLS point clouds were used to classify each discontinuity trace as a trace with both ends contained (T_{cc}), a trace with one end contained in the other end censored (T_{tc}) or a trace with both ends censored (T_{tt}). For example, discontinuity number 1 in Fig. 4.2a is T_{cc} in R; number 2 is T_{tt} in R and T_{tc} in both EW and WW; number 3 is T_{tc} in both R and EW; and number 4 is T_{tc} in EW (censored by the ballast bed).

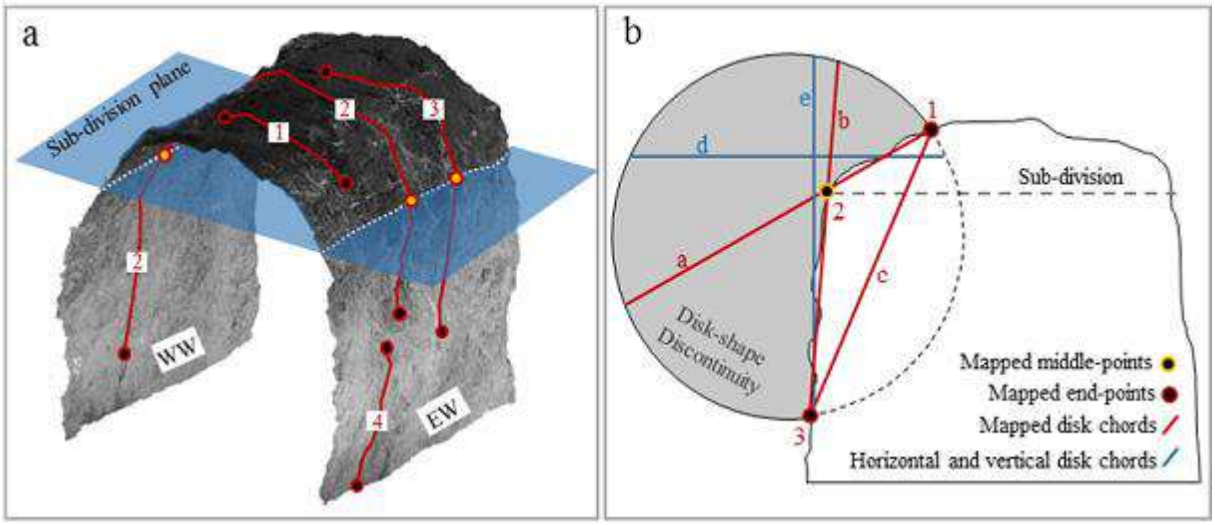

Fig. 4.2. Indication of the method used to measure traces in the point cloud. **a** Example of the point cloud sub division in R, EW and WW regions with four discontinuity traces indicated. **b** Example of the end-point and middle-point mapping of discontinuity number 3 in **a.**

Another important consideration in discontinuity mapping using TLS 3D surfaces is the biased trace rakes of traces projected on 2D surfaces (trace maps). Once the trace lengths are measured by straight lines connecting the end-points and middle-points of the 3D irregular traces (intersections between discontinuities and the tunnel rock face in Fig. 4.2a), the rake variability among the projections of these lines on 2D sampling surfaces does not reflect the true orientation variability of the discontinuity plane along the 3D rock face. In Fig. 4.3, for example, the 2D trace map of well-exposed discontinuities on the EW tunnel rock face (Fig. 4.3a) indicates high variability among the trace rakes (Fig. 4.3b). However, as indicated by Figs. 4.3c (discontinuity planes orthogonal to the plane of the computer screen) and 2.3d (stereonet with discontinuity orientations), the orientation variability of the same discontinuities in Fig. 4.3a is actually low. With this in mind, it is important to avoid using 2D trace rakes for discontinuity

analyses and to choose sampling methods in which both discontinuity orientations and trace lengths (or trace end-points) obtained from TLS mapping are considered.

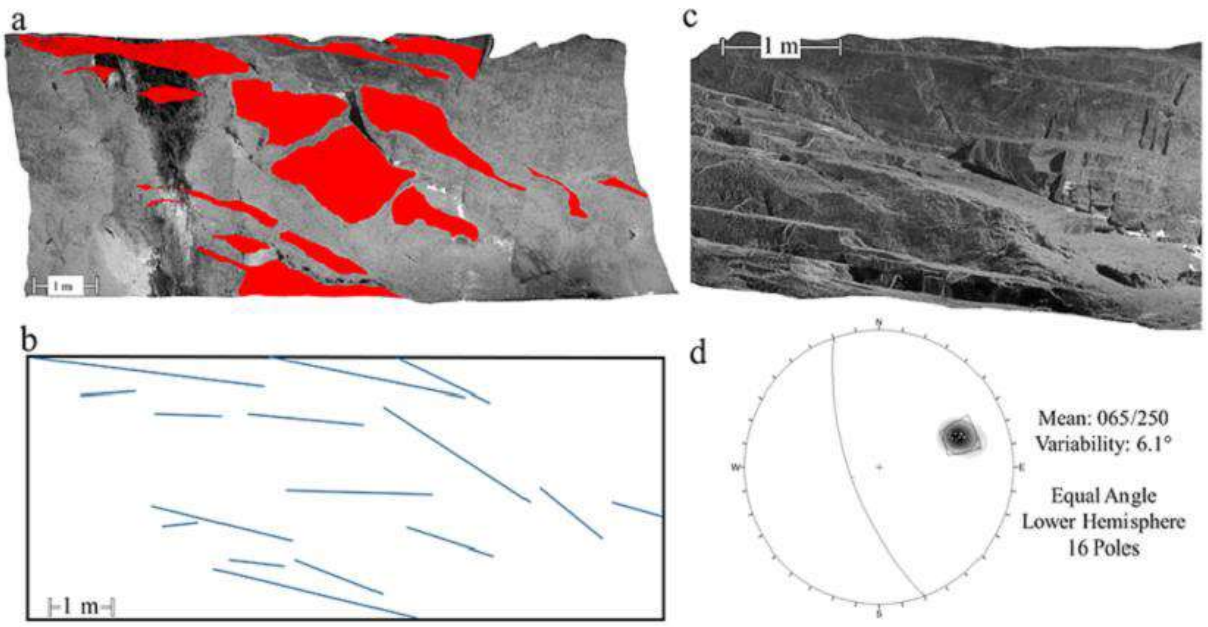

Fig. 4.3. Comparison of orientation variabilities obtained from discontinuity planes and resulting trace maps. **a** Point cloud indicating the exposed area of discontinuity planes; **b** trace map with the measured trace lengths; **c** view of the point cloud with discontinuities perpendicular to the plane of the computer screen; **d** stereonet showing the variability in orientation.

4.3 Automatic methodology for discontinuity analysis and continuous DFN modeling

The geometrical parameters required to generate DFN models in 3DEC are the orientation, size and intensity of each discontinuity set. Both orientation and size are described by probability density functions, and the intensity is a constant value corresponding to the PTC for discontinuity generation. A three-step automatic methodology was developed for discontinuity analyses to obtain these parameters along the tunnel and generate continuous DFNs. This methodology is summarized in the flowchart of Fig. 4.4. Step **I** is automated in Excel and Visual Basic subroutines, which apply different discontinuity analyses to obtain discontinuity size and orientation distributions. In step **II**, FISH codes (Itasca 2014) read the data exported from Excel to automatically calculate the reference P_{32} along the tunnel. In Step **III,** the continuous DFNs

are generated using the previously calculated P_{32} values. Next, important aspects of these steps are described in detail.

4.3.1 Step I: Discontinuity Analyses

The data exported from Polyworks are trace end-points, middle-points, discontinuity normal vectors (with the x,y,z positions), region boundary lines and the tunnel axis. The distribution forms of the measured trace length [$f(l)$] of each discontinuity set are obtained by applying the Kolmogorov-Smirnov goodness-of-fit-tests to all measured trace length data from the entire tunnel (step **Ia** in Fig. 4.4). Initially, the data exported from Polyworks contain the original coordinates from the tunnel. Considering that tunnels may not be linear and that they often have a strongly irregular geometry (uncovered tunnels), it is not simple to automatically fit sampling windows at different positions and regions without a reference object. Here, we used the tunnel axis (which is a polyline drawn in the tunnel point cloud) as a reference to orientate the data.

In DFN-3DEC models, discontinuity size is represented by the PDF of the diameters of disk-shaped discontinuities. However, in field geological mapping, it is only possible to measure the discontinuity traces (or chords of these disks), which are often censored in rock outcrops. There are several methods to correct the mean trace length and standard deviation using planar sampling windows (Cruden 1977; Baecher 1980; Pahl 1981; Kulatilake and Wu 1984; Zhang and Einstein 1998; Mauldon 1998; Mauldon et al. 2001; Wu et al. 2011). Cacciari and Futai (Cacciari and Futai 2016b) applied different window-sampling methods to a tunnel section and discussed the influence of the rock face orientation in the mean trace length results. In this work, the authors found that the method proposed by Wu et al. (Wu et al. 2011) is more suitable because of the following advantages:

(1) The windows are rectangular. Therefore, even with a rock face longer in one direction than in the other, the window can cover the entire area.
(2) The method can be applied to non-parallel traces. The trace rakes are not inferred directly from the trace maps but are calculated using both discontinuity and rock face orientations. This is important because the final aspect of the trace map does not interfere in the mean trace length estimate (Fig. 4.3).

The formulation considers the variability in rock face orientation. Thus, the results from different tunnel regions can be compared to each other.

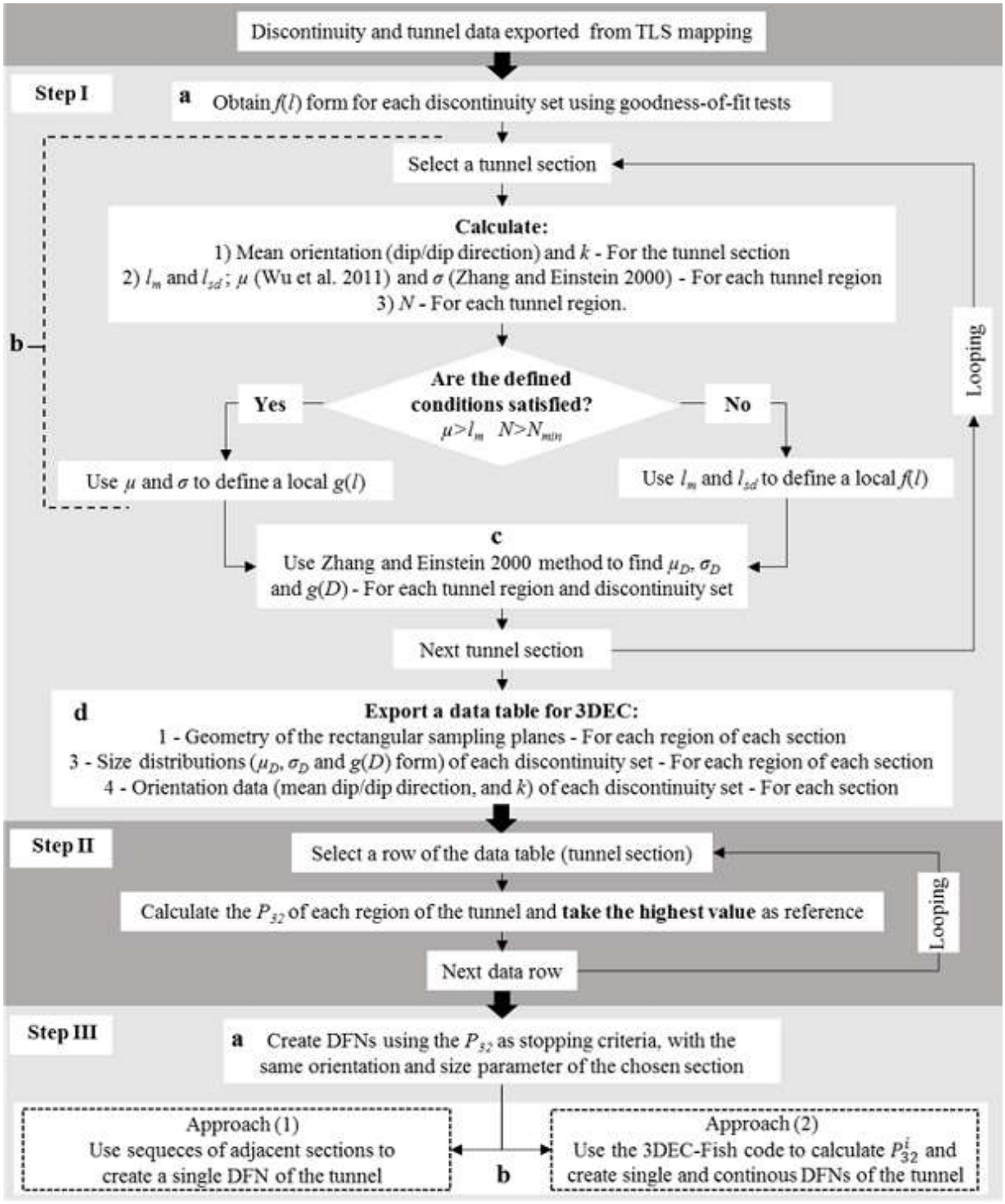

Fig. 4.4. Flowchart of methodology developed.

Considering that tunnels have different rock face orientations and that the resultant trace maps may not lead to parallel traces, even when discontinuity planes are nearly parallel to each other, the method proposed by Wu et al. (2011) is used (Step **Ib**). Note that this method requires orientation measurement from all parts of the tunnel (wall and roof) to calculate rakes and

relative frequencies (Wu et al. 2011; Cacciari and Futai 2016b). Because TLS images are being used, all regions of the tunnel can be equally evaluated.

Essentially, rock outcrops are irregular 3D surfaces; however, they are generally represented as 2D sampling surfaces for trace mapping and sampling window analysis. Sturzenegger et al. (2011) introduced the concept of topographic windows as a practical means of applying 2D sampling methods based on trace end-points (Mauldon 1998; Mauldon et al. 2001). The authors showed the practical advantages of using topographic windows to map discontinuities that would not be visible in planar windows of the same size and position (often smaller discontinuities and sub parallel to the planar surfaces). However, once traces are considered the chords of disks, for which the actual diameters and center positions are unknown, it is not possible to affirm whether a given discontinuity mapped on the 3D rock surface will cut a mean planar surface of the same size and position, unless the trace is contained in both. Therefore, to validate applications of 2D sampling methods to 3D irregular sampling surfaces, it is necessary to assume the existence of a representative 2D sampling surface that crosses the same portion of the rock mass and the same discontinuities mapped in the TLS point cloud and results in the same number and types (T_{tt}, T_{tc} and T_{cc}) of traces. In Fig. 4.5a, for example, the red plane cutting the limits of the rock mass portion of the tunnel region R (black dashed box) indicates the representative 2D sampling surface. Once this is accepted, traces can be represented by lines that connect end-points and middle-points and are projected onto representative 2D sampling surfaces, and computational programs can be used to automatically identify the trace types in each region.

Considering differences in total area and spatial distributions of the 3D and 2D surfaces in Fig. 4.5a, the intersection probability between discontinuities and the 3D rock face (TLS point cloud) will always be higher than the intersection probability between discontinuities and the 2D sampling surface. In tunnels, the number of sub divisions (i.e., R, EW and WW) can be increased to create rock faces that are geometrically closer to planar surfaces, minimizing differences between intersection probabilities. However, the lengths of these regions around the tunnel perimeter define the widths of the rectangular sampling windows fitted; thus, the μ values calculated via the methodology of Wu et al. (2011) or similar methods could be affected by high numbers of T_{tt} traces. Cacciari and Futai (2016b) considered the effects of increasing the number of sub divisions of the Monte Seco tunnel and concluded that fitting rectangular

sampling windows to regions smaller than R, EW and WW may significantly overestimate the μ values thus determined.

In tunnels containing a fully exposed rock face, discontinuity traces are censored only by the ballast bed (such as trace number 4 in Fig. 4.2a), and most trace lengths could be directly obtained via the distance between end-points. However, the trace lengths from discontinuities that cut across more than one region, as measured by the distance between end-points (such as chord **c** in Fig. 4.2b), are not contained in either of these and, thus, cannot be considered to the μ estimates obtained by representative 2D rectangular sampling windows. Moreover, the differences in trace intensities between tunnel regions (i.e., R, WE and WW) depend not only on the natural discontinuity distribution in space but also on the aspects described in the previous chapter (damage to the rock face, failed blocks and orientation bias) that hinder the identification of discontinuities. Therefore, it is important to evaluate the unbiased mean trace lengths separately for each region (different rock face orientations) of the tunnel using 2D window-sampling methods.

To simplify estimates of μ, the R region was considered as a horizontal sampling surface and the EW and WW regions as vertical sampling surfaces along the entire tunnel. The end-points and middle-points of traces (Fig. 4.2b) and the positions of orientation measurements were projected on these 2D surfaces. In step **Ib**, a tunnel section was chosen using the tunnel axis as a reference of length (Fig. 4.5b). Subsequently, the angle between the tunnel axis (in this particular section of the tunnel) and the Y-axis was calculated, and all of the trace data and region boundary lines were rotated by this angle. Thus, the tunnel section length (in the Y direction) and the minimum distance between the boundary lines of the region (in the X direction for the R region and in the Z direction for the EW and WW regions) define the dimensions of the sampling window used. Fig. 4.5c exemplifies this procedure, showing the rotated data from the R region with a rectangular sampling window fitted inside the region boundaries. It is important to note that this method does not have limitations when the tunnel is curved because the rotation angle is different for each tunnel section and the axes inside these sections can be considered straight lines.

The method of Wu et al. (2011) incorporates the corrected (due to orientation bias) relative frequencies of discontinuities appearing on 2D sampling surfaces. Therefore, because trace type sampling of the 3D rock faces was considered valid for the representative 2D rectangular windows employed, the relative frequencies of discontinuities were calculated for horizontal

(R region) and vertical (EW and WW regions) sampling surfaces, in which the strikes were parallel to the tunnel axes. Therefore, the estimated values of μ are equivalent to the unbiased mean chord lengths in the horizontal (R samples) and vertical (EW and WW samples) directions. In Fig. 4.2b, for example, chords **a** and **b** become chords **d** (horizontal direction) and **e** (vertical direction), respectively; thus, the rectangular window in Fig. 4.5b is applied to estimate the unbiased mean trace (or chord) length in the horizontal (R) direction for a particular tunnel section.

Discontinuity orientation measurements are used for two different purposes: (1) to obtain the Fisher distribution for the tunnel section (mean orientation and *k*) for each discontinuity set and (2) to calculate relative frequencies to estimate μ for each discontinuity set and each tunnel region. The x,y,z position and region name (R, EW or WW) are associated with and are used to locate and classify each orientation measurement along the tunnel. For a given tunnel section, the orientation data from all regions are used to define the Fisher distributions. Data specific to each region are used to estimate the associated unbiased mean trace lengths using the methodology of Wu et al. (2011).

Preferably, every discontinuity mapped in each TLS point cloud should have an identified trace and an orientation measurement for each tunnel region crossed. However, once care is taken to determine discontinuity normal vectors solely in well-exposed planes, the number of orientation measurements required for TLS mapping becomes considerably lower than the number of traces identified. Consequently, the number of relative frequencies calculated is lower than the number of trace types identified (T_{tt}, T_{tc} and T_{cc}). It is important to note that the absence of some relative frequencies does not prevent estimates of μ using this method, once the available values can be considered representative of the orientation of each discontinuity set. In contrast, forcing orientation measurements in poorly exposed planes would result in biased values of relative frequencies, thus hindering estimates of μ. To better define the Fisher distributions along the tunnel, the sections used for orientation analyses can be longer than the section used for identifying trace types, provided that the latter is inside the first and, preferably, has the same center position.

Although it is assumed that trace types mapped on 3D TLS regions remain the same in representative 2D sampling surfaces, the trace lengths are actually different. When the actual position of the representative 2D sampling surface inside the rock mass limits (Fig. 4.5a) is unknown, the actual trace lengths in these surfaces cannot be determined. Therefore, the

measured trace-length parameters (l_m and l_{sd}) were calculated (for each region) by the average of the trace lengths projected on representative 2D sampling surfaces (as indicated in Figs. 2.3b and 2.5c). The measured lengths of traces that cut through more than one region are considered separately for each case, using the distance between the projected end-points and middle-points.

The three regions (with fitted sampling windows as in Fig. 4.5c) from the tunnel section chosen are used to calculate the measured and unbiased parameters of the trace lengths (step **Ib** in Fig. 4.4) and the number of discontinuity traces cutting each region (N). The program implemented in step I automatically calculates both l_m and μ; however, one of them must be chosen to define the local (section analyzed) unbiased trace length PDF [$g(l)$] or the local $f(l)$. As described by Zhang and Einstein (2000), when $\mu<l_m$, most traces are contained in the window; thus, μ does not give a reliable estimate, and l_m should be used. On the other hand, when $\mu>>l_m$, most traces transect the window, so discontinuities may be considered persistent. When non-persistent discontinuities are being evaluated, this type of result is not expected, but in some cases, there is only one (or a few) discontinuity transecting the sampling region, resulting in extremely high value of μ. Thus, it is important to establish a minimum number of traces (N_{min}) as a condition for choosing between μ and l_m.

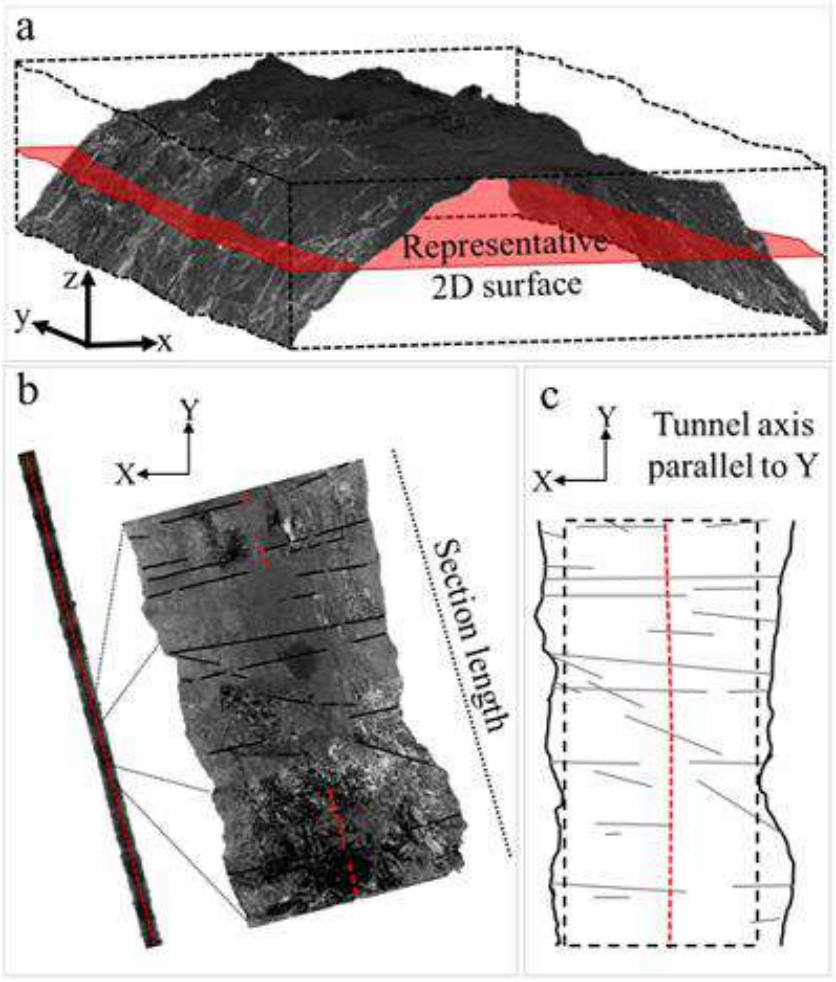

Fig. 4.5 a Portion of rock mass (black dashed box) containing the 3D rock face (TLS point cloud) of the tunnel region R and a representative 2D sampling surface (red). **b** Section of the mapped point cloud to be analyzed in its original orientation. **c** Rotated data with tunnel axis parallel to Y and a rectangular sampling window fitted.

Step **Ic** consists of defining the discontinuity diameters PDF. Warburton (1980) developed a stereological relationship between trace length distributions and discontinuity diameter distributions, considering traces as chords of disc-shaped discontinuities. Zhang and Einstein (2000) used this relationship and proposed a methodology to find the diameter distribution from the trace length distribution. This method is used here to obtain the discontinuity diameter distributions $g(D)$ from the local $g(l)$ or $f(l)$ previously defined (the same method was used in Han et al. (2016)). Thus, the final results of the discontinuity size analysis of a tunnel section are the $g(D)$, with a mean discontinuity diameter (μ_D) and standard deviation (σ_D), obtained for

each region, along with the location, geometry and orientation of the rectangular sampling window used.

Step **Ib** anc **Ic** can be applied to consecutive tunnel sections, using an input data table with the positions and lengths of these sections and a built-in looping (Fig. 4.4). Finally, in step **Id**, the results from the discontinuity analyses are exported into data tables in which every row represents the results from a tunnels section. Each of these data rows contains the Fisher distribution of each discontinuity set and $g(D)$, N and the dimensions of the rectangular sampling windows for each discontinuity set sampled in each tunnel region.

4.3.2 Step II: Reference P_{32} calculation

In step **II** (Fig. 4.4), a 3DEC-FISH (Itasca 2014) code was written to read the data table exported from Excel. Once the code opens and reads a data row (tunnel section), it runs the same row multiple times, obtaining three values of P_{32} (one for each tunnel region) for each discontinuity set. Next, the method used to calculate P_{32} from the results obtained in step **I** is explained in detail.

P_{32} is the most representative intensity parameter for DFN modeling because it considers both unbiased frequency and size components (Rogers et al. 2014; Havaej et al. 2016), while 2D intensity parameters (traces in sampling surfaces) depend on the rock face and the discontinuity set orientations. Nevertheless, it is impossible to measure P_{32} directly in rock masses; thus, it has to be estimated from discontinuity traces. Dershowitz and Herda (1992) developed an approach to estimate P_{32} using P_{21} (total length of fracture traces per area of sampling surface) from field mapping, based on the linear relationship between both parameters. The method basically consists in taking different P_{32} values as the DFN PTC and in measuring the resulting P_{21} several times (using a sampling plane inside the model). Then, a best-fit linear relationship (C_{21} value) is estimated, and the P_{32} compared to the field (or TLS) P_{21} is checked. This approach was also used in Havaej et al. (2016), and details are explained in Elmo (2006).

Here, we propose a different approach based on the parameter N, which is an easy parameter to obtain automatically using a computer program. However, the N value apparent in the tunnel face could be a result of infinite discontinuity distributions in the rock mass (with different P_{32}). Thus, N was used as the PTC of several DFN generations, and sampling planes with the same

dimensions of the tunnel regions (where N was calculated) were built in the model for intersection counting. P_{32} was calculated and stored for each simulation as:

$$P_{32} = \frac{\sum_{i=1}^{N} S_i}{V} \tag{4.1}$$

where S_i is the area of each disk-shaped discontinuity generated and V is the volume of the DFN domain. After a defined number of simulations, the P_{32} mean and standard deviation were calculated. It was verified that the P_{32} standard deviations do not vary significantly after 10 DFN simulations, so this number will be used in further analysis.

Table 4.1 shows a comparison of this method with that proposed by Dershowitz and Herda (1992) using C_{21}. Five real rectangular sampling windows with similar dimensions (5 m length and width varying from 3.7 m to 4.6 m) were taken from the roof of the Monte Seco tunnel in different positions. The DFN volume used in these examples was 15^3 m^3 for all cases. Table 4.1 shows that the mean P_{32} values obtained from N are similar to those obtained using C_{21} and P_{21}, and the differences between them did not exceed the standard deviations.

To verify whether the mean P_{32} obtained is a representative value, a parametric analysis can be performed and the mean P_{32} results checked with different N, discontinuity sizes, sampling window dimensions and DFN volumes (Fig. 4.6). A DFN volume can be considered a representative volume element (RVE) if the rock mass parameter obtained in this volume (i.e., P_{32}) does not vary significantly from values obtained in larger volumes. In this case, P_{32} varies with N, discontinuity size and orientation, so the DFN volume will also depend on these parameters. The discontinuity orientation effects can be minimized using cubic volumes, and comparing the P_{32} results obtained from sampling windows of the same dimension and orientation inside the DFN volumes generated.

Figs. 2.6a and 2.6b show the results of the mean P_{32} obtained from different DFN volumes (cube edge lengths indicated) and N, considering log-normal distributed discontinuities with μ_D/σ_D =2.0/1.0 m and μ_D/σ_D =4.0/2.0 m, respectively. In this case, sub-vertical discontinuities (mean orientation 90/360 and Fisher $k=70$) were generated perpendicularly to a square surface (5x5 m^2) placed in the center of the DFN volumes simulated. It is possible to see that for both μ_D/σ_D values, there is a significant decrease in P_{32} values for lower volumes. In most cases, however, it tends to remain unchanged after volumes of 15^3 m^3. The greater the P_{32} obtained (high values of N and μ_D) in this analysis, the greater the DFN volume required. In Fig. 4.6a for

example, for μ_D/σ_D =2.0/1.0 m and N=5, P_{32} remains practically unchanged for all volumes tested, while in Fig. 4.6b, for μ_D/σ_D =4.0/2.0 m and N=60, P_{32} remains unchanged only for volumes greater than 25^3 m^3.

Figs. 2.6c and 2.6d show the P_{32} results from the 20 m DFN edge length, indicating that both the mean and standard deviation of P_{32} increase linearly with N (Fig. 4.6c), and the coefficient of variation of P_{32} (P_{32} standard deviation/mean P_{32}) decreases exponentially with the increase of N. In this case, three different sampling areas were used (5x5 m^2, 5x10 m^2 and 5x15 m^2). As expected, for the same N and μ_D/σ_D values, P_{32} decreases with the increase of the sampling area (Fig. 4.6c). For low values of N, the coefficient of variation is high and varies significantly for different discontinuity size distributions (Fig. 4.6d). In this case, for $N \geq 5$, the coefficient of variation is always lower than 0.5 and does not depend significantly on the discontinuity size and the sampling window dimensions.

The main advantages of this approach are the facility for calculating N automatically and the implementation as PTC using a FISH code (Itasca 2014) counting the number of discontinuity intersections until the target value is reached. P_{21} is also automatically calculated from TLS by checking the censored traces and measuring the portions of these traces contained inside the sampling plane for each tunnel region. However, this parameter cannot be used directly as the PTC because it would be nearly impossible to create DFNs reaching the same exact P_{21} from the TLS using virtual sampling planes. The Dershowitz and Herda (1992) methodology could be implemented in FISH (Itasca 2014) with greater effort, but it would be necessary to computationally find C_{21} for each region of each tunnel section. Moreover, for each C_{21} (calculated) and P_{21} (from TLS) pair, a single P_{32} value would be obtained, preventing direct evaluation of the P_{32} variability.

In step **II**, the mean P_{32} obtained for the three tunnel regions are compered, and the highest value is taken as a reference for the tunnel section analyzed. The program then automatically moves to the next data row (or next tunnel section to be simulated) using a built-in looping (Fig. 4.4). The P_{32} values calculated for each tunnel section are stored to be used as the new PTC to generate DFNs (with the same size and orientation parameters used to obtain these P_{32}).

Table 4.1. Comparison of P_{32} obtained from different approaches.

Size (log-normal) (m)		Orientation (Fisher):			P_{32} (m^{-1}) from P_{21}(m^{-1})			P_{32} (m^{-1}) from N	
μ_D	σ_D	*Dip°*	*Dip Dir°.*	*k*	C_{21}	P_{21}	P_{32}	*N*	P_{32}*(mean/sd)*
2.00	1.4	85	175	30	0.86	1.59	1.37	21	1.31/0.27
1.71	0.8	70	179	22	0.87	0.62	0.54	13	0.64/0.16
1.80	1.0	70	179	22	0.87	2.14	1.86	30	1.68/0.29
2.42	1.5	80	175	21	0.85	0.68	0.58	12	0.70/0.20
0.95	0.7	79	180	30	0.89	1.39	1.24	36	1.40/0.29

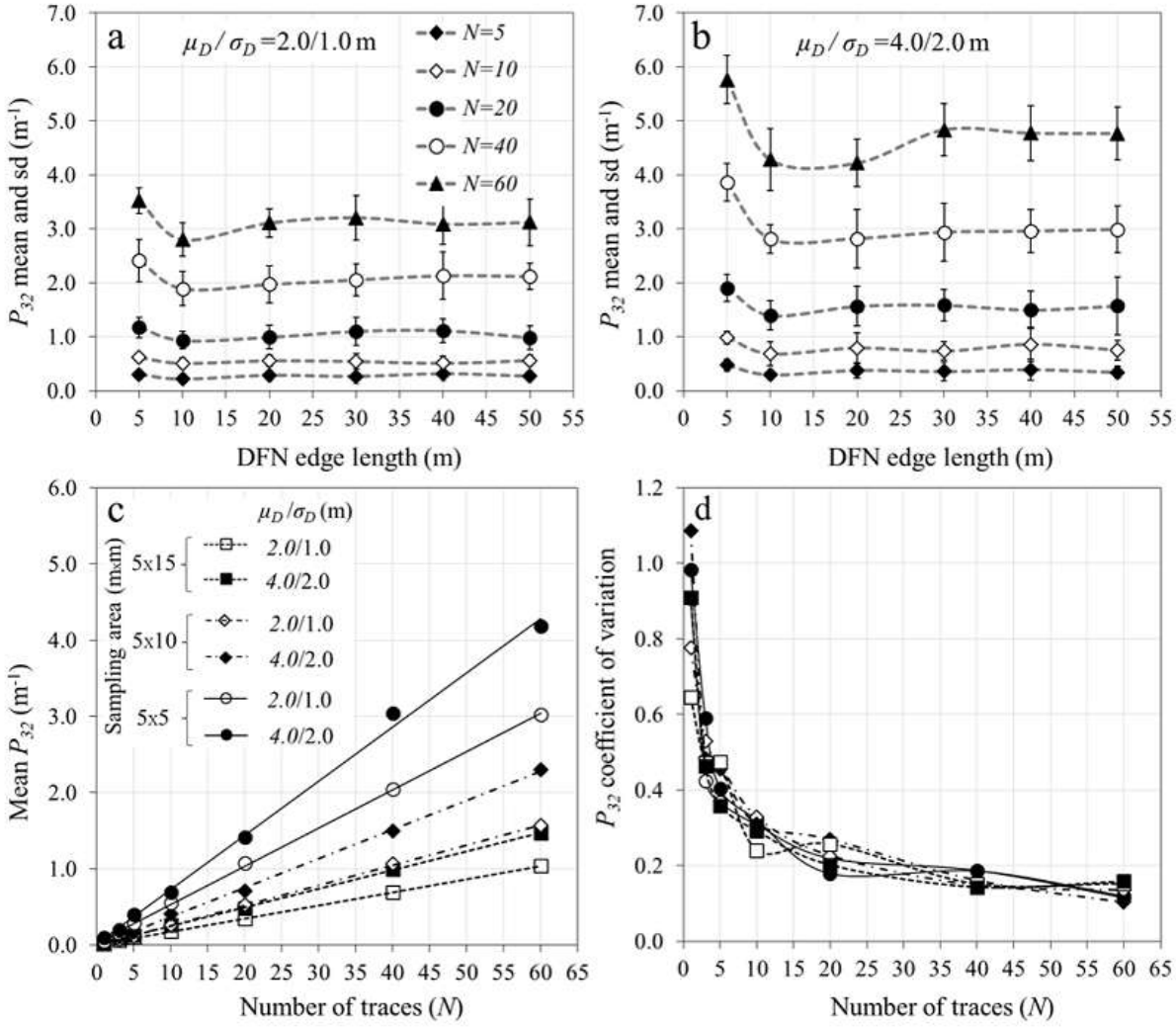

Fig. 4.6. Parametric analysis using *N* as PTC for DFN generation. **a** And **b** mean and standard deviation of P_{32} obtained from different DFN volumes (cube edge length indicated) for μ_D/σ_D

=2.0/1.0 m and 4.0/2.0 m, respectively. **c** Mean and standard deviation of P_{32} obtained from different N, μ_D/σ_D and sampling areas, using the 20 m DFN edge length. **d** P_{32} coefficient of variation obtained from different N, μ_D/σ_D and sampling areas, using the 20 m DFN edge length.

4.3.3 Step III: Continuous DFN modeling

In steps **I** and **II**, the necessary parameters for creating DFNs are automatically obtained for each discontinuity set (*pfd* of discontinuity diameters and orientations and the reference P_{32}). Thus, if one intends to model a single section of a tunnel, the DFN can be directly generated. However, the greater the length of the tunnel section, the greater the lengths of the sampling windows used in step **I**, thus increasing the heterogeneity of traces distribution in these windows (heterogeneous trace maps). The methodology of Zhang and Einstein (2000), which is used to obtain discontinuity diameter distributions, operates under the assumption that discontinuity positions in space follow a Poisson distribution. Thus, it is unlikely that the DFN trace maps obtained will be similar to TLS maps in these cases. Moreover, even if particular position distributions could be identified using TLS discontinuity mapping, this would not be a reasonable approach considering the assumptions of the Zhang and Einstein (2000) method.

When DFNs are used to create 3DEC models to assess the stabilities of blocks around tunnels, it is important to increase the similarities between discontinuity distributions obtained from DFN models and TLS (real) mapping. Thus, in step **III**, two different approaches are proposed to automatically create DFNs that better represent the variability in discontinuity positions along the tunnel:

(1) Use consecutive reference values of P_{32} from adjacent tunnel sections to create a single DFN for each discontinuity set. For example, a 30-m-long section of a tunnel could be modeled by two adjacent 15 m, three adjacent 10 m or 6 adjacent 5 m smaller sections using the methodology described in step **II**. However, this is a geometrical segmentation, which may overlook some small variations of P_{32}.
(2) Create a single and continuous DFN (for each discontinuity set) considering smaller variations of the P_{32} along the tunnel using a computational approach consisting of the following steps:
    - Select a constant section length (i.e., 5, 10 or 15 m) and run **steps I** and **II** multiple times, moving along the position of the section meter by meter, resulting in a curve

containing the variability of the reference P_{32} (between R, WW and EW) along the tunnel. This process is automated using Visual Basic subroutines (step **I**) and 3DEC-FISH codes (Itasca 2014) (step **II**).

- For every tunnel position (or every P_{32} value), run step **IIIa** multiple times (in the same tunnel position) using the cubic DFN volume (L^3 m^3), and calculate the central volumetric intensity for each DFN realization:

  $$P_{32}^{i} = A_i/(L \times L \times 1) \quad (4.2)$$

  where A_i is the total area of fractures with the center contained in the central meter of the model (Fig. 4.7a)

- Compare the similarity between P_{32}^{i} and the reference P_{32} used to create the DFN using the P_{32} error:

  $$Er\ (i) = abs\left[\left(P_{32}^{i} - P_{32}\right)/P_{32}\right)\right] \quad (4.3)$$

  The program continues looping until the minimum pre-established P_{32} error (i.e., $Er\ (i) \leq 0.1$) is reached.

- Stop looping, delete the unused fractures, append the remaining (central) fractures in the adjacent DFNs from previous tunnel positions (Fig. 4.7b) and move to the next tunnel position.

- The volumetric intensity of any finite section of the tunnel, beginning in an initial position (*ip*) and ending in a final position (*fp*), can be calculated as:

  $$P_{32}^{t} = \sum_{ip}^{fp} P_{32}^{i}\ /(fp - ip) \quad (4.4)$$

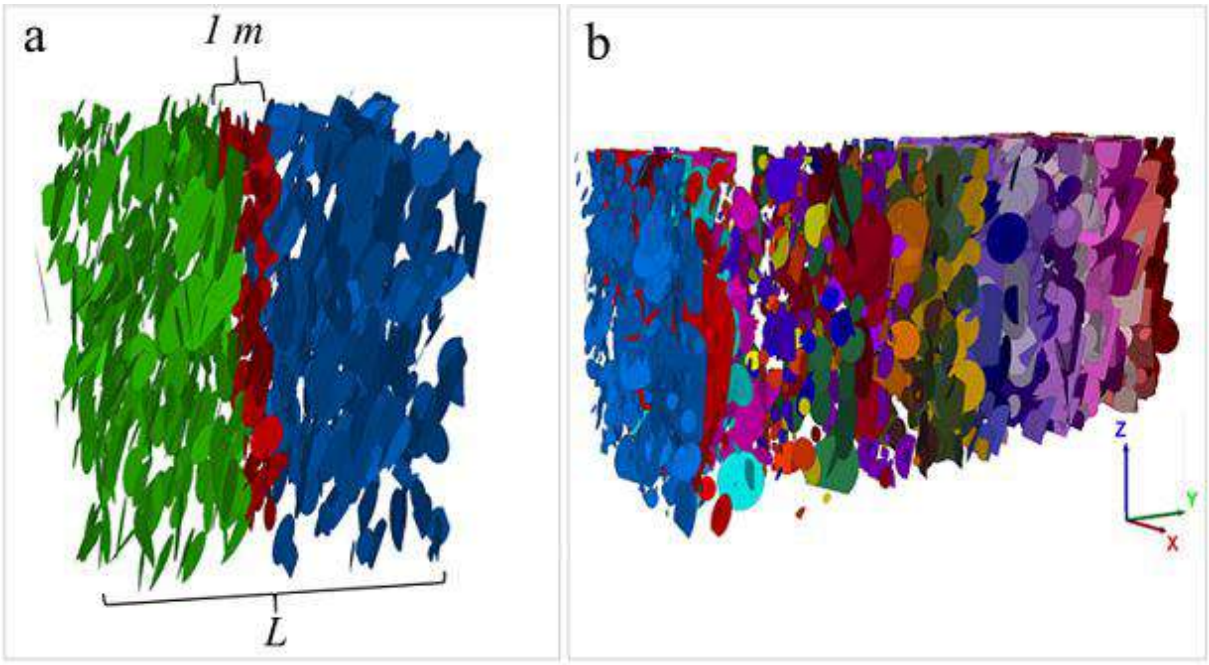

Fig. 4.7. a Central portion of a DFN used to calculate P_{32}^{i}. **b** Continuous DFN created by several adjacent tunnel positions.

Examples and a comparison of approaches (1) and (2) will be shown further, using the discontinuity TLS mapping from the Monte Seco tunnel. Approach (2) will be used to generate single and continuous DFNs of each discontinuity set and create block models of different sections of the tunnel.

4.4 Results from the Monte Seco tunnel

The Monte Seco tunnel is constructed in a foliated gneiss from the *Nova Venécia* complex, which is part of the *Araçuaí* Paleoproterozoic orogenic belt. The 324 m first portion of the tunnel was chosen for this study because of the large number of discontinuities in this area identified in the field inspections.

Four discontinuity sets were identified during the geological field mapping: two shear fracture sets (F_1 and F_2); one sheet joint set (F_3); and the rock foliation (S_n). Fig. 4.8a shows an outcrop nearby the tunnel indicating the intersections between these discontinuities and the rock block geometry commonly observed at the tunnel site. Figs. 4.8b-e show examples of the tunnel point

cloud with similar intersections between these discontinuities. Fig. 4.8f shows the projection containing all the orientation data from the 324 m scanned. The similarity between hand-made geological mapping and TLS mapping was demonstrated for the same tunnel in Cacciari and Futai (2016b). F_1, F_2 and F_3 were analyzed as non-persistent discontinuities, using the methodology described in sections 4.2 and 4.3. The rock foliation is assumed to be a persistent structure, because it may be inappropriate to estimate a mean trace length (and discontinuity diameter) for S_n based on images, considering the genesis of such geological structures (Cacciari and Futai 2016b).

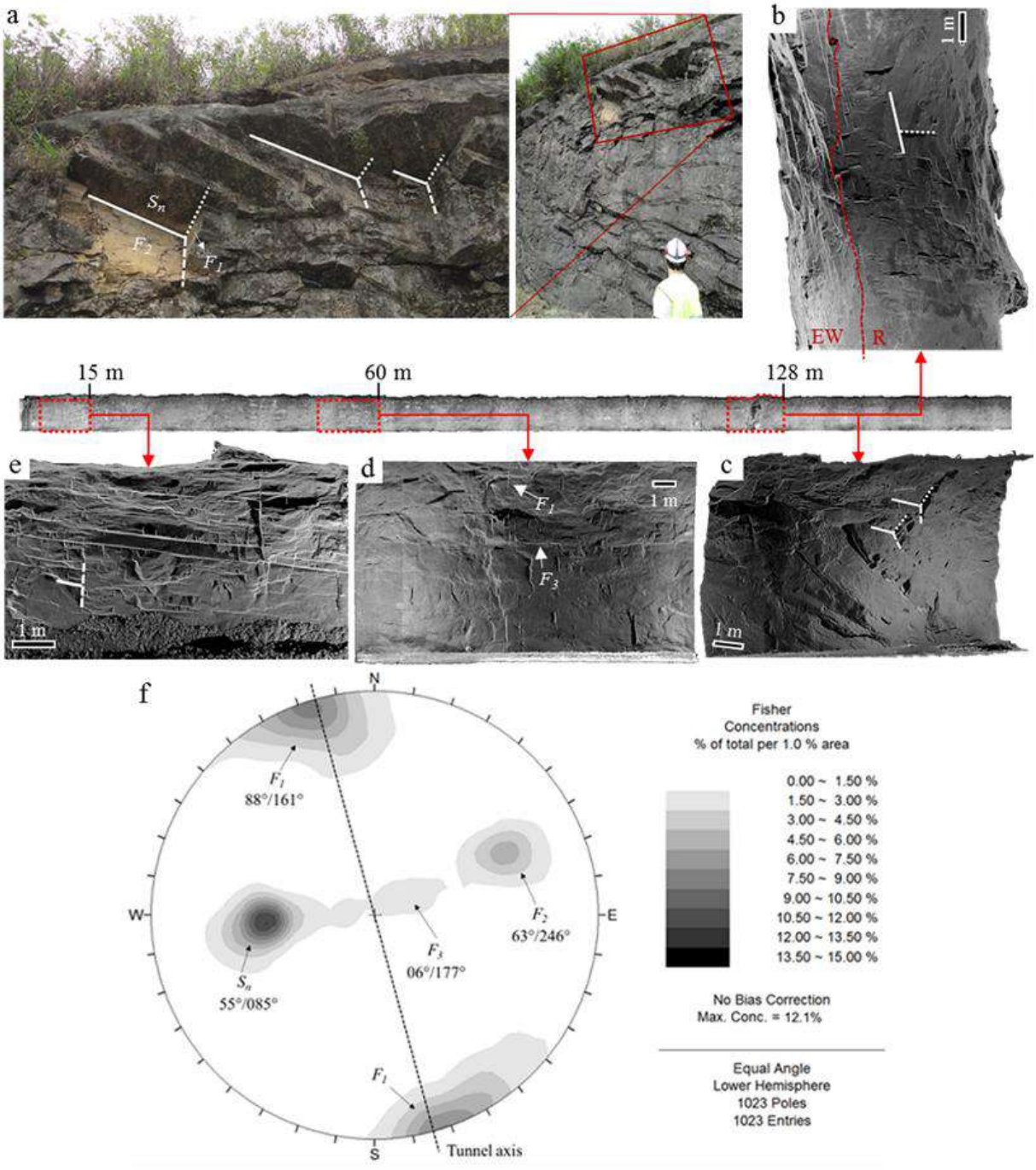

Fig. 4.8. Discontinuity sets and rock block geometry at the tunnel site. **a** Outcrop next to the tunnel entrance indicating rock blocks defined by F_1, F_2 and S_n planes. **b** Section of the tunnel point cloud (EW and R) with S_n parallel and F_1-F_2 perpendicular (traces in white) to the plane of the computer screen. **c** Different view of the EW of the same tunnel section in **b**, indicating the rock blocks defined by F_1, F_2 and S_n planes. **d** Section of the tunnel point cloud (EW) containing F_1 (vertical) and F_3 (horizontal) traces. **e** Section of the tunnel point cloud (EW) with F_2 parallel and S_n-F_1 perpendicular (traces in white) to the plane of the computer screen. **f** Orientation of discontinuities mapped with TLS (contours of pole concentrations).

All the traces from the F_1, F_2 and F_3 sets were mapped in the tunnel point cloud, as indicated in section 4.2. Kolmogorov-Smirnov (K-S) tests were performed with all the trace length data (EW, WW and R) from each set to check the best-fitted distribution forms of the measured trace lengths. Table 4.2 summarizes the results from the trace length mapping. For each set, the data were tested for log-normal, gamma and exponential negative distributions, which are the most common probability density functions for describing discontinuity size (Zhang and Einstein 2000). The log-normal distribution was found to be the best fit for all cases (Table 4.2).

Table 4.2. Results from the TLS trace length mapping.

Discont.	Number of traces				Mean trace	K-S statistics		
Set	R	EW	WW	Total	length	Log-normal	Gamma	Exponential
F_1	671	542	645	1858	1.01	0.028	0.094	0.200
F_2	263	326	87	676	1.04	0.026	0.071	0.250
F_3	0	79	177	256	1.68	0.036	0.140	0.190

4.4.1 Applications of Steps I and II along the tunnel

The discontinuity analyses described in step **I** were applied to the TLS discontinuity mapping results of the Monte Seco tunnel. Three section lengths of 5 m, 10 m and 15 m were defined, and built-in looping (Fig. 4.4) was used to continuously change the position of these sections,

meter by meter, along the tunnel. Here, we assumed N_{min}=7 because the μ values were not overestimated ($\mu >> l_m$) in this condition. After running the program, nine data tables were generated, one for each section length and discontinuity set. Each row in these data tables contains the results of one section length and position, comprising the Fisher distribution of discontinuity orientations, N, $g(D)$ and the dimensions (length and width) of the rectangular sampling windows used to obtain these parameters in each tunnel region. The dimensions of the rectangular windows fitted in the tunnel regions were defined as presented in Fig. 4.5. The position of each section along the tunnel is the center of the rectangular sampling windows in the tunnel axis direction. The number of orientation data (1023 measurements) is much lower than the number of trace data (2790 measurements); thus, sections lengths of 30 m were used to define the Fisher distribution for each tunnel section position (meter by meter). The same Fisher distribution was used in the first and last 15 m of the tunnel, due to the size of the sampling section (30 m). Table 4.3 shows the structure of the data tables generated by step **I**, which contains few data rows pertaining to the results of the F_1 set obtained from analyses using 5 m section lengths.

Table 4.3. Example of the structure of data tables obtained by step **I,** with selected results of the F_1 set analysis obtained using 5 m tunnel sections (LN: log-normal and EX: exponential negative).

Tunnel Position (m)	Window dimensions: length/width (m)			*N*			*g*(*D*): μ_D/σ_D (m)/distribution form			Fisher Distribution	
	EW	WW	R	EW	WW	R	EW	WW	R	*Dip°/ Dip Dir.°*	*k*
2.5	5.0/3.6	5.0/3.8	5.0/3.7	17	2	15	0.8/0.6/LN	2.0/1.1/LN	1.6/0.8/LN	083°/175°	31
3.5	5.0/3.6	5.0/3.8	5.0/3.7	21	3	16	0.9/0.7/LN	2.1/0.8/LN	1.9/1.0/LN	083°/175°	31
⋮	⋮	⋮	⋮	⋮	⋮	⋮	⋮	⋮	⋮	⋮	⋮
150	5.0/3.6	5.0/3.8	5.0/4.1	7	19	17	1.9/0.8/LN	0.7/0.4/LN	2.1/1.4/LN	072°/177°	32
151	5.0/3.6	5.0/3.8	5.0/4.1	9	21	27	2.2/1.0/LN	0.6/0.4/LN	1.4/0.9/LN	072°/177°	32
⋮	⋮	⋮	⋮	⋮	⋮	⋮	⋮	⋮	⋮	⋮	⋮
321	5.0/3.6	5.0/3.8	5.0/4.8	8	12	1	0.8/0.3/LN	0.9/0.4/LN	0.2/0.2/EX	071°/178°	11
322	5.0/3.6	5.0/3.8	5.0/4.8	7	13	1	0.7/0.3/LN	1.0/0.3/LN	0.2/0.2/EX	071°/178°	11

The data tables generated in step **I** were imported into 3DEC, and the FISH code (Itasca 2014) developed automatically assigns the columns of each variable to arrays. For each data row (results of a tunnel section and discontinuity set), the program calculates three P_{32} (one for each region), as described in step **II**, and takes the highest P_{32} value as the reference value for the section. The DFN cubic volumes used for calculating P_{32} were 15^3 m^3 for 5-m sections, 25^3 m^3 for 10-m sections and 35^3 m^3 for 15-m sections, with the sampling windows in the center of the model. The N and μ_D values obtained from rectangular windows fitted in each of these section lengths were checked along the tunnel to ensure that these DFN volumes could be considered as REV (based on the parametric analysis depicted in Fig. 4.6).

Fig. 4.9 shows the results for each discontinuity set (Figs. 4.9a-c) and the sum of the three intensities (Fig. 4.9d). Each point in each line of Fig. 4.9 represents a P_{32} calculated for a given tunnel section (indicating the position of the section center). With this result, it is possible to continuously evaluate the P_{32} variation along the tunnel for each discontinuity set. Thus, it is easier to highlight zones of high intensity and to define sections of the tunnel to be modeled and analyzed by 3DEC or other approaches.

F_1 fractures are the most frequent discontinuities in the rock mass, and the three highest P_{32} peaks are located between 100 and 160 m (Fig. 4.9a). For F_2 fractures, the highest P_{32} are clearly concentrated between 100 and 140 m of the tunnel (Fig. 4.9b). Moreover, F_1 and F_2 are shear fractures concentrated in shear zones of the rock mass; thus, the tunnel crosses several F_1 shear zones (peaks and valleys in Fig. 4.9a) and only one F_2 shear zone. These results were expected because F_1 is approximately perpendicular and F_2 approximately parallel to the tunnel axis. F_3 are sheet joints distributed along the tunnel, but P_{32} does not reach values higher than 1 m^{-1} in any portion (Fig. 4.9c).

Here, three examples of tunnel section lengths (5, 10 and 15 m) were used with a space between samples of 1 m, but the user can customize these parameters. The differences in P_{32} between these tunnel section lengths are related to the fracture distributions for each set. From Fig. 4.9, it is clear that the P_{32} values tend to be more scattered (acute peaks and valleys) for smaller section lengths because of the local variations in fracture intensities. In Fig. 4.9a, for example, between 100 m and 160 m, it is possible to see differences of approximately 0.7 m^{-1} between the P_{32} samples from 5 m and 15 m lengths. Therefore, care must be taken when choosing the length and the position of the tunnel section to be modeled, analyzing intensities obtained from different section lengths (or rectangular sampling windows dimensions).

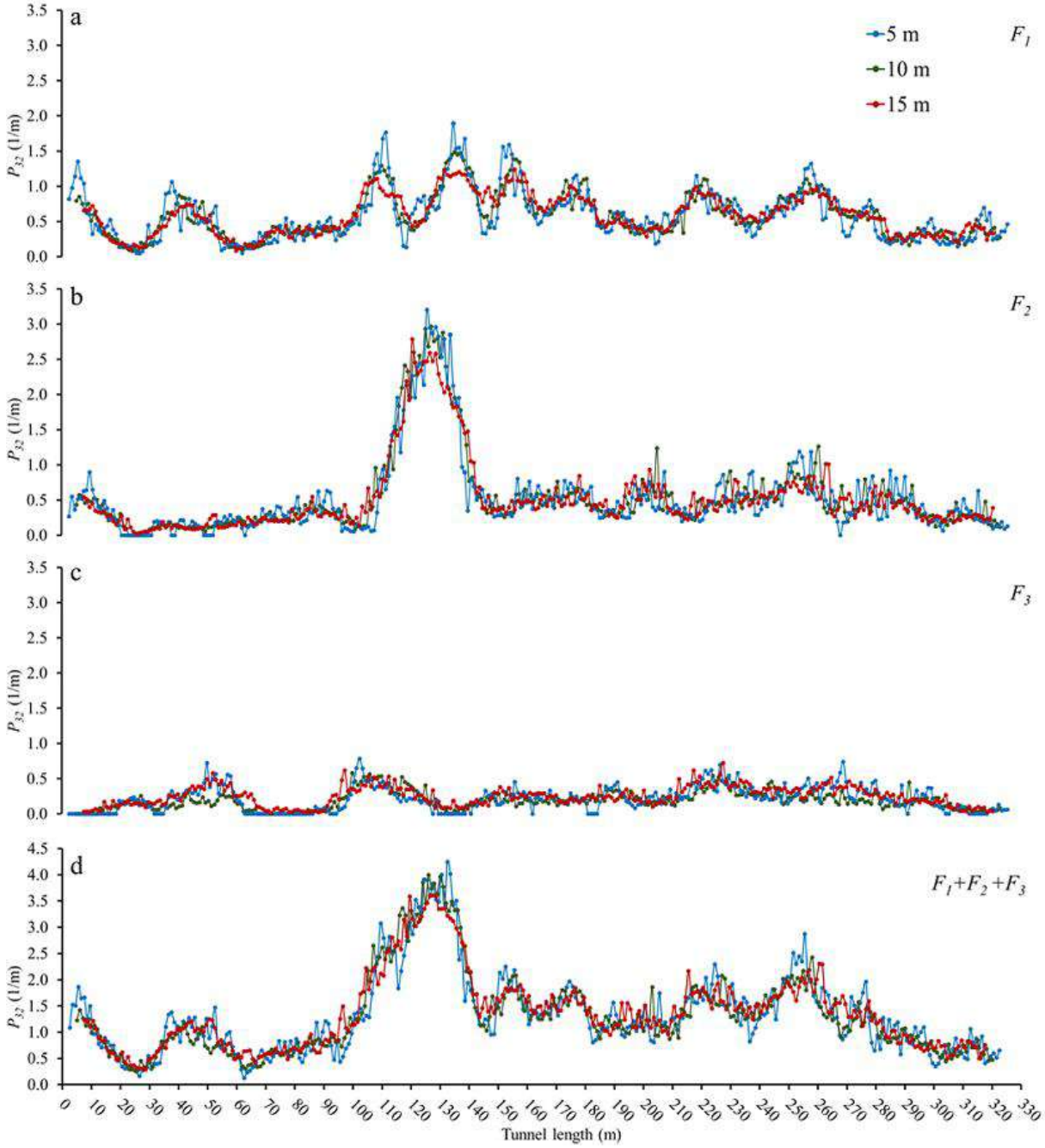

Fig. 4.9. P_{32} volumetric intensity distribution along the tunnel using three different section lengths (5 m, 10 m and 15 m) for discontinuity sets **a** F_1; **b** F_2; **c** F_3 and **d** sum of volumetric intensities.

4.4.2 Application of step III for Continuous DFNs generation

The results presented in Fig. 4.9 are used to create new DFNs, taking the P_{32} values as PTC for discontinuity generation, with the same size and orientation distributions used to calculate them by intersection counting (method proposed in section 4.3.2). As described by approach (1) in step **III** (Fig. 4.4), a single DFN model can be created using consecutive values of P_{32} from different tunnel sections. For example, the section between 130 and 140 m can be created by a single 10-m-long section (or longer) for each discontinuity set or by consecutive 5-m-long sections. Fig. 4.10 shows the P_{32} values from this portion of the tunnel in detail, in which the diamonds represent the P_{32} values from different section lengths used to generate the DFNs. From the trace maps of F_1 and F_2 (Figs. 4.10a and 4.10b respectively), it is possible to see that the heterogeneity of fracture distribution along the tunnel is better represented when a sequence of sections (DFNs) is used to construct the model. However, for low intensities (small number of traces mapped in the rock face), such as the case of F_3 in Fig. 4.10c, it may be better to use a single DFN generated from longer sampling planes. Note that when the N value used to calculate P_{32} is too small, the mean P_{32} obtained from the proposed method may not be representative of the tunnel section (Fig. 4.6c). Thus, longer sampling planes are generally more suitable for creating models for sections of the tunnel with lower number of discontinuities. It is important to note that the approach (1) imposes geometrical segmentations controlled by the position of the P_{32} values used along the tunnel. Therefore, certain local P_{32} variations are overlooked, as indicated by the red arrow in Fig. 4.10a.

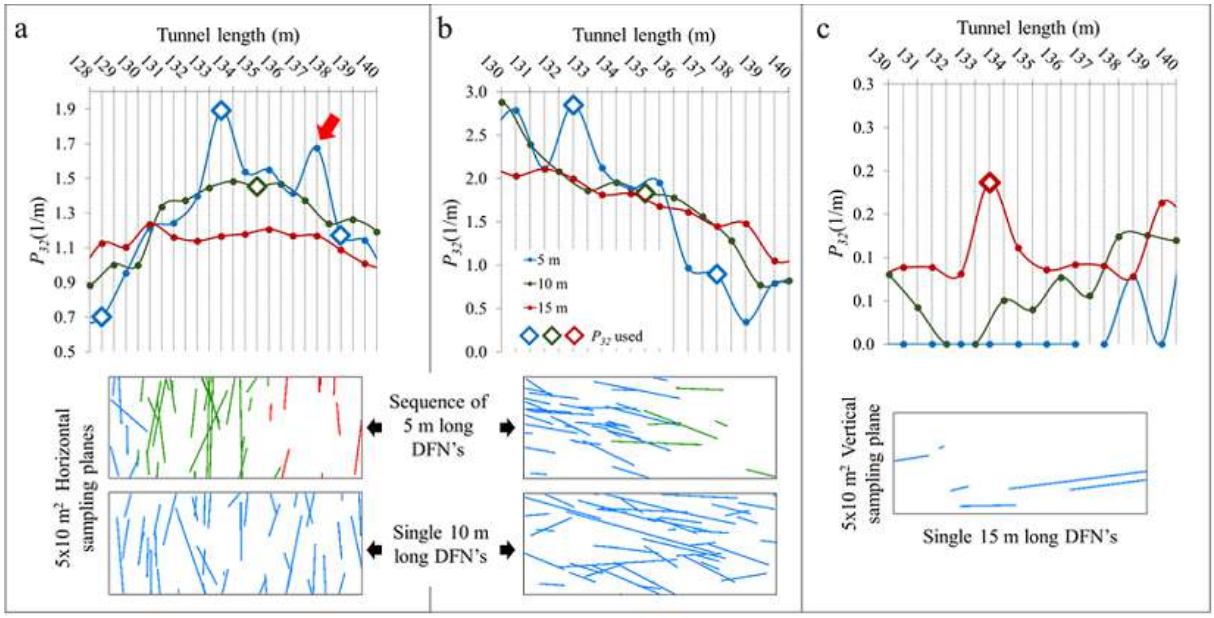

Fig. 4.10. Differences between the resulting trace maps from models generated using a single DFN or a sequence of DFNs. **a** F_1 set; **b** F_2 set and **c** F_3 set. Diamonds represents the P_{32} values used to generate DFNs and the red arrow indicate a P_{32} value overlooked by approach (1).

Using approach (2), described in step **III**, P_{32}^{i} values are calculated for each meter of the tunnel using the P_{32} curves presented in Fig. 4.9. Thus, the same P_{32} variation along the tunnel is maintained (with $Er\ (i) \leq 0.1$ in this case), and it is possible to build single and continuous DFNs for the entire tunnel for each discontinuity set. Fig. 4.11a shows an example of the continuous DFN from F_1 fractures using the 5 m curve (Fig. 4.9a), obtained by approach (2). Fig. 4.11b shows the comparison between P_{32} values from the sequence of DFNs (approach (1), described in step **III**) and the P_{32}^{t} calculated in the same positions (every 5 m) using the continuous DFN (Eq. 4.4). Despite the small differences between the red and blue lines in Fig. 4.11b, the volumetric intensities from samples taken every 5 m in both approaches are similar. However, using approach (1), the discontinuity positions are homogeneously distributed inside each 5 m of the tunnel (using fixed P_{32}, discontinuity size and orientation distributions of each section selected). Using approach (2), the variability of P_{32} is maintained; thus the continuous DFN better represents the heterogeneity of the fracture distributions along the tunnel (varying P_{32}^{i}, discontinuity size and orientation distributions meter by meter).

To verify the quality of the DFNs generated, it is important to compare 2D features in the model with the real trace from the TLS mapping. The methodology proposed herein is based on

comparing results of P_{32} from rock faces (tunnel regions) of different orientations and taking the highest value as a reference (reference region) for the given tunnel section being evaluated. Thus, the comparison between the DFN model and the real trace data was performed using 2D rectangular planes with the same size and orientation of the reference regions (R, WW or EW) in each tunnel position. The parameter used here to compare the DFN models and trace data was the P_{21}, which was also automatically calculated, using the TLS mapping, for any position of the tunnel and any rectangular window length.

The low number of discontinuities in certain sections of the tunnel inherently increases the uncertainty of the mean P_{32} calculated (Figs. 4.6c and 4.6d). Thus, P_{32} curves obtained from longer tunnel sections (i. g. 15 m curves in Fig. 4.9) are preferred to create DFNs in these cases, noting that it may ignore some small intensity variabilities along the tunnel. To compare P_{21} from DFN and TLS and validate the methodology, the continuous DFNs were generated using the 5 m curve of Figs. 4.9a and 4.9b for F_1 and F_2, respectively. For F_3, the 15 m curve of Fig. 4.9c was used because of the low intensities (low number of fractures) of this set along the entire tunnel. It is important to note that it is difficult to create a 3DEC block model using large continuous DFNs (such as in Fig 4.11a) and it could not be used for most applications, due to hardware and software limitations. Therefore, the P_{32} curve used for each discontinuity set can be different for each tunnel section selected. For example, the number of F_2 discontinuities is constantly low between 30 and 80 m (Fig 4.9b); thus, the continuous DFN could be created using the 15 m P_{32} curve in this case.

Fig. 4.12a shows comparisons between the DFN and TLS trace intensities. The TLS line (black line) represents a single set of data, with one sample for each meter of the tunnel (from the reference region), using a 5-m-long rectangular window for F_1 and F_2 and a 15-m-long rectangular window for F_3. The DFN line (red dashed line) is the mean P_{21} of 10 realizations obtained in a rectangular sampling window with the same size and orientations as those of the reference regions in TLS for each tunnel position. In each realization, one continuous DFN (Fig. 4.11a) was generated for each discontinuity set to compute P_{21} along the tunnel. The standard deviation of these 10 realizations was also calculated for every tunnel position (Fig. 4.12a).

Fig. 4.12a verifies that the P_{21} from DFN follows the same trends as those of the TLS and, in most cases, the P_{21} from TLS is within the range (mean+s.d./mean-s.d.) of the P_{21} obtained with DFN. In these cases, it is possible to assume that the P_{21} of TLS traces could be obtained with

one DFN realization of the method proposed in this work. In most cases in which the TLS P_{21} falls outside the DFN range, the P_{21} value from DFN is overestimated. Thus, the P_{32} intensity of the model is also probably overestimated, but it would not be unsafe to keep this value for 3DEC block model generation. However, in cases in which the DFN P_{21} is underestimated, the discontinuity geometrical parameters (size and orientation) and the tunnel section length (window length) used to continuously calculate P_{32} (curves in Fig. 4.9) should be reevaluated before generating the 3DEC block model.

Fig. 4.12b shows the trace maps of the three regions of the tunnel from TLS and the 10th DFN realization. Comparing both trace maps, it is possible to verify the similarity of trace distributions along the tunnel. However, it is worth highlighting that the DFN was generated with the highest P_{32} between tunnel regions for each tunnel position. Thus, a DFN trace map is expected to appear more fractured than the TLS trace map.

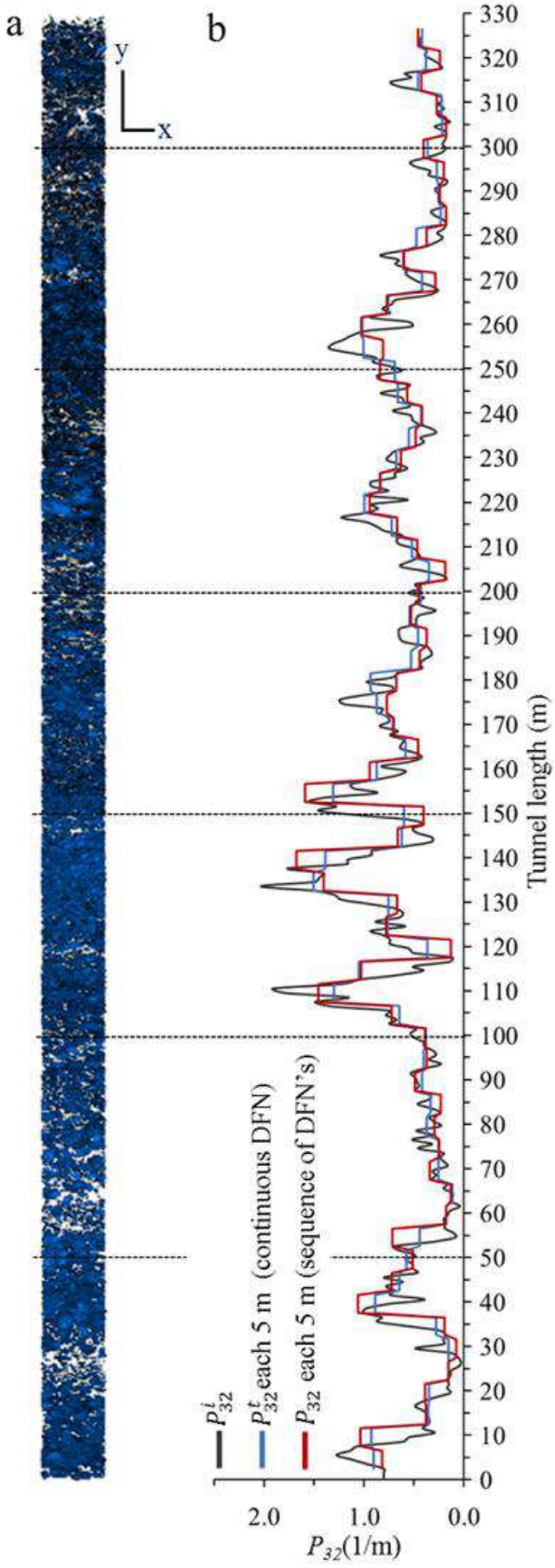

Fig. 4.11. a Continuous DFN of F_1 set. **b** Comparison between P_{32} from the sequence of DFNs and P_{32}^{t} from the continuous DFN of F_1 set.

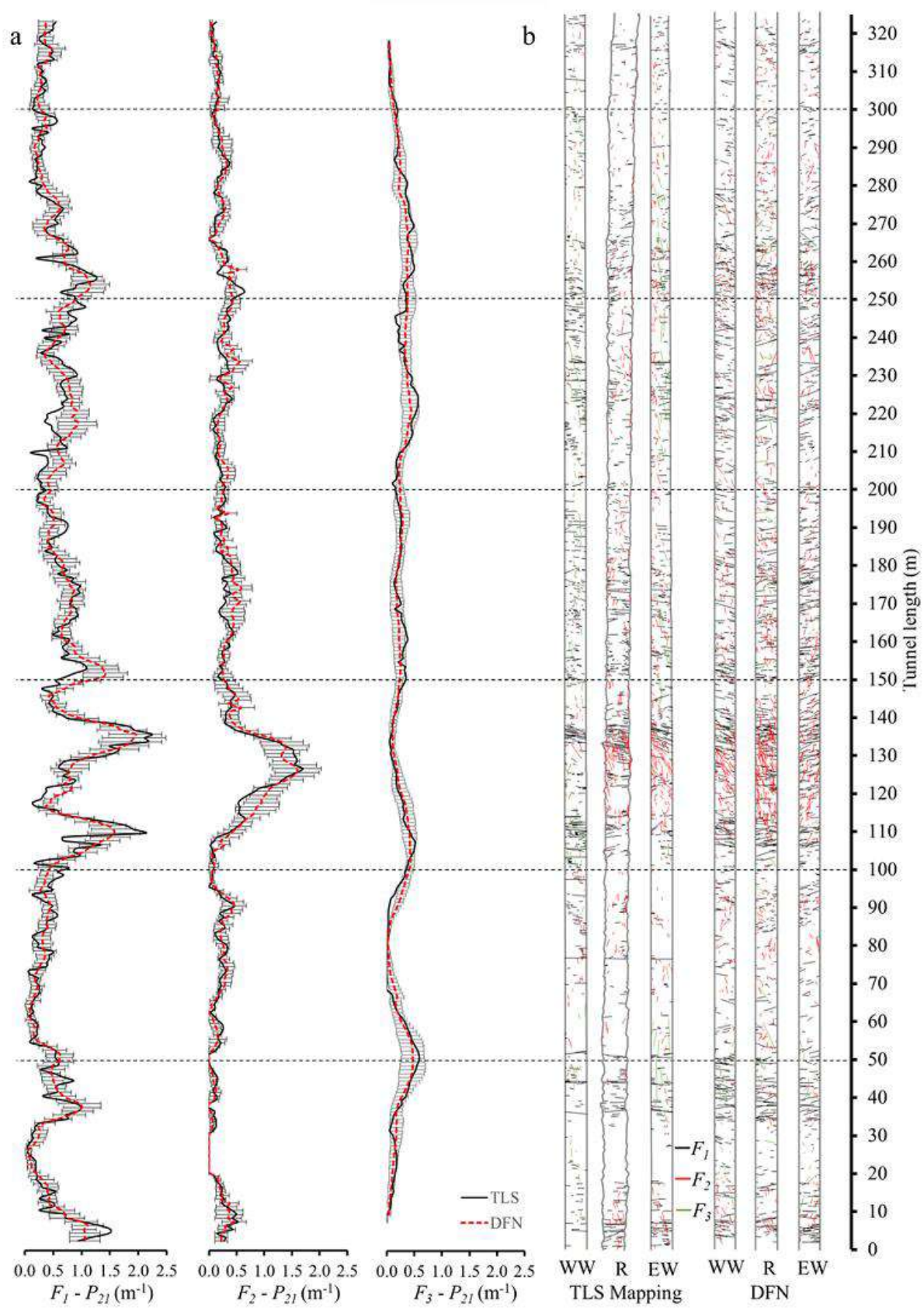

Fig. 4.12. a Comparison between P_{21} and **b** trace maps, obtained from TLS and DFN generation (Scale in trace maps: 1V=1.5H). F_1 traces in black; F_2 in red and F_3 in green.

4.4.3 3DEC block model generation

For shallow tunnels, it is important to include the bedrock and ground surface in the model. These features were created using the topographic contours (for the ground surface) and interpreted geotechnical surveys (for the bedrock), indicated in Fig. 4.1. These geotechnical surveys (including eight geoelectrical imaging profiles and three drilling boreholes) were analyzed in Cacciari (2014), and only the resulting bedrock DXF surface interpreted is presented here. The DXF files were created using the Rhinoceros 5.0 software (McNeel 2014) by the interpolation of data points. Fig. 4.13a shows these surfaces crossing the 3DEC model. The model was cut by these features using the DENSIFY command and new geometry logics available in 3DEC 5.0. The final model (first 324 m of the tunnel) is presented in Fig. 4.13b.

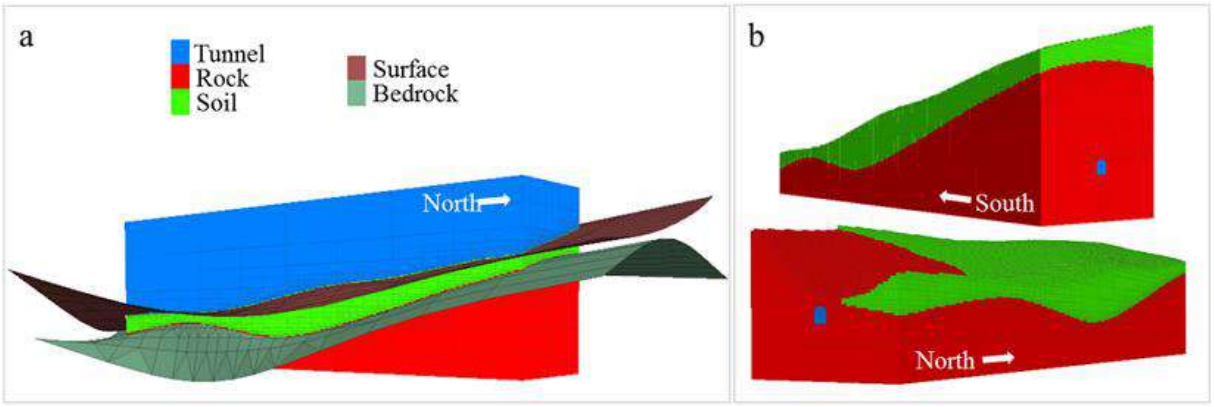

Fig. 4.13. a Bedrock and ground surfaces cutting the 3DEC model. **b** Final model with the soil and rock layers and the tunnel position.

In 3DEC, the blocks are generated by intersecting the discontinuities cutting the model. By the program logic, all the discontinuities must end forming a block. Thus, when a given discontinuity (with a given orientation and diameter) is inserted in the model, the program selects and cuts only the already existing blocks in contact with this discontinuity. However, when the first discontinuity set is inserted in the model, there is only one block to be cut; thus, part of its planes will become persistent. Therefore, in cases in which one of the discontinuity sets in rock mass is considered persistent (as the rock foliation here), it should be the first to be inserted in the model.

Foliation (S_n) is a geological structure formed by layers with different mineralogical compositions. After the tunnel construction, there must be several S_n planes that were not exposed in the rock face. However, it is reasonable to assume that the exposed S_n planes are the weakest between them, and they can be used to estimate the S_n intensity. Here, we used scanlines (Priest 1993) fitted in the point cloud (Fig. 4.14a) to obtain S_n linear intensity (P_{10}). The linear intensity is obtained by dividing the number of S_n planes (N_l) cutting both the tunnel roof (L_R) and one of the walls (L_w) by the total scanline length (L_T). To avoid data redundancy in S_n frequency, only one of the two walls is sampled with scanlines (redundancy area in Fig. 4.14a). A scanline with the same position and orientation is introduced in the model, and the S_n persistent planes are generated until the same P_{10} measured in TLS is obtained (Fig. 4.14b).

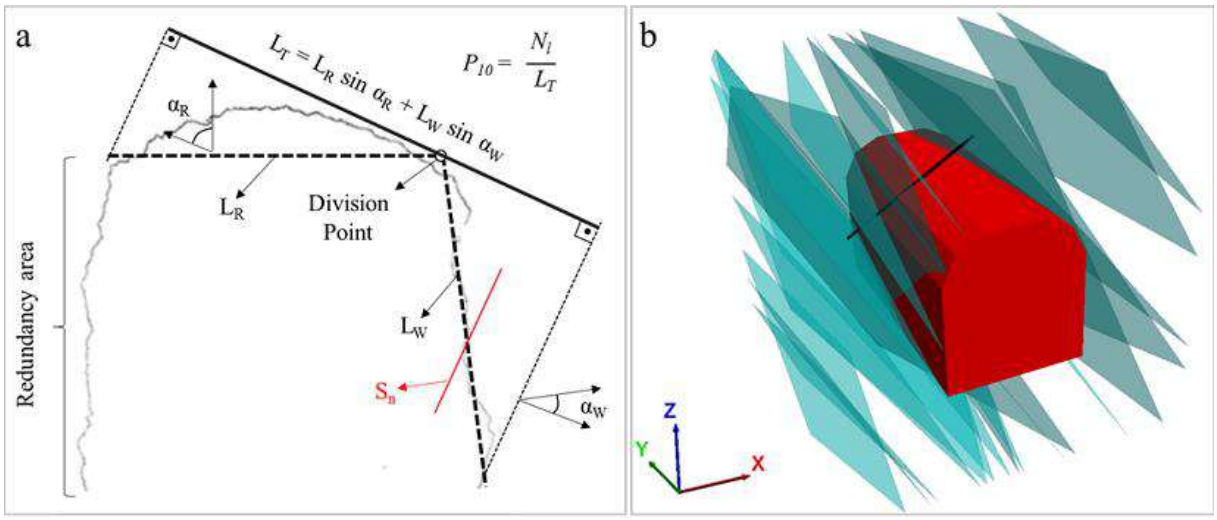

Fig. 4.14. a Scanlines used to find P_{10} in TLS images. **b** Virtual scanline inserted in the model to use P_{10} as PTC.

The methodology proposed allows the generation of block models with any section length and position between the scanned and mapped portion of the tunnel. The continuous DFNs generated for F_1, F_2 and F_3 can be directly used to cut the model and to create blocks. Fig. 4.15 shows 3 examples of block models from different positions of the tunnel with different DFN characteristics and bedrock/surface geometries. S_n planes were generated using the mean P_{10} value from 3 scanline samples for each section. Blocks were generated only in the center of the models to reduce the time consumed to obtain these examples.

The examples in Fig. 4.15 show that it is possible to create block models containing the important characteristics of each position of the tunnel using this DFN-3DEC approach. In the model in Fig. 4.15a, for example, the P_{32} for all discontinuities sets are moderate, but the tunnel is extremely shallow in this area, justifying further stability analysis. The section between 125 and 135 m (Fig. 4.15b) has the highest F_2 and $F_1 + F_2 + F_3$ volumetric intensities of the entire tunnel. Moreover, the bedrock surface dips steeply in this area, resulting in a great variability in the soil thickness. On the other hand, the tunnel section between 250 and 260 m (Fig. 4.15c) also has some high discontinuity intensities, but the bedrock surface may not play a significant role in the tunnel stability.

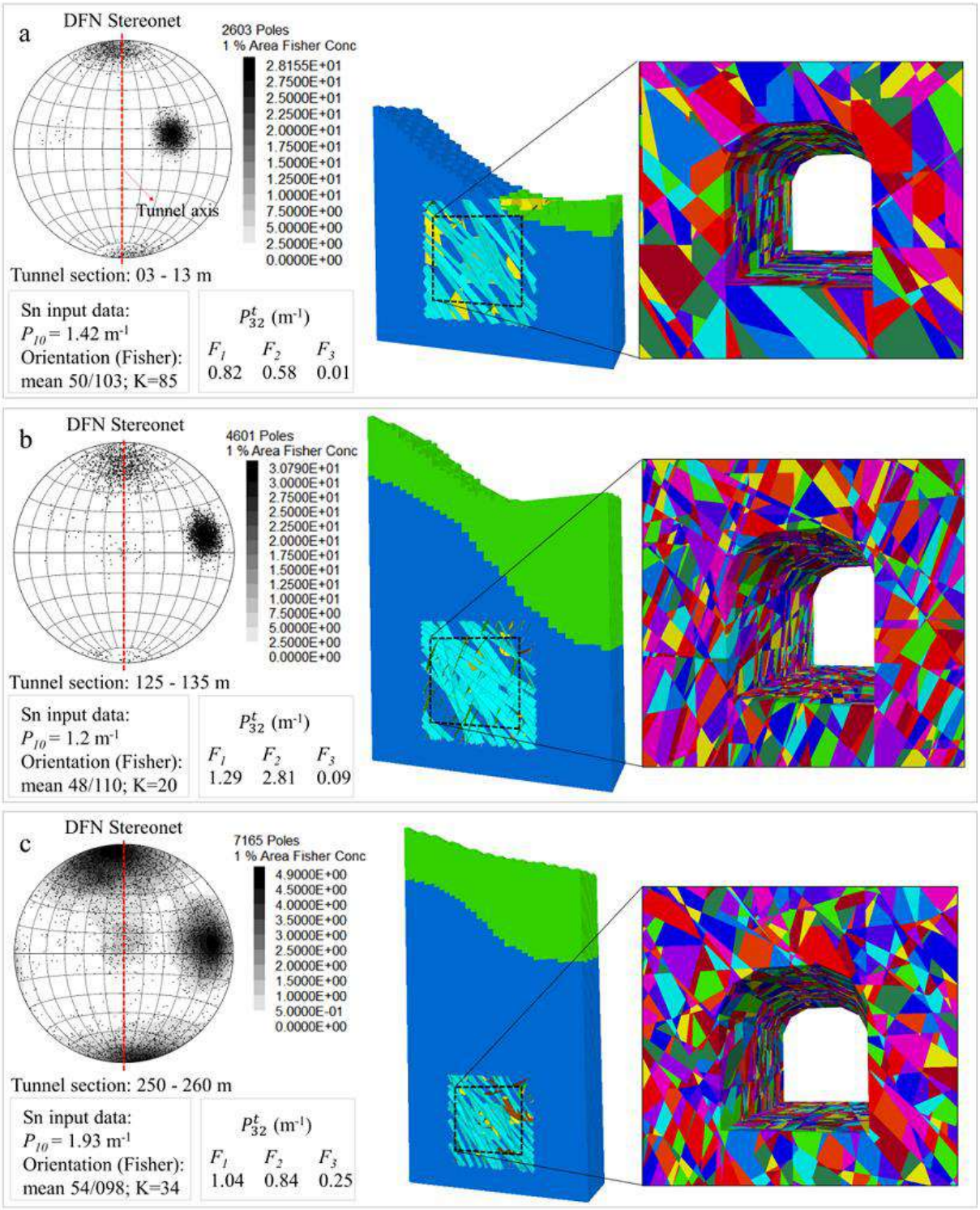

Fig. 4.15. Examples of block models generated with DFNs (equal area and lower hemisphere stereonets) from different sections of the tunnel. **a** Section between 03 and 13 m; **b** section between 125 and 135 m and **c** section between 250 and 260 m.

4.5 Discussion

The methodology developed here can be applied to the uncovered rock tunnels along Brazilian railways and roads to find zones of high discontinuity intensity, to evaluate each set separately, and to generate 3DEC block models to perform stability analysis. The manual discontinuity mapping using TLS images can be arduous and time-consuming work. However, with previous visual inspection in the field, it is possible to pre-select only critical portions of the tunnel and to reduce the number of images to be mapped.

Laboratory tests are being performed to characterize the mechanical behavior of the intact rock and discontinuities of the Monte Seco tunnel, mainly regarding the rock foliation strength under different weathering conditions. Stability analysis with 3DEC block models generated by the present methodology will be performed with the support of results from laboratory tests and will be published in future works.

The rock foliation has some characteristics that must be taken into account to generate DFNs and block models. In addition to the size and spacing issues mentioned before, the variability in the orientations of rock foliation may be more related to the waviness of such geological structures. Thus, in these cases, it may be better to consider them as parallel planes and to take the waviness into account in the strength characterization.

As discussed before, it is not possible to associate one orientation measurement to every trace mapped in TLS because of the limited exposures of a great part of discontinuity planes in the tunnel rock face. Moreover, traces mapped in TLS images may present high rake variabilities, as indicated in Fig. 4.3. Therefore, one limitation of the present methodology is that every trace must be assigned to a discontinuity set during TLS mapping, without using automatic clustering analysis. This fact increases the importance of having reliable conventional field mapping to support the TLS mapping to assist the geologist's judgments.

Here, we directly used the Fisher distributions for the orientation data without applying goodness-of-fit tests. This decision was based on two factors: Visually, only the F_3 orientation data (Fig. 4.8) appear to follow an anisotropic distribution (with greater variability in dip and less variability in dip direction); and the number of orientation data in tunnel sections was insufficient to define different local orientation distributions. Thus, we simplify the orientation analysis by assuming Fisher distributions for all the tunnel sections. Moreover, the Wu et al.

(2011) method applied to estimate μ does not require the definition of the orientation distribution form.

The good correlation between P_{21} from TLS and DFN (Fig. 4.12) indicates that the method used to calculate volumetric intensities (using N) is representative once the discontinuity diameters and orientations are well defined. In cases in which the P_{21} correlation is unacceptable, mainly when it indicates unsafe results (DFN P_{21} lower than TLS P21), the discontinuity analyses (of the orientations and trace lengths) should be reassessed. The continuous DFNs generated in this way better represent the heterogeneity of discontinuity distributions along the tunnel (in the tunnel axis direction), making this methodology a practical alternative that increases similarities between TLS mapping and DFN-3DEC models, an important factor in stability analyses of shallow tunnels constructed in fractured rock masses (such as the Monte Seco tunnel).

Unlike P_{21}, the P_{32} values obtained from different rock face orientations allow comparison between results without concern for the orientation bias (Terzaghi 1965). However, in artificial outcrops, such as tunnels, the presence of visible traces does not depend solely on geometrical discontinuity parameters and the rock face orientation. As described in section 4.2, other parameters related to the tunnel construction methods and discontinuity strength also influence the geological mapping results. Moreover, specifically in railway tunnels with diesel train traffic (such as VMR), the excess soot in the tunnels (mainly in the roof) hinders geological mapping by hiding discontinuity traces with poorly exposed areas. Considering these difficulties, it is not possible to assume that all the samples from different rock face orientations are representative for a given tunnel section. Thus, the maximum P_{32} values (among EW, WW, and R) were taken here instead of P_{32} averages, considering that these averages could be reduced by factors not related solely to the geometrical parameters of discontinuities.

Currently, linear or areal intensity measurements (P_{10}, P_{21} or similar) are often used in engineering practice for tunnel stability and support assessment purposes, especially when rock mass classification systems are used for empirical support design. However, the intensity parameters alone do not describe the true fracture intersection density, rock bridge content and hence cannot be used to assess unstable rock blocks in tunnels. Therefore, methodologies integrating DFN and discontinuous numerical methods (such as presented herein) are suitable and could be used more frequently, especially for rock masses containing three or more discontinuity sets with different geometrical and strength characteristics.

Fekete et al. (2010) discussed several advantages of using TLS for as-built controls during tunnel construction. Discontinuity mapping is time-consuming work when an entire tunnel is going to be evaluated. However, once the TLS imaging becomes a daily task and the tunnel discontinuity mapping is continuously updated (for each excavation advance), the presented methodology becomes a practical and powerful tool. Taking the Monte Seco Tunnel as an example and considering a hypothetical excavation front in 129 m of the tunnel (Fig. 4.16a), the discontinuity mapping at this position would be that presented in Fig. 4.16b. After a tunnel advance of, say, 3 m, the discontinuity mapping would be updated (Fig. 4.16b), as would the discontinuity analysis, leading to updated DFNs. The block model of this excavation front example is presented in Fig. 4.16c. In real situations, the excavation front would also be mapped and used as a region to perform the discontinuity analyses in step **I**.

The time needed for the stability analysis depends on several factors, such as the type of 3DEC model (rigid or deformable blocks), the number of blocks (or zones), the size of the model, and the criteria used for convergence (number of steps, block maximum displacements or velocities; maximum unbalanced forces, etc.). However, with the present computer technology, the authors believe it is possible to update the geological mapping to automatically generate the 3DEC model and to perform the stability analysis using the period of time between the tunnel advances and the support installation (for drill and blast tunnels). Thus, the methods would be useful for verifying whether the support used is appropriate and for predicting the stability state of the next advance, considering the rock mass in conditions similar to the previous advance.

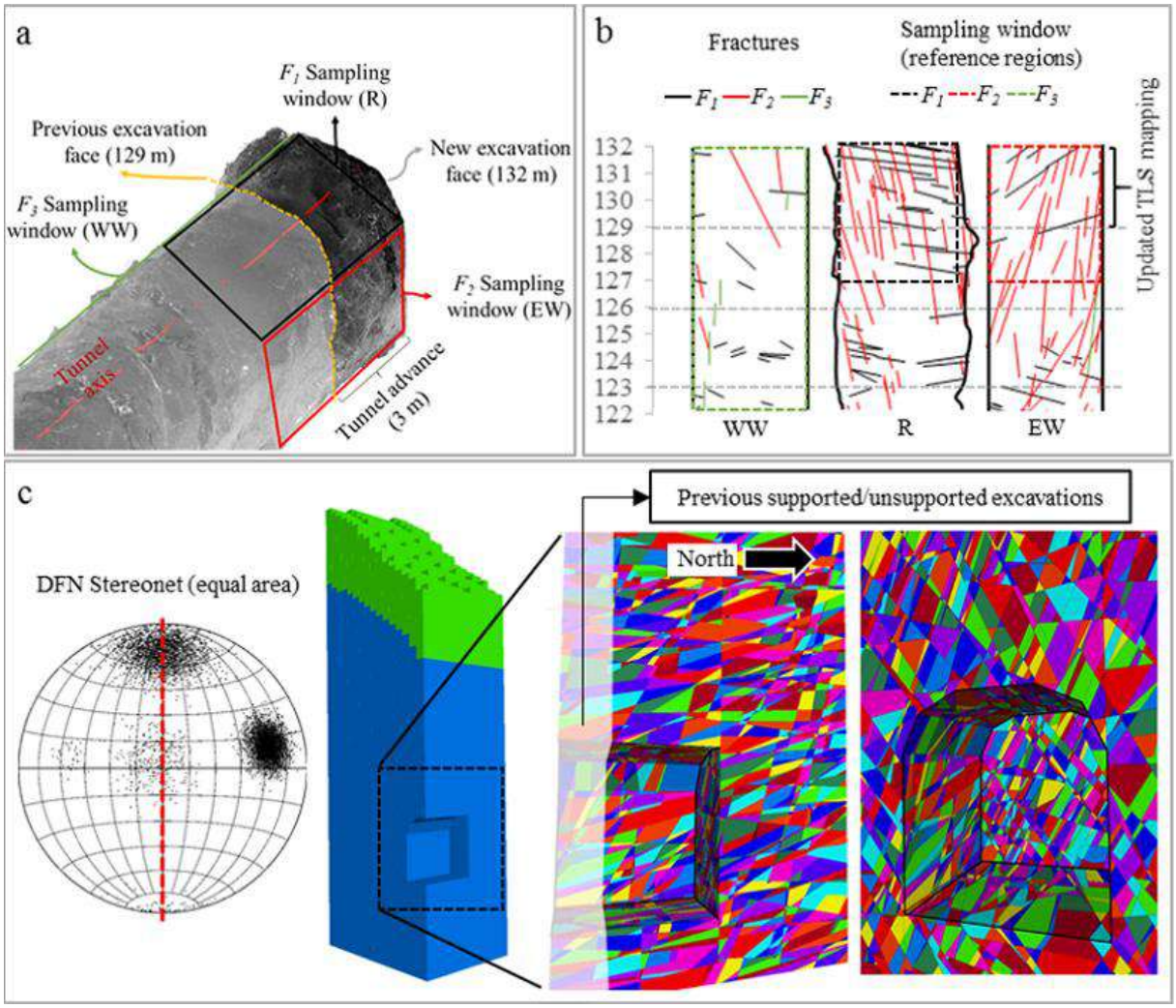

Fig. 4.16. a Hypothetical position of the excavation front with the sampling planes used for each discontinuity set. **b** Updated trace map with fitted sampling planes from each representative region. **c** 3DEC block model of the hypothetical excavation front.

4.6 Conclusions

The following summary and conclusions can be provided for the study conducted:

1. TLS is a suitable tool for discontinuity mapping in tunnels because it allows the same level of detail in all the regions of the tunnel. However, care must be taken when selecting the longest traces contained in discontinuity planes (Fig. 4.3) to represent the chords of disk-shaped discontinuities in DFNs. Moreover, it is not possible to attribute one orientation value to every trace length measured if many of the discontinuities apparent in the tunnel have insufficient exposed area for a reliable orientation measurement.

2. The discontinuity size analysis in this work is based mainly on the Kulatilake and Wu (1984), Zhang and Einstein (2000) and Wu et al. (2011) methods for unbiased trace length and discontinuity size determination. These methods were considered more suitable for discontinuity size determination in tunnels, mainly due to the variability in rock face orientations (Cacciari and Futai 2016b).

3. All the discontinuity analyses were automatically performed, and P_{32} was automatically calculated along the tunnel using Excel and Visual Basic integrated with DFN-3DEC-FISH codes (Itasca 2014). The method proposed to calculate P_{32} (based on the number of traces intersecting rectangular sampling planes) showed good results when compared to the Dershowitz and Herda (1992) method; however, it is more efficient and suitable for automatic analysis and computational implementations. Moreover, it is possible to evaluate the variability of P_{32} and to check whether the mean value is representative for use as PTC for new DFN generations. The variability in rock face orientations in the tunnel was taken into account by comparing their P_{32} results and taking the highest value as a reference for each tunnel section.

4. A computational approach for generating single and continuous DFNs was developed and applied to 324 m of the Monte Seco tunnel. Comparison of P_{21} values was used to verify good agreement between the P_{21} values obtained from TLS mapping and the DFN models generated for each discontinuity set. Continuous DFNs are a practical alternative that better represent the heterogeneity of discontinuity distributions along the tunnel (in the tunnel axis direction) and increase similarities between TLS mapping and DFN-3DEC models.

5. 3DEC block models were generated for 3 sections of the tunnel, with distinct DFN, ground surface and bedrock characteristics. These examples show the applicability of the present study for modeling shallow tunnels constructed in fractured rock masses. Moreover, the same method can be used in several other tunnels along Brazilian roads and railways under conditions similar to those of the Monte Seco tunnel.

6. Finally, an example of the present method is applied to a hypothetical tunnel excavation front, indicating that it can be promising in these cases. However, it is necessary to perform real tests to verify whether it is suitable, considering the operational difficulties in tunnel construction environments.

Chapter 5

The Influence of Fresh and Weathered Rock Foliation Planes on the Stability of the Monte Seco Tunnel

This chapter presents an article in preparation to be submitted to an international journal.
Authors: Pedro P. Cacciari & Marcos Massao Futai.

Abstract

The Monte Seco tunnel (MST) is one of several old unlined tunnels constructed for Brazilian railways in the 1950s, and the MST still receives intense train traffic (primarily for iron ore transportation). The MST was constructed in a fractured gneissic rock mass, which has potential instability problems associated with gravity-driven block falls (at low stress confinements) defined by discontinuity sets: F1, F2 and F3 fractures and metamorphic foliation. Previous geological and geotechnical surveys at the MST site have included basic geomechanical classifications from outcrops and drill core specimens, detailed terrestrial laser scanning (TLS) discontinuity mapping, geoelectrical imaging and laboratory tests. These surveys discovered two sections of the tunnel (referred to herein as MS1 and MS2) with major potential for instability problems (i.e., poor rock mass qualities). In this paper, the 3D discrete element method (DEM) was used to assess the potential stability problems in these sections with particular interest on the role of the rock foliation strength on the current stability state of these sections. Three instability indicators were developed and monitored during and after the DEM simulations: the total failed block volume (*FBV*), the average displacement of the tunnel face (*AD*), and the percentage of slipping contacts near the tunnel face (*SC*). The weathering effects were considered in two different scenarios: the occurrence of isolated weathered foliation planes (*WFPs*) and the discontinuity weathering advance through potentially weathered regions. In the latter scenario, the percentage of weathered contacts (*WC*) increased progressively. The overall results indicated that fresh foliation planes ensured the current tunnel stability due to the moderate mica content (M_a) in such geological structures. Thus, underestimating the strength of foliation planes causes unrealistic instability conditions in the tunnel. However, the weathering advance on fractures and foliation planes can trigger important instability problems over time.

Keywords: Monte Seco Tunnel; Tunnel Stability; Foliation; Weathering; DEM.

5.1 Introduction

The Monte Seco tunnel (MST) is one of several tunnels constructed for Brazilian railways in the 1950s, and the MST still receives intense train traffic (primarily for iron ore transportation). Most of these tunnels are located at shallow depths (less than 200 m), constructed in hard rock masses (granites and gneisses) and do not have bolt or liner support systems along the majority of their lengths. In the past few years, new safety requirements have been implemented, and some of these tunnels, including the MST, showed the need for advanced stability analyses using modern tools, such as terrestrial remote sensing, discrete element modeling, and geophysical prospecting. In this scenario, the MST became a laboratory tunnel that is currently being used by the GeoInfraUSP group for multiple rock mechanics and engineering geology purposes, including terrestrial laser scanning (TLS) mapping and analyses (Cacciari and Futai 2016b, 2017), geophysical prospecting and weathering advance studies (Monticelli 2019).

The MST was constructed in a fractured gneissic rock mass, which has potential instability problems associated with gravity-driven block falls at shallow depths (low stress confinements). These blocks are defined by different geological structures (discontinuities) on the rock mass, including shear fractures, sheet joints and gneissic banding and foliation. Considering the aforementioned geological fabric and low stress conditions, discrete models are preferred for performing tunnel stability analyses because they simulate the mechanisms of block falls, creating discontinuity-controlled overbreak patterns similar to those observed in situ. The 2D and 3D versions of the discrete element method (DEM) (Cundall 1988; Hart et al. 1988) are often used for tunnel stability analyses (Bhasin and Hoeg 1998; Ferrero et al. 2004; Vardakos et al. 2007; Solak 2009; Fekete et al. 2010; Wu and Kulatilake 2012; Fekete and Diederichs 2013; Oliveira and Diederichs 2017; Bahrani and Hadjigeorgiou 2018; He et al. 2018; Merlini et al. 2018).

The International Society for Rock Mechanics (ISRM) (1978) defined discontinuity as “the general term for any mechanical discontinuity in a rock mass having zero or low tensile strength”. In practical rock mechanics, discontinuity sets are often generalized as joint sets, regardless of the type and genesis of each geological structure. In these cases, it is usual to assume friction-based models (linear and nonlinear) to represent the mechanical behavior of discontinuities, ignoring any cohesion or tensile strength. It is important to note that the ISRM definition uses the term “mechanical discontinuity”, which are discontinuities formed by

mechanical processes, such as tectonism. Therefore, before ignoring any cohesion or tensile strength values, two aspects should be taken into account:

1 - Incipient rock bridges can provide considerable tensile strength and cohesion to nonpersistent discontinuities. Thus, the geomechanical model must consider discontinuities as finite-size planes within the rock mass.

2 - Geological structures characterized by mineralogical distribution and alignment on the rocks, such as foliation, schistosity, bedding planes, and banding contacts, are not “mechanical discontinuities”, and these structures can have considerable tensile strength and cohesion due to connection forces within mineralogical contacts. For practical rock engineering applications in blocky rock masses, such geological structures were defined as “intrablock”, whereas fractures and joints were defined as “interblock” structures (Day et al. 2017).

The first aspect listed above has been widely discussed in the literature. Usually, discontinuity analysis is used to define the probability distribution of discontinuity sizes on discrete fracture networks (DFNs). The second aspect listed above has not been discussed much in the literature, and the particular mechanical properties of such intrablock structures are often ignored. Rock foliation, for example, is a type of intrablock structure characterized by the alignment of minerals along planes during metamorphism. In this case, it is predictable that the contents of mineral types will directly affect the strength of such geological structures.

Gneisses, for example, are both heterogeneous (due to the different mafic and felsic bands) and anisotropic (due to the orientation of the metamorphic foliation). Cacciari and Futai (2019) showed the importance of the mica content in the foliation planes on the shear and tensile strength of a biotite gneiss. These authors verified that, even for foliation planes with 90% surface area covered by biotite, the tensile strength and inherent shear strength (cohesion) are not negligible, especially under low stress confinements.

In this paper, the 3D DEM is used to assess the influence of fresh and weathered foliation on the stability of the MST. The geological-geotechnical investigations on the MST have included basic geomechanical classifications from outcrops and drill core specimens, detailed TLS discontinuity mapping, geoelectrical imaging and laboratory tests. These investigations have revealed two sections of the MST with major potential for instability problems due to the following characteristics: the existence of a shear zone of high fracture intensity with evidence of discontinuity weathering and the existence of an extremely shallow section of moderate

fracture intensity with evidence of discontinuity weathering. These sections were modeled using a coupled TLS-DFN-DEM approach with particular interest on the role of the rock foliation strength on the actual stability state of these sections. Moreover, different weathering scenarios were simulated based on the observations from the aforementioned geological and geotechnical investigations.

5.2 DNF-DEM modeling methodology

Cacciari and Futai (2017) developed a coupled TLS-DFN modeling methodology for creating continuous DFNs (C-DFNs) from TLS discontinuity mapping along tunnels. This methodology is based on full discontinuity orientation, trace length and position mapping on TLS point clouds and automatic application of window sampling methods to obtain the probability distributions of discontinuity geometrical parameters and create C-DFNs.

The flowchart in Fig. 5.1 summarizes the aforementioned methodology, which starts with TLS mapping of discontinuity orientations, trace lengths and endpoint positions apparent in the tunnel (I). Next, discontinuity analyses by window sampling methods are performed continuously and automatically along the tunnel to obtain the probability density functions (PDFs) of discontinuity diameters and orientations (II). A 3DEC-Fish (Itasca 2014) code uses the discontinuity analysis results to generate DFNs and continuously calculate the mean volumetric intensity (P_{32}) along the tunnel (III). Finally, the continuous P_{32} and the PDFs of the discontinuity diameters and orientations are used to create the C-DFNs (IV). This process is performed separately for each discontinuity set (for more details, see Cacciari and Futai 2017).

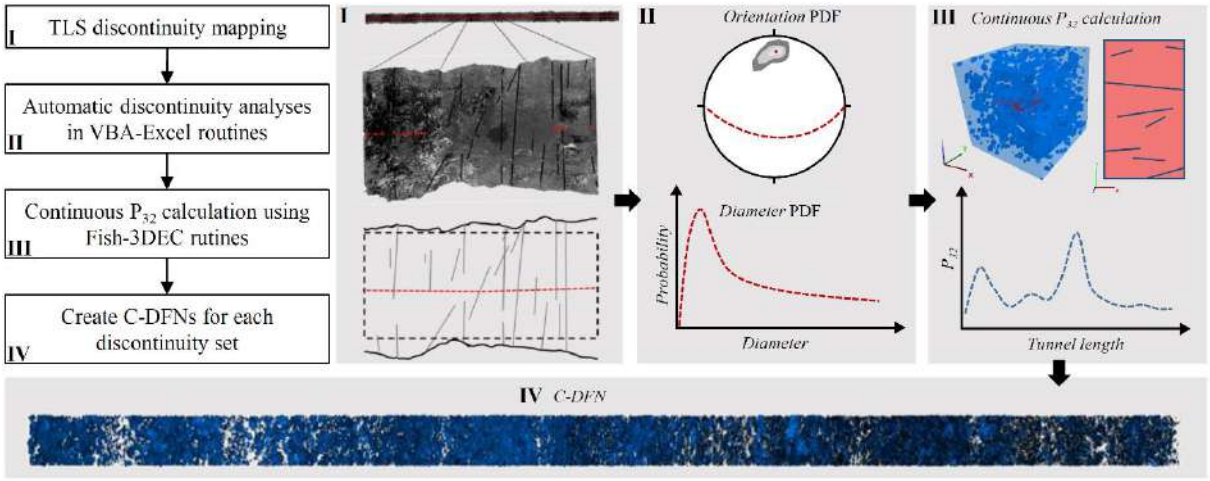

Fig. 5.1. Flowchart of the methodology developed by Cacciari and Futai (2017) used herein to create the C-DFNs of the MST.

After obtaining the C-DFNs, DEM models were created by the 3DEC cutting logic, which selects and separately cuts only the blocks in contact with each discontinuity (from the largest to the smallest). The rock foliation was assumed to be persistent because it may be inappropriate to estimate a mean trace length (and discontinuity diameter) from TLS images in this case, considering the genesis of such geological structures (Cacciari and Futai 2016b, 2017). Moreover, the orientation and spacing were considered deterministic for foliation planes, based on mean linear frequencies and attitudes measured in the TLS point cloud (Cacciari and Futai 2017). Therefore, the cutting process started with the foliation planes, followed by the C-DFNs according to each disc-shaped discontinuity diameter. The bedrock and surface topographies are also included in the DEM models.

5.2.1 Initial under- and over-break condition

Drilling and blasting cause excavation damage to tunnels, leading to irregular under- and overbreak geometry. In several cases (such as the MST), the drilling and blasting design is unknown, making it difficult to estimate the extent of the excavation damage zone and the actual damage to the rock mass in terms of mechanical parameter degradation. In this case, it is not possible to create initial over- and underbreak conditions in the DEM models similar to the real tunnel by degrading mechanical parameters of discontinuities and intact rock obtained in

laboratory tests. Therefore, an alternative method is proposed to establish the initial under- and overbreak conditions based on removing blocks inside a range defined by the real tunnel boundary. This methodology is described as follows:

1 - Import the tunnel digital model as a triangular mesh into 3DEC (Fig. 5.2a);

2 - Create microscopic disc-shaped planes inside each triangle of the tunnel mesh (the discs must have the same orientation as the triangles and should not be larger than the triangle) (Fig. 5.2b);

3 - Cut the blocks touching the discs and group the blocks inside the tunnel boundary (Fig. 5.2c).

The final appearance of the DEM model is exemplified in Fig. 5.2d, wherein the geometry is almost identical to that in the TLS digital model. The same method can be applied to any type of surface, such as natural slopes and open pits.

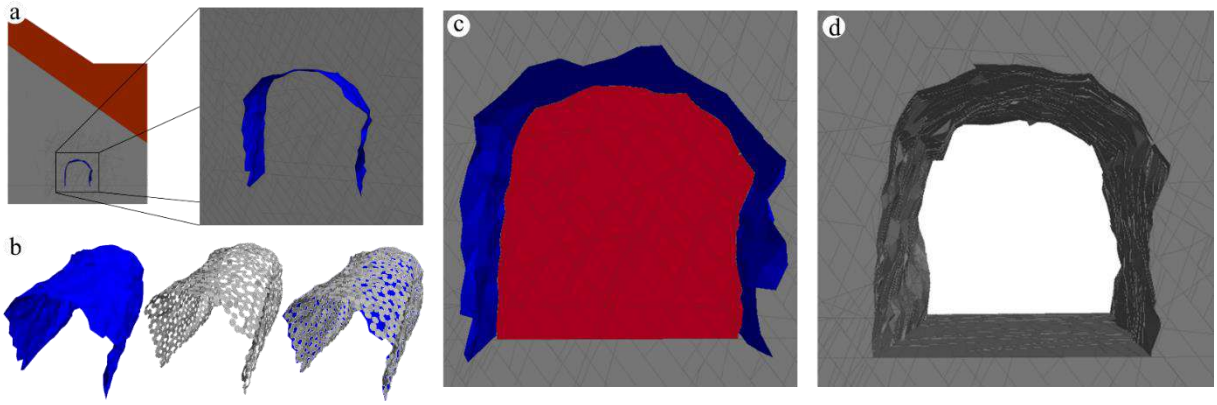

Fig. 5.2. Computational process used to create initial under- and overbreak conditions in DEM models of tunnels.

It is important to note that this methodology reproduces the actual irregular geometry of the tunnel, which modifies the stress distributions along the excavation boundary. However, the extent of the damage inside the rock mass caused by drilling and blasting remains unknown. It is important to note that the regularly designed shape (horseshoe, circular, etc.) for tunnels in blocky rock masses under low stress conditions (such as the MST) is hardly achieved after

drilling and blasting. Thus, the DEM simulation of such cases should not start with the designed excavation geometries because the stress arching effect associated with such regular shapes can affect the results of DEM simulations.

5.3 Case study: Monte Seco tunnel

The MST is located in Espirito Santo State in southeastern Brazil (Fig. 5.3) and is part of the Vitória-Minas Railway, which is responsible for most of the iron ore transportation in the country. The tunnel was excavated from gneissic rock of the Nova Venécia Complex in the northern portion of the Mantiqueira Province, which is part of the Araçuaí orogenic belt. The local structural fabric is composed of four discontinuity sets: gneissic foliation (parallel to the gneissic banding), shear fractures (F1 and F2), and sheet joints (F3). The rock is a paragneiss composed of quartz, plagioclase, alkaline feldspar, biotite, cordierite, hypersthene, and garnet (from the highest to the lowest content).

The MST has been used as a model for some rock mechanics studies, including TLS mapping (Cacciari and Futai 2016b), DFN-DEM modeling (Cacciari and Futai 2017), laboratory tests, and geophysical and drilling borehole surveys (Monticelli 2019). More recently, a conceptual model for the weathering advance through discontinuities into the tunnel has been developed by correlating multiple regional and local geological aspects with geoelectrical imaging profiles and TLS mapping (Monticelli 2019). In this case, two sections of the tunnel (named MS1 and MS2) showed potential for instability problems. Fig. 5.3 shows the geographic locations of MS1 and MS2 in the MST and the positions of the geoelectrical imaging profiles and drilling boreholes. Next, the important aspects of MS1 and MS2 are described in detail.

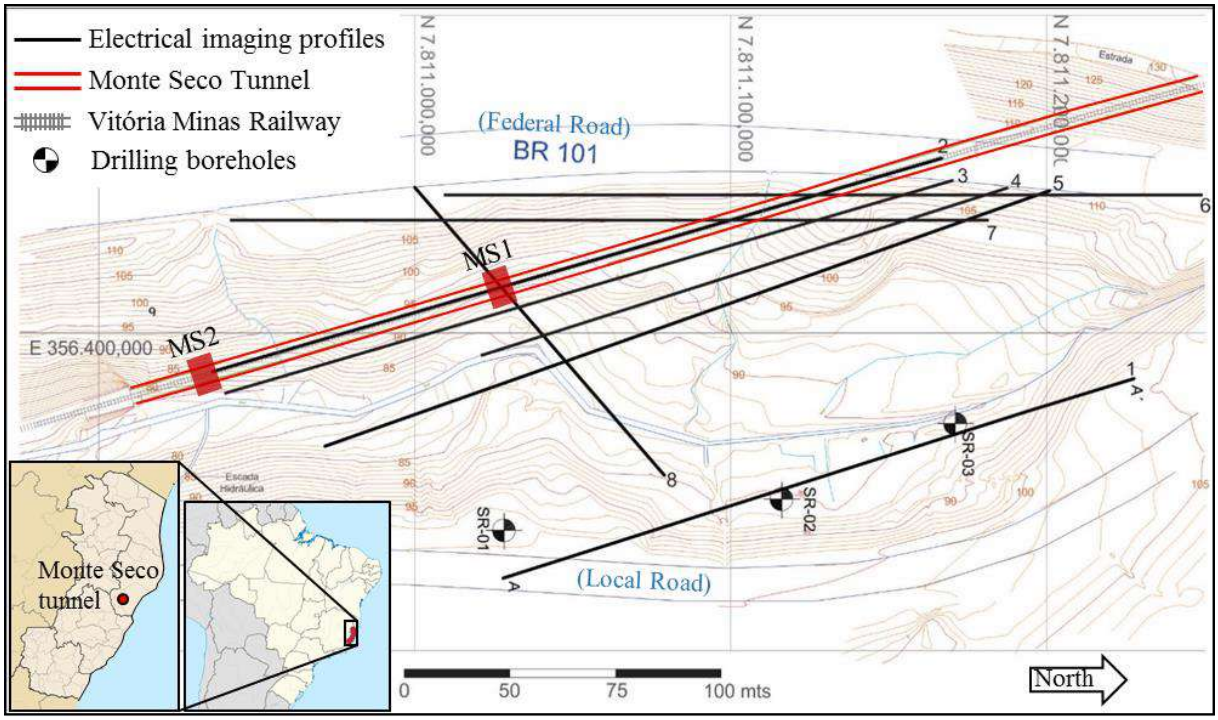

Fig. 5.3. Locations of MS1 and MS2 in the MST and the important geotechnical investigations at the tunnel site (Cacciari and Futai 2017).

MS1: This section crosses an *F2* shear zone, corresponding to a high total P_{32} (*F1 + F2 + F3*) along the tunnel (Fig. 5.4). The overburden of MS1 varies from 30 to 20 m, and the bedrock dips steeply in the ENE direction. The bedrock was defined by an association of drilling boreholes and geoelectrical imaging profiles (Monticelli 2019). Both bedrock and surface geometries are simplified in the final DEM model to avoid errors caused by undesired convex blocks and excessive construction planes, which affect the DFN block cutting and mesh distribution inside the model.

The MS1 shear zone was identified in both TLS mapping and geoelectrical imaging profiles. Fig. 5.4 shows the continuous P_{32} along the tunnel obtained by Cacciari and Fitai (2017), indicating that P_{32} of *F2* abruptly increases between 110 and 140 m, where the *F2* shear zone and MS1 are located. Fig. 5.5 shows the location of MS1 on the geoelectrical imaging profile of line 2 (positioned above the tunnel axis) (Fig. 5.3), which is inside the high conductivity anomaly generated by the water flow through the *F2* shear zone towards the tunnel. Fig. 5.5b shows the TLS trace and orientation mapping of the tunnel region containing the *F2* shear zone

and MS1. Fig. 5.6a shows the wet and dripping rock face on the east wall and roof of the MS1-TLS point cloud.

Figs. 5.7a and 5.7b show the final DEM model of MS1 (5 m long), indicating the C-DFN used to create the *F2* shear zone. In this case, the rock mass above and below the *F2* shear zone was modeled using mean discontinuity parameters instead of using a unique larger DFN domain, which results in an excessively complex model and low computational performance. The thickness of the shear zone (in the NNW-SSE direction) was estimated as the maximum perpendicular distance of the traces mapped on the roof of the tunnel.

MS2: This section is located 20 m ahead of the south entrance of the tunnel after the end of the structural concrete liner, which was most likely used to support the soil and soil-rock transition at the beginning of the excavation. From Fig. 5.4, MS2 shows a small P_{32} peak, but this peak is not much different from the other regions of the tunnel (e.g., 150-160 m and 250-260 m). However, MS2 is particularly interesting because it is an extremely shallow and wet portion of the tunnel that exhibits potential for advanced weathering processes. Fig. 5.5c shows the TLS trace and orientation mapping of the tunnel region containing MS2. Fig. 5.6b shows the wet and dripping rock face on the roof of the MS2 TLS point cloud. Figs. 5.7a and 5.7b show the final DEM model of MS2 (5 m long). As P_{32} is moderate and there is no specific shear zone in this section, a large C-DFN domain was used to cut the blocks in the entire MS2-DEM model.

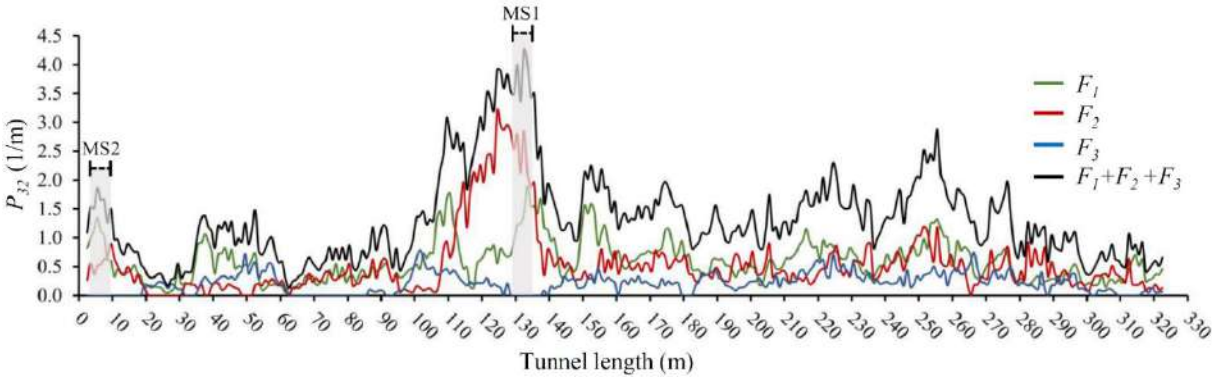

Fig. 5.4. P_{32} distribution along the MST (Cacciari and Futai 2017) and the locations of MS1 and MS2.

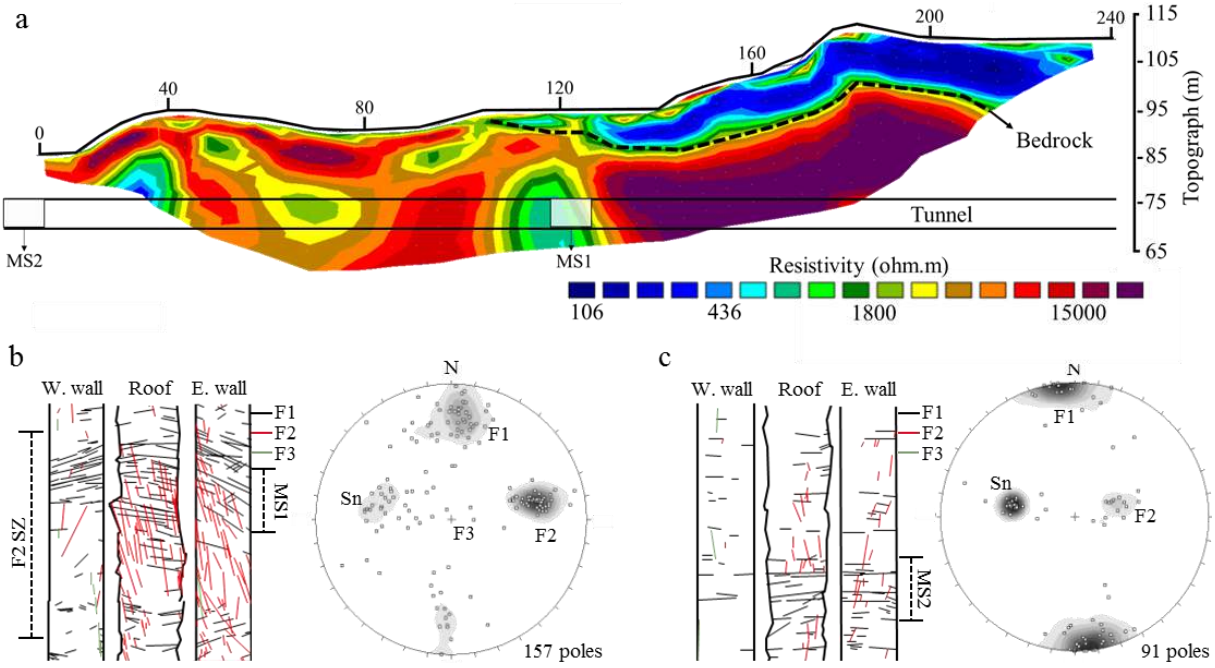

Fig. 5.5. Geological aspects of MS1 and MS2: (a) geoelectrical imaging profile of line 2 positioned above the tunnel axis (Monticelli 2019); (b) TLS traces and orientation of the tunnel region containing MS1; (c) and TLS traces and orientation of the tunnel region containing MS2. Note that Sn represents the foliation planes.

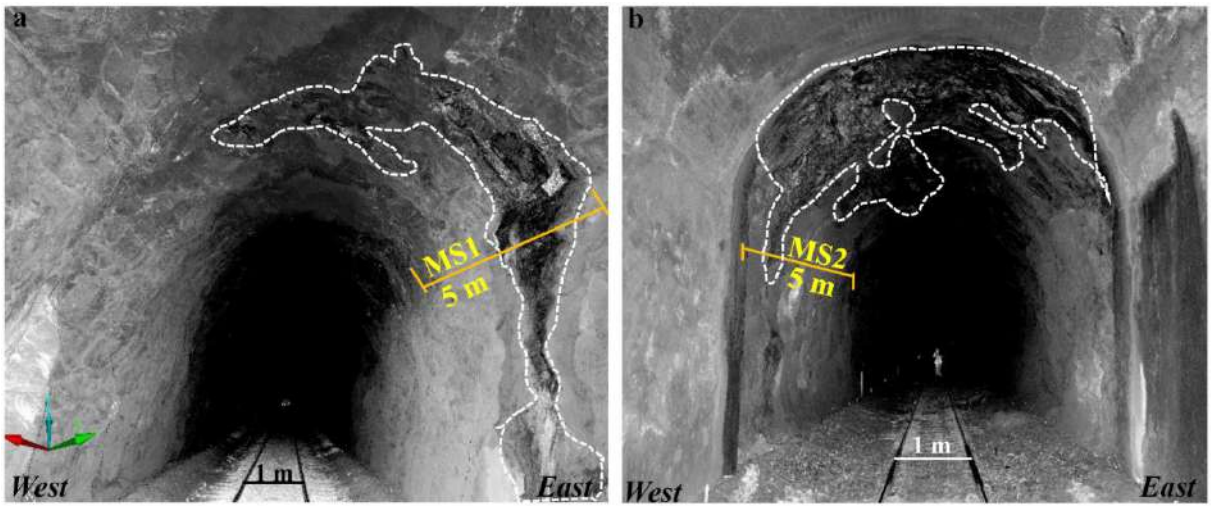

Fig. 5.6. TLS point clouds of (a) MS1 and (b) MS2, indicating the wet and dripping rock faces (white dashed lines).

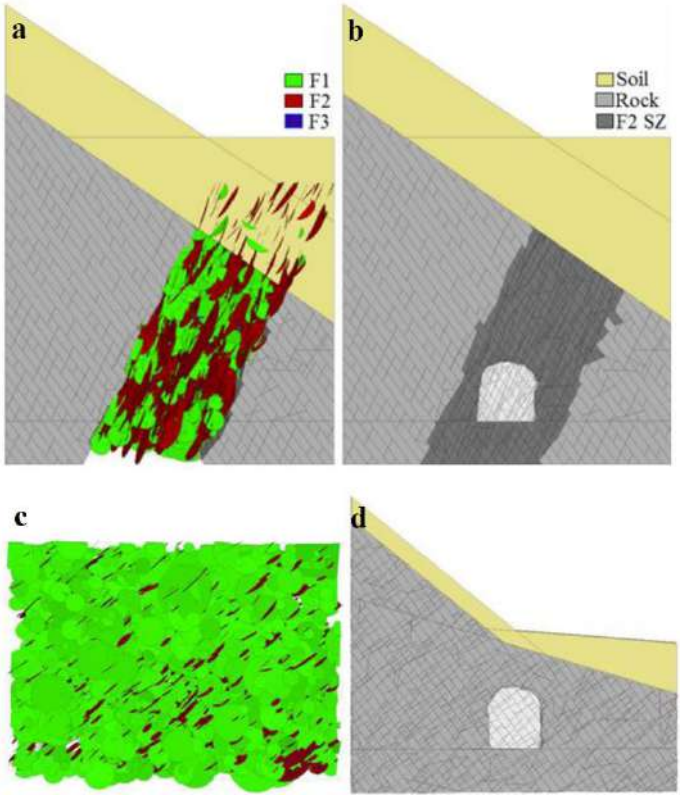

Fig. 5.7. (a and b) DFN used to create the F2 shear zone and the final DEM model of MS1. (c and d) DFN used to create the entire model and the final DEM model of MS2.

Both MS1 and MS2 were classified with the rock mass rating (RMR_{14}) (Celada et al. 2014), the rock mass quality (Q) (Barton et al. 1974) and the geological strength index (GSI) (Marinos and Hoek 2000), which was recently updated by Schlotfeldt and Carter (2018); the results are shown in Table 5.1. The ranges of each rock mass classification system are determined by the extreme discontinuity weathering conditions found on the MST. In Q and GSI, the weathering conditions are determined by the J_a parameter (Barton et al. 1974), whereas in RMR_{14}, the weathering effects are determined by the joint conditions and alterability index (I_{d2}). The P_{32} values obtained by Caccairi and Futai (2017) were used to estimate the GSI, according to the methodology proposed by Schlotfeldt and Carter (2018).

Table 5.1: Summary of the rock mass classification ranges of MS1 and MS2 for extreme weathering conditions.

MST section	RMR_{14}	Q	GSI
MS1 (fresh)	49.5 (class III)	5.57 (fair)	75
MS1 (weathered)	45.5 (class III)	1.39 (poor)	52.5
MS2 (fresh)	54.5 (class III)	5.89 (fair)	85
MS2 (weathered)	50.5 (class III)	1.46 (poor)	62.5

It is important to note that the MST was constructed in the 1950s before the development of these classification systems. Moreover, there are no documents available with details of the MST design methods and criteria, including drill and blast planning, previous geological surveys, and excavation front mapping and characterization. The only indirect information pertaining to the excavation method is the drill and blast borehole marks, which indicate that they did not follow a systematic arrangement. In addition to differences in the RMR_{14} and Q values of MS1 and MS2, both sections have the same general class (III for RMR_{14} and fair or poor for Q), which shows the lack of sensitivity of such methods for moderate differences in discontinuity intensities.

5.4.1 Mechanical properties of intact rock and discontinuities

In this study, the discontinuities are considered discrete planes that are mechanically described by the Coulomb-slip joint model available in 3DEC, which is defined by the tensile strength (σ_t), cohesion (c) and friction angle (φ). Due to the low stress conditions at shallow depths, intact rock failure is ignored, and the linear-elastic model is used for both intact rock and soil materials. As the foliation is considered a set of discrete and full-persistent planes, the elastic parameters—Young's modulus (E) and Poisson's ratio (v)—of the intact rock were taken from uniaxial compression tests perpendicular to the foliation planes (data not published). The values used in all DEM analyses were E = 48 GPa and v=0.2 for the intact rock (from laboratory tests) and E = 0.48 GPa and v=0.2 for the residual gneissic soil (inferred).

5.4.1.1 Mechanical properties of the fresh gneissic foliation and banding planes

Gneissic foliation is a planar geological structure formed by the alignment of minerals along recrystallization planes during metamorphism. In the MST, this structure is parallel to the gneissic banding (differentiation in the mafic and felsic bands), which is characterized by abrupt transitions in some portions of the rock mass creating biotite-rich contact planes exhibiting low shear and tensile strength. Fig. 5.8 shows an example of a rock block from the MST containing this structure.

Fig. 5.8. Biotite-rich banding contact.

The biotite content plays an important role in the shear and tensile strengths of gneissic foliation. Cacciari and Futai (2019) performed an extensive laboratory campaign with a biotite gneiss from the Ana Matos tunnel (also part of the Vitória-Minas Railway) and obtained a strong correlation between the shear and tensile strengths and the percentage of biotite area (M_a) after failure of the foliation planes. Moreover, these authors obtained a 3D strength envelope defined by Eqs. 5.1 and 5.2, wherein M_a is an independent variable.

$$(\sigma_t, c \text{ or } \varphi) = \beta_{t,c,\varphi}/(1 + (\alpha_{t,c,\varphi} M_a)^{n_{t,c,\varphi}}) \quad (5.1)$$

$$\sigma_s = \sigma_n \tan\varphi + c \quad (5.2)$$

Eq. 5.1 describes the variation in the tensile strength (σ_t), cohesion (c) and friction angle (φ) with respect to M_a, using the equivalent values for α, β and n (subscripts t, c and φ, respectively). Eq. 5.2 is the Mohr-Coulomb shear strength criteria, and σ_t is the tension cut-off. In their case,

the parameters in Eq. 5.1 were β_t= 4.70 MPa, α_t= 0.022 and n_t= 3.42; β_c= 9.10 MPa, α_c= 0.022 and n_t= 4.08; and β_φ= 56.80 MPa, α_φ= 0.0113 and n_φ= 2.83. Note that $\beta_{t,c,\varphi}$ represent the equivalent σ_t, c and φ for M_a=0% (null mica content).

A series of pull-off tests (POTs) were performed on rock blocks from the MST. The POT was recently introduced to rock mechanics applications, which consists of pulling a metal disc attached to a partial core drilled against a flat rock surface (Cacciari and Futai 2018a). All POTs were performed perpendicular to the foliation/banding planes to obtain the tensile strength values and estimate M_a. The same methodology used by Caccari and Futai (2018 and 2019) was applied herein, including the POT devices and image analyses for M_a quantification. More details on the POT and M_a can be found in these aforementioned works.

Fig. 5.9 shows the POT results from the MST gneiss plotted with the results obtained by Cacciari and Futai (2019) for biotite gneiss. The same tendency of both results indicates that M_a can also be used to predict the tensile strength of foliation planes on the MST gneiss (Eq. 5.1 with subscript *t*). However, M_a =61% and M_a=21% had the highest and lowest biotite contents, respectively (I and II highlighted in Fig. 5.9). Specimen II in Fig. 5.9 represents the lowest tensile strength from mafic/felsic banding contacts, as indicated in Fig. 5.8.

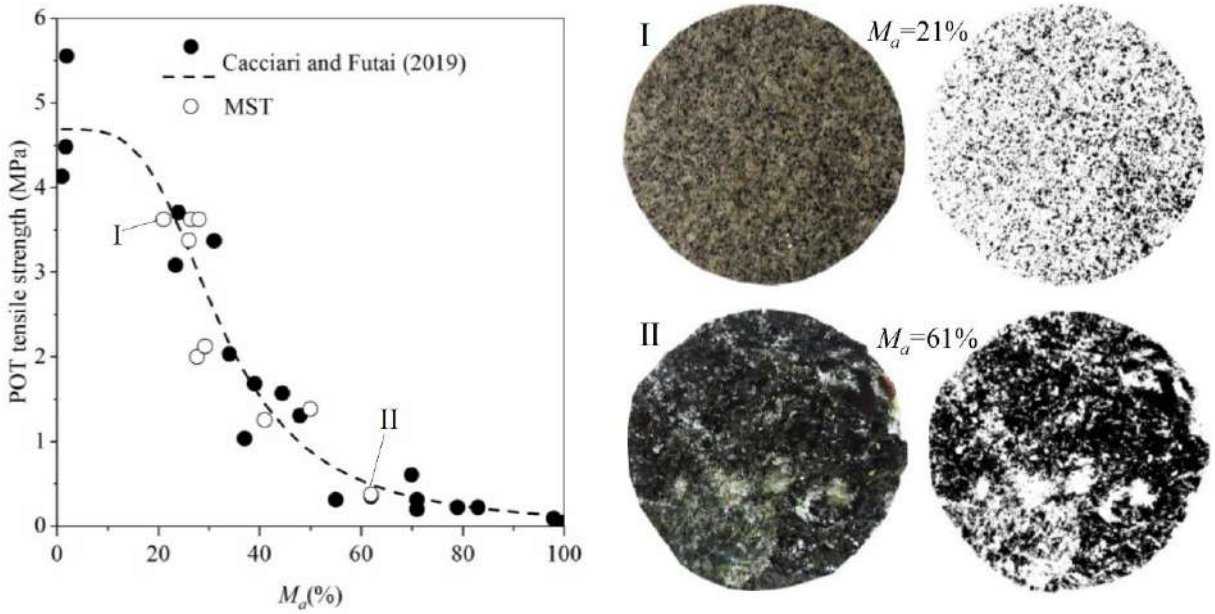

Fig. 5.9. POTs from MST gneiss plotted with POTs from biotite gneiss.

Four direct shear tests (DSTs) were performed with specimens taken from the biotite-rich contact (Fig. 5.8) and isolated inside a 1-cm-thick shear zone (Fig. 5.10). The two-stage testing method (Cacciari and Futai 2019) was used to allow M_a quantification before causing major shear damage to the banding contact surface. The first stage (the peak stage) is the DST of the intact foliation plane (intrablock), which ends after capturing the complete stain softening behavior of the shear stress vs. shear displacement curve (red lines in Figs. 5.10a-d). The second stage (the postpeak stage) consists of the DST of the open foliation plane (interblock) created after the peak stage (black lines in Figs. 5.10a-d). In the postpeak stage, the DST ends after achieving a total shear displacement equivalent to 10% of the specimen length in the shear direction.

The DSTs were performed under constant normal load boundary conditions with normal stress values of 0.5, 1.5, 3.0 and 5.0 MPa. The M_a=60% and M_a=70% lines in Fig. 5.10e are particular cases of the 3D shear envelope defined by Cacciari and Futai (2019) for a biotite gneiss (Eqs. 1 and 2). The MST specimens showed good agreement with these envelopes within the shear strength range corresponding to $60<M_a<70\%$. The mean shear stiffness (K_s) of the peak and postpeak stages were 6.1 GPa/m and 1.6 GPa/m, respectively. Considering the good agreement between the MST gneiss and the biotite gneiss obtained by both POTs and DSTs, the 3D strength envelope (Eqs. 1 and 2) is suitable to represent the strength of the foliation planes on the MST gneiss. Details of the laboratory results and analysis used to develop the 3D strength envelope for foliation planes with different mica contents (M_a) can be found in the work referenced above.

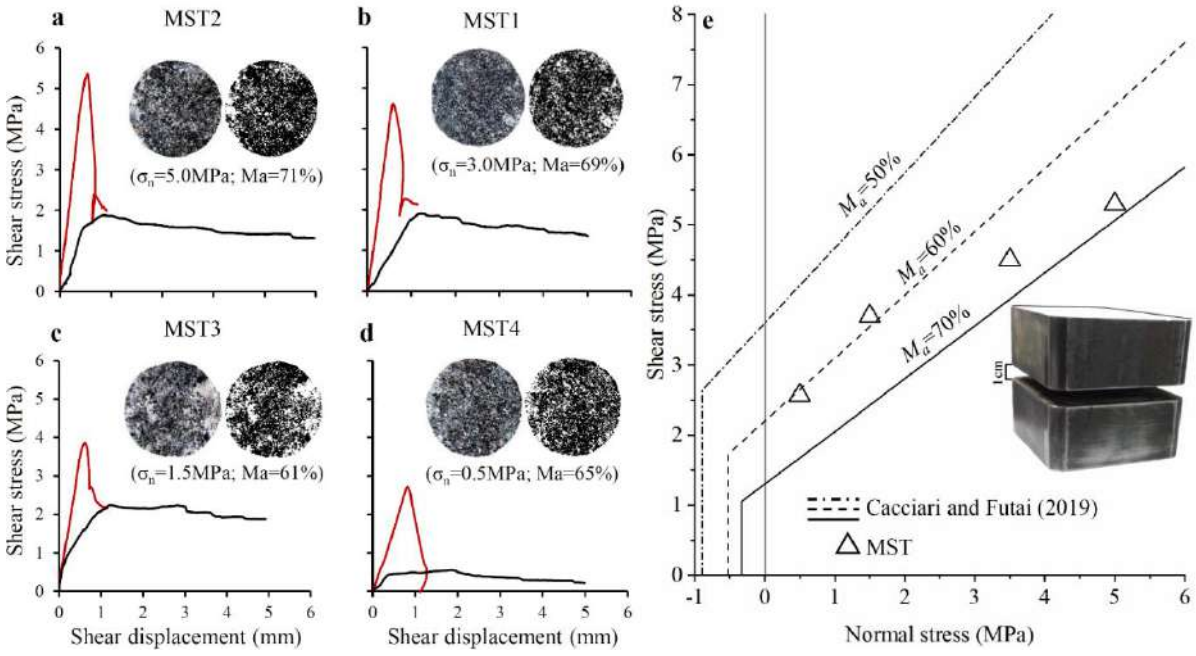

Fig. 5.10. (a-d) DSTs of MST specimens, including the M_a estimates (red lines and black curves are the peak and postpeak DSTs, respectively). (e) Peak shear strength values of the MST specimens plotted with the specific envelopes from Cacciari and Futai (2019).

5.4.1.2 Mechanical properties of the fracture sets.

The mechanical properties of the *F1*, *F2* and *F3* fracture sets were determined empirically using the joint roughness coefficient (*JRC*), the joint compressive strength (*JCS*) and the residual friction angle (φ_r) from Barton and Choubey (1977). The *JRC* was assessed in field outcrops and drill core specimens with manual 30-cm and 10-cm profilometers (Barton's comb), respectively. Additionally, 3D plane amplitudes from well-exposed discontinuities were measured via TLS point clouds and converted to *JRC* values using Barton's chart (Monticeli et al. 2015). *JCS* and φ_r values were obtained by (Monticelli 2019) using empirical correlations between the Schmidt hammer rebound and uniaxial compressive strength of fresh and weathered cylindrical core specimens. As the *JRC* values were noticeably different among fracture sets, a single envelope was used for all these structures. The mean and standard deviation of *JRC*, *JCS* and φ_r for the fracture sets were 9.7 (2.3), 105 MPa (24 MPa) and 25.5° (2.1°), respectively.

For the fracture sets (*F1*, *F2* and *F3*), the Coulomb-slip envelopes were defined by linearizing the Barton-Bandis envelopes, following the secant-line method suggested by Prassetyo et al. (2017), which results in null cohesion and tensile strength for such geological structures. The linearization method resulted in an equivalent secant friction angle of 40°. The shear stiffness of open foliation planes (*OFPs*) in Fig. 5.10 (1.6 GPa/m) was also used for the fracture sets. For both fractures and foliation planes, the normal stiffness (K_n) was calculated as K_n=10*Ks*, according to the tendency observed by Bandis et al. (1983). Considering that *OFPs* and fractures have similar mechanical behavior (friction-based with null cohesion and tensile strength), the φ_r of fractures was also used to characterize the postpeak behavior of *OFPs*.

5.4.1.3 Mechanical properties of weathered fracture and foliation planes

Monticelli (2019) described the weathering effects on the MST site that affected the individual discontinuity planes on the drill core specimens. As noted by the authors, isolated discontinuities, including fracture and foliation planes, show advanced weathering grades, but the tunnel rock face does not show significant weathering effects on the rock matrix. Foliation planes with advanced weathering grades split on the drill cores, indicating a lack of tensile strength and cohesion in such conditions. Fig. 5.11a shows the variations in φ_r with respect to porosity (η) for foliation, *F1* and *F2* planes. The φ_r values of weathered foliation and fracture planes decrease substantially with increasing η. Moreover, the *F2* and foliation planes had more advanced weathering grades than the *F1* planes, indicating that the former had lower φ_r values. Fig. 5.11b shows the foliation specimen with the highest η and lowest φ_r. Fig. 5.11c shows a micrograph taken from this specimen, perpendicular to the foliation plane, indicating that the weathering path may reach substantial distances (e.g., over 5 mm). Weathered minerals have characteristic colors and textures (see example highlighted in yellow in Fig. 5.11c), which are the result of cordierite grains replaced by pinite, chlorite, iron oxides and hydroxides and fissures filled by carbonate and clay (Monticelli 2019).

In this work, the discontinuity weathering is simulated only in extreme conditions, wherein φ_r=20° for all discontinuity sets (foliation and fractures); these conditions represent the intermediate value of the total φ_r range from the drill core specimens. Considering that the Coulomb-slip model is linear, to simulate such extreme weathering conditions, the φ_r was directly used in the model without considering any influences of weathered *JRC* or *JCS*

parameters that would increase the equivalent friction angle obtained by the secant-line method (Prassetyo et al. 2017).

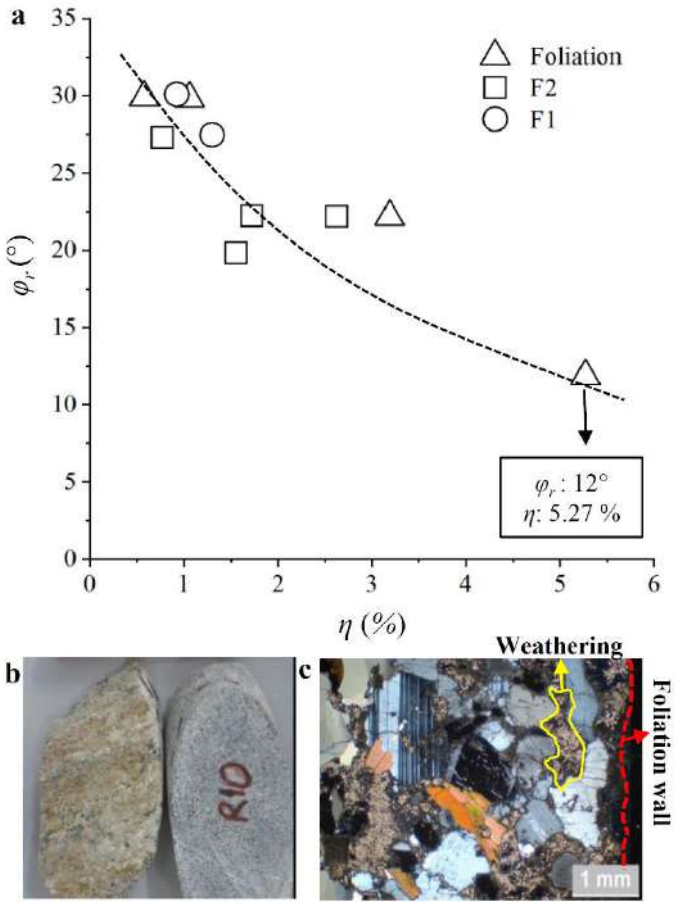

Fig. 5.11. (a) Residual friction angles of discontinuities decreasing with increasing porosity due to weathering. (b) Foliation specimens with advanced watering grade, and (b) a micrograph taken perpendicular to the foliation wall indicating weathered minerals (highlighted in yellow). Modified from Monticelli (2019).

5.5 DFN-DEM results

A series of DFN-DEM analyses were carried out to assess the role of rock foliation on the stability of the Monte Seco tunnel. As mentioned before, both MS1 and MS2 sections do not have any kind of support systems. The RMR_{14}, Q and GSI values of these sections (Table 5.1) suggest that some support system should have been applied during tunnel construction; however, these methods were developed after the excavation period, and the excavation methods adopted at the time (if there were any specific methods) are unknown.

The fact that the MST stands stable without apparent major stability problems indicates that the traditional empirical classification methods in Table 5.1 are conservative (as they should be) and overlook certain important characteristics of the rock mass that are favorable to tunnel stability. Next, DFN-DEM analyses show the influence of rock foliation on MST stability, including the mechanical characteristics presented in Section 5.4.1.1. The in situ stresses were included in 3DEC using the surface topography (INSITU TOPOGRAPHY command) and the intact rock density (26.5 kN/m^3) to calculate the vertical stresses along depth. The horizontal stresses in both the x and y directions were considered equal to the vertical stresses along the depth (K_0=1.0). Although in situ stress measurements were not available, the regional geology does not suggest the occurrence of a high horizontal/vertical stress ratio. First, there are no active tectonics in the territory, and inactive faults are far from the tunnel. Moreover, the last acting deformational event at the tunnel site was distensional (Cretaceous), which is related to the formation of *F1* fractures (Monticelli 2019); this phenomenon tends to relieve horizontal stresses on the rock mass.

All discontinuity mechanical parameters used in the following DEM analyses are summarized in Table 5.2. Case *a* represents the unweathered *OFP*s and fractures; cases *b-g* represent the intact foliation planes with different M_a values (particular cases of the 3D strength envelope from Cacciari and Futai (2019)); and case *h* represents the foliation and fracture planes with advanced weathering grade.

Table 5.2. Coulomb-slip parameters of the discontinuities used in the DEM analyses: M_a (percentage of mica area); K_s (shear stiffness); K_n (normal stiffness); σ_t (tensile strength); c (cohesion); φ_p (peak friction angle); φ_r (residual friction angle); *OFP* (open foliation plane); *WFP* (weathered foliation plane); *F1*, *F2* and *F3* (fracture sets); and *WFR* (weathered fracture).

Case	*Application*	M_a (%)	σ_t (MPa)	K_s (GPa/m)	K_n (MPa/m)	c (MPa)	φ_p (°)	φ_r (°)
a	*OFP*; *fractures*	-	0.0	1.6	16	0.0	40	25
b	*Foliation*	*100*	0.10	6.1	61	0.35	23.5	25

c	*Foliation*	*90*	0.15	6.1	61	0.60	27.5	25
d	*Foliation*	*80*	0.21	6.1	61	0.80	32.0	25
e	*Foliation*	*70*	0.33	6.1	61	1.30	37.0	25
f	*Foliation*	*60*	0.53	6.1	61	2.20	42.0	25
g	*Foliation*	*50*	0.90	6.1	61	3.60	47.0	25
h	*WFP; fractures*	-	0.0	1.6	16	0.0	-	20

The main parameter used to analyze the DEM results was the total failed block volume (*FBV*), obtained by a Fish function that calculates the sum of block volumes for three different displacement magnitude thresholds (D>0.1, D>0.05 and D>0.01 m). Additionally, a Fish function computed the average displacement of the tunnel face (*AD*) and the total number of slipping contacts (*SC*) near the tunnel face while stepping to monitor the excavation behavior during the analyses. In these cases, the Fish function found the grid-points of the blocks on the tunnel face and contacts 0.25 m from the tunnel face and computed *AD* and *SC*, respectively. All DEM models stopped running after 100×10^3 calculation steps (approximately 10 hours for MS1 and 6 hours for MS2 models).

5.5.1 Effects of fresh foliation on the MST stability

The gneissic foliation planes have cohesion and tensile strength, which vary with respect to the biotite content (M_a). Thus, using friction-based models for these structures can significantly underestimate the actual stability condition of the rock mass. To demonstrate this problem, the DEM models in Fig. 5.7 were ran using the 3D peak shear strength envelope described by Eqs. 1 and 2, in which M_a is an independent variable (as the normal stress). Case *a* (Table 5.2) was used for *OFP*, *F1*, *F2* and *F3*, and cases *b* to *g* (Table 5.2) were used for foliation planes with different mica contents.

Fig. 5.12 shows the *FBV* results obtained for MS1 and MS2. Four *FBV* zones were defined: zone I represents released block volumes higher than 10^2 m^3, which is associated with global instability problems; zone II represents released block volumes between 10 and 10^2 m^3, which is associated with large instabilities around the excavation; zone III represents released block volumes between 1 and 10 m^3, which is associated with intermediate instabilities around the excavation; and zone IV represents released block volumes lower than 1 m^3, which is associated with small block releases and generally stable conditions.

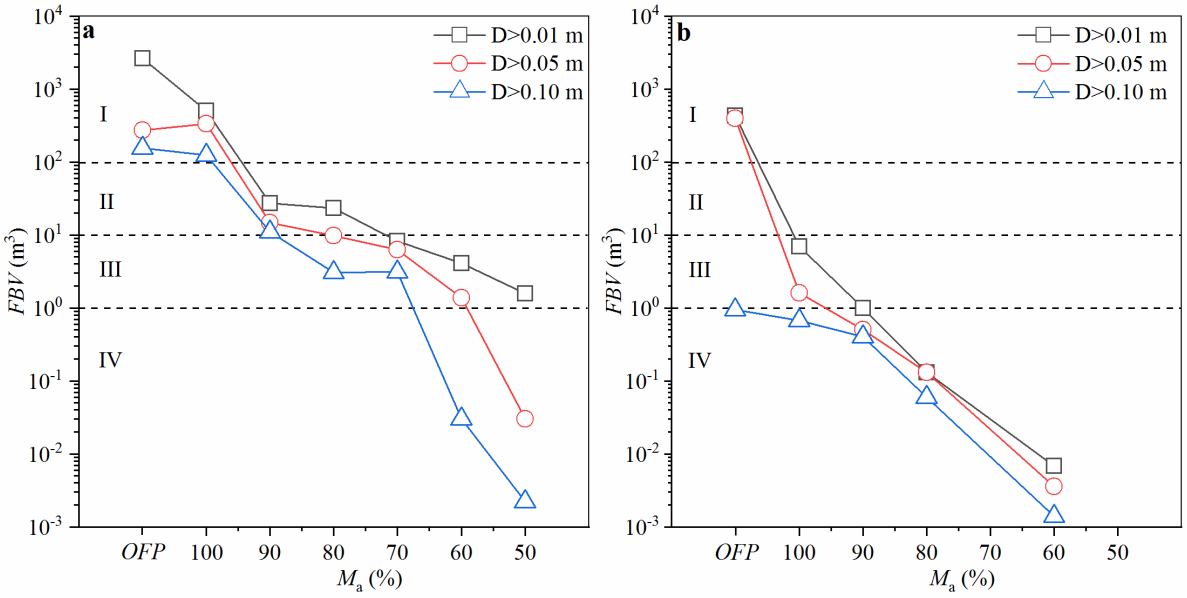

Fig. 5.12. Variation in the *FBV* values of (a) MS1 and (b) MS2 with respect to M_a for different displacement magnitude thresholds (D>0.01, 0.05 and 0.1 m): (I) global instability zone, (II) large instability zone, (III) intermediate instability zone, and (IV) stable zone.

Fig. 5.13 shows examples of the results in Fig. 5.12a for MS1. The potential instability problems of this section are clearly controlled by the *F2* shear zone. DEM models with *OFP* (null cohesion and tensile strength) and M_a=100% (Table 5.2) showed a global failure pattern with extremely high *FBV* values for displacements higher than 0.1 m. It is important to note that the failure reaches the bedrock, suggesting that daylight collapse could occur for such low foliation strengths. As M_a increases, the tunnel becomes more stable. For M_a=90%, major discontinuity-controlled failure occurred surrounding the excavation. For M_a=60%, only the east wall showed a significant discontinuity-controlled failure. For M_a=50% or less, only isolated failures of small blocks occurred on the east wall.

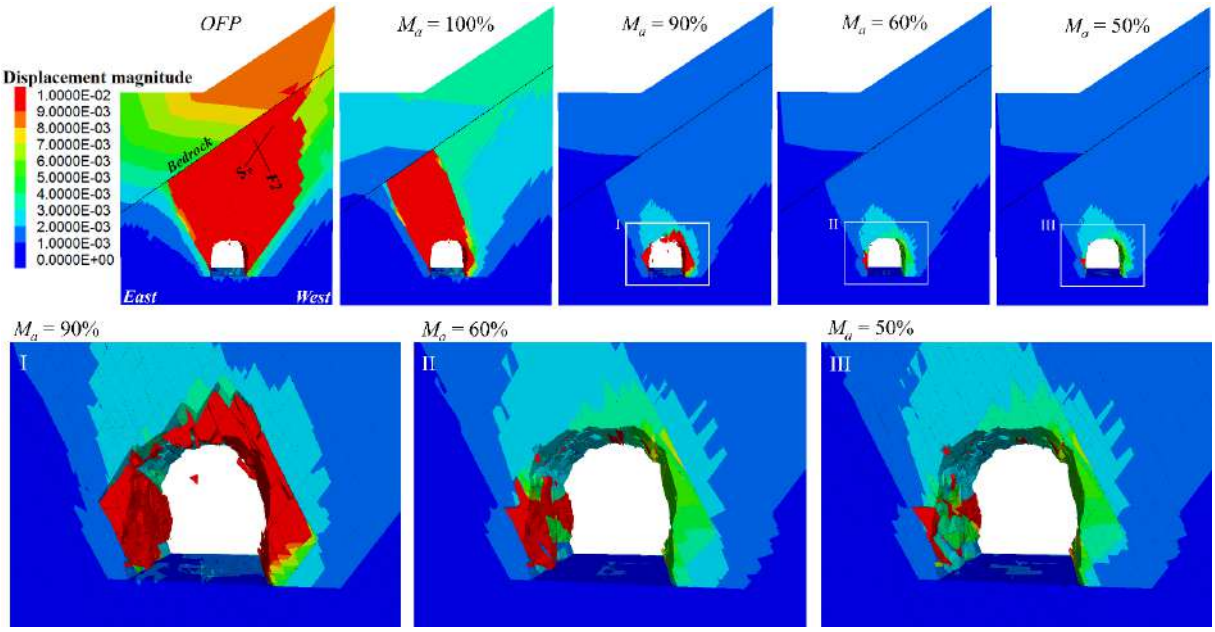

Fig. 5.13. Examples of MS1 DEM results for different foliation plane conditions (DEM models facing south).

Fig. 5.14 shows examples of the results in Fig. 5.12b for MS2. The potential instability problems of MS2 are controlled by the foliation planes, as the fracture intensity is much lower than in MS1 (Fig. 5.4). As MS2 is extremely shallow, the low cohesion and tensile strength values are sufficient to maintain the tunnel stability. The mechanical parameters of *OFP* (null cohesion and tensile strength) triggered global failure patterns by shear failure of persistent foliation planes on the west wall of the tunnel. For M_a=90%, only the east wall showed a significant discontinuity-controlled failure. For M_a=80% or less, the tunnel shows stable conditions with isolated failures of small blocks on the east wall and roof.

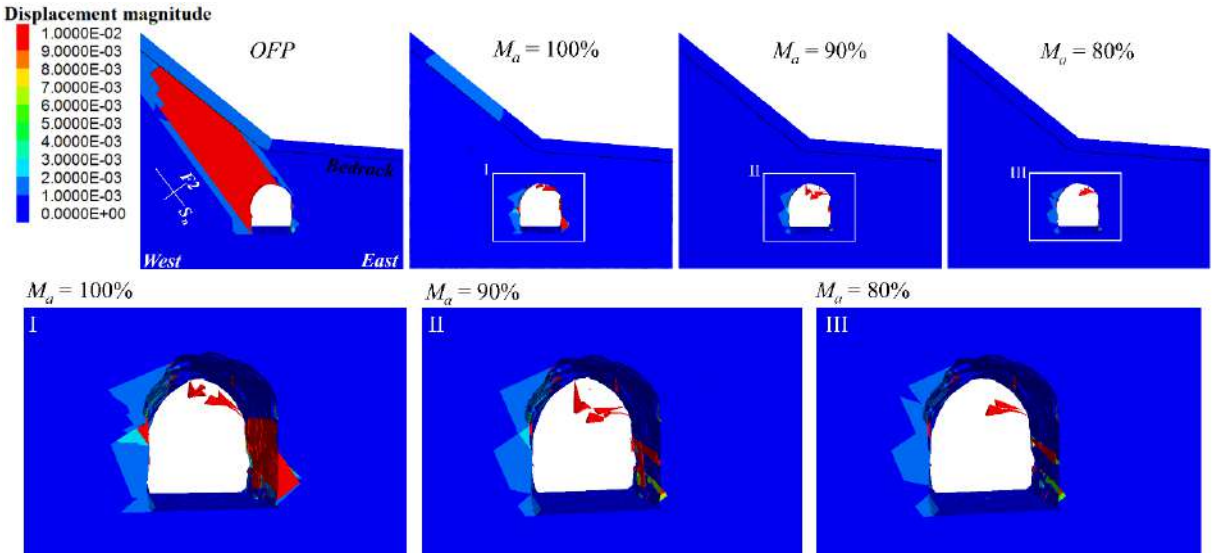

Fig. 5.14. Examples of MS2 DEM results for different foliation plane conditions (DEM models facing north).

The *FBV* values from different displacement magnitude thresholds (D>0.1, D>0.05 and D>0.01 m) indicate the homogeneity of the block velocities in the models. In unstable conditions (zones I, II and III), close *FBV* values indicate the existence of defined unstable regions in the model (defined masses of blocks moving with similar velocity). In stable conditions (zone IV), close *FBV* values indicate general stability (lack of significant movement). On the other hand, outlying *FBV* values indicate heterogeneous distributions of block movements (masses of blocks moving with different velocities in the models).

Fig. 5.15a shows the calculated variations in *AD* from *OFPs* (condition I) and M_a=60% (conditions I and II) for MS1, which corroborates the stable conditions observed above by the *FBV* for foliation planes with such mica content (Fig. 5.12a). Conditions II and III in this figure show slight changes in *AD* after removing free falling blocks with D>0.01 m. Fig. 5.15b shows the calculated variations in *AD* from *OFPs* (condition IV), M_a=80% (conditions V and VI) and M_a=60% (conditions VII and VIII) for MS2. For M_a=80%, *AD* continued to increase due to small blocks free falling from the tunnel roof (condition V in Fig. 5.15). After removing blocks with D>0.01 (condition VI in Fig. 5.15), *AD* was in agreement with the stable conditions observed for M_a=80% by the low *FBV* values (Fig. 5.12b). MS2 with M_a=60% showed inexpressive *AD* during the entire analysis, before and after removing blocks with D>0.01 m (conditions VII and VIII).

Fig. 5.15c shows the *SC* monitored for MS1 and MS2 using *OFPs* and M_a=60% (cases *a* and *f* in Table 5.2). For all cases, the *SC* starts with higher values and decreases rapidly, reaching a relative stability after 20×10^3 calculation steps. These results indicate that a characteristic instability pattern is achieved after 100×10^3 calculation steps. Note that *SC* is considerably higher and much more unstable for *OFPs* than for M_a*=60%*, which indicates that only a few blocks near the tunnel are in motion during the analyses in the second case. For MS1 with M_a=60%, *SC* decreases drastically after removing blocks with D>0.01 (condition III in Figs. 5.15a and c), reaching an *SC* value similar to that from MS2 under the same conditions (condition VIII in Figs. 5.15b and c). Fig. 5.15d shows the slipping contacts surrounding the excavation boundary for MS1 (conditions I and II) and MS2 (conditions IV and VII). Note that only the slipping contacts 0.25 m from the excavation boundary were used to calculate *SC*.

This work is based on the assumption that DEM analysis with a fixed DFN (fixed discontinuity geometrical parameters) can be representative of the overall rock mass condition. Moreover, the actual tunnel geometry is built in the model (Section 5.2.1); thus, to find a representative stable condition for MS1 and MS2, significant failures along the foliation planes leading to additional over- and underbreaks should not occur. As the DFN generation is stochastic, the discontinuities on the DEM tunnel face are not equal (in size, position and orientation) to the real discontinuities mapped via TLS on MS1 and MS2. Therefore, small block failures cannot be associated with actual unstable conditions, while major failures of block sets can.

There is no specific parameter to verify the stability state of tunnel models in 3DEC. Monitoring the parameters introduced herein (*FBV*, *AD* and *SC*), along with the total unbalanced forces of the models, one can indicate stable or unstable conditions in the tunnel. Unstable models with a high volume of moving blocks show high and oscillatory unbalanced forces, whereas stable models with a low volume of moving blocks show steady and low unbalanced forces. For example, after removing the small volume of free falling blocks from MS1 (M_a=60% in Fig. 5.15a) and MS2 (M_a=80% in Fig. 5.15a), the total unbalanced forces were steady at 22.9 N and 93 N, respectively, and *AD* stopped increasing. On extremely unstable models, such as the *OFP* cases (Figs. 5.13 and 5.14), the total unbalanced forces oscillated from 10^4 to 10^5 N.

The DSTs in Fig. 5.10 indicated M_a values closer to 60%; however, these specimens represent the worst-case (such as the biotite-rich contact in Fig. 5.8) observed on the MST gneiss. The POT results (Fig. 5.9) corroborate this statement, as 61% was the lowest estimated M_a. In addition to the block failures observed on the east wall of the MST for M_a=60%, after removing

blocks with D>0.01 m, the *AD* decreased to 0.0035 m (Fig. 5.15a), and the *SC* decreased to 0.3%, indicating stable conditions. Therefore, the mechanical parameters associated with M_a=60% (case *f* in Table 2) can be considered representative of actual stable conditions in the MST.

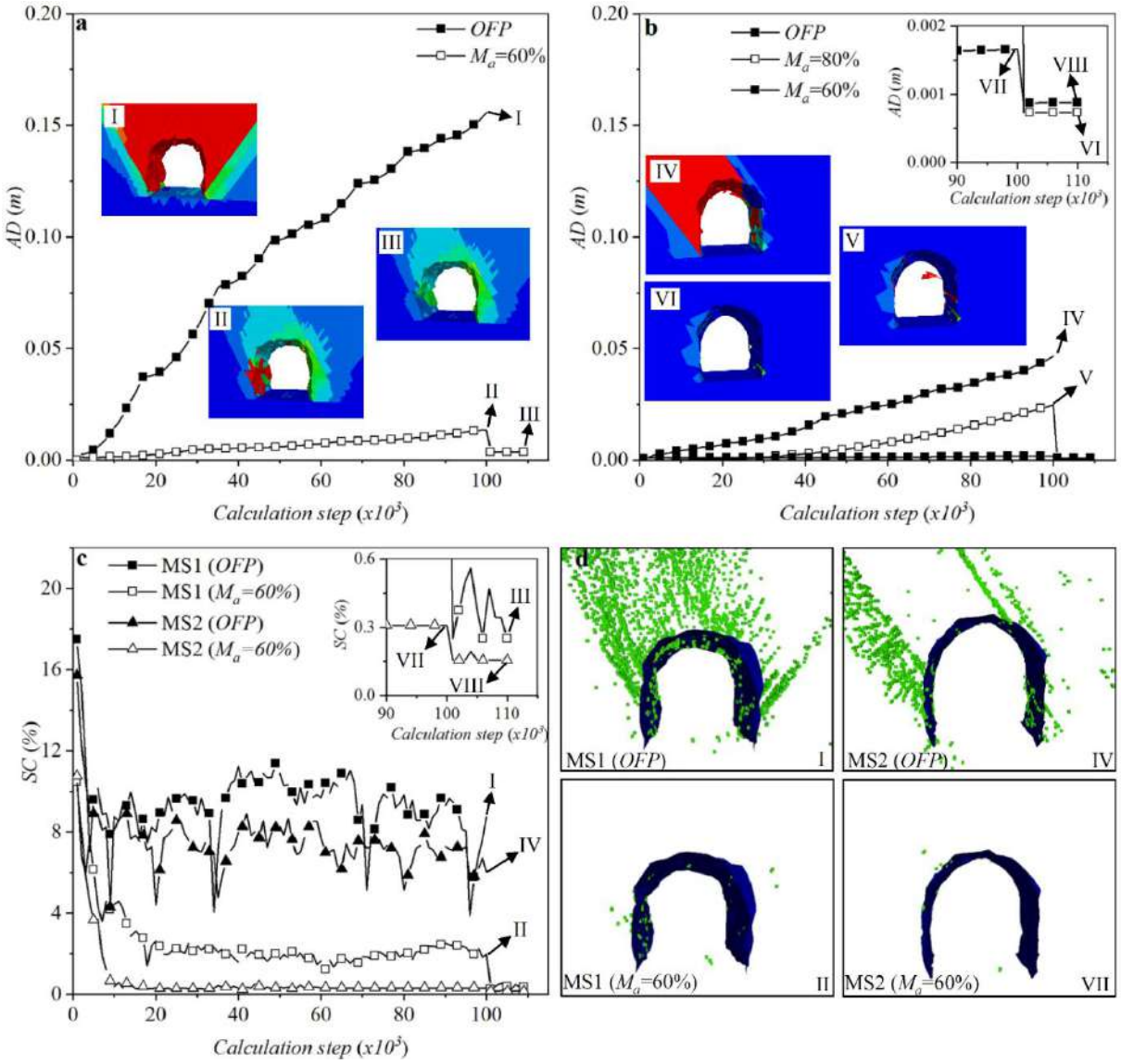

Fig. 5.15. Calculated *AD* and *SC* values while stepping from worst-case and best-case scenarios of (a) MS1 (DEM models facing south) and (b) MS2 (DEM models facing north). I-III and IV-VIII indicate different DEM conditions of *AD* and *SC* for MS1 and MS2, respectively.

From the results in Figs. 5.15c and d, 100×10^3 calculation steps were sufficient to define the failure pattern in these models. Increasing the number of calculation steps would increase the amount of time to complete the analysis without resulting in additional relevant information. On the other hand, a lower number of calculation steps would decrease the final displacement of the failed blocks, which would not highlight the failed zones in the models. Considering that *SC* and *AD* indicated 100×10^3 calculation steps suitable to obtain representative stability patterns, hereafter only the *FBV* will be used to analyze the numerical results.

The results presented in this section indicate that foliation plays an important role in the stability of the tunnel; thus, ignoring the inherent cohesion and tensile strength of such geological structures creates unrealistic instability conditions. It is interesting to note that null cohesion and tensile strength (*OFP*) triggered global unstable conditions for both MS1 and MS2. In this case, there is an agreement between the numerical results with the general classification results in Table 5.1, which would recommend immediate support installation on these sections of the tunnel. The discontinuity description in these classification systems considers the roughness and weathering conditions but starts from the assumption that discontinuities have null tensile strength (ISRM 1978).

In practical geological mapping, the exposed foliation planes are commonly described as a "joint set", with the same classification parameters used for different structures, such as fractures and sheet joints, which is conservative because it underestimates the real shear strength and tensile strength of such geological structures. This fact becomes evident after reassessing old tunnels (such as the MST) constructed before the development of the most popular rock mass classification systems. It is important to note that the classification systems are not wrong, as they should be conservative. However, using these classification systems as definitive empirical design methods causes direct consequences on the support system design.

In the case of the MST, M_a=60% satisfied the actual stability of the tunnel without support systems. However, the possible weathering effects noted in Section 5.4.1.3 were not included. In the following sections, a parametric study is presented considering the weathering effects in different scenarios, affecting both the foliation and fracture planes.

5.5.2 Weathering effects on foliation and fractures

In this section, a parametric study is performed considering possible weathering distributions on the rock mass. Monticelli (2019) showed that the weathering advanced through discontinuities on the MST and did not affect the intact rock. As indicated in Section 5.4.1.3, advanced weathering drastically decreases the discontinuity strength.

Next, the effects of weathering on MS1 and MS2 are evaluated in two different ways: the effects of isolated and persistently weathered foliation planes (*WFPs*) on the stability of the tunnel and the effect of a percentage of weathered discontinuity planes (including foliation and fractures) distributed on a defined weathered domain.

5.5.2.1 Effects of isolated weathered foliation planes

Field surveys, drill cores and visual inspections inside the MST showed evidence of isolated foliation planes in advanced weathering conditions, named herein as *WFPs*. *WFPs* have high porosity (Fig. 5.11); thus, *WFPs* contribute significantly to the water inflow on the MST (Fig. 5.6).

Considering the aforementioned evidence, a single *WFP* with critical mechanical properties associated with advanced weathering was inserted at different positions in the MS1 and MS2 models. The parameters in case *h* (Table 5.2) were attributed to the *WFP*s, and the parameters in cases *f* and *a* were attributed to the remaining foliation and fracture planes, respectively (Table 5.2). Fig. 5.16 shows the position of each *WFP* in MS1 and MS2 and the respective *FBV* results of each simulation. Fig. 5.17 shows examples of these results indicating the position of the *WFP* and the magnitude of block displacements.

In MS1, *WPF* 09, which is near the top-east corner of the tunnel (Fig. 5.16a), caused major instability problems with large failure surrounding the excavation (Figs. 5.16b and 5.17a). Above *WFP* 09, *WFP*s 10 to 13 did not cause significant block failures, and the final stability state was similar to that in the case of M_a=60% without *WFP*s (Figs. 5.12a and 5.13). Below *WFP* 09, *WFPs* 08 and 07 also caused large local instabilities (*FBV* values inside zone II); however, *WFP*s near the top-west corner (*WFP*s 03-06) did not trigger unstable conditions in

the tunnel. *WFPs* 01 and 02, which are near the bottom-west corner, caused intermediate to large unstable conditions

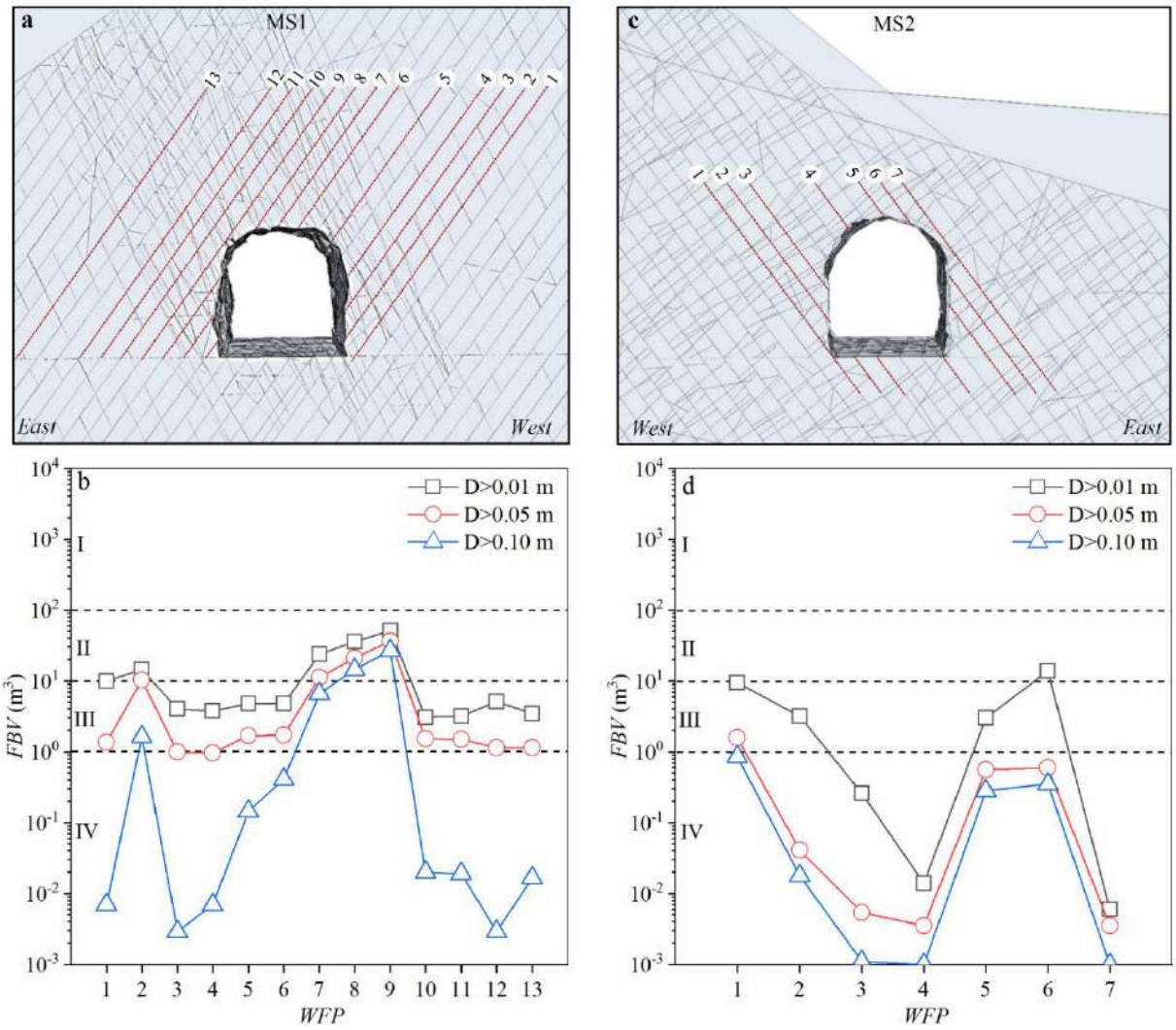

Fig. 5.16. Location and the respective *FBV* results of each *WFP* in (a and b) MS1 and (c and d) MS2 for different displacement magnitude thresholds (D>0.01; 0.05 and 0.1 m): (I) global instability zone, (II) large instability zone, (III) intermediate instability zone, and (IV) stable zone. Note that the MS1 DEM models face south and the MS2 DEM models face north.

(*FBV* values between zones III and II). Therefore, a single *WFP* could cause significant instability in MS1 (inside zone II) as long as it is located near the top-east or the bottom-west corners of the tunnel; however, the first case is much more critical. It is important to highlight that the water inflow occurs through the *F2* shear zone (Monticelli 2019) in MS1, and the top-east corner of the tunnel is constantly wet and dripping (Fig. 5.6a).

Overall, MS2 is less affected by isolated *WFPs* than MS1; however, MS2 showed expressive *FBV* values for *WFPs* 01 and 06, which are located near the bottom-west and top-east corner of the tunnel, respectively (Figs. 5.16d and 5.17b). These *WFPs* triggered intermediate to large block failures (*FBV* values between zones III and II) on the walls but triggered general failures around the excavation, such as the *WFP* 09 in MS1.

Both MS1 and MS2 showed important instability problems associated with *WFPs* crossing the rock mass near the top and bottom corners of the tunnel. In this case, it is interesting to verify the consequences of two *WFPs* in such positions. Figs. 5.18a and 5.18b show the DEM results of MS1 with *WFPs* 02 and 09 and MS2 with *WFP*s 01 and 06, respectively. Both cases indicated major failures (*FBV* values higher than all cases in Fig. 5.16), which would compromise the integrity of the tunnel. However, in MS2, two parallel *WFPs* in such positions, among foliation planes of high strength (M_a=60%), are necessary to trigger the same conditions observed for *OFP* (null cohesion and tensile strength for all foliation planes in the DEM model) in Fig. 5.14.

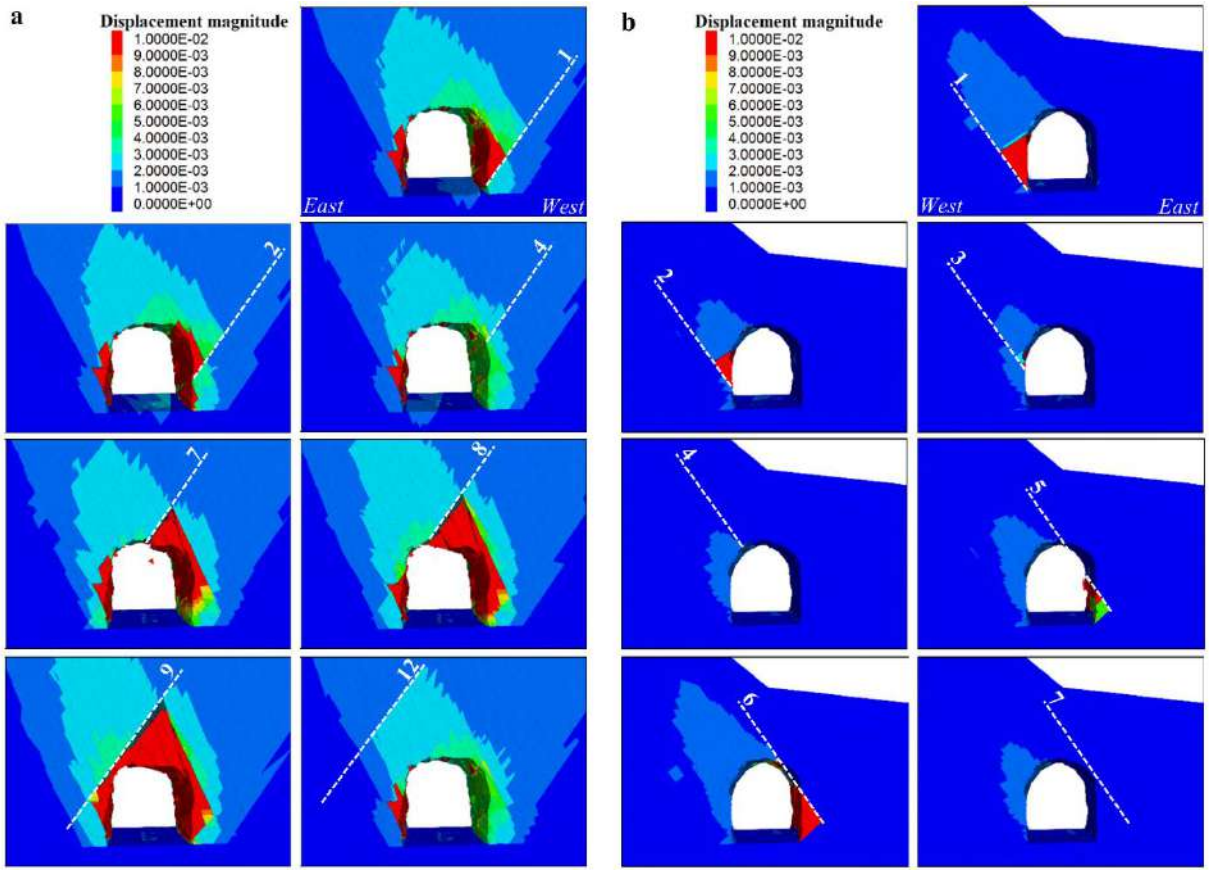

Fig. 5.17. DEM simulations with *WFPs* in different positions of (a) MS1 and (b) MS2. Note that the MS1 DEM models face south and the MS2 DEM models face north.

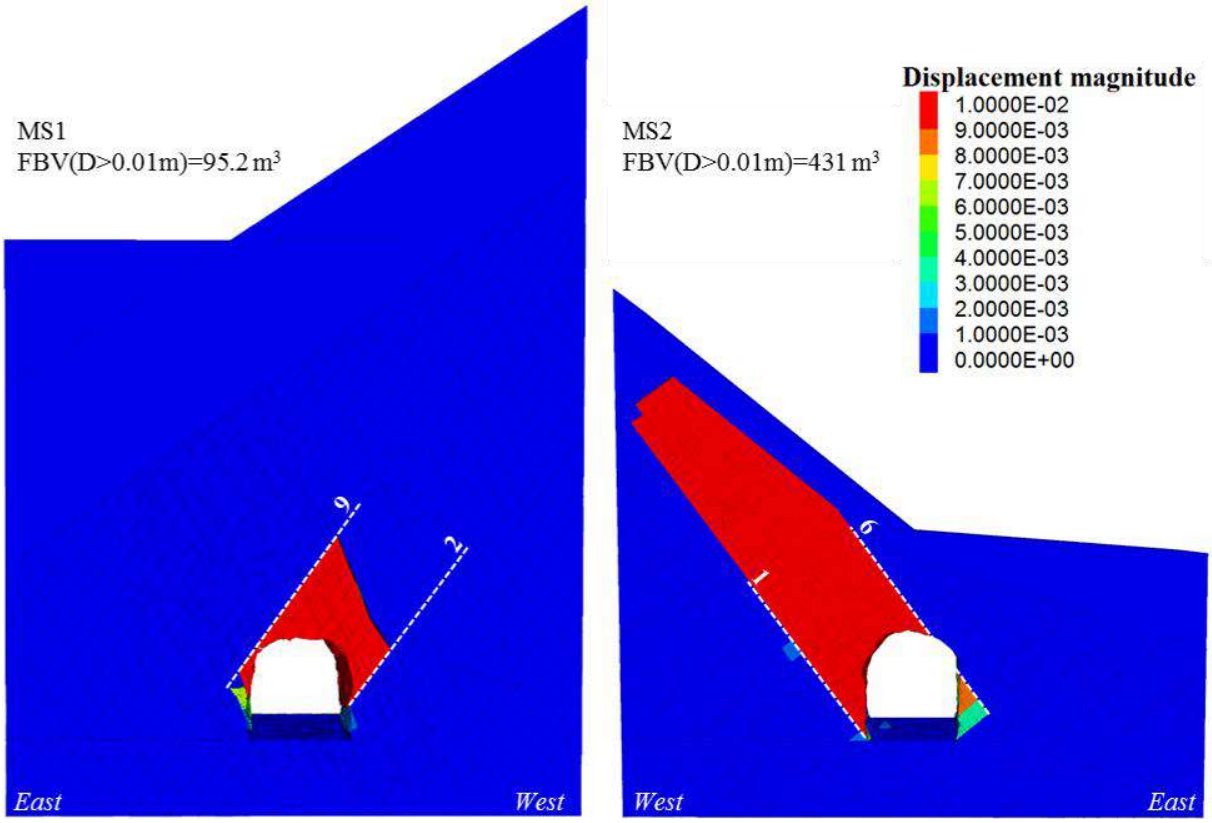

Fig. 5.18. DEM models of MS1 and MS2 containing two *WFPs* at critical positions. Note that the MS1 DEM model faces south and the MS2 DEM model faces north.

Currently, model-scale *WFPs* in such critical grade may not exist; however, there are two strong pieces of evidence causing concerns regarding this issue: The drill cores showed isolated laboratory-scale *WFPs* of equal or worse strength conditions than those used in the analyses presented above (case *h* in Table 5.2); In addition, water is constantly inflowing through discontinuities on these sections of the MST. Moreover, weathering is a dynamic process that evolves over time, progressively decreasing the mechanical properties of foliation planes and discontinuities. Therefore, model-scale *WFP*s close to reaching such critical weathering grades can exist and cause unexpected instability problems in the future.

5.5.2.2 General weathering advance

The evidence of weathering at the MST site indicates the occurrence of isolated planes (including foliation and fracture planes) of advanced weathering grades rather than a general

weathering advance through all discontinuities in the rock mass. Nevertheless, it is interesting to assess the effects of a progressive weathering advance on potentially weathered regions in MS1 and MS2. The following analyses verify the effects of the weathering advance, affecting both foliation and discontinuity planes. The potentially weathered regions in MS1 and MS2 were defined after Monticelli (2019). In MS1, this region was defined by the *F2* shear zone, which is responsible for the water inflow towards the tunnel. In MS2, the TLS images showed water dripping on the roof of the tunnel (Fig. 5.6b). In this case, the water is likely seeping from the west slope and top surface towards the tunnel through the *F1* and foliation planes, as *F2* has lower intensity in this section and dips west. Fig. 5.19 shows the potentially weathered regions in MS1 and MS2.

The weathering advance was modeled in 3DEC using a Fish code that selects block contacts and changes their mechanical properties to the same weathered properties used in the analyses presented above (case *h* in Table 5.2). The selection process was random, and the percentage of weathered contacts (*WC*) was used to stop the process. *WC* is calculated as the sum of the selected contact areas (green contacts in Fig. 5.19) divided by the sum of all contact areas on the potentially weathered regions (green and blue contacts in Fig. 5.19) of MS1 and MS2. The increase in *WC* is a simplified interpretation of the general weathering advance in these regions, which decreases the rock mass quality surrounding the excavation. Note that *WC* is equivalent to the weathered percentage of P_{32} on the potentially weathered regions.

Fig. 5.20 shows the *FBV* values for *WC* values ranging from 10 to 90%, and Fig. 5.21 shows examples of graphical DEM results. For MS1 (Figs. 5.20a and 5.21a), the increase in *WC* caused a progressive increase in *FBV*. MS1 exhibited substantial local instability problems (zone II) for *WC*>50%, and global instability problems for *WC*>80%. MS2 exhibited local instability problems (between zones III/II) only for *WC*>90%; thus, 10% of unweathered discontinuity planes (foliation and fracture planes) was sufficient to avoid global instability problems in this case (Figs. 5.20b and 5.21b).

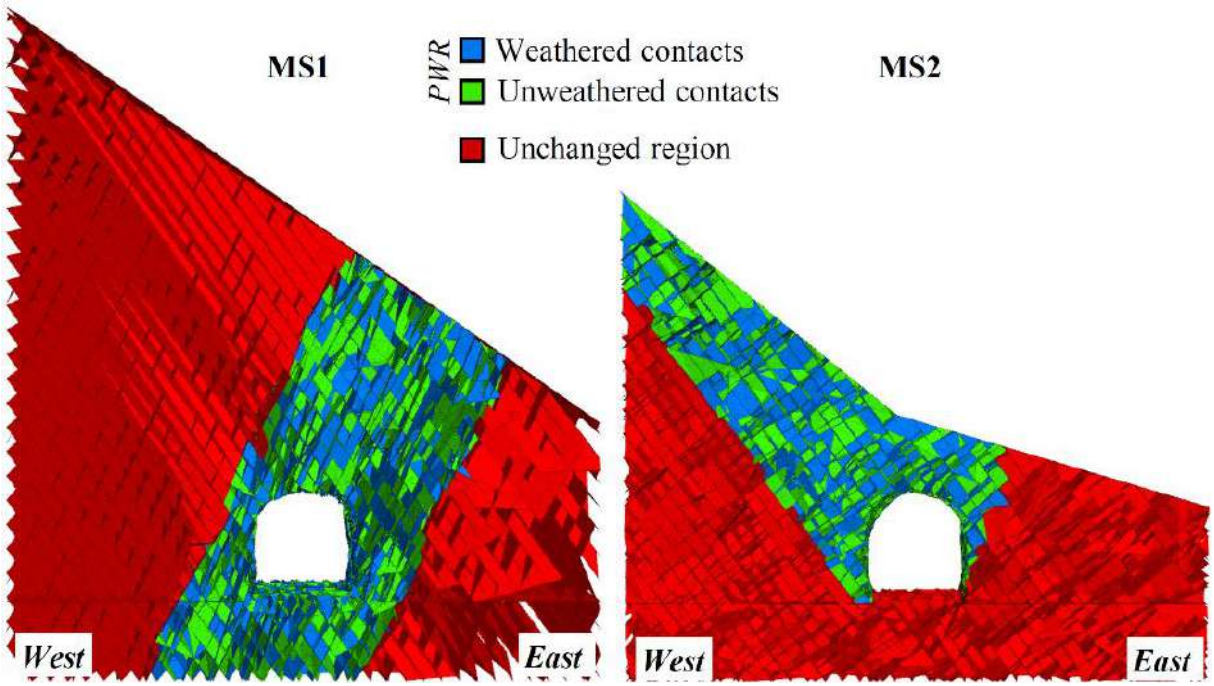

Fig. 5.19. Potentially weathered regions defined for MS1 and MS2 with *WC=50%*. Green contacts are weathered foliation and fracture planes; the blue contacts are untethered and inside the potentially weathered regions; and the red contacts are untethered and outside the potentially weathered regions. Note that the MS1 and MS2 DEM models face north.

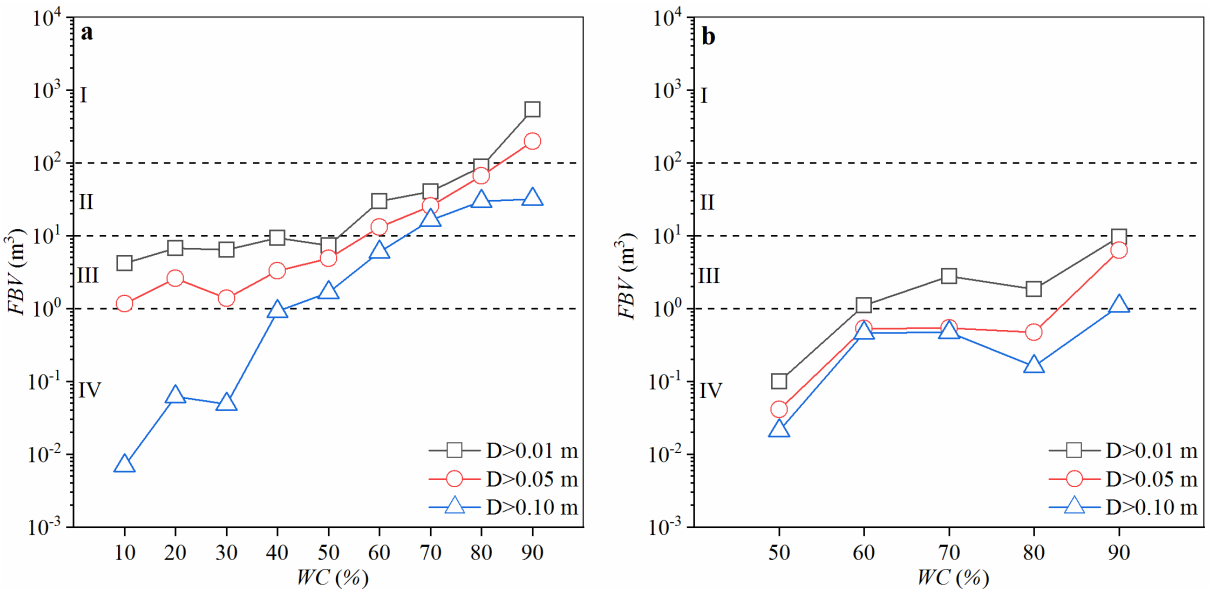

Fig. 5.20: *FBV* results of each *WC* in (a) MS1 and (b) MS2 for different displacement magnitude thresholds (D>0.01, 0.05 and 0.1 m): (I) global instability zone, (II) large instability zone, (III) intermediate instability zone, and (IV) stable zone.

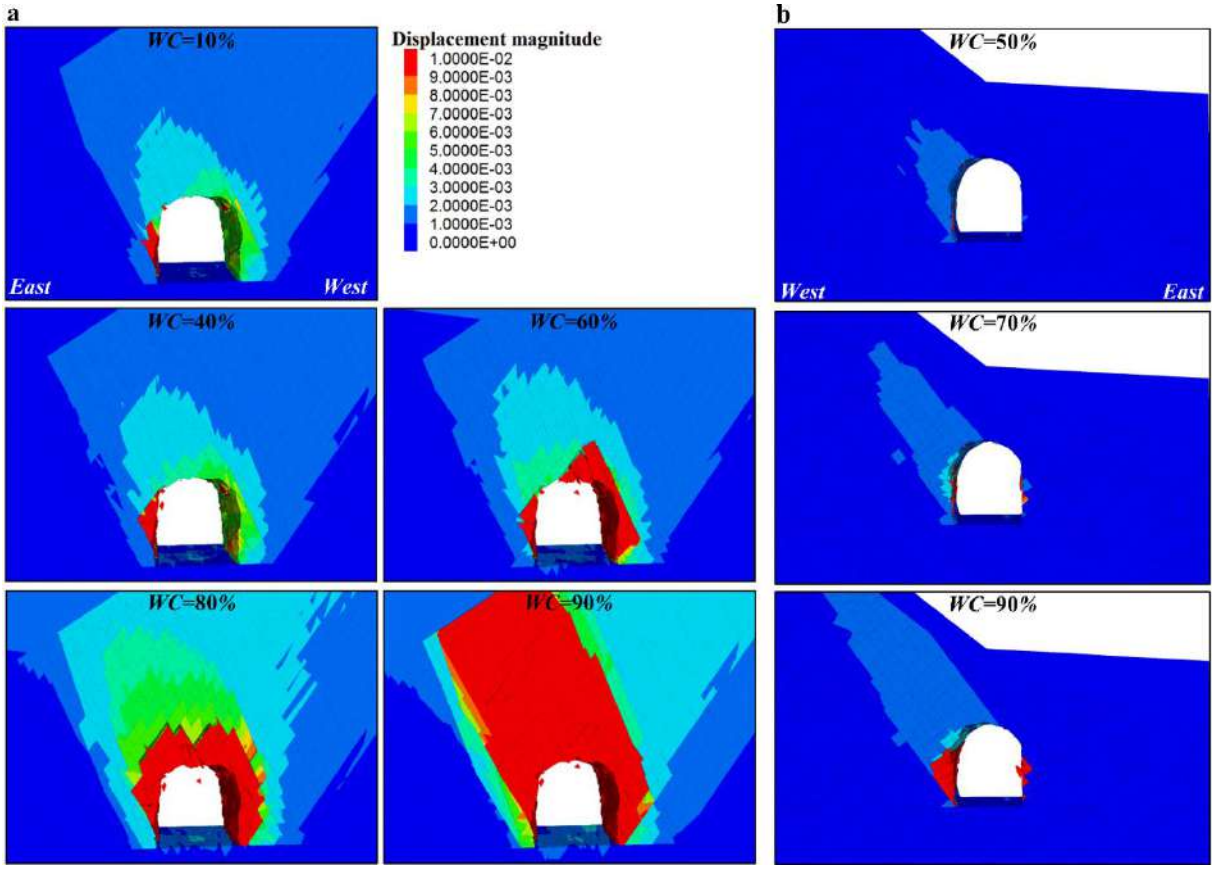

Fig. 5.21. Examples of DEM simulations with different *WC* values for (a) MS1 and (b) MS2. Note that the MS1 DEM model faces south and the MS2 DEM model faces north.

Interestingly, isolated *WFPs* 07, 08 and 09 (Fig. 5.17a) and *WC*=60% (Fig. 5.22a) trigger similar failure patterns and magnitudes in MS1. However, from geotechnical-geological surveys and site observations, isolated *WFPs* are more likely to occur than general weathering distributions of such magnitudes. However, the weathering advance can cause major instability problems in both cases.

MS2 showed stable conditions for most simulations, including *WFP* and *WC*. Due to extremely low confinements, for *WC*=90%, the remaining untethered foliation planes (less than 10%) with M_a=60% avoided global instability problems. On the other hand, the low confinement was unfavorable in the critical cases of isolated *WFP*s with null cohesion and tensile strength (Fig. 5.18b).

5.6 Conclusions

The following summary and conclusions can be provided for the study conducted:

1. The MST is an old tunnel with intense train traffic that is important for iron ore transportation on the Vitória-Minas Railway. The tunnel was constructed in the 1950s in a gneissic rock mass and contains four discontinuity sets, including fractures (F1, F2 and F3) and metamorphic foliation. Regardless of 5 m of structural concrete in each portal, the MST does not have any kind of support system and has remained stable since its excavation.

2. The results of RMR_{14}, Q and GSI indicated moderate to poor rock mass qualities for MS1 and MS2. This result agrees with the DEM results, ignoring the inherent cohesion and tensile strength of foliation planes. However, this assumption is unrealistic and substantially underestimates the rock mass quality. The laboratory tests and DEM results indicated that M_a=60% (or lower) is representative of the actual tunnel conditions; thus, the fresh foliation planes on the MST gneissic rock mass can explain the current tunnel stability.

3. Even though the MST is currently stable, the evidence of weathering advances on MS1 and MS2 pointed to the need for DEM analyses considering this issue. From the DEM results, isolated *WFPs* can cause significant instability problems, especially in MS1. Moreover, two *WFPs* in critical positions could cause global instabilities in both MS1 and MS2. The increase in *WC* caused progressive instability problems in MS1, which became critical for *WC*>50%. MS2 was stable in intense weathering conditions represented by *WC*. In this section, only *WC*=90% caused relevant instability problems in the tunnel. However, even in such weathering conditions, a few fresh foliation contacts (e.g., 10%) with expressive cohesion and tensile strength (M_a=60%) guaranteed global tunnel stability.

4. In practical rock mechanics applications, discontinuity sets are often treated as joint sets, regardless of the type and genesis of each geological structure, and friction-based models (linear and nonlinear) are assumed to represent the mechanical behavior of such discontinuity sets. The case study in this paper indicated that more attention should be given to understanding the mechanical behavior of intrablock structures, such as metamorphic foliation, as these structures play an important role in the stability of engineering structures such as the MST.

Chapter 6

Final Remarks

6.1 General conclusions

This thesis presented a coupled TRS-DFN-DEM approach developed for modeling tunnels in discontinuous rock masses with marked metamorphic foliation. The laboratory program focused on assessing the shear and tensile strength of isolated foliation planes with variable mica content. The direct shear test (under CNL and CNS conditions) and the pull-off test were used for these purposes.

The pull-off test is a practical method for estimating the direct tensile strength of rocks and geological discontinuities and can be employed in situ. However, the POT failure modes must be described because they are important for verifying the influence of the partial core boundary conditions that underestimate the tensile strength. Moreover, this test is suitable for assessing the tensile strength of geological discontinuities along anisotropic and heterogeneous rocks because it captures the natural strength variability of the rock fabric. In situ, the POT can be applied perpendicular to large bedding and foliation planes exposed on rock outcrops and blocks.

This thesis introduced the M_a (percentage of foliation surface area covered by mica) as a practical parameter for quantifying the mica content on foliation planes. The image analysis method used for quantifying M_a was simple and efficient because biotite was the only dark mineral with a substantial content in the biotite gneiss. The two-step direct shear test avoided major damages to the foliation surfaces before quantifying M_a.

Laboratory results showed that the shear and tensile strength varies nonlinearly with respect to M_a, and a power function with 3 constant parameters ($\alpha_{t,c,\varphi}$, $\beta_{t,c,\varphi}$ and $n_{t,c,\varphi}$) showed a good fit to the laboratory data. The peak shear strength was strongly influenced by M_a. In the postpeak stage, M_a had a partial effect on the shear strength because of the variable failure surface morphologies created after the peak stage. The same effects were observed on the postpeak shear stiffness and dilation angle. Thus, the M_a parameter alone is effective in predicting the peak shear strengths of foliation planes but not in predicting their postpeak behaviors.

Most foliation planes dilated both during the peak stage due to the mineral fracturing process and during postpeak stages due to the surface morphology. Under CNS conditions, this dilation caused an increase in normal stress; hence, the shear strength increased in both DST stages. On the other hand, shear failures of the foliation planes with high M_a and thick biotite layers occurred as a result of normal stress relief caused by excessive damage (contraction), which

reduced the shear strength. It is important to mention that the shear zones in DSTs are laterally unconfined, which may not be the case in most real CNS conditions. The nonlinear 3D peak strength envelope presented in this thesis included M_a as an independent variable for predicting the tensile strength cut-off, cohesion and friction angle. The good fit obtained indicates that this 3D envelope is suitable for low confinement conditions.

The DFN generation and, consequently, the creation of representative DEM models were feasible after the detailed discontinuity mapping via TRS (TLS in this case). TLS is a suitable tool for discontinuity mapping in tunnels because it allows the same level of detail in all the regions of the tunnel. However, care must be taken when selecting the traces contained in discontinuity planes to represent the chords of disk-shaped discontinuities in DFNs. Moreover, many of the discontinuities apparent in the tunnel have insufficient exposed area for a reliable orientation measurement; thus, it is not possible to attribute one orientation value to every trace length measured.

The discontinuity size analysis in this work is based on window sampling methods for unbiased trace length and discontinuity size determination. The automation of these methods allowed the continuous calculation of P_{32} along the tunnel and creation of continuous DFNs. Comparisons of DFN-based and TLS-based P_{21} indicated the good agreement between TLS mapping and the DFN models generated for each discontinuity set. Therefore, continuous DFNs are a practical alternative that better represent the heterogeneity of discontinuity distributions along the tunnel (in the tunnel axis direction) increasing similarities between TLS mapping and DFN-3DEC models.

The coupled TRS-DFN-DEM approach was applied to the MST, which is an old tunnel with intense train traffic, important to the iron ore transportation on the Vitória-Minas Railway. Although the results of RMR_{14}, Q and GSI indicated sections of moderate to poor rock mass qualities, the MST does not have any kind of support system and stands stable since its excavation (regardless 5m of structural concrete in each portal).

The DEM results from models with null cohesion and tensile strength attributed to foliation planes (*OFP* cases) showed an agreement with the classification system (requirement of immediate support installation). However, this assumption is unrealistic and underestimates substantially the rock mass quality. The laboratory tests and DEM results indicated that

M_a=60% (or lower) is representative to the actual tunnel conditions; thus, the mica content on fresh foliation planes of the gneissic rock mass can explain the current MST stability.

Although the tunnel is currently stable, the weathering advance on the tunnel sections MS1 and MS2 pointed to the need for DEM analyses considering different weathering scenarios. Isolated *WFP* can cause significant instability problems, especially to MS1. General weathering advance (represented by the *WC* parameters) causes instability problems only for *WC*>50%, but such conditions were not observed at the tunnel site. Nevertheless, weathering is a dynamic process, which evolves over time. Thus, general weathering advances over potentially weathered zones should be taken into account depending on the remaining life-time of the tunnel.

In practical Rock Mechanics, discontinuity sets are often treated as joint sets, regardless the type and genesis of each geological structure, assuming friction-based models (linear and non-linear) to represent their mechanical behavior. This case study indicated that more attention should be given for understanding the mechanical behavior of intact foliation planes, as they have an important hole on the stability of engineering structures such as the MST.

6.2 Recommendations

Further experiments are required to extend the number of rock types tested by the POT, DTT, and BDT, improving the correlations between tests. Moreover, numerical analyses using fracture mechanics principles are required to better explain and quantify the difference between σ_{POT}, σ_{DTT} and σ_{BDT} for rocks and geological discontinuities associated with the failure modes observed in laboratory tests.

The analysis method used for quantifying M_a was simple and efficient because biotite was the only dark mineral with a substantial content in the biotite gneiss. Other methods may be necessary for quantifying mica minerals of different colors (such as muscovite) in other rock types.

For higher confinements (>10 MPa of normal stress) the relation between normal and shear stresses is likely non-linear. In this case, the 3D strength envelope would be non-linear in both M_a and σ_n directions; thus, the Mohr-Coulomb criteria would not be suitable. More lab tests are necessary to confirm such double non-linear behavior.

The example used in Fig. 4.16 showed that DEM created by C-DFNs could be promising for assessing the stability of tunnel excavation fronts within the time frames available between tunnel advances. However, it is necessary to perform real tests to verify whether it is suitable, considering the operational difficulties in tunnel construction environments.

6.3 List of academic contributions of this thesis

Journal articles (published)

Cacciari, PP; Futai, MM. Modeling a Shallow Rock Tunnel Using Terrestrial Laser Scanning and Discrete Fracture Networks. *Rock Mechanics and Rock Engineering*, v. 50, p. 1217-1242, 2017.

Cacciari, PP; Futai, MM. Assessing the tensile strength of rocks and geological discontinuities via pull-off tests. *International Journal of Rock Mechanics and Mining Sciences*, v. 105, p. 44-52, 2018.

Journal articles (submitted or in preparation)

Cacciari, PP; Futai, MM. Laboratory assessment of rock foliation strength with different mica content. (Under review - journal: *International Journal of Rock Mechanics and Mining Sciences*).

Cacciari, PP; Futai, MM. The Influence of Fresh and Weathered Rock Foliation Planes on the Stability of the Monte Seco Tunnel. (In preparation - journal: *to be defined*).

Fully refereed conference papers (published)

Cacciari, PP; Futai, MM. Integrating Terrestrial Laser Scanning and Discrete Fracture Networks Approaches for Tunnel Modelling in Fractured Rock Masses. In: VII Simpósio Brasileiro de Mecânica das Rochas, 2016, Belo Horizonte

Cacciari, PP; Morikawa, DS; Futai, MM. Modelling a Railway Rock Tunnel Using Terrestrial Laser Scanning and The Distinct Element Method. In: 8th South American Congress on Rock Mechanics, 2015, Buenos Aires. Proceedings of the 8th South American Congress on Rock Mechanics, 2015.

Cacciari, PP; Vizini, VOS; Futai, MM. The pull-off test for obtaining the tensile strength of rock materials. In: 52nd US Rock Mechanics / Geomechanics Symposium, 2018, Seattle. US Rock Mechanics / Geomechanics Symposium. Washington: AMRA, 2018.

Collaborative articles related to this thesis (submitted or in preparation)

Monticelli, JP; **Cacciari, PP**; Futai, MM. Conceptual weathering model of gneissic rock masses in tropical climate conditions (In preparation - journal: *to be defined*).

Vizini, VOS; **Cacciari, PP**; Futai, MM. Numerical assessment of factors influencing the tensile strength of rocks via Pull-off test. (Under review - journal: International Journal of Geomechanics).

References

Amadei B (1996) Importance of anisotropy when estimating and measuring in situ stresses in rock. Int J Rock Mech Min Sci Geomech 33:293–325. doi: 10.1016/0148-9062(95)00062-3

ASTM (2013) Standard Test Method for Tensile Strength of Concrete Surfaces and the Bond Strength or Tensile Strength of Concrete Repair and Overlay Materials by Direct Tension (Pull-off Method). ASTM Int 1–4. doi: 10.1520/C1583

Attewell PB, Sandfordt MR (1974) Intrinsic Shear Strength of a Brittle, Anisotropic Rock - III Textural Interpretation of Failure. Int J Rock Mech Min Sci Geomech Abstr 11:439–451

Austin S, Robins P, Pan Y (1995) Tensile bond testing of concrete repairs. Mater Struct 28:249–259. doi: 10.1007/BF02473259

Baecher GB (1980) Progressively Censored Sampling of Rock Joint Traces 1. Math Geol 12:33–40. doi: 10.1007/BF01039902

Bahrani N, Hadjigeorgiou J (2018) Influence of Stope Excavation on Drift Convergence and Support Behavior: Insights from 3D Continuum and Discontinuum Models. Rock Mech Rock Eng 51:2395–2413. doi: 10.1007/s00603-018-1482-5

Bandis SC, Lumsden AC, Barton NR (1983) Fundamentals of Rock Joint Deformation. Int J Rock Mech Min Sci Geomech Abstr 20:249–268

Barton N, Choubey V (1977) The shear strength of rock joints in theory and practice. Rock Mech 10:1–54. doi: 10.1007/BF01261801

Barton N, Lien R, Lunde J (1974) Engineering classification of rock masses for the design of tunnel support. Rock Mech 6:189–236. doi: 10.1007/BF01239496

Basu A, Mishra DA, Roychowdhury K (2013) Rock failure modes under uniaxial compression, Brazilian, and point load tests. Bull Eng Geol Environ 72:457–475. doi: 10.1007/s10064-013-0505-4

Behrestaghi MHN, Seshagiri Rao K, Ramamurthy T (1996) Engineering geological and geotechnical responses of schistose rocks from dam project areas in India. Eng Geol

44:183–201. doi: 10.1016/s0013-7952(96)00069-5

Bewick RP, Kaiser PK, Bawden WF (2014a) DEM simulation of direct shear: 2. Grain boundary and mineral grain strength component influence on shear rupture. Rock Mech Rock Eng 47:1673–1692. doi: 10.1007/s00603-013-0494-4

Bewick RP, Kaiser PK, Bawden WF (2014b) Shear rupture under constant normal stiffness boundary conditions. Tectonophysics 634:76–90. doi: 10.1016/j.tecto.2014.07.016

Bewick RP, Kaiser PK, Bawden WF, Bahrani N (2014c) DEM simulation of direct shear: 1. Rupture under constant normal stress boundary conditions. Rock Mech Rock Eng 47:1647–1671. doi: 10.1007/s00603-013-0490-8

Bhasin R, Hoeg K (1998) Parametric study for a large cavern in jointed rock using a distinct element model (UDEC-BB). 35:17–29

Bonaldo E, Barros JAO, Lourenço PB (2005) Bond characterization between concrete substrate and repairing SFRC using pull-off testing. Int J Adhes Adhes 25:463–474. doi: 10.1016/j.ijadhadh.2005.01.002

Bungey J, Madandoust R (1992) Factor influencing pull-off tests on concrete. Mag Concr Res 44:21–30. doi: 10.1680/macr.1992.44.158.21

Cacciari PP (2014) Study of a tunnel constructed in a fractured rock mass using geological and geotechnical surveys and the distinct element method. Martser Dissertation. University of São Paulo

Cacciari PP, Futai MM (2016a) Integrating Terrestrial Laser Scanning and Discrete Fracture Networks Approaches for Tunnel Modelling in Fractured Rock Masses. An do VII Simpósio Bras Mecânica das Rochas. doi: 10.20906/cps/sbmr-06-0030

Cacciari PP, Futai MM (2016b) Mapping and characterization of rock discontinuities in a tunnel using 3D terrestrial laser scanning. Bull Eng Geol Environ 75:223–237. doi: 10.1007/s10064-015-0748-3

Cacciari PP, Futai MM (2017) Modeling a Shallow Rock Tunnel Using Terrestrial Laser Scanning and Discrete Fracture Networks. Rock Mech Rock Eng 50:1217–1242. doi: 10.1007/s00603-017-1166-6

Cacciari PP, Futai MM (2018a) Assessing the tensile strength of rocks and geological discontinuities via pull-off tests. Int J Rock Mech Min Sci 105:44–52. doi: 10.1016/j.ijrmms.2018.03.011

Cacciari PP, Futai MM (2018b) The pull-off test for obtaining the tensile strength of rock materials. 52nd US Rock Mech / Geomech ARMA Symp Seattle

Cacciari PP, Futai MM (2019) Effects of Mica Content on Rock Foliation Strength. Int J Rock Mech Min Sci (paper under review)

Cacciari PP, Morikawa DS, Futai MM (2015) Modelling a railway rock tunnel using terrestrial laser scanning and the distinct element method. ISRM Reg Symp - 8th South Am Congr Rock Mech SACRM 2015 2015-Novem:101–108. doi: 10.3233/978-1-61499-605-7-101

Celada B, Tardáguila I, Varona P, Bieniawski ZT (2014) Innovating Tunnel Design by an Improved Experience-based RMR System. World Tunn Congr 2014 – Tunnels a better Life 3:1–9

Chen YF, Wei K, Liu W, et al (2016) Experimental Characterization and Micromechanical Modelling of Anisotropic Slates. Rock Mech Rock Eng 49:3541–3557. doi: 10.1007/s00603-016-1009-x

Cho J-W, Kim H, Jeon S, Min K-B (2012) Deformation and strength anisotropy of Asan gneiss, Boryeong shale, and Yeoncheon schist. Int J Rock Mech Min Sci 50:158–169. doi: 10.1016/j.ijrmms.2011.12.004

Cho N, Martin CD, Sego DC (2008) Development of a shear zone in brittle rock subjected to direct shear. Int J Rock Mech Min Sci 45:1335–1346. doi: 10.1016/j.ijrmms.2008.01.019

Coviello A, Lagioia R, Nova R (2005) On the measurement of the tensile strength of soft rocks. Rock Mech Rock Eng 38:251–273. doi: 10.1007/s00603-005-0054-7

Cox MR, Budhu M (2008) A practical approach to grain shape quantification. Eng Geol 96:1–16. doi: 10.1016/j.enggeo.2007.05.005

Crosta G (1997) Evaluating rock mass geometry from photographic images. Rock Mech Rock Eng 30:35–58. doi: 10.1007/BF01020112

Cruden DM (1977) Describing the size of discontinuities. Int J Rock Mech Min Sci 14:133–137. doi: 10.1016/0148-9062(77)90004-3

Cundall PA (1988) Formulation of a Three-dimensional Distinct Element M odel Part I. A Scheme to Detect and Represent Contacts in a System Composed of Many Polyhedral Blocks. Int J Rock Mech Min Sci Geomech 25:107–116

Curtaz M, Ferrero AM, Roncella R, et al (2014) Terrestrial photogrammetry and numerical modelling for the stability analysis of rock slopes in high mountain areas: Aiguilles marbrées case. Rock Mech Rock Eng 47:605–620. doi: 10.1007/s00603-013-0446-z

Day JJ, Diederichs MS, Hutchinson DJ (2017) New direct shear testing protocols and analyses for fractures and healed intrablock rockmass discontinuities. Eng Geol 229:53–72. doi: 10.1016/j.enggeo.2017.08.027

Dershowitz WS, Einstein HH (1988) Characterizing rock joint geometry with joint system models. Rock Mech Rock Eng 21:21–51. doi: https://doi.org/10.1007/BF01019674

Dershowitz WS, Herda HH (1992) Interpretation of fracture spacing and intensity. In: 33th U.S. Symposium on Rock Mechanics (USRMS). Santa Fe, pp 757–766

Donath FA (1972) Effects of Cohesion and Granularity on Deformational Behavior of Anisotropic Rock. Geol Soc Am Mem 95–128. doi: 10.1130/mem135-p95

Donath FA (1961) Experimental study of shear failure in anisotropic rocks. Geol Soc Am Bull 72:985–990. doi: 10.1007/bf00203353

Elmo D (2006) Evaluation of a hybrid FEM/DEM approach for determination of rock mass strength using a combination of discontinuity mapping and fracture mechanics modelling, with particular emphasis on modelling of jointed pillars. Thesis. University of Exter

Erarslan N, Williams DJ (2012) Experimental, numerical and analytical studies on tensile strength of rocks. Int J Rock Mech Min Sci 49:21–30. doi: 10.1016/j.ijrmms.2011.11.007

Faro Technologies (2016) Focus 3D laser scanner. Faro Technologies Inc. 2016

Fekete S, Diederichs M (2013) Integration of three-dimensional laser scanning with discontinuum modelling for stability analysis of tunnels in blocky rockmasses. Int J Rock

Mech Min Sci 57:11–23. doi: 10.1016/j.ijrmms.2012.08.003

Fekete S, Diederichs M, Lato M (2010) Geotechnical and operational applications for 3-dimensional laser scanning in drill and blast tunnels. Tunn Undergr Sp Technol 25:614–628. doi: 10.1016/j.tust.2010.04.008

Ferrero a. M, Forlani G, Roncella R, Voyat HI (2008) Advanced Geostructural Survey Methods Applied to Rock Mass Characterization. Rock Mech Rock Eng 42:631–665. doi: 10.1007/s00603-008-0010-4

Ferrero AM, Maria M, Paolo GG (2004) Analysis of tunnel stability: comparison between continuous and discontinuous approaches. Int J Rock Mech Min Sci 41:646–651. doi: 10.1016/j.ijrmms.2004.03.113

Ferrero AM, Umili G (2011) Comparison of methods for estimating fracture size and intensity applied to Aiguille Marbrée (Mont Blanc). Int J Rock Mech Min Sci 48:1262–1270. doi: 10.1016/j.ijrmms.2011.09.011

Firpo G, Salvini R, Francioni M, Ranjith PG (2011) Use of Digital Terrestrial Photogrammetry in rocky slope stability analysis by Distinct Elements Numerical Methods. Int J Rock Mech Min Sci 48:1045–1054. doi: 10.1016/j.ijrmms.2011.07.007

Francioni M, Salvini R, Stead D, Litrico S (2014) A case study integrating remote sensing and distinct element analysis to quarry slope stability assessment in the Monte Altissimo area, Italy. Eng Geol 183:290–302. doi: 10.1016/j.enggeo.2014.09.003

Ghazvinian E, Diederichs MS, Labrie D, Martin CD (2015) An Investigation on the Fabric Type Dependency of the Crack Damage Thresholds in Brittle Rocks. Geotech Geol Eng 33:1409–1429. doi: 10.1007/s10706-015-9909-1

Han X, Chen J, Wang Q, et al (2016) A 3D Fracture Network Model for the Undisturbed Rock Mass at the Songta Dam Site Based on Small Samples. Rock Mech Rock Eng 49:611–619. doi: 10.1007/s00603-015-0747-5

Hart R, Cundall PA, Lemos J (1988) Formulation of a three-dimensional distinct element model-Part II. Mechanical calculations for motion and interaction of a system composed of many polyhedral blocks. Int J Rock Mech Min Sci 25:117–125. doi: 10.1016/0148-

9062(88)92294-2

Hashiba K, Okada T, Tani K, et al (2017) Literature survey and experimental study on the direct tension test on rocks. Geotech Test J 40:335–344. doi: 10.1520/GTJ20160201

Havaej M, Coggan J, Stead D, Elmo D (2016) A combined remote sensing–numerical modelling approach to the stability analysis of delabole slate quarry, Cornwall, UK. Rock Mech Rock Eng 49:1227–1245. doi: 10.1007/s00603-015-0805-z

He S, Li Y, Aydin A (2018) A comparative study of UDEC simulations of an unsupported rock tunnel. Tunn Undergr Sp Technol 72:242–249. doi: 10.1016/j.tust.2017.11.031

Hudson JA, Crouch SL, Fairhurst C (1972) Soft, stiff and servo-controlled testing machines: a review with reference to rock failure. Eng Geol 6:155–189. doi: 10.1016/0013-7952(72)90001-4

Indraratna B, Haque A (1997) Experimental study of shear behavior of rock joints under constant normal stiffness conditions. 34:141.e1-141.e14. doi: doi: 10.1016/S1365-1609(97)00068-3

InnovMetric Software (2014) Polyworks version 2014. 561–565

ISRM (1978) Suggested methods for determining tensile strength of rock materials. Int J Rock Mech Min Sci Geomech Abstr 15:99–103

Itasca (2014) 3DEC version 5.00. Itasca Consulting Group Inc. 2014

Jiang Y, Xiao J, Tanabashi Y, Mizokami T (2004) Development of an automated servo-controlled direct shear apparatus applying a constant normal stiffness condition. Int J Rock Mech Min Sci 41:275–286. doi: 10.1016/j.ijrmms.2003.08.004

Johnston IW, Lam TSK, Williams AF (1987) Socketed Pile Design in Weak Rock. 37:83–89. doi: 10.1680/geot.1987.37.1.83

Kemeny J, Turner K, Norton B (2006) LIDAR for rock mass characterization: hardware, software, accuracy and best-practices. In: Proceedings of the workshop on laser and photogrammetric methods for rock face characterization. In: Proceedings of the workshop on laser and photogrammetric methods for rock face characterization. Golden, pp 49–61

Kim BH, Cai M, Kaiser PK, Yang HS (2007) Estimation of block sizes for rock masses with non-persistent joints. Rock Mech Rock Eng 40:169–192. doi: 10.1007/s00603-006-0093-8

Kulatilake PHSW, Wu TH (1984) Estimation of mean trace length of discontinuities. Rock Mech Rock Eng 17:215–232. doi: 10.1007/BF01032335

Lato M, Diederichs MS, Hutchinson DJ, Harrap R (2009) Optimization of LiDAR scanning and processing for automated structural evaluation of discontinuities in rockmasses. Int J Rock Mech Min Sci 46:194–199. doi: 10.1016/j.ijrmms.2008.04.007

Lato MJ, Diederichs MS, Hutchinson DJ (2010) Bias correction for view-limited lidar scanning of rock outcrops for structural characterization. Rock Mech Rock Eng 43:615–625. doi: 10.1007/s00603-010-0086-5

Laws S, Eberhardt E, Loew S, Descoeudres F (2003) Geomechanical properties of shear zones in the eastern aar massif, Switzerland and their implication on tunnelling. Rock Mech Rock Eng 36:271–303. doi: 10.1007/s00603-003-0050-8

Leichnitz W (1985) Mechanical properties of rock joints. Int J Rock Mech Min Sci 22:313–321. doi: 10.1016/0148-9062(85)92063-7

Li D, Wong LNY (2013) The brazilian disc test for rock mechanics applications: Review and new insights. Rock Mech Rock Eng 46:269–287. doi: 10.1007/s00603-012-0257-7

Liu J, Chen L, Wang C, et al (2014) Characterizing the mechanical tensile behavior of Beishan granite with different experimental methods. Int J Rock Mech Min Sci 69:50–58. doi: 10.1016/j.ijrmms.2014.03.007

Mah J, McKinnon SD, Samson C, Thibodeau D (2016) Wire mesh filtering in 3D image data of rock faces. Tunn Undergr Sp Technol 52:111–118. doi: 10.1016/j.tust.2015.11.005

Mah J, Samson C, McKinnon SD (2011) 3D laser imaging for joint orientation analysis. Int J Rock Mech Min Sci 48:932–941. doi: 10.1016/j.ijrmms.2011.04.010

Marinos PG, Hoek E (2000) GSI: A geologically friendly tool for rock mass strength estimation. Proc GeoEng2000 Int Conf Geotech Geol Eng

Mauldon M (1998) Estimating Mean Fracture Trace Length and Density from Observations in Convex Windows. Rock Mech Rock Eng 31:201–216. doi: 10.1007/s006030050021

Mauldon M, Dunne WM, Jr MBR (2001) Circular scanlines and circular windows : new tools for characterizing the geometry of fracture traces. 23:247–258

McCabe WM, Koerner RM (1975) High pressure shear strength investigation of an anisotropic mica schist rock. Int J Rock Mech Min Sci 12:219–228. doi: 10.1016/0148-9062(75)91402-3

McLamore R, Gray KE (2011) The Mechanical Behavior of Anisotropic Sedimentary Rocks. J Eng Ind 89:62. doi: 10.1115/1.3610013

McNeel (2014) Rhinoceros, modelling tool for designers. McNeel North America

Mello LGF. de (EPUSP), Sadowski GR (IGc U, Nieble CM (Matr. E (2004) Shear Resistance Of Biotite-Schist : Peak And Post- Peak Behaviour. Adv Geotech Eng Skempt Conf 1–10

Merlini D, Stocker D, Falanesca M, Schuerch R (2018) The Ceneri Base Tunnel: Construction Experience with the Southern Portion of the Flat Railway Line Crossing the Swiss Alps. Engineering 4:235–248. doi: 10.1016/j.eng.2017.09.004

Momayez A, Ehsani MR, Ramezanianpour AA, Rajaie H (2005) Comparison of methods for evaluating bond strength between concrete substrate and repair materials. Cem Concr Res 35:748–757. doi: 10.1016/j.cemconres.2004.05.027

Monticeli JP, Cantarella VP, Cacciari PP, Futai MM (2015) Roughness characterization of discontinuity sets by profilometer and scanner images. ISRM Reg Symp - 8th South Am Congr Rock Mech SACRM 2015 2015-Novem:85–92. doi: 10.3233/978-1-61499-605-7-85

Monticelli J (2019) Appendix I - Conceptual weathering model of gneissic rock masses in tropical climate conditions. University of São Paulo

Nasseri MHB, Rao KS, Ramamurthy T (2003) Anisotropic strength and deformation behavior of Himalayan schists. Int J Rock Mech Min Sci 40:3–23. doi: 10.1016/S1365-1609(02)00103-X

Niemeijer AR, Spiers CJ (2005) Influence of phyllosilicates on fault strength in the brittle-ductile transition: insights from rock analogue experiments. Geol Soc London, Spec Publ 245:303–327. doi: 10.1144/gsl.sp.2005.245.01.15

Oliveira D, Diederichs MS (2017) Tunnel support for stress induced failures in Hawkesbury Sandstone. Tunn Undergr Sp Technol 64:10–23. doi: 10.1016/j.tust.2017.01.003

Pahl PJ (1981) Estimating the mean length of discontinuity traces. Int J Rock Mech Min Sci 18:221–228. doi: 10.1016/0148-9062(81)90976-1

Park B, Min K (2015) International Journal of Rock Mechanics & Mining Sciences Bonded-particle discrete element modeling of mechanical behavior of transversely isotropic rock. Int J Rock Mech Min Sci 76:243–255. doi: 10.1016/j.ijrmms.2015.03.014

Park JW, Lee YK, Song JJ, Choi BH (2013) A constitutive model for shear behavior of rock joints based on three-dimensional quantification of joint roughness. Rock Mech Rock Eng 46:1513–1537. doi: 10.1007/s00603-012-0365-4

Perras MA, Diederichs MS (2014) A Review of the Tensile Strength of Rock: Concepts and Testing. Geotech Geol Eng 32:525–546. doi: 10.1007/s10706-014-9732-0

Petit JP (1988) Normal stress dependent rupture morphology in direct shear tests on sandstone with applications to some natural fault surface features. Int J Rock Mech Min Sci 25:411–419. doi: 10.1016/0148-9062(88)90981-3

Prassetyo SH, Gutierrez M, Barton N (2017) Nonlinear shear behavior of rock joints using a linearized implementation of the Barton–Bandis model. J Rock Mech Geotech Eng 9:671–682. doi: 10.1016/j.jrmge.2017.01.006

Ramamurthy T, Rao GV, Singh J (1993) Engineering behaviour of phyllites. Eng Geol 33:209–225. doi: 10.1016/0013-7952(93)90059-L

Rasband W (2004) ImageJ - Image Processing and Analysis in Java. National Institutes of Health, Bethesda, Maryland, USA. Available at: http://rsb.info.nih.gov/ij/.

Rawling GC, Baud P, Wong T (2002) Dilatancy, brittle strength, and anisotropy of foliated rocks: Experimental deformation and micromechanical modeling. J Geophys Res Solid Earth 107:ETG 8-1-ETG 8-14. doi: 10.1029/2001jb000472

Rogers S, Elmo D, Webb G, Catalan A (2014) Volumetric Fracture Intensity Measurement for Improved Rock Mass Characterisation and Fragmentation Assessment in Block Caving Operations. Rock Mech Rock Eng 48:633–649. doi: 10.1007/s00603-014-0592-y

Saeb S, Amadei B (1992) Modelling of rock joints under shear and normal loading. Int J Rock Mech Min Sci Geomech Abstr 29:267–278. doi: 10.1016/0148-9062(92)93660-C

Sainsbury BL, Sainsbury DP (2017) Practical Use of the Ubiquitous-Joint Constitutive Model for the Simulation of Anisotropic Rock Masses. Rock Mech Rock Eng 50:1507–1528. doi: 10.1007/s00603-017-1177-3

Saroglou H, Tsiambaos G (2008) A modified Hoek-Brown failure criterion for anisotropic intact rock. Int J Rock Mech Min Sci 45:223–234. doi: 10.1016/j.ijrmms.2007.05.004

Schlotfeldt P, Carter TG (2018) A new and unified approach to improved scalability and volumetric fracture intensity quanti fi cation for GSI and rockmass strength and deformability estimation. Int J Rock Mech Min Sci 110:48–67. doi: 10.1016/j.ijrmms.2018.06.021

Seidel JP, Haberfield CM (2002) A theoretical model for rock joints subjected to constant normal stiffness direct shear. Int J Rock Mech Min Sci 39:539–553. doi: 10.1016/S1365-1609(02)00056-4

Shang J, Hencher SR, West LJ (2016) Tensile Strength of Geological Discontinuities Including Incipient Bedding, Rock Joints and Mineral Veins. Rock Mech Rock Eng 49:4213–4225. doi: 10.1007/s00603-016-1041-x

Shea WT, Kronenberg AK (1993) Strength and anisotropy of foliated rocks with varied mica contents. J Struct Geol 15:1097–1121. doi: 10.1016/0191-8141(93)90158-7

Slob S, Hack HRGK, Feng Q, et al (2007) Fracture mapping using 3D laser scanning techniques. 11th Congr Int Soc Rock Mech 299-302.

Solak T (2009) Ground behavior evaluation for tunnels in blocky rock masses. Tunn Undergr Sp Technol 24:323–330. doi: 10.1016/j.tust.2008.10.004

Spagnoli G, Jahn A, Halbach P (2016) First results regarding the influence of mineralogy on the mechanical properties of seafloor massive sulfide samples. Eng Geol 214:127–135.

doi: 10.1016/j.enggeo.2016.10.007

Spreafico MC, Francioni M, Cervi F, et al (2016) Back analysis of the 2014 san leo landslide using combined terrestrial laser scanning and 3D distinct element modelling. Rock Mech Rock Eng 49:2235–2251. doi: 10.1007/s00603-015-0763-5

Strouth A, Eberhardt E (2006) The use of LiDAR to overcome rock slope hazard data collection challenges at Afternoon Creek, Washington. Proc 41st US Symp Rock Mech Golden Am Rock Mech Assoc CD 6–993

Sturzenegger M, Stead D (2009) Quantifying discontinuity orientation and persistence on high mountain rock slopes and large landslides using terrestrial remote sensing techniques. 267–287

Sturzenegger M, Stead D, Elmo D (2011) Terrestrial remote sensing-based estimation of mean trace length, trace intensity and block size/shape. Eng Geol 119:96–111. doi: 10.1016/j.enggeo.2011.02.005

Szemerey-Kiss B, Török Á (2017) Failure mechanisms of repair mortar stone interface assessed by pull-off strength tests. Bull Eng Geol Environ 76:159–167. doi: 10.1007/s10064-016-0964-5

Tang Z, Tolooiyan A, Mackay R (2017) Unconfined Expansion Test (UET) for measuring the tensile strength of organic soft rock. Comput Geotech 82:54–66. doi: 10.1016/j.compgeo.2016.09.016

Terzaghi RD (1965) Sources of Error in Joint Surveys. Géotechnique 15:287–304. doi: 10.1680/geot.1965.15.3.287

Thirukumaran S, Indraratna B (2016) A review of shear strength models for rock joints subjected to constant normal stiffness. J Rock Mech Geotech Eng 8:405–414. doi: 10.1016/j.jrmge.2015.10.006

Umili G, Ferrero a., Einstein HH (2013) A new method for automatic discontinuity traces sampling on rock mass 3D model. Comput Geosci 51:182–192. doi: 10.1016/j.cageo.2012.07.026

Vardakos SS, Gutierrez MS, Barton NR (2007) Back-analysis of Shimizu Tunnel No. 3 by

distinct element modeling. Tunn Undergr Sp Technol 22:401–413. doi: 10.1016/j.tust.2006.10.001

Warburton PM (1980) A stereological interpretation of joint trace data. Int J Rock Mech Min Sci Geomech 17:181–190. doi: 10.1016/0148-9062(80)91084-0

Wu Q, Kulatilake PHSW (2012) Application of equivalent continuum and discontinuum stress analyses in three-dimensions to investigate stability of a rock tunnel in a dam site in China. Comput Geotech 46:48–68. doi: 10.1016/j.compgeo.2012.05.013

Wu Q, Kulatilake PHSW, Tang H ming (2011) Comparison of rock discontinuity mean trace length and density estimation methods using discontinuity data from an outcrop in Wenchuan area, China. Comput Geotech 38:258–268. doi: 10.1016/j.compgeo.2010.12.003

Zeeb C, Gomez-Rivas E, Bons PD, et al (2013) Fracture network evaluation program (FraNEP): A software for analyzing 2D fracture trace-line maps. Comput Geosci 60:11–22. doi: 10.1016/j.cageo.2013.04.027

Zhang L, Einstein HH (1998) Estimating the mean trace length of rock discontinuities. Rock Mech Rock Eng 31:217–235. doi: 10.1007/s006030050022

Zhang L, Einstein HH (2000) Estimating the intensity of rock discontinuities. Int J Rock Mech Min Sci 37:819–837. doi: 10.1016/S1365-1609(00)00022-8